POST-INFARCTION RESCUE OF MYOCARDIAL FUNCTION USING HEMIN

by

Ashley Lynn Eadie

Submitted in partial fulfilment of the
requirements for the degree of Doctor of Philosophy

at

Dalhousie University
Halifax, Nova Scotia
January 2024

A smooth sea
never made a good sailor.

TABLE OF CONTENTS

LIST OF TABLES

LIST OF FIGURES

ABSTRACT

Acute myocardial infarction is a major contributor to heart failure but has yet to be fully addressed through current therapeutic interventions. In experimental models of myocardial infarction, pre-emptive heme oxygenase-1 induction directly reduces oxidative stress and inflammation, while limiting pathological fibrotic remodeling and promoting functional cardioprotection. Heme oxygenase-1 elicits cytoprotection through the catabolism of free heme—the functional group by which oxygen is transported in proteins such as hemoglobin, myoglobin, and cytochromes involved in ATP production—into antioxidant and anti-inflammatory by-products. Whether heme oxygenase-1 induction is effective when initiated post-myocardial infarction and how cardiac heme content is endogenously regulated in response to injury is unclear.

Here we show that experimental acute myocardial infarction causes temporal dyssynchrony between left ventricular heme content and heme regulatory enzyme expression. Further, we show that hemin—a potent inducer and substrate of heme oxygenase-1—improves cardiac function in experimental models of acute myocardial infarction in a time-dependent manner. We also show for the first time that hemin is capable of directly increasing human cardiac tissue contractility *in vitro* (by an apparently calcium-independent mechanism), and explore the therapeutic potential of two novel strategies that could be translated for more rapid/targeted delivery of HMOX1/hemin to the infarcted heart: the encapsulation of hemin into a nanoparticle shell (Niohemin), and the exogenous delivery of functional HMOX1 using a cell-penetrating peptide (HMOX1-CPP). Collectively, the findings presented herein provide fundamental information with which to advance the therapeutic targeting of heme metabolism in the heart.

LIST OF ABBREVIATIONS USED

5-ALA	δ-aminolevulinic acid
ABCB	ATP Binding Cassette Subfamily B Member
ACE	angiotensin-converting enzyme
ADP	adenosine di-phosphate
AIP	acute intermittent porphyria
ALAD	δ-aminolevulinic acid dehydratase
ALAS	δ-aminolevulinic acid synthases
AMI	acute myocardial infarction
AMCM	adult mouse cardiomyocyte
ANOVA	Analysis of Variance
AP-1	activator protein-1
ARB	angiotensin II receptor blocker
ARNi	angiotensin II receptor blocker/neprilysin inhibitor
ARRIVE	Animal Research: Reporting of *In Vivo* Experiments
ATP	adenosine tri-phosphate
Bach1	BTB and CNC homolog 1
BCA	bicinchoninic acid assay
Bcl-2	B-cell lymphoma-2
b.i.d.	*bis in die*, twice a day
BLA	Biologics License Application
BSA-CF	body surface area-conversion factor
BVR	biliverdin reductase
CABG	coronary artery bypass grafts
cGMP	cyclic guanosine monophosphate
CircFlx	circumflex
cMyBP-C	cardiac myosin binding protein-C
CO	carbon monoxide
CORM	carbon monoxide-releasing molecule
CPOX	coproporphyrinogen-III oxidase

CPP	cell-penetrating peptide
DAMP	damage-associated molecular pattern
DAPI	4′, 6-diamidino-2-phenylindole
DCytB	duodenal cytochrome B
dieb. alt	*diebus alternis*, every other day
DLS	dynamic light scattering
d.nm	hydrodynamic diameter (in nanometers)
DMEM-HG	Dulbecco's Modified Eagle Medium-High Glucose
DMSO	dimethyl sulfoxide
DMT1	divalent metal transporter 1
dP/dt	rate of pressure change (derivative of pressure/derivative of time)
DTT	dithiothreitol
EBSS	Earle's Balanced Salt Solution
EC_{50}	half maximal effective concentration
EDC	1-ethyl-3-(3-dimethylaminopropyl) carbodiimide
EDTA	ethylenediaminetetraacetic acid
EDV	end diastolic volume
EGFP	enhanced green fluorescent protein
eIF2α	eukaryotic initiation factor 2α
eIF2αK1	eukaryotic initiation factor 2α kinase-1
$FADH_2$	flavin adenine dinucleotide + hydrogen
FBS	fetal bovine serum
FDA	Food and Drug Administration
FOXO1	forkhead box protein O1
FPN1	ferroportin
FTH1	ferritin heavy chain
FTL	ferritin light chain
GAPDH	glyceraldehyde 3-phosphate dehydrogenase
GATA1	GATA-binding factor 1 (Erythroid Transcription Factor)
GT	guanine-thymine
GTP	guanosine-5'-triphosphatecyclic

HBSS	Hanks' Balanced Salts Solution
HCP1	heme-carrier protein-1
HEP	hepcidin
HEPH	hephaestin
HIF	hypoxia inducible factor
hIPSC	human induced-pluripotent stem-cell
HMOX1	heme oxygenase
HO-1	heme oxygenase-1 gene
HRIK	heme-regulated inhibitor kinase
i.p.	intraperitoneal
IR	ischemia-reperfusion
IRP2	iron regulatory protein-2
i.v.	intravenous
KEAP1	Kelch-like ECH-associated protein 1
LAD	left anterior descending coronary artery
LD_{50}	lethal dose, 50%
LD_{75}	lethal dose, 75%
LLD	lower limit of differential detection
LV	left ventricle
LVAD	left ventricular assist device
LVEDP	left ventricular end diastolic pressures
LVP	left ventricular pressure
MEM	Minimum Essential Media
MHC	myosin heavy chain
MLC	myosin light chain
N/A	not available
NAC	N-Acetyl-L-Cysteine
NADH	nicotinamide adenine dinucleotide + hydrogen
NADP(H)	nicotinamide adenine dinucleotide phosphate (reduced)
NCT	National Clinical Trial
NDS	New Drug Submission

NETosis	neutrophil extracellular trap-mediated vessel occlusion
NFkB	nuclear factor kappa-B
NRCM	neonatal rat cardiomyocyte
NRF1	nuclear regulatory factor-1
Nrf2	nuclear factor erythroid 2-related factor 2
NSTEMI	non-ST-elevation myocardial infarction
OD	optical density
ODA	octadecylamine
PAGE	polyacrylamide gel electrophoresis
Pak1	p21-activated kinase-1
PBGD	porphobilinogen deaminase
PBS	phospho-buffered saline
pCa^{2+}	-log10 of $[Ca^{2+}]$ in Molar units
PCR	polymerase chain reaction
PdI	polydispersity index
PEG	polyethylene glycol
PGC-1α	peroxisome proliferator-activated receptor gamma coactivator 1α
P_i	free phosphate
PINK1	PTEN-induced kinase-1
POMaC	poly(octamethylene maleate [anhydride] citrate)
PPOX	protoporphyrinogen oxidase
PSR	picrosirius red
q.d.	*quater in die*, four times a day
RAAS	renin-angiotensin-aldosterone system
RBF	round-bottomed flask
RCA	right coronary artery
rcf	relative centrifugal force
RPM	rotations per minute
ROS	reactive oxygen species
RV	right ventricle
SD	standard deviation

SDS	sodium dodecyl sulfate
SDS-PAGE	sodium dodecyl sulfate-polyacrylamide gel electrophoresis
sGC	soluble guanylate cyclase
SLC46A1	solute carrier family 46 member-A1
TAT	transactivator of transcription
TCA	trichloroacetic acid
TBS-T	tris-buffered saline-tween
TFR1	transferrin receptor
TLR4	toll-like receptor 4
TM	tropomyosin
TNF-α	tumor necrosis factor-α
TnI	troponin I
TnT	troponin T
TTC	triphenyltetrazolium chloride
TUNEL	terminal deoxynucleotidyl transferase dUTP nick end labeling
UROD	uroporphyrinogen decarboxylase
UROS	uroporphyrinogen III synthase
U.S. FDA	United States Food and Drug Administration

ACKNOWLEDGEMENTS

First and foremost, I would like to thank my father, David, for all his love and support. I could not have done this without you. I love you (more). I would also like to thank Andrew Cowie and Dr. Purvi Trivedi for their continued friendship. Andy, thank you for vouching for me at DMNB all those years ago and for your guidance when life got rough. Purvi, thank you for always being there for me and my family when we needed it most. Your support has meant the world to me. To Allie Titus, Michael Connolly and Meagan London—the best summer students I could have ever asked for. You joined the lab at a difficult time in my life and I am so thankful for you making it easier with your scientific curiosity and hard work. To Lorie deVarennes and Luisa Vaughn, thank you for taking such good care of the graduate students at Dalhousie Medicine New Brunswick. You have contributed so much work towards my education behind the scenes and I appreciate you. To Dasse Nadaradjan—technologist extraordinaire, thank you for always being there to support the graduate students (no matter what or when). To Adithi Pisapathi and (soon-to-be doctor) Maggie Pickard, thank you for bringing such positive energy to the lab every day (and also letting me pilfer all those leftover tissues).

I would also like to thank my lab mates—both at Dalhousie Medicine New Brunswick and the University of Guelph—for their comradery and contributions. To Benny Habiyambere and Kyle Wells, thank you for always keeping me on my toes. To MinJi Kim and Tori Nelson, thank you for your infectious energy and going above and beyond to keep the lab operating smoothly. To Dr. Vikki Northrup, thank you for being my sister-in-arms throughout this entire process, and lifting my status as an only lab student. Thank you to Dr. Brittany Edgett for your mentorship. Thank you to Dr. Sidra Sarfaraz, Leslie Ogilvie and Jade Marrow for making me feel at home during my residency at the University of Guelph. Thanks to Dr. Mathew Platt and Dr. Jason Huber for teaching me how to perform surgeries and echocardiography. Many thanks to Dr. Glen Pyle for assisting with the myofilament study and for helping me troubleshoot all the way from Ontario—this work could not have been completed without your generosity.

I would also like to thank Dr. Jean-Francois Légaré and Dr. Sohrab Lutchmedial for allowing me to shadow you and your teams in the Cardiac Care Unit. Thank you for immersing me in the clinical realities of applied pharmacology on the frontlines of cardiovascular medicine. Special thanks to Dr. Jeremy ‘Jer-Bear’ Simpson for all of your guidance and mentorship over the years, for which I am eternally grateful. To the Faculty who have supported my candidacy, many thanks for your counsel. Specifically, thank you to Dr. Jim Fawcett and Dr. Chris McMaster for keeping me on the right track. Most importantly, to Dr. Keith Brunt—words could never do justice in expressing just how thankful I am to have had you as my supervisor or for the generous gift that is my education. Thank you for your unwavering belief in me and for allowing me to explore my own path through science. I appreciate you more than you will ever know.

STATEMENT

The ideas, hypotheses and experiments presented herein are the result of collaboration between Ashley Eadie and Dr. Keith Brunt. Chapters 3 and 4 were the products of collaboration between Ashley Eadie, Dr. Jeremy Simpson (University of Guelph), and Dr. Keith Brunt. Ashley Eadie was responsible for designing, conducting, analyzing, and interpreting all experiments unless otherwise stated. AMI surgeries from Chapters 3 and 4 were performed by Mathew Platt at the University of Guelph. Hemodynamic and echocardiographic data were jointly analyzed by Ashley Eadie and Mathew Platt. Representative images in Fig. 3.1B i, ii were also provided by Mathew Platt. In Fig. 4.5, infarct size, thickness, and collagen were measured by Kyle Wells under the direction of Ashley Eadie. Biowire II measurements in Figs. 4.6 and 4.7 were performed by Dr. Rooz Sobbi at Tara Biosystems under the direction of Ashley Eadie. The final ATPase activity assay and myofilament phosphorylation gel in Figs. 4.15 and 4.16 were performed by Dr. Glen Pyle at the University of Guelph with the guidance of Ashley Eadie (and with help from Dr. Jeremy Simpson). The ATPase activity assay and myofilament phosphorylation gel in Figs. 4.15 and 4.16 were analyzed by both Ashley Eadie and Dr. Glen Pyle. Niohemin design was conceived by Dr. Naga Puvvada and Dr. Keith Brunt. Niosomes were synthesized, optimized, and characterized by Ashley Eadie. Allison Titus performed the Western Blot in Fig. 5.15 under the direction of Ashley Eadie. Ashley Eadie and Dr. Keith Brunt had full access to all data in the study and take full responsibility for data integrity and accuracy of analysis.

Chapter 3 in its entirety has been submitted for peer review/publication by Ashley Eadie (First Author). Figures 3.2 B, D, E and 3.6 B, D, E of Chapter 3 have therefore been adapted from the MSc. thesis of Ashley Eadie (©Copyright by Ashley Lynn Eadie, 2016); all other figures were produced during Ashley Eadie's doctoral thesis. AMI control animals in Chapter 3 and Chapter 4 were collected from a larger (concurrent) study comparing the effects of hemin on therapeutic outcomes when initiated at different times relative to cardiac injury; thus, the same animals served as controls across both chapters.

CHAPTER 1: INTRODUCTION

Current strategies for the treatment of acute myocardial infarction (AMI) are limited and thus novel therapeutic interventions are required to improve patient outcomes. AMI occurs when coronary arteries supplying the heart with oxygenated blood become occluded, causing downstream cardiac tissue necrosis and reduced ventricular function. In the United States alone, 3.0% of adults will experience an AMI [1], with 605,000 incident AMIs and 200,000 recurrent AMIs occurring each year and costing the government $12.1 billion per annum [2,3]. AMI is also a leading cause of heart failure [4], the progressive consequence of one or more cardiovascular diseases that reduce the heart's ability to meet the body's metabolic demands. Within the first year post-AMI approximately 30% of patients are diagnosed with heart failure—and less than 50% of patients with heart failure survive more than five years post-diagnosis [4–7]. Thus, novel interventional strategies are required to better treat AMI and prevent progression to heart failure.

In pre-clinical models of AMI, elevating levels of heme oxygenase-1 (HMOX1) exerts robust cardioprotection by promoting neovascularization, and reducing inflammation, oxidative stress, and fibrosis—thus improving cardiac function and survival [8–13]. HMOX1 elicits cytoprotection through the catabolism of free heme—the functional group responsible for transporting oxygen in proteins such as hemoglobin, myoglobin, and cytochromes in the electron transport chain (i.e. ATP production)—into equimolar quantities of biliverdin, carbon monoxide, and free iron (sequestered by ferritin heavy chain, FTH1) [14]. Together, heme catabolic by-products exert potent antioxidant, anti-inflammatory, anti-apoptotic, and vasodilatory effects [14–16]. Yet, translational investigations into HMOX1 induction for post-AMI therapy are limited and typically focus on the enzyme alone or the by-products of heme catabolism, without consideration for temporal changes in endogenous HMOX1 or heme substrate bioavailability.

As a heme surrogate and potent inducer/substrate of HMOX1, hemin presents a novel pharmacological approach to the treatment of AMI [17,18]. Hemin (also known clinically as Panhematin, Normosang, and heme arginate) is an FDA-approved orphan

drug indicated for the treatment of porphyria—a rare disorder characterized by a deleterious accumulation of heme precursors. Like heme, hemin is also catabolized by HMOX1 into biliverdin, carbon monoxide and free iron—eliciting anti-inflammatory, anti-oxidant, and pro-survival properties in a variety of experimental pre-clinical settings [17,18].

In pre-clinical models of cardiac ischemic-reperfusion injury, prophylactic hemin administration at a dose above the approved human therapeutic equivalent range preserves cardiac contractility and relaxation [17]. In one *in situ* rat model of AMI, prophylactic hemin administration reduced infarct size, mitochondrial damage, and oxidative stress; hemin also increased fractional shortening in a second *in situ* rat model of AMI (although it is unclear whether treatment was initiated before or after injury) [9,17]. Despite being on the market for 40 years, hemin's pharmacokinetic and pharmacodynamic characterization has been limited—leaving fundamental gaps in our understanding of hemin pharmacology. Whether hemin is capable of improving cardiac function when initiated post-AMI (and within a clinically-approved human equivalent dose range) also remains uncertain.

Fundamentally, it also remains unclear how cardiac heme content and its rate-limiting enzymes are affected by AMI or hemin over time. Cardiac heme content is reportedly elevated in patients with end-stage heart failure, though how heme metabolism (beyond HMOX1 alone) is altered acutely prior to advanced disease is unknown [19]. Although heme is essential to cellular respiration due to the oxygen-carrying capacity of its iron core, it may also exert noxious effects when not encapsulated in heme-proteins (though these negative effects may be over-generalized by association with studies of iron overload and ferroptosis). As a result, heme metabolism is tightly regulated by four principal enzymes: the heme-synthesizing enzymes δ-aminolevulinic acid synthases ALAS1 and ALAS2, and catabolic enzymes HMOX1 (heme- and/or stress-inducible; rate-limiting) and HMOX2 (constitutive; basal expression) (Fig.1.1). How heme metabolism is regulated after AMI, and its potential to be an agent of therapy (or molecular liability) is a distinct interest in translational pharmacology to advance clinical trial rationale and design.

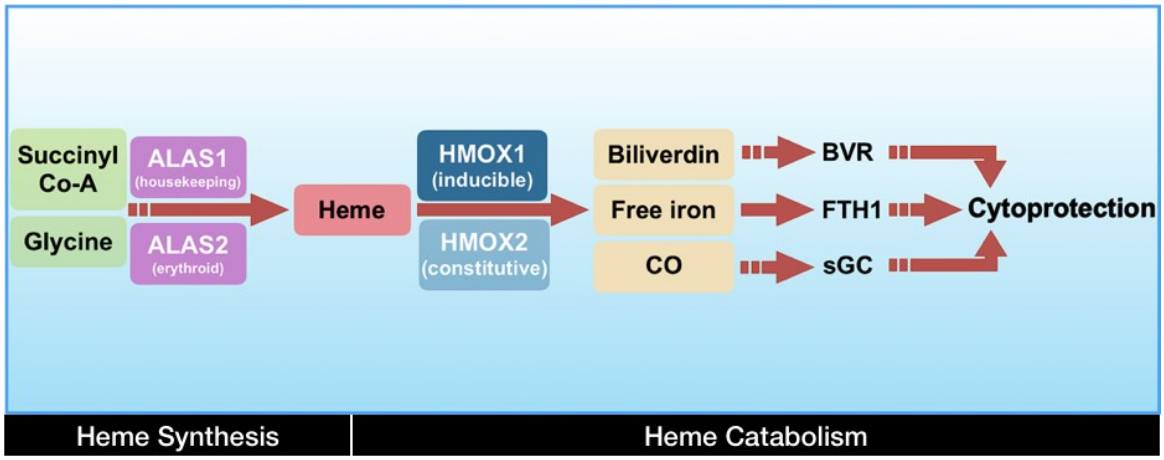

Figure 1.1 Overview of key enzymes regulating heme synthesis and catabolism. Heme is synthesized from glycine and succinyl Co-A via an eight-step enzymatic process regulated by the rate-limiting delta-aminolevulinic acid synthases (ALAS). Two highly conserved ALAS isoforms have been identified: ALAS1 which is purported to be ubiquitous and constitutively expressed, and ALAS2, the isoform regulating heme synthesis predominantly for erythroid cells. Heme is catabolized by heme oxygenases (HMOX), HMOX1 (the stress- and heme-inducible isoform) and the constitutive HMOX2 isoform. HMOX1 and HMOX2 catabolize heme into biliverdin, free iron (Fe^{2+}), and carbon monoxide (CO). Biliverdin is reduced to bilirubin—a potent antioxidant—by biliverdin reductase (BVR), while CO activates soluble guanylyl cyclase (sGC) — exerting anti-inflammatory and vasodilatory effects. Free iron is sequestered by ferritin, a heteromeric protein cage and the primary site of intracellular iron storage. Ferritin is composed of self-assembling heavy (FTH1) and light chain subunits which exert ferroxidase and stabilizing effects respectively. Free iron storage by ferritin prevents iron overload or excess reactive oxygen species formation via the Fenton reaction.

In this thesis, I have collated and added new, foundational information necessary to advance our fundamental understanding of heme metabolism and the potential for its therapeutic targeting post-AMI. In Chapter 1, a fundamental background related to AMI, its pathophysiological progression, and current therapeutic interventions are contextualized. Essential information regarding heme physiology, the mechanisms underlying HMOX1's cytoprotective benefits, and existing strategies to harness HMOX1's therapeutic potential (as well as their limitations) are explored therein.

In Chapter 2, the key literature related to hemin pharmacokinetics/dynamics is extracted from primary and grey literature. This includes knowledge regarding hemin pharmacology added through a comprehensive review of regulatory submission documents obtained from Health Canada following hemin's market approval in 2018.

In Chapter 3, using a pre-clinical model, we perform the first temporal characterization of cardiac heme regulation post-AMI and with hemin, uncovering an apparent dyssynchrony between cardiac heme content and anabolic/catabolic heme regulatory enzyme expression. We also perform a direct comparison between hemin treatment initiated pre-injury versus post-injury in cardiomyotubules (*in vitro*) and AMI (*in vivo*). Here we show that hemin is capable of conferring cardioprotection against AMI—even when initiated post-injury, as would be necessary for real-world clinical intervention.

In Chapter 4, our studies expand the investigation into the effects of hemin on late myocardial infarction intervention. The question of whether hemin is capable of increasing contractile function directly and works to elucidate potential underlying mechanisms of action in cardiac tissues are addressed. Here, it is shown for the first time that hemin is capable of directly increasing human cardiac tissue contractility by an apparently calcium-independent mechanism.

In Chapter 5, the therapeutic potential of two novel strategies that could be clinically translated for more rapid/targeted delivery of HMOX1/hemin to the infarcted heart were tested for proof-of-concept evidence: the encapsulation of hemin into a nanoparticle shell (Niohemin), and the exogenous delivery of functional HMOX1 using a cell-penetrating peptide (HMOX1-CPP). In this chapter, it is established that Niohemin and HMOX1-CPP are both capable of conferring cytoprotection to cardiomyotubules *in*

vitro and at a lower concentration than hemin alone (despite equivalent HMOX1 induction) albeit with some early caveats of pharmacodynamic distinction for safety.

Finally, in Chapter 6, a cumulative summary of these contributions to the fields of pharmacology and heme metabolism is presented, focusing on future directions and remaining knowledge gaps/challenges limiting therapeutic translation.

Collectively, this body of work provides valuable insights into the fundamental biology and therapeutic potential of novel strategies for the treatment of AMI through heme metabolism.

1.1 Clinical characteristics of acute myocardial infarction (AMI)

1.1.1 Overview

In an AMI, coronary arteries supplying the heart with oxygenated and nutrient-rich blood become partially or completely occluded—occurring as a result of vasospastic constriction, atherosclerotic plaque accumulation or rupture, the formation of a platelet-activated thrombus, or combinations thereof. Consequently, the delivery of substrate energy and oxygen to cardiomyocytes downstream of the occlusion is reduced and toxic anaerobic metabolites accumulate (in ischemia) [20]. Persistent deprivation of these metabolic substrates (coupled with waste accumulation) causes cardiomyocyte death and a pathophysiological cascade to contractile insufficiency, myocardial remodeling, reduced cardiac output, breathlessness, fatigue, cardiac transplant, and/or death from heart failure (when the heart can no longer meet the metabolic demands of the body). Current therapies are limited to the prevention of recurrent infarction, limiting cardiac workload, and the reperfusion of occluded vessels (if eligible).

1.1.2 Acute injury

AMIs are characterized by three phases: acute injury, early remodeling, and late remodeling. In the acute phase of AMI injury, initial occlusion of the coronary arteries leads to a sudden restriction in blood supply to the myocardium. The myocardium—as

the largest consumer of molecular oxygen by mass—requires a constant supply of oxygen to maintain essential cellular functions and survive [21]. Absence or reduction in oxygen bioavailability (hypoxia) results in impaired ATP production, an accumulation of reactive oxygen species (ROS)/oxidative stress, induction of apoptosis, and consequently a loss of viable contractile cardiomyocytes via necrosis and necroptosis without reperfusion or collateralization [22,23]. Loss of viable contractile tissue limits the heart's ability to properly contract and deliver oxygenated blood to other areas of the body necessary to maintain its essential functions. In a healthy patient, the volume of blood ejected from the heart's ventricle during systole (contraction) compared to the volume of blood within the chamber at the end of diastole (relaxation/filling) typically ranges from 60-80%. In AMI and heart failure, this ejection fraction can be reduced to 50% or below— significantly limiting cardiac output and decreasing a patient' ability to perform daily living activities due to shortness of breath, exertional fatigue, and other end organ damage. The acute phase of AMI injury is also characterized by a rapid accumulation of cytokines released from injured cells [24]. Cytokines are essential modulators of inflammation and macrophage recruitment post-AMI [24,25]. Although deleterious due to their ability to propagate ROS generation and negative extracellular matrix remodeling via pro-inflammatory macrophages, cytokines are also critical for spurring myocardial repair through the stimulation of myofibroblast differentiation and proliferation—initiating the remodeling (wound-healing) phase of AMI progression [25].

1.1.3 Early remodeling

The early remodeling phase of AMI is characterized by substantive morphological and structural changes to the surviving cardiomyocytes in the myocardium and the associated extracellular matrix, which manifest clinically as changes to the heart's size, shape and function [26]. Morphologically, the infarcted ventricle undergoes chamber dilatation (eccentric hypertrophy) post-AMI as a result of hemodynamic volume overload and wall thinning (from cardiomyocyte necrosis and remodeling of the extracellular matrix by metalloproteases) [26]. Hemodynamic volume overload occurs when the heart's ability to eject blood from the ventricle is reduced—leading to the accumulation

of blood volume within the affected chamber, chamber expansion, hemodynamic congestion, and fluid extravasation into the extracellular space (edema). Hemodynamic volume overload also contributes to myocardial slippage, the misalignment of myosin and actin filaments within surviving cardiomyocytes that results in an impaired ability to contract efficiently (systolic dysfunction), further impairing the ventricle's oxygen-delivering capabilities [27]. In turn, surviving cardiomyocytes in the peri-infarct region of the heart compensate for the loss of contractile tissue and increased hemodynamic stress through hypertrophic remodeling. This increase in cardiomyocyte size provides compensatory adaptation post-AMI by reducing ventricular wall stress and adding additional sarcomeric units to maintain contractile performance [28,29]. However—as the oxygen demands of hypertrophying cardiomyocytes rise to meet the increased mechanical load, collateral neovascularization becomes critical to supply nutrients and oxygen to the myocardium to maintain proper function and avoid decompensatory heart failure [30,31].

Downstream in the infarct region and border zone, stabilization of the weakened ventricular wall is critical to preventing ventricular dilatation and sudden cardiac death from hemorrhagic (ventricular) rupture [26]. This stabilization occurs through reparative remodeling: the removal of necrotic myocardial tissue by infiltrating macrophages and subsequent replacement with fibrotic scar tissue [26,32]. Increases in hemodynamic load (from loss of viable cardiomyocytes) and cytokine levels (as well as mechanotransduction) signal rapid fibroblast proliferation, differentiation, and production of extracellular matrix proteins such as fibrin, fibronectin, and collagens I and III [33,34]. Initially, fibroblasts synthesize the more elastic collagen III—re-establishing structural integrity of the infarcted heart and reducing the risk of immediate wall rupture [34]. However, an overly elastic scar is susceptible to overstretching, causing progressive eccentric cardiac hypertrophy, thinning of the ventricular wall, systolic dysfunction and reduction in cardiac output. Thus, provisional collagen III is progressively fortified with the overlaying and cross-linking of collagen I, resulting in a thicker, stiffer and more stable scar [34]. However, this also presents a risk as an overly stiff scar resists passive stretching and filling during diastole [35].

1.1.4 Late remodeling

Additional structural changes are also observed in late remodeling post-AMI. In the compensated heart, fibroblasts differentiate with myofibrotic features (myofibroblasts), passively depositing extracellular matrix to stabilize the existing fibrotic scar [36]. Meanwhile, simultaneous compensatory hypertrophy in surviving cardiomyocytes (and their neovascularization) maintains cardiac output [36]. However, decompensatory remodeling can emerge from microvascular rarefaction (reduction in capillary density), any iterative cell death, reactivated fibroblast proliferation, infarct expansion into the peri-infarct zone, or scar thinning and dilatation—thus increasing the probability of heart failure [37]. Chronic elevation of hemodynamic load puts additional mechanical stress on fibroblasts in the peri-infarct zone—stimulating fibroblast proliferation that results in a diffuse reactive interstitial fibrosis compared to the focal fibrotic scar [32]. This diffuse deposition of extracellular matrix impairs the structure-function of the ventricle in systole and diastole [38,39]. In diastole, increased ventricular stiffness from reactive fibrosis increases tensile strength at the cost of chamber elasticity, impairing the ventricle's natural ability to expand as it fills with blood and reducing the heart's ability to deliver a sufficient blood volume to meet the body's metabolic demands. In systole, expanding fibrosis and remodeling impairs the ventricle's ability to contract efficiently by shifting the alignment of cardiomyocytes and limiting the interaction between myosin and actin (myocardial slippage) [40]. Progressively, myocardial decompensation causes the deterioration of previously preserved ejection fractions and progression to heart failure over time.

1.2 Key molecular and cellular adaptations to acute myocardial infarction

1.2.1 Ischemia and hypoxia

The molecular responses to AMI are complex, but can be thematically categorized by their primary ischemic stimuli: hypoxia, nutrient deprivation, metabolite accumulation, oxidative stress, and inflammation. In the injured myocardium, persistent

tissue hypoxia—or low oxygen availability—is a major determinant of outcomes [36]. Hypoxia occurs both acutely and chronically in AMI and AMI-derived heart failure. Acutely, coronary artery occlusion prevents oxygenated blood flow to cardiac tissue. In patients where reperfusion therapies (such as thrombolytics, percutaneous coronary intervention, or coronary artery bypass grafts) are appropriate, a continuous supply of oxygen can be reinstated. However, permanent coronary occlusion in patients ineligible for reperfusion therapies and/or with limited collateral circulation leads to chronic hypoxia and tissue necrosis in the infarct region. With progressive cardiomyocyte death and chronic low-flow ischemia, tissue hypoxia can also occur in the peri-infarct region. Compensatory hypertrophy of surviving cardiomyocytes in the peri-infarct zone (resulting from the transfer of mechanical load from dying cardiomyocytes) increases cellular requirements for ATP and the metabolic demand for oxygen of which supply is limited.

To adapt to limited oxygen availability, intracellular protein expression is modulated to attenuate oxidative stress, inflammation, improve myocardial oxygen delivery, and maintain cardiomyocyte viability. Collectively these stimuli have essential drivers to increase the stress-inducible expression of proteins such as heme oxygenase-1 (HMOX1) and related cytoprotective molecules – including those regulated by hypoxia-inducible transcription factors HIF1α and HIF2α [41,42]. Hypoxia inducible factors (HIFs) are the primary regulators of the cellular response to low oxygen bioavailability. HIF1α increases oxygen bioavailability and confers cytoprotection through the regulation of over 200 genes, such as vascular endothelial growth factor (neovascularization for oxygen delivery) and HMOX1, whereas HIF2α contributes to the regulation of erythropoietin (red blood cell formation for oxygen transport), iron absorption and transportation [42–45]. Due to risk of harm from transient or persistent low oxygen levels, HIFs are continually synthesized and degraded even in oxygen homeostasis (for rapid response during conditions of low oxygen tension) [41].

1.2.2 Oxidative stress

Oxidative stress results from a disproportional formation of reactive oxygen species (ROS) relative to antioxidants (e.g. glutathione, biliverdin) required for their

neutralization, causing damage to lipids, proteins, nucleic acids, and cell death. Following AMI, several factors contribute to the development of oxidative stress such as: mitochondrial dysfunction, ROS from inflammatory macrophages, the depletion of antioxidants, and—in cases of coronary reperfusion—ischemia-reperfusion injury from sudden oxygen influx (ischemia-reperfusion injury results from ROS generated by mitochondria adapted to a state of anaerobic glycolytic metabolism) [28,46]. The molecular response to oxidative stress is critically regulated by the transcription factor Nrf2 (nuclear factor erythroid 2-related factor 2) [47]. In the presence of ROS, Nrf2 disassociates from the cytoplasmically-anchored adaptor protein KEAP1 (Kelch-like ECH-associated protein 1) and binds to stress-responsive/antioxidant response elements in the promoter regions for proteins such as glutathione, thioredoxin, and HMOX1 [47–49].

1.2.3 Inflammation

The molecular response to inflammation in AMI is a double-edged sword. Triggered by ischemia and cell damage/death following AMI, cardiomyocytes secrete pro-inflammatory cytokines or release damage-associated molecular patterns (DAMPs or alarmins, such as ATP, interleukins, heme, and heat shock proteins) [50–54]. In turn, immune cells such as neutrophils and macrophages are recruited to the site of injury for cell debris clearance and to initiate wound healing processes. Resident macrophage activation and the infiltration of monocytes mobilized from the blood, spleen, or bone marrow, occurs in phases early after AMI injury (classical/M1-polarization), with reparative contributions (non-classical/M2-polarization) occurring during later remodelling. However, excessive or prolonged inflammation can further exacerbate myocardial injury, cause secondary occlusion (e.g. NETosis), or contribute to myocardial wall instability (e.g. through the stimulation of matrix metalloproteinases).

NFkB (nuclear factor kappa-B) is a major transcriptional regulator of cellular inflammation and is sensitive to concomitant hypoxic signalling or oxidative stress [55]. Under normal conditions, NFkB translocation is inhibited by inhibitor of kappa-B binding. In inflammation, cytokines such as interleukin-1β, tumor necrosis factor-α

(TNF-α), or toll-like receptors activate cell signalling cascades resulting in the intracellular activation of inhibitor-of-kappa-B kinase. Inhibitor-of-kappa-B kinase subsequently phosphorylates inhibitor of kappa-B, causing NFkB to dissociate, translocate to the nucleus and initiate transcription for cell adhesion molecules (immune cell recruitment), chemokines (e.g. monocyte chemoattractant protein-1), pro-inflammatory cytokines, matrix metalloproteinases (extracellular matrix remodeling), and anti-apoptotic proteins (e.g. Bcl-2, HIF1α and HMOX1) [56–59].

1.3 Clinical management of acute myocardial infarction

Recent advances in pharmacological and surgical interventions have significantly decreased the incidence of re-infarction post-AMI, however, current therapeutic strategies are still limited and morbidity and mortality remain high [4–6]. Thrombolytics/anticoagulants, beta-blockers, and renin-angiotensin-aldosterone system (RAAS) inhibitors are the primary pharmaceutical interventions used as standard-of-care in the treatment of patient AMI [60,61]. As first-in-line drugs, thrombolytics (e.g. tissue plasminogen activators) and anticoagulants (e.g. heparin, warfarin, rivaroxaban) are implemented post-AMI to reduce blood clotting that can contribute to coronary artery occlusion and reperfuse the heart with oxygenated blood. Surgical interventions such as percutaneous coronary intervention and coronary artery bypass grafts (CABG) may also be required to reperfuse the occluded vessel (however these options are significantly more complex, invasive, and costly compared to pharmaceutical strategies) [60,61]. However, due to pharmaceutical contraindications, anatomically inaccessible occlusions, and/or delayed clinical presentation, 33% of all patients with complete-occlusion AMIs are ineligible for reperfusion therapies and thus invariably experience worse clinical outcomes [62].

Unlike reperfusion therapies that aim to re-establish oxygen supply to the infarcted myocardium, beta-blockers and RAAS inhibition confer therapeutic benefit by suppressing cardiac workload to reduce the demand for molecular oxygen [63]. Beta-blockers (such as metoprolol or propranolol) inhibit the binding of epinephrine and norepinephrine to β_1-adrenergic receptors in the heart—resulting in decreased heart rate

and cardiac output via sympathetic inhibition. Non-selective beta-adrenergic receptor antagonists (such as carvedilol) provide additional therapeutic benefit through the inhibition of α_1-adrenergic receptor-mediated vasoconstriction. Inhibition of RAAS by angiotensin-converting enzyme (ACE) inhibitors (e.g. enalapril), angiotensin II receptor blockers (ARBs; e.g. valsartan, candesartan), and ARB/neprilysin inhibitors (ARNi; e.g. sacubitril/valsartan) also reduces cardiac workload and afterload (e.g. peripheral hypertension).

In patients wherein cardiovascular prognosis is in decline, surgical insertion of ventricular assist devices (LVADs; devices implanted to mechanically propel blood through the affected ventricle) or cardiac transplant may be necessary [63]. However, these procedures are reserved for end-stage heart failure as they are resource-limited and prone to adverse events. These procedures also include the risk of immune rejection/activation without necessarily eliminating the pathologic factors contributing to the initial AMI or progression to heart failure.

Currently, treatment options offer no definitive cure for AMI-induced heart failure but rather aim to alleviate symptoms (i.e. dyspnea, exertional fatigue, etc.), manage risk factors, or delay cardiac decompensation [63]. Thus, pharmacological targeting of novel molecular pathways capable of targeting the weakening cardiac muscle directly, resolving cumulative stress, and improving overall cardiomyocyte function is an unmet medical need.

1.4 Preclinical models of acute myocardial infarction

Understanding the regulation of molecular signaling pathways in the heart post-AMI and in response to therapeutic intervention is invaluable to the successful clinical translation of novel therapeutics. Although patient biopsies provide important insights into such molecular mechanisms, they are often obtained from hearts in end-stage heart failure in preparation for transplant—providing only a brief snapshot of the terminal stages of post-AMI signalling. Concomitant comorbidities and prior pharmacological intervention may also mask key molecular mechanistic events in patient cardiac biopsies. Thus, preclinical models of AMI are currently necessary to provide temporal and

systemic insights into the regulation of molecular signaling pathways of therapeutic interest.

Surgical ligation of the left anterior descending coronary artery (LAD) is the principal technique used to model AMI (Fig.1.2) [64–66]. As the largest coronary artery, the LAD is responsible for supplying oxygen-rich blood to the majority of the heart's left side and its occlusion by surgical ligation significantly decreases left ventricular perfusion while increasing oxidative stress and cardiomyocyte death [67]. Similar to human hearts, occlusion of the LAD in murine and porcine AMI models results in increased left ventricular volumes from infarct dilatation and decreased left ventricular ejection fractions [67]. The LAD ligation model also facilitates the study of both permanent occlusion AMI and cardiac ischemia-reperfusion injury, providing equal opportunity to mimic patients ineligible or eligible for reperfusion therapy [64,66]. While this model requires surgical proficiency and excludes clinical contributing factors such as atherosclerosis, it more closely reflects clinical AMI compared to other models (e.g. cryoinjury, electrocautery, or subcutaneous isoproterenol infusion models that generate myocardial weakening by direct cardiomyocyte necrosis only) [65].

Although the incipient causes of preclinical AMI may not be entirely identical to patients, LAD ligation models provide invaluable information regarding altered molecular responses in myocardial injury—from acute injury to cardiac (de)compensation.

1.5 Therapeutic potential of heme oxygenase-1 (HMOX1) induction in AMI

1.5.1 Physiological role of heme oxygenase-1

Elevating levels of HMOX1 exerts robust cardioprotection in pre-clinical models of AMI—nevertheless, successful clinical translation requires careful consideration of HMOX1's physiological role and the potential impact of its modulation [8–10,12,13,68]. Heme oxygenases (like HMOX1) catabolize free heme into equimolar amounts of

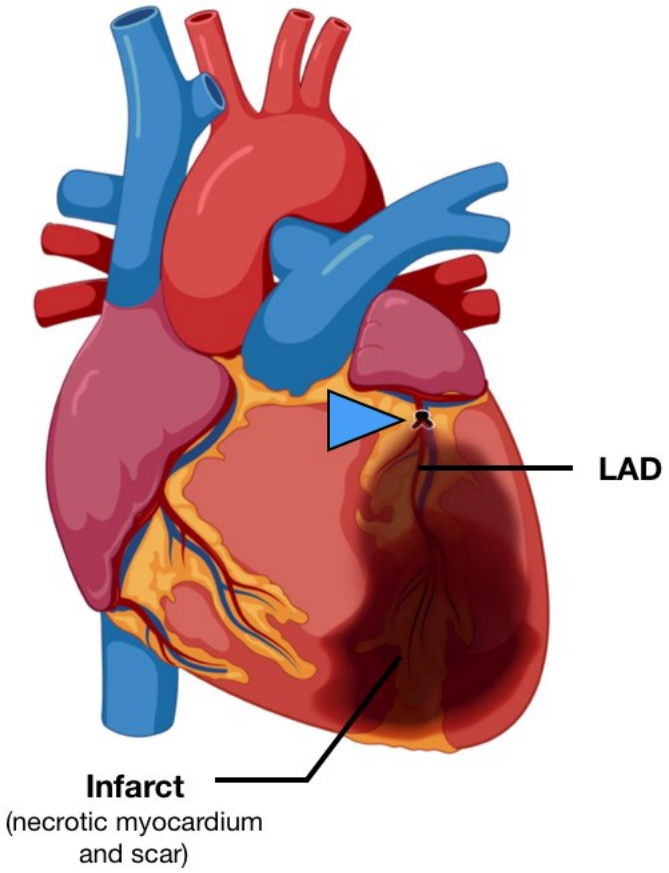

Figure 1.2 Surgical model of acute myocardial infarction (AMI). Permanent ligation of the left anterior descending coronary artery (LAD; arrowhead) inhibits blood flow to the downstream myocardium, resulting in cardiac tissue necrosis and scarring. Created with BioRender.com.

biliverdin, carbon monoxide (CO), and free ferrous iron (Fig.1.1) [14,69]. Although heme is vital to oxygen-dependent function through its roles in redox catalysis and oxygen transport, free heme can also be cytotoxic in excess: highly lipophilic regions within the heme moiety are capable of destabilizing lipid membranes and DNA by peroxidation and intercalation, and if improperly degraded, free heme's iron core can promote/propagate reactive oxygen species production via the Fenton reaction [70–72]:

1) $Fe^{2+} + H_2O_2 \rightarrow Fe^{3+} + HO\bullet + OH^-$

2) $Fe^{3+} + H_2O_2 \rightarrow Fe^{2+} + HOO\bullet + H^+$

Thus, heme oxygenases serve to reduce potentially pro-oxidant free heme by regulating its catabolism. HMOX1 is one of three heme oxygenase isoforms identified to-date: the heme- and stress-inducible HMOX1 (32kDa), the constitutive HMOX2 (36kDa), and variants referred to as HMOX3—a purported HMOX2 pseudogene(s)/variant frame-shift of no known function and demonstrating little heme-catalytic capacity [73–76]. As the products of two separate genes, HMOX1 and HMOX2 exhibit distinct differences in their anatomical expression, physiological roles, and regulation [77]. Unlike HMOX2 which is most abundant in the brain and testes [76], HMOX1 is most abundantly expressed in the liver, which contains high levels of cytochrome hemoproteins [76,78]. HMOX1 is also highly expressed in bone marrow and in splenic macrophages, due to their roles in sequestering and catabolizing heme-rich red blood cells, and in tumor cells as a mechanism to promote angiogenesis/survival [76,78]. Intracellularly, HMOX1 is anchored to the endoplasmic reticulum by its COOH-terminus [69], however a COOH-truncated form associated with the loss of enzymatic activity has been found within the nuclei and mitochondria [79–81]. Although it remains unclear what role HMOX1 serves within the nucleus, HMOX1 regulates mitochondrial quality control in the heart by upregulating PGC1α (regulator of mitochondrial biogenesis) and PINK1/Parkin (mediators of mitochondrial autophagy) in response to oxidative injury [82]. Both HMOX1 and HMOX2 are ubiquitously expressed [77].

In contrast to its constitutive HMOX2 counterpart, HMOX1 is largely regulated at the transcriptional level in response to heme bioavailability and stress [69]. In the presence of free heme, transcriptional repressor protein Bach1 (BTB and CNC homolog 1) is released from the promoter/enhancer region of HMOX1 and is subsequently subjected to proteasomal degradation (Fig.1.3) [83]. With the promoter/enhancer region exposed, HMOX1 can then be transcriptionally activated by stress-responsive transcription factors NFkB (inflammation), Nrf2 (oxidative stress), HIF1α (hypoxia), or AP-1 (activator protein-1; regulation of cellular differentiation, proliferation, and regeneration in response to growth factors and inflammatory cytokines) [14,84,57,48,44]. Bach1 is similarly released by the biologic heme surrogate, hemin—leading to HMOX1 induction [83]. However, mimetic heme precursors (protoporphyrins) such as zinc protoporphyrin demonstrate HMOX1 inhibition through occupation of HMOX1's heme-binding domain (without subsequent degradation by HMOX1) [85]. Transcriptional activity of HMOX1 may be further regulated by microsatellite polymorphisms within the enzyme's promoter sequence [86,87]. These polymorphisms present as tandem repeats of (GT) nucleotides and may regulate the rate and robustness of HMOX1 induction and disease susceptibility, with longer repeats being associated with impaired promoter activity and fewer repeats being associated with faster promoter activity [87]. In rat aortic smooth muscle cells transfected with HMOX1 luciferase reporter DNA containing either 20, 26, or 30 (GT) tandem repeats, luciferase activity decreased significantly with increasing (GT) repeats [87]. Different HMOX1 (GT) repeat lengths have also been shown to correlate with cardiovascular disease. In a meta-analysis of 10,170 patients with coronary artery disease and 6,868 controls, <25 HMOX1 (GT) tandem repeats was associated with a reduced incidence of myocardial infarction in sex- and aged matched groups [88]. In a clinical study by Doberer *et al.* 2010 (NCT00682370), healthy males homozygous for >27 (GT) tandem repeats exhibited higher levels of serum bilirubin, heme, and hemopexin (a free-heme-scavenging glycoprotein responsible for shuttling heme released from red blood cells) [89]. Increased free heme and hemopexin levels in the serum suggested that heme catabolism by HMOX1 was impaired at baseline. However, intravenous injection of hemin (the heme surrogate and potent inducer of HMOX1) revealed no significant difference in HMOX1 mRNA induction in peripheral

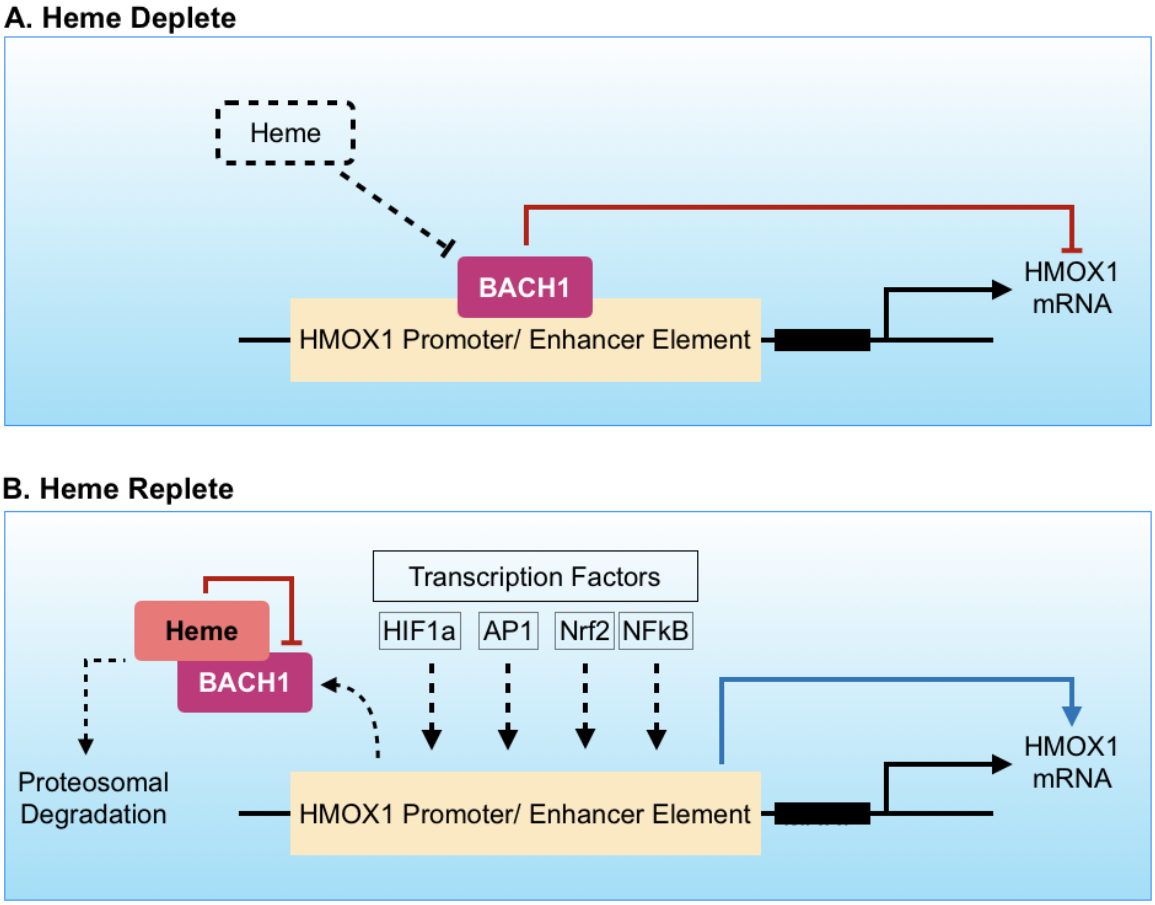

Figure 1.3 Heme-dependent regulation of HMOX1. (A) In the absence of free heme, HMOX1 is transcriptionally repressed by Bach1 (BTB and CNC homolog 1). Bach1 negatively regulates HMOX1 transcription by occupying Maf recognition elements within the HMOX1 promoter/enhancer region. **(B)** In the presence of free heme, Bach1 is released from the promoter/enhancer region of HMOX1 and is subsequently subjected to proteasomal degradation following ubiquitination by heme-responsive E3, HOIL-1. With the promoter/enhancer region exposed, HMOX1 can then be transcriptionally activated by stress-responsive transcription factors NFkB (inflammation), Nrf2 (oxidative stress), HIF1/2α (hypoxia), or AP-1 (activator protein-1).

blood mononuclear cells between short allele (<27 repeats) and long allele (>27 repeats) individuals [89]. The exact (GT) lengths, cell types and physiological circumstances under which HMOX1 microsatellite polymorphisms affect HMOX1 promoter activity remain to be characterized. Still, (GT)-dependent differences in HMOX1 promoter activity remain an important clinical consideration: understanding how (GT) length affects HMOX1 activity could identify early on the potential differences in therapeutic efficacy of HMOX1-based therapeutics across different patient subsets.

Genetic knockouts and clinical incidences of HMOX1 deficiency highlight the enzyme's physiological significance. In HMOX1-deficient mice, the development of microcytic anemia, spleen enlargement, and iron deposition in the liver and kidney (despite low serum iron) has been observed [90]. With age, HMOX1-deficient mice exhibit greater iron deposition, splenic atrophy, fibrosis, and fewer macrophages [91]. HMOX1 deficiency further affects cardiac adaptation to hypoxia, with $HMOX1^{-/-}$ mice exhibiting significantly more right ventricular dysfunction, cardiac hypertrophy, fibrosis, and apoptosis when exposed to 10% O_2 for 5-7weeks [92]. In the first of two known cases of HMOX1 deficiency in humans, a 6 year-old male with complete loss of HMOX1 presented with stunted growth, low serum bilirubin and persistent hemolytic anemia [93]. Further investigation revealed 490-fold higher levels of serum heme than normal, as well as elevated levels of the iron-storage protein ferritin, suggesting improper heme degradation. Hepatomegaly and asplenia were also observed. In peripheral blood mononuclear cells and lymphoblastoid cells isolated from the patient, HMOX1 was not detected and induction was not observed in response to cadmium compared to cells isolated from the patient's parents and controls (although HMOX2 was still present). In the second known case of HMOX1 deficiency, a 15 year-old female with a homozygous missense mutation in HMOX1 exon 2 also presented with asplenia, persistent hemolysis, elevated serum ferritin, inflammation, and hematuria [94]. Both patients died of intracranial hemorrhage.

1.5.2 Mechanisms of heme oxygenase-1-mediated cytoprotection

HMOX1 confers cytoprotection through the catabolism of pro-oxidant free heme into biliverdin (a potent antioxidant), carbon monoxide (CO; a potent anti-inflammatory

and vasodilator), and free ferrous iron (an essential electron carrier in ATP production). Biliverdin—and its reduction product bilirubin—are bile pigments formed from the cleavage of heme's pyrrole rings and are most commonly recognized as the green and yellow-red pigments (respectively) observed in bruising. Following heme catabolism, biliverdin reductase reduces biliverdin to bilirubin. In turn, bilirubin acts as a potent anti-oxidant by accepting otherwise harmful free-radical electrons from nearby proteins [16]. The potency of bilirubin's antioxidant capacity lies in its conversion back to biliverdin by accepting free-radical electrons, where it can repeat the anti-oxidation process until excreted by the liver (Fig.1.4). Endogenous CO serves as a critical contributor to cardiovascular health through its roles as an anti-inflammatory agent and vasodilator [95]. CO reduces inflammation through direct inhibition of platelet activation and circulating monocyte extravasation to inflamed tissues [15,96]. Inhibition of monocyte and platelet cytokine cascades reduces the risk of thrombosis, which can result in vascular occlusion injuries such as AMI or stroke. Similar to nitric oxide, CO also serves as a potent vasodilator [95,97,98]. CO stimulates the activation of soluble guanylate cyclase, a hemoprotein responsible for the production of cyclic guanosine monophosphate (cGMP) [95]. In turn, cGMP stimulates protein kinase G to activate myosin phosphatases, inhibiting Ca^{2+} influx through L-type Ca^{2+} channels in smooth muscle cells, resulting in vascular relaxation/dilation and increased blood flow [95].

Free iron released from heme catabolism is often overlooked as a contributor to the beneficial effects of HMOX1 induction. Iron readily accepts and donates electrons, making it a valuable part of oxygen binding/transport in heme and hemoproteins, as well as electron transport in the form of iron-sulfide clusters in Complex I, II, and III of ATP synthesis [99]. Because iron is not synthesized, cells are dependent on dietary uptake, storage, and recycling through HMOX1 to maintain physiological iron levels. Iron-deficiency anemia (i.e. insufficient hemoglobin production in red blood cells due to low iron levels) is common in patients suffering from AMI/heart failure and is closely associated with worsened outcomes such as increased rates of reinfarction and death [100,101]. Low serum iron is also associated with higher levels of pro-inflammatory

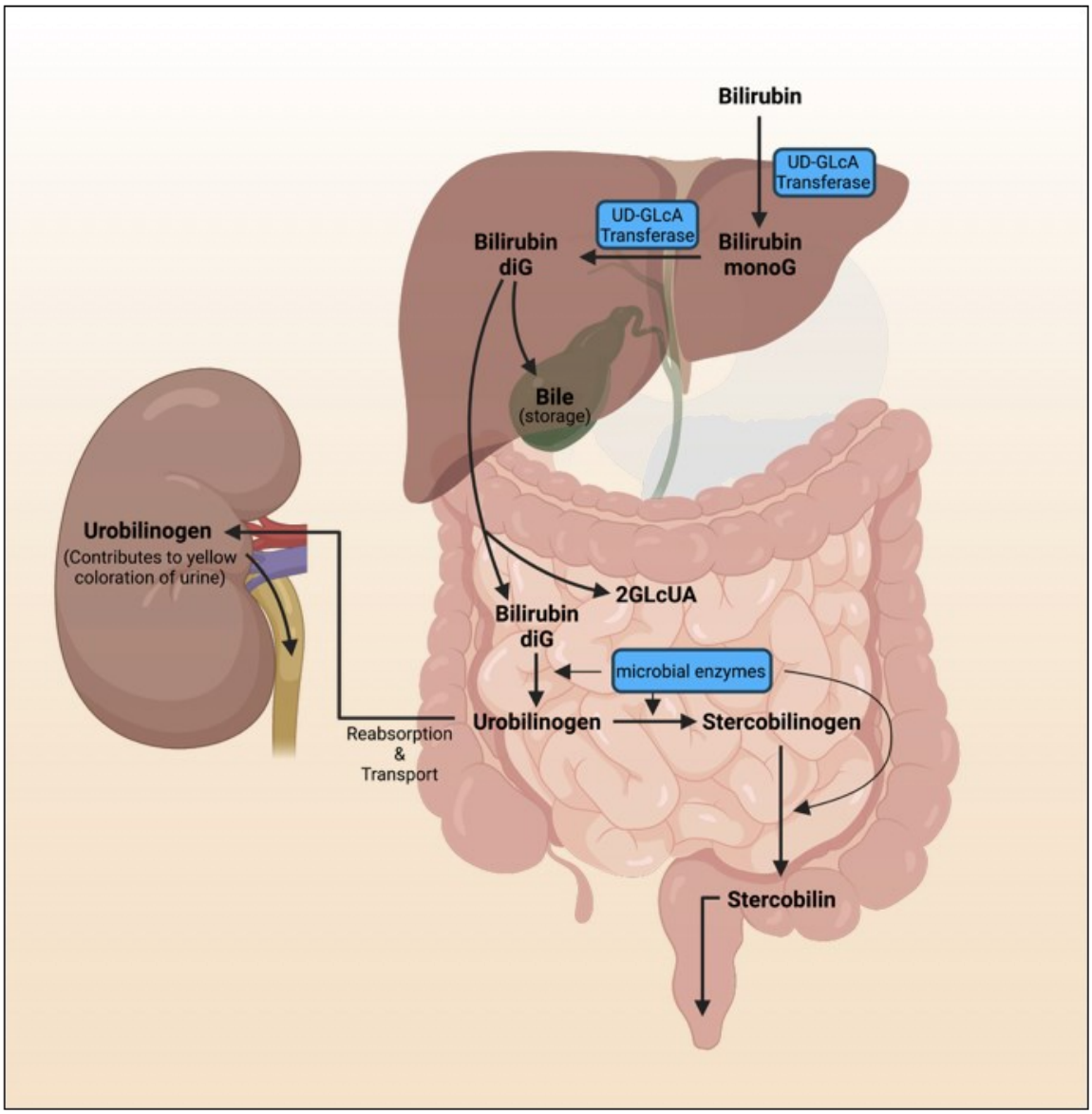

Figure 1.4 Mechanisms of biliverdin/bilirubin catabolism. Following its reduction from biliverdin by biliverdin reductase, bilirubin is exported into the bloodstream via an unknown mechanism. Bilirubin is subsequently transported to the liver by albumin, where it undergoes further catabolism into bile. Bile is concentrated in the gallbladder and serves important functions in lipid digestion and the elimination of excess cholesterol. Bilirubin that is not converted into bile is transported to the intestines for microbial digestion and subsequent elimination by the kidneys or digestive tract. (diG, diglucuronide; monoG, monoglucuronide; UD-GLcA transferase, uridine glucuronosyltransferase; GLcUA, glucuronic acid). Created with BioRender.com.

markers, and impaired responses to hypoxia in humans [102] [NCT01847352]. In otherwise healthy volunteers exposed to two 6 hour periods of isocapnic hypoxia, individuals with iron deficiency show greater increases in pulmonary artery systolic pressure than in iron-replete individuals with the first exposure to hypoxia. With a second 6h exposure to hypoxia, intravenous infusion of iron prior to hypoxia in iron-deplete individuals results in no difference in pulmonary artery systolic pressure, peripheral oxyhemoglobin saturation, and partial pressures of O_2 and CO_2 compared to-iron replete individuals. Intravenous administration of iron and blood transfusion is often insufficient to treat cardiac patient anemia, suggesting that there may be an incipient cause beyond more obvious factors such as blood loss (i.e. improper regulation of iron uptake, storage, and transporting proteins). HMOX1 therefore presents cytoprotective opportunities via the enhancement of intracellular iron recycling.

1.5.3 Heme oxygenase-1 induction in preclinical models of myocardial injury

Prophylactic elevation of cardiac HMOX1 demonstrates significant cytoprotection and functional improvement in preclinical models of AMI. In transgenic mice subjected to left anterior coronary artery occlusion followed by reperfusion (*in vivo* and *ex vivo*), cardiac-specific HMOX1 overexpression significantly reduces infarct area, inflammatory cell infiltration, oxidative damage, and left ventricular end diastolic pressures (LVEDP; indicative of improved diastolic function) compared to wild-type controls [12,103]. Improvements to systolic function are also observed with increased left ventricular developed pressures (the difference between maximum left ventricular pressure and LVEDP) among transgenic mice overexpressing HMOX1 in the heart [12,103].

Similar benefits are also conferred to cardiomyocytes *in vitro* and *in vivo* with viral HMOX1 overexpression [11,104]. In rats subjected to ischemia-reperfusion injury, prophylactic delivery of adenoviral HMOX1 overexpression vectors to the heart significantly improves overall survival and systolic function after 1 year via increased left ventricular developed pressures and maximum rate of contraction (dP/dt Max), as well as diastolic function by attenuating injury-induced increases in LVEDP and end diastolic

volumes (EDV) compared to LacZ controls [11]. Infarct size is also decreased in mice pre-treated with intramyocardial administration of adeno-associated virus HMOX1 overexpression vectors, and in mice administered hypoxia-response-element-regulated adeno-associated virus HMOX1 overexpression vectors immediately following permanent LAD ligation [8,105]. Mice intramyocardially administered adeno-associated virus HMOX1 overexpression vectors following permanent LAD ligation additionally demonstrate increased left ventricular wall thickness, capillary density, cardiac output, and recruitment of mononuclear cells to the heart [8]. In HL-1 cells (mouse atrial cardiac muscle), pre-emptive adenoviral HMOX1 overexpression significantly reduces H_2O_2-mediated ROS, inflammation, and hypertrophy—demonstrating that HMOX1 elevation is capable of conferring direct protection to cardiomyocytes [104]. Similar results are also observed in H9C2 cells (embryonic rat cardiomyoblasts) transfected with HMOX1 expression plasmids prior to ischemia-reperfusion injury [105].

1.5.4 Current limitations to the clinical translation of heme oxygenase-1 therapy

HMOX1 induction has long been investigated as a therapeutic strategy for the treatment of different pathophysiological conditions, yet despite 31 years since the first study of HMOX1's cytoprotective capacity, HMOX1-targeted therapeutics have yet to be translated to the clinic [106]. Clinical consideration of the translatability of novel HMOX1-based therapeutics, the timing of treatment administration, and the potential impacts of HMOX1 modulation on its physiological roles and heme regulation have been largely overlooked. Although transgenic and viral HMOX1 overexpression provide important and fundamental information regarding the enzyme's therapeutic potential, these gene expression strategies are not currently translatable. Pre-emptive HMOX1 elevation also remains limited in clinical translatability as patients seek care only *after* AMI symptoms present. Further, failure to consider the health of heme metabolism as a whole by focusing exclusively on HMOX1 alone could lead to serious adverse events when administering HMOX1-based therapeutics in the clinic. Despite substantive evidence supporting HMOX1's beneficial effects, chronic (transgenic) overexpression of HMOX1 in the hearts of otherwise healthy mice show spontaneous development of

cardiac dysfunction after 1 year [107]. This dysfunction is characterized by significant reductions in left ventricular pressure, dP/dt Max and Min (rates of left ventricular contraction and relaxation respectively), increases in end diastolic pressures, hypertrophy, and atriomegaly compared to wild-type controls. Yet in transgenic mice from the same cohort, chronic HMOX1 overexpression attenuates cardiac dysfunction, interstitial fibrosis, and hypertrophy induced by 2 weeks of isoproterenol-induced catecholamine stress compared to wild-type controls [107]. Meanwhile in pressure-overload models of heart failure, chronic HMOX1 overexpression exacerbates cardiac dysfunction induced by 2 weeks transverse aortic constriction [107]. Similar results are reported by Chen *et al*. 2011, where HMOX1 overexpression under the control of an α-actin promoter exacerbates cardiac hypertrophy from transverse aortic constriction in mice [108]. In a study by Jais *et al*. 2014, HMOX1 is also shown to exert a negative role in driving metabolic inflammation, with deletion of HMOX1 in macrophages and hepatocytes reducing inflammation in adipose tissue [109]. Together, these studies highlight that HMOX1 can exert vastly diverse effects under different conditions. Critically evaluating when and through which mechanisms HMOX1 exerts these effects in pre-clinical models assists in preventing unintended adverse events when translating HMOX1-based therapeutics to the clinic. Understanding the physiological effects of HMOX1 modulation—and its impact on heme metabolism and regulation—will enable safer and more efficient strategies for its therapeutic targeting.

1.6 Physiological roles of heme

1.6.1 The structure of heme and its contribution to physiological function

Heme is a complex molecule that serves important roles across a variety of physiological processes—particularly those involved in oxygen transport, storage, and ATP production [110]. Chemically, heme is characterized as a cofactor/prosthetic group and consists of a porphyrin ring (a cyclic molecule made up of four interconnected pyrroles—smaller rings of four carbons and nitrogen) with an iron center (Fe^{2+}) (Fig.1.5). Iron is essential for heme's reversible oxygen-binding capabilities and the ability to bind

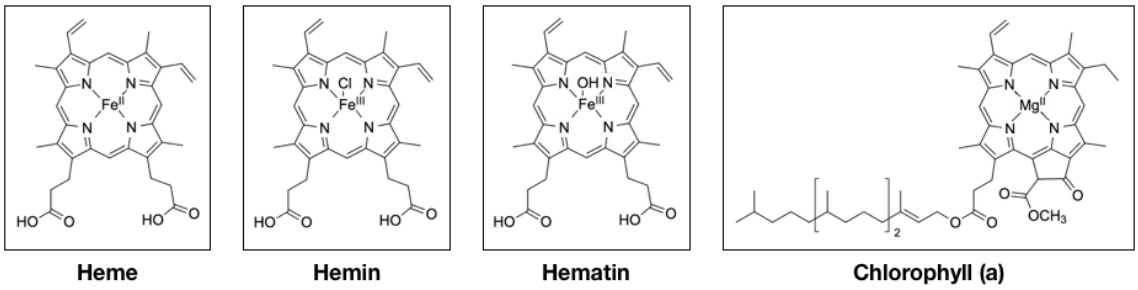

Figure 1.5 Structural differences/similarities between heme, hemin, hematin, and plant chlorophyll.

other molecules such as nitric oxide, CO, and hydroxyl groups—whereas heme's porphyrin structure enables the molecule to act as a cofactor/prosthetic group to different heme-containing proteins (i.e. hemoproteins). As a porphyrin, heme is similar in structure to hemin, hematin (the product of hemin and sodium carbonate), and chlorophyll (Fig.1.5).

1.6.2 The role of heme in oxygen transport and storage

Heme is most notably recognized as the oxygen-carrying component of the erythroid hemoprotein, hemoglobin, which contains four heme-binding pockets per protein. Via heme, hemoglobin in red blood cells transports oxygen from the lungs to other tissues for aerobic cellular respiration/ATP production. Damaged or degraded hemoglobin is excreted by the liver via haptoglobin binding, while free heme in the bloodstream is transported to the liver for recycling/excretion by the vascular heme-carrier protein, hemopexin. Heme also serves as the oxygen-receiving component of myoglobin, a monomeric hemoprotein found mainly in muscle and responsible for the intracellular storage of oxygen (and its release during muscle activity). Low heme bioavailability (such as in anemia) can thus significantly impact oxygen transport and storage, resulting in symptoms of exhaustion, weakness, and dyspnea.

1.6.3 The role of heme in ATP production

Heme not only acts as a prosthetic group to hemoglobin and myoglobin, but also serves a critical supporting role in ATP synthesis [111]. ATP synthesis is dependent on a series of electron donations in order to generate a proton gradient, which in turn activates synthase proteins to catalyze the conversion of ADP + inorganic phosphate to ATP. Electrons donated from NADH (nicotinamide adenine dinucleotide + hydrogen) and $FADH_2$ (flavin adenine dinucleotide + hydrogen) produced in earlier stages of aerobic respiration are carried along the mitochondrial electron transport chain by iron in iron-sulfur clusters within Complexes I, II, and III, as well as through the hemoprotein, cytochrome C (both an independent electron carrier and part of Complexes III and IV)

(Fig.1.6) [111]. Modulating heme and/or iron bioavailability could thus impact the production of ATP.

1.6.4 The role of heme in signal transduction and redox metabolism

Heme supports important signalling functions involved in gasotransmission, the innate immune response, the regulation of protein translation, and erythropoiesis. Nitric oxide—a gaseous signalling molecule capable of stimulating smooth muscle relaxation/vasodilation through the activation of guanylate cyclase—is produced by the nitric oxide synthase family of hemoproteins [112,113]. Heme within nitric oxide synthases binds oxygen and acts as an electron acceptor, enabling the conversion of L-arginine to nitric oxide. Heme is also a central gaseous-molecule/electron-sensing component of (soluble) guanylate cyclase (sGC), the hemoprotein responsible for the conversion of GTP (guanosine-5'-triphosphatecyclic) into cGMP (guanosine 3',5'-cyclic monophosphate). cGMP is a second messenger molecule involved in neurotransmission, inhibition of platelet aggregation, and the stimulation of vasorelaxation (e.g. via activation of myosin light-chain phosphatases) [114,115]. Consequently, sGC has become a therapeutic target of interest in the treatment of pulmonary hypertension (e.g. Riociguat, a heme-dependent sGC stimulator) and of acute episodes of decompensation in patients with heart failure (e.g. Vericiguat, a second heme-dependent sGC stimulator) [115].

Heme has also been found to regulate protein synthesis through eukaryotic initiation factor 2α (eIF2α) and its kinase, eIF2αK1 (also known as 'heme-regulated inhibitor kinase' or HRIK)—balancing the synthesis of globins with heme bioavailability [116]. eIF2 proteins mediate the binding of transfer-RNA to ribosomes. In heme deficiency, eIF2αK1 is activated by autophosphorylation, which subsequently phosphorylates eIF2α. As a result, eIF2α phosphorylation prevents its own recycling—leading to the cessation of protein synthesis [116]. In other words, heme inhibits eIF2αK1 which leads to the initiation of protein synthesis.

In addition to the direct beneficial effects conferred by heme catabolism and generation of its metabolites, heme facilitates cytoprotection by the formation of

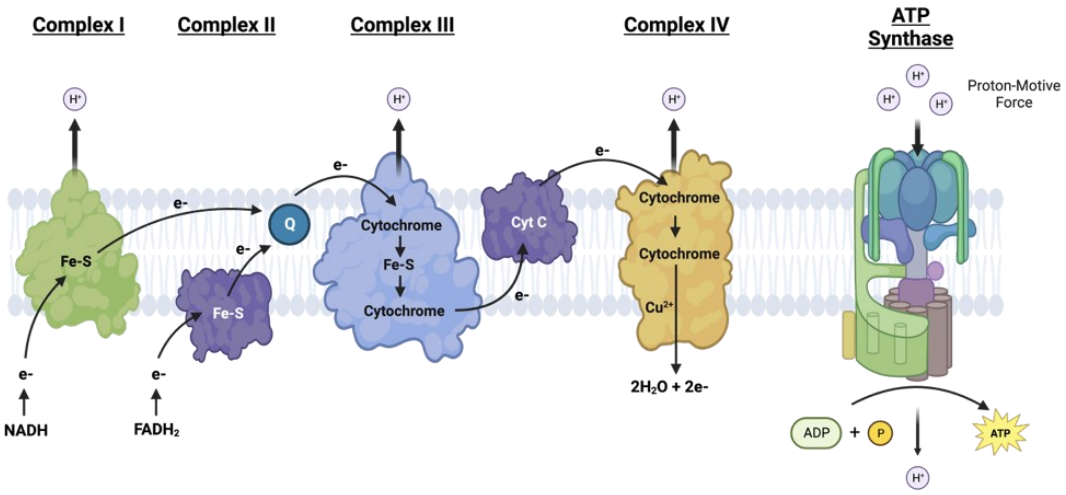

Figure 1.6 The roles of iron sulfur clusters and hemoproteins in ATP synthesis. Electrons donated from NADH (nicotinamide adenine dinucleotide + hydrogen) and $FADH_2$ (flavin adenine dinucleotide + hydrogen) produced in earlier stages of aerobic respiration are carried along the mitochondrial electron transport chain by iron in iron-sulfur clusters (Fe-S; located within Complexes I, II, and III), quinone (Q), and through the hemoprotein, cytochrome-C (both an independent electron carrier and part of Complexes III and IV). In turn, electron donations generate a proton gradient—activating synthase proteins to catalyze the conversion of ADP + inorganic phosphate to ATP. Created with BioRender.com.

hemoproteins such as cytochromes p450, catalase, and myeloperoxidase. Cytochromes p450 serve pivotal roles in the oxidation, breakdown, and clearance of xenobiotics (such as toxins) and endogenous compounds. Catalase protects the cell from oxidative damage by mediating the decomposition of hydrogen peroxide. In contrast, myeloperoxidase is directly responsible for the formation of reactive oxygen species used by lysosomes (as well as neutrophils and monocytes) to neutralize bacteria and/or other pathogens. Recent evidence suggests that free heme may also participate in signal transduction by functioning as an alarmin [54,117]. Alarmins are endogenous molecules released from damaged/dying cells that—when sensed by extracellular recognition receptors on other cells—promote sterile inflammatory responses. Collectively, modulating heme bioavailability could vastly affect its roles in cell signaling, inflammation and metabolism.

1.7 Heme anabolism, transport, and catabolism

1.7.1 Heme synthesis and transport

Heme is essential for oxygen-dependent life as a direct result of the oxygen-binding capacity of its iron core [71]. Thus, heme is ubiquitous (and ubiquitously synthesized) with ~80% of all heme in humans located in/produced in erythrocytes and another ~15% produced by the liver (wherein hemoprotein cytochrome levels are in high abundance). The synthesis of heme involves 8 enzymatic reactions, beginning in the mitochondria (Fig.1.7) [118]. Here, glycine (amino acid) and succinyl CoA (Krebs Cycle) are first condensed into δ-aminolevulinic acid (5-ALA) by the rate-limiting enzyme, δ-aminolevulinic acid synthase (ALAS) [119]. This step is regulated by one of two ALAS isoforms: ALAS1 or ALAS2. ALAS2 is characterized as the dominant isoform involved in erythroid heme synthesis and is translationally regulated by iron availability [120]. Transcriptionally, ALAS2 is regulated by the transcription factor GATA1—the ‘master’ regulator of erythropoiesis [121,122]. In contrast, ALAS1 is commonly characterized as the ‘housekeeping’ isoform and is predominantly responsible for non-erythroid heme synthesis [120]. In liver, ALAS1 transcription is mediated by

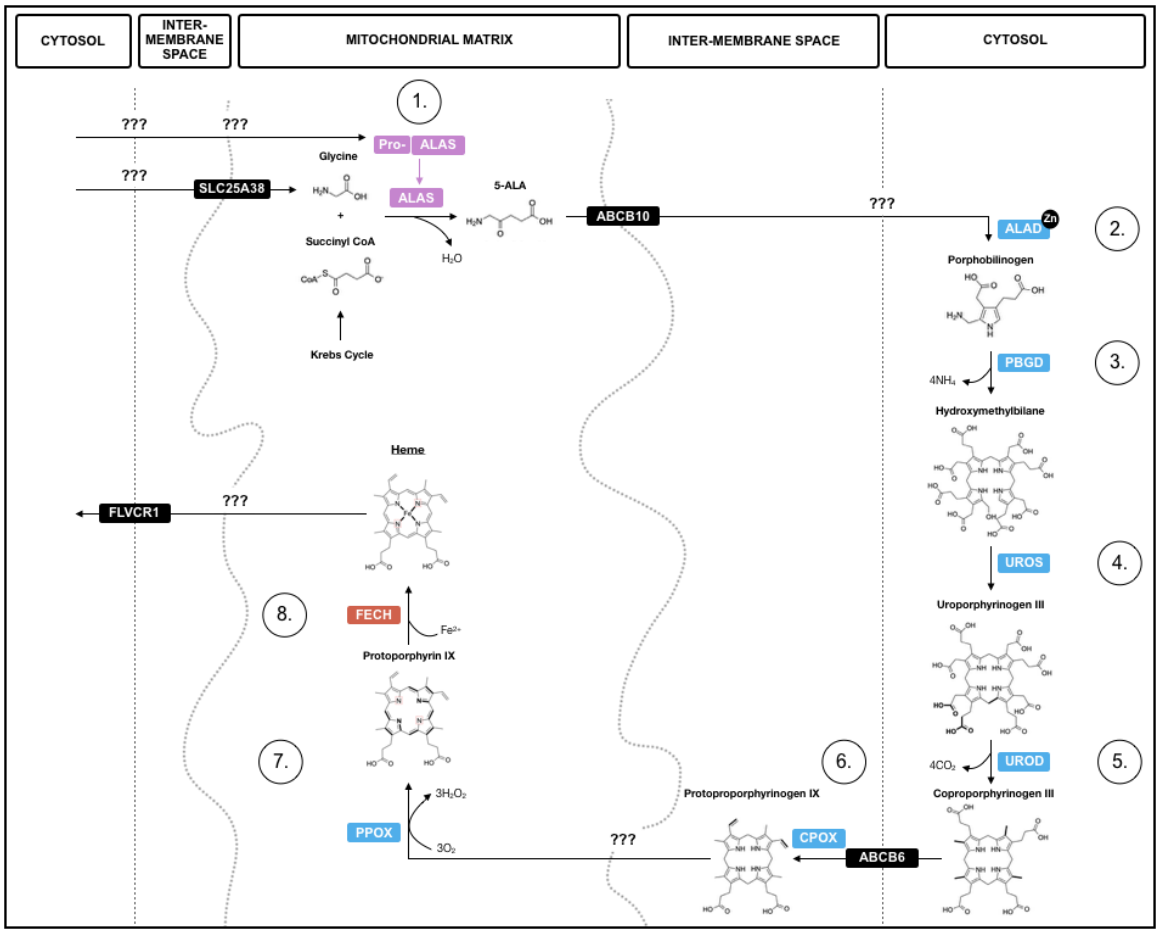

Figure 1.7 Molecular assembly of heme in the mitochondria. Heme is synthesized from glycine and succinyl Co-A via an eight-step enzymatic process regulated by the rate-limiting delta-aminolevulinic acid synthases (ALAS). (5-ALA, δ-aminolevulinic acid; ABCB6, ATP binding cassette subfamily-B member-10; ABCB10, ATP Binding Cassette Subfamily B Member 10; ALAD, δ-aminolevulinic acid dehydratase; CPOX, coproporphyrinogen-III oxidase; FECH, ferrochelatase; FLVCR1, feline leukemia virus subgroup C receptor-related protein 1; PBGD, porphobilinogen deaminase; PPOX, protoporphyrinogen oxidase; SLC25A38, solute carrier family-25 member-38; UROD, uroporphyrinogen decarboxylase; UROS, uroporphyrinogen III synthase).

peroxisome proliferator-activated coactivator-1α (PGC-1α), with nuclear regulatory factor-1 (NRF-1) and forkhead box protein O1 (FOXO1) acting as co-mediators [123]. However, it is not yet clear whether this mechanism of transcriptional ALAS1 regulation is conserved in the heart or other tissues.

In the second enzymatic reaction, 5-ALA is exported to the cytoplasm via ABCB10 (ATP Binding Cassette Subfamily B Member 10) where it is converted to porphobilinogen by 5-ALA dehydratase (ALAD). ALAD activity is inhibited by succinyl acetone and most notably lead, which displaces ALAD's zinc cofactor in 5-ALA and prevents heme synthesis in lead poisoning [124–126]. In the third enzymatic reaction, porphobilinogen is converted to hydroxymethylbilane by porphobilinogen deaminase (PBGD), which is then converted to uroporphyrinogen by uroporphyrinogen III synthase (UROS) in the fourth step of heme synthesis. Uroporphyrinogen is subsequently converted to coproporphyrinogen III by uroporphyrinogen decarboxylase (UROD) in the fifth enzymatic reaction before returning to the mitochondria via ABCB6. In the sixth enzymatic reaction, protoporphyrinogen IX is formed by coproporphyrinogen-III oxidase (CPOX) in the intermembrane space just prior to entering the mitochondrial matrix. Once inside the mitochondrial matrix, protoporphyrinogen IX is converted to protoporphyrin IX by protoporphyrinogen oxidase (PPOX) as the seventh enzymatic reaction in heme synthesis. In the final enzymatic reaction, ferrous iron is inserted into protoporphyrin IX by ferrochelatase—thus forming heme. Heme is subsequently exported from the mitochondria, however the mechanism(s) responsible remain unclear.

Elucidation of the molecular mechanisms underlying heme transport and hemoprotein insertion remain ongoing (Fig.1.8), however it should be noted that earlier characterization of SLC46A1 (solute carrier family 46 member-A1) as a long sought-after potential dietary heme importer is no longer supported [127,128]. In the original study identifying SLC46A1 (previously known as heme-carrier protein-1, HCP1) as a heme importer, SLC46A1 overexpression was intracellularly associated with increased ^{55}Fe-conjugated heme administered through diet [129]. However, SLC46A1 has since been identified as a folate importer (folate stimulates erythropoiesis and by extension, heme synthesis), with further evidence suggesting that increases in intracellular isotope-

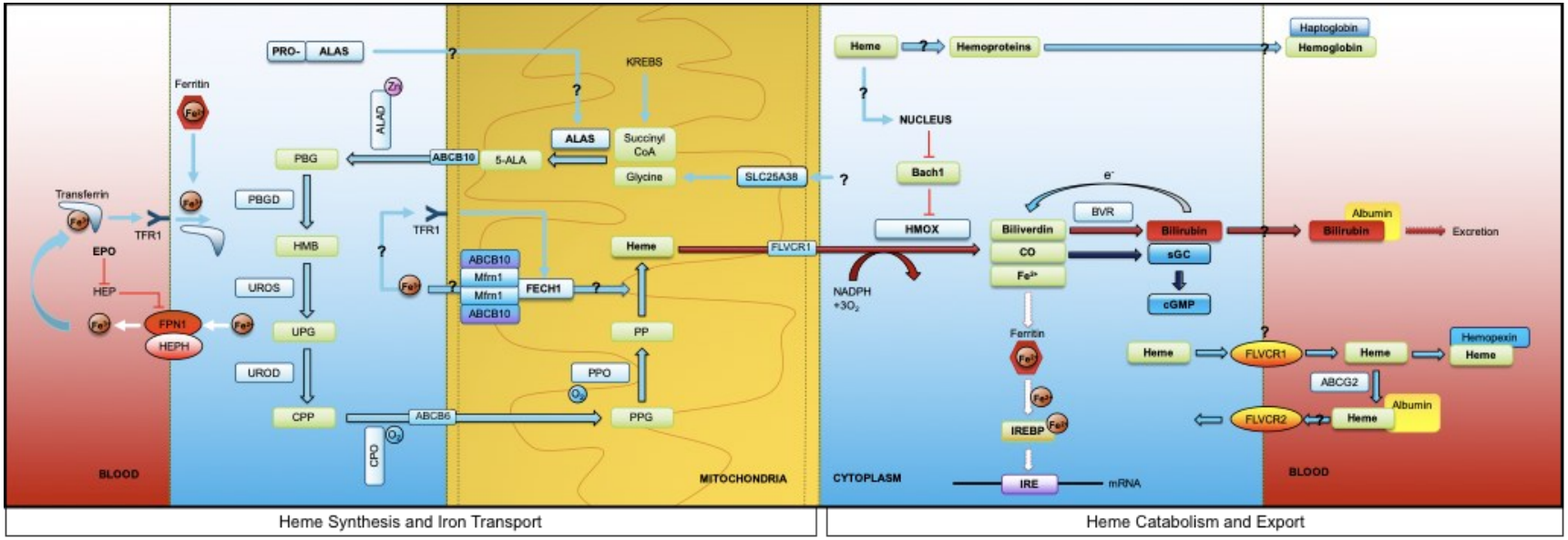

Figure 1.8 Summary of intracellular heme metabolism pathways and existing knowledge gaps. (Heme synthesis and iron transport) 5-ALA, δ-aminolevulinic acid; ABCB6, ATP binding cassette subfamily-B member-6; ABCB10, ATP binding cassette subfamily-B member-10; ALAD, δ-aminolevulinic acid dehydratase; ALAS, delta-aminolevulinic acid synthase; CPO, coproporphyrinogen-III oxidase; CPP, coproporphyrinogen III; EPO, erythropoietin; FECH, ferrochelatase; FLVCR, feline leukemia virus subgroup C receptor-related protein; FPN1, ferroportin-1; HEP, hepcidin; HEPH, hephaestin; HMB, hydroxymethylbilane; Mfrn, mitoferrin; PBG, porphobilinogen; PBGD, porphobilinogen deaminase; PP, protoporphyrin IX; PPG, protoporphyrinogen IX; PPO, protoporphyrinogen oxidase; SLC25A38, solute carrier family-25 member-38; TFR1, transferrin receptor-1; UPG, uroporphyrinogen; UROD, uroporphyrinogen decarboxylase; UROS, uroporphyrinogen III synthase). **(Heme catabolism and export)** ABCG2, ATP-binding cassette super-family G member 2; Bach1, BTB and CNC homolog 1; BVR, biliverdin reductase; cGMP, cyclic guanosine monophosphate; CO, carbon monoxide; IRE, iron response element; IREBP, iron response element-binding protein; NADPH, nicotinamide adenine dinucleotide + hydrogen; sGC, soluble guanylate cyclase.

tagged heme may not have resulted from 'heme importation', but new heme produced using recycled ^{55}Fe [127,128].

Defects in heme biosynthesis cause serious disorders in humans, such as porphyria and/or anemia [118]. Porphyrias are rare disorders, either inherited or acquired, characterized by defective enzymes involved in the synthesis of heme and the accumulation of heme precursors. Clinical symptoms of porphyria include cutaneous photosensitivity and acute attacks involving abdominal pains, anxiety, depression, confusion, and neurological manifestations [118]. Defects in ALAS2 have also been linked to sideroblastic anemia, a disorder caused by the lack of red blood cells and excess iron [118]. Although defects and mutations completely abolishing heme synthesis have not been found, homozygous ALAS1 deletion is embryonic lethal [130].

1.7.2 Regulation of iron bioavailability

Heme synthesis is intricately linked to iron bioavailability. Because iron is not synthesized and its excretion is not regulated, cells are dependent on dietary iron uptake, storage and recycling to maintain iron levels. The mechanisms regulating these processes are highly coordinated—intracellularly and systemically (Fig.1.9) [99]. Iron is first taken up by the apical villi of enterocytes lining the intestinal lumen [131]. Here, dietary iron is absorbed in two principle forms: heme iron or non-heme iron. The mechanisms mediating absorption of iron stored in heme are poorly understood, however the absorption of non-heme iron has been better characterized. For non-heme dietary iron, the ferrireductase duodenal cytochrome B (DCytB) first converts Fe^{3+} to its more soluble Fe^{2+} state using ascorbate as an electron donor. Fe^{2+} is subsequently transported into the cytoplasm via divalent metal transporter 1 (DMT1), a proton-pump-dependent transmembrane transporter. In humans, daily absorption of approximately 1-2mg dietary iron is necessary to maintain iron homeostasis, however actual uptake can vary significantly based on diet. Once internalized into enterocytes, iron is either stored or is exported into the bloodstream [131]. Free iron is stored within ferritin, a ubiquitous cage-like complex capable of storing up to 4500 iron molecules in a soluble, non-toxic state within its core—thus preventing free-iron-induced formation of reactive oxygen species

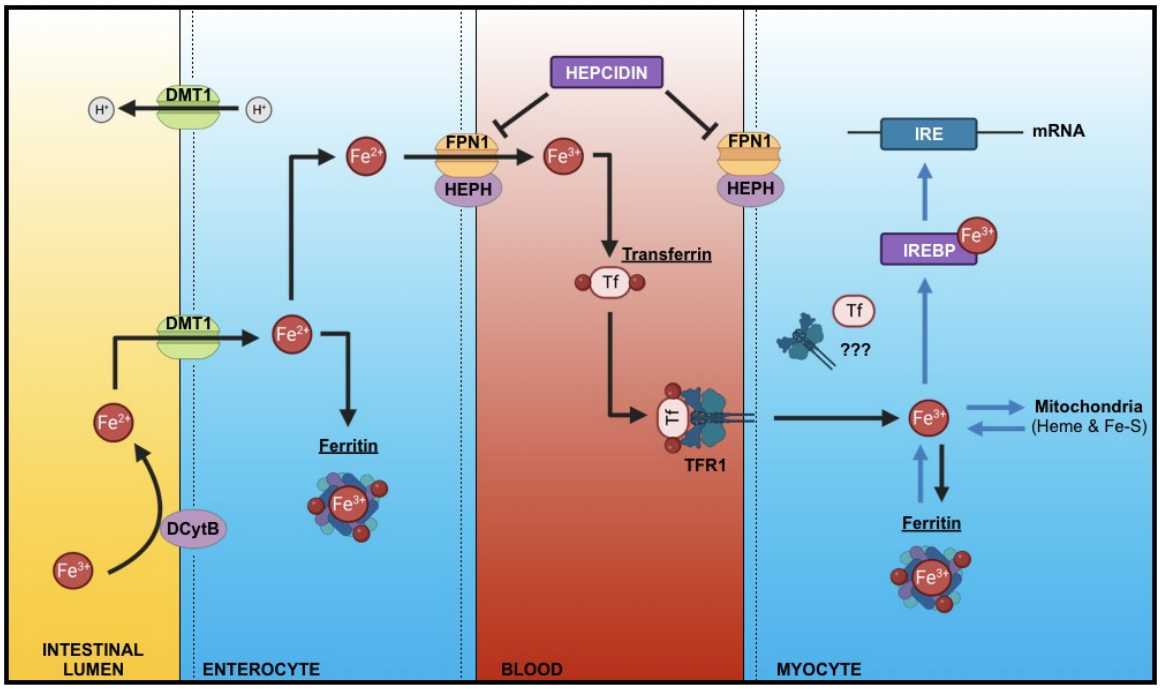

Figure 1.9 Regulation of iron bioavailability. Dietary iron (III; Fe^{3+}) is converted to iron (II; Fe^{2+}) by duodenal cytochrome B (DCytB) in the intestinal lumen. Iron (II) is then imported into enterocytes by divalent metal transporter 1 (DMT1) where it is stored in ferritin, or is converted to iron (III) by hephaestin (HEPH) and exported into the blood by ferroportin (FPN1). Ferroportin is inhibited by liver-derived hepcidin (HEP). Iron (III) is transported by transferrin in the blood where it binds the transferrin receptor (TFR1) along the cell membrane. Transferrin, iron (III) and transferrin receptor are internalized, releasing iron (III) to the intracellular space. Free iron (III) is then stored in ferritin, incorporated into heme or iron-sulfur clusters in the mitochondria, or binds iron response element (IRE)-binding proteins (IREBPs) to regulate iron-sensitive gene expression. Created with BioRender.com.

[132]. The ferritin complex is the primary storage site for both intracellular and serum iron, and consists of two types of protein subunits (24 subunits in total): ferritin heavy chain (FTH1; a ferroxidase) which converts reactive Fe^{2+} (ferrous iron) to a Fe^{3+} (ferric) state, and ferritin light chain (FTL) whose precise role is less clear but contributes to Fe^{3+} storage [133]. Although ferritin-iron complexes are primarily localized to the cytoplasm, low amounts of iron-saturated ferritin can be released into the bloodstream when iron levels are high, making ferritin a valuable biomarker for measuring body iron levels. In turn, iron-saturated ferritin released into the bloodstream can be returned to the cytoplasm via receptor-mediated endocytosis [134].

If not stored within the cell by ferritin, iron is exported into the bloodstream by the dual actions of the transmembrane proteins hephaestin (HEPH) and ferroportin (FPN1) along the basolateral membrane of enterocytes, enabling iron delivery to other sites within the body [99]. Ferroportin is the only known iron exporter and is regulated by the liver-derived peptide, hepcidin (HEP; which causes ferroportin internalization/degradation) [131,135]. The exact mechanisms regulating hepcidin are not fully understood, however it is hypothesized that binding of iron-deficient iron carrier proteins (apotransferrin) or iron-replete transferrin to receptor complexes on the liver act to induce or suppress hepcidin induction [136]. Fe^{3+} exported into the bloodstream by ferroportin is rapidly taken up by the iron chaperone, transferrin, limiting free-iron toxicity and bacterial access during infection [131]. Once bound to the homodimeric transmembrane transferrin receptor (TFR1), transferrin is endocytosed and iron is released into the cytoplasm. Free iron within the cytoplasm can then be stored by ferritin or imported into the mitochondria by mitoferrin-ferrochelatase for insertion into heme or iron-sulfur clusters. Aside from the direct modulation of iron uptake, iron levels can also be maintained through recycling [131]. Recycling of heme-iron is mediated by heme oxygenases, and—although ubiquitous—is significantly higher in macrophages, spleen and liver due to their physiological roles. When heme levels are elevated, HMOX1 and ferritin are simultaneously co-expressed, increasing the cell's capacity to store released iron [137]. Ferritin-stored iron is itself released for recycling via lysosomal autophagy [138].

Similar to heme overload, iron overload can also result in adverse effects via the Fenton reaction (e.g. fatigue, joint pain, liver damage, and organ failure) [139,140]. Clinically, patients with iron overload are characterized by high transferrin saturation (greater than 45%), high serum ferritin (greater than 200ng/ml in females and 300ng/ml in males), genotyping for HFE (hemochromatosis gene) mutations, and high iron staining in liver biopsies [139]. Patients diagnosed with iron overload are often treated with iron chelators (e.g. desferrioxamine) or frequent phlebotomy as a way of artificially reducing blood iron levels. In heart failure however, iron levels are reduced (with one third of all patients diagnosed with anemia). Thus, understanding the regulation of iron has important implications for the study of heme—and its potential therapeutic modulation—in AMI/heart failure.

1.8 Current approaches to the therapeutic targeting of heme metabolism: opportunities and challenges

HMOX1-targeted therapeutics for the treatment of AMI have yet to be translated to the clinic, however, understanding current approaches to harnessing the enzyme's therapeutic potential—as well as the potential risks and benefits associated with each—can help to identify critical obstacles.

1.8.1 Gene therapy targeting HMOX1

Genetic overexpression of HMOX1 is a potent method of cytoprotection in pre-clinical models of AMI. In isolated mouse hearts subjected to ischemia-reperfusion injury, cardiac-specific HMOX1 overexpression significantly improves cardiac performance compared to wild-type controls, resulting in increased left ventricular developed pressure, rate pressure product (the product of heart rate and left ventricular developed pressure) and reductions in LVEDP [12]. Transgenic overexpression of HMOX1 in the isolated mouse heart also significantly attenuates changes in dP/dt Max, dP/dt Min, and LVEDP following ischemia-reperfusion injury [103]. Similarly, cardiac-specific HMOX1 overexpression significantly decreases infarct area, interstitial fibrosis,

and macrophage infiltration following *in vivo* permanent LAD coronary artery ligation (no differences were observed between transgenic and non-transgenic mice at baseline) [12,141]. Yet, transgenic HMOX1 overexpression is not a clinically viable strategy for the treatment of AMI.

Delivery of HMOX1 mRNA or transient expression plasmids might present an alternative method of delivery. However, due to the instability of mRNA and the chronic nature of AMI-induced injury (with the need to maximize HMOX1 delivery to the heart), repetitive intramyocardial mRNA injection would likely be required. Thus, HMOX1 overexpression vectors have been developed to overcome the translational barriers. In rats intramyocardially transfected with human HMOX1 adeno-associated viral particles 8 weeks prior to LAD ischemia-reperfusion injury, infarct size is significantly reduced compared to LacZ controls [13]. HMOX1 transduction also increases survival by 40% after 1 year post-AMI, and significantly attenuates AMI-mediated changes in dP/dt, stroke volume, ejection fraction, maximal left ventricular pressure (LVP Max), and cardiac output (a product of heart rate and stroke volume) [11]. Similar results are also reported in porcine models of LAD coronary artery ischemia-reperfusion injury, wherein pigs intravenously transfected with human HMOX1 adeno-associated viral particles demonstrate significant reductions in infarct size, apoptotic DNA fragmentation (TUNEL), and LVEDP [142]. Yet despite the effectiveness of viral vectors overexpressing HMOX1, there remain major barriers to their clinical translation due to safety concerns associated with applying viral vectors in the clinic (e.g. viral septicemia) [143,144]. Although new strategies are being pursued to increase the efficiency of mRNA delivery and reduce the risk of adenoviral vectors via intermediary stem cell transfection, they have yet to be clinically translated [142].

1.8.2 Delivery of heme's catabolic byproducts

The delivery of heme's catabolic byproducts—independent of HMOX1—are also being explored as therapeutic strategies for cytoprotection [14]. In mice subjected to 8-10% O_2 for 7 weeks, atmospheric exposure to 20-60ppm CO immediately prior to—and throughout—hypoxia prevents increases in right ventricular systolic pressures and

pulmonary wall thickness [145]. Similarly, mice administered 50umol/kg biliverdin 1X hydrochloride i.p. immediately prior to the same hypoxic conditions (with daily maintenance doses) demonstrate significantly higher survival than vehicle controls and CO alone [145]. Greater survival is also observed in neonatal rat cardiomyocytes exposed to biliverdin 1X hydrochloride in anoxia-reoxygenation [145]. However, CO and biliverdin are independently associated with toxicity at supraphysiologic levels: a factor that must be taken into consideration. Excess biliverdin (without concomitant upregulation of biliverdin reductase and other regulatory machinery) can lead to jaundice or cause irreversible neural damage via hyperbilirubinemia and kernicterus, whereas scaling inhaled CO to therapeutic levels in humans increases the risk of CO poisoning/asphyxia [15,146].

To overcome the delivery problems associated with therapeutically scaling CO levels, CO-releasing molecules (CORMs; compounds designed to release or chemically generate controlled amounts of CO) were developed [147]. First-generation CORMs produced CO via cytochrome p450-mediated transformation of methylene chloride, however evidence of acute central nervous system toxicity and carcinogenicity was observed. Second generation CORMs used transition metals to generate CO which also exhibited toxicity. By comparison, the current generation of CORMs (CORM-3) shows smaller CO-hemoglobin accumulation compared to inhaled gas [148]. However, the degradation products left over from CO-generating reactions are also associated with toxicity [147]. Collectively, the clinical translation of CO via CORMs still requires tools to monitor the purity/safety of degradation products and to trigger mechanisms for cardiac-specific delivery and monitoring.

Although CO and biliverdin show cytoprotective effects independently, simultaneous upregulation of both by HMOX1 may collectively confer greater cytoprotection. In rats subjected to cardiac transplant ischemia, administration of both inhaled CO and biliverdin prior to transplant significantly increases survival by 80% compared to the administration of either alone [149]. Simultaneous CO and biliverdin administration also significantly increases dP/dt and LVDevP compared to either reagent alone, while reducing mitochondrial swelling, structural intracellular disorganization, and infarct size [149]. Thus, CO and biliverdin appear to exhibit greater cytoprotection when

administered together. However, optimizing the dose and delivery of two different compounds increases the challenges associated with the clinical translation of exogenous CO and biliverdin delivery (such as regulatory approval barriers). Harnessing the cytoprotective qualities of CO and biliverdin via HMOX1 induction instead may therefore present the safest and most efficient option to therapeutically target the heme metabolism pathway for the treatment of AMI.

1.8.3 Delivery of exogenous HMOX1 via cell-penetrating peptide

Cell-penetrating peptides are an emerging strategy for the therapeutic targeting of HMOX1 [150]. As short oligopeptides, cell-penetrating peptides deliver cargo to cells that would otherwise be impermeable to the cell membrane. Unlike gene therapies that require transcriptional activation and mRNA translation before HMOX1 can be produced, cell-penetrating peptides are capable of delivering functionally active HMOX1 to target cells. However, cell-penetrating peptides are still in early stages of development. It remains unclear how HMOX1 delivery via cell-penetrating peptides impacts heme metabolism and whether it is capable of conferring direct protection to cardiomyocytes post-AMI.

1.8.4 Hemin

Hemin presents a clinically feasible strategy for harnessing the pleiotropic benefits of HMOX1 and the byproducts of heme catabolism. Hemin is an FDA-approved heme-surrogate used for the treatment of acute intermittent porphyrias—a rare disease caused by the accumulation of heme precursor proteins. Identical to heme with the exception of a single chloride group bound to its iron core, hemin also serves as a potent inducer and substrate of HMOX1 and is catabolized into biliverdin, CO and ferrous iron [151]. Hemin exerts anti-inflammatory [152–155], anti-oxidant [153,154,156,157], and pro-survival properties [153] in response to a variety of injuries (as well as anti-coagulant properties) [158].

In pre-clinical models of AMI and cardiac ischemic reperfusion injury, prophylactic hemin preserves cardiac contractility, relaxation, and reduces infarct size, mitochondrial damage, and oxidative stress [9,17]. Yet despite market approval by the FDA in 1983 for porphyria, hemin's pharmacokinetic and pharmacodynamic characterization has been limited—leaving fundamental knowledge gaps in hemin pharmacology. Whether hemin is capable of improving cardiac function when initiated post-AMI (and within a clinically-approved human equivalent dose range) has not been established. It also remains unclear how cardiac heme content and its rate-limiting enzymes are affected by AMI or hemin over time.

1.9 Overarching rationale

Elevating levels of heme oxygenase-1 (HMOX1) confers robust cardioprotection in pre-clinical models of AMI and ischemic reperfusion injury by promoting neovascularization, reducing oxidative stress, inflammation, and fibrosis, thus improving cardiac function and survival [8–10,12,13,68]. HMOX1 catabolizes free heme—the functional group by which oxygen is transported in proteins such as hemoglobin, myoglobin or cytochromes involved in ATP production—into biliverdin, carbon monoxide, and free iron (sequestered by ferritin heavy chain, FTH1) [14]. Together, heme by-products exert potent antioxidant, anti-inflammatory, and vasodilatory effects [159–161]. Yet, translational investigations into HMOX1 induction for post-AMI therapy are limited and typically focus on the enzyme alone or its immediate by-products, without consideration for temporal or endogenous changes in heme substrate bioavailability/metabolism. As a heme surrogate and potent inducer/substrate of HMOX1, hemin could be a viable pharmacological strategy for the treatment of AMI [17,162].

1.10 Hypothesis and objectives

We hypothesize that hemin is directly capable of conferring cytoprotection to cardiomyocytes and improves myocardial function when administered post-AMI. Thus,

the following objectives were formed:

1) Characterize the effects of hemin and AMI on cardiac heme regulation;

2) Perform a direct comparison between hemin treatment initiated pre-injury versus post-injury in cardiomyotubles and AMI;

3) Investigate the effects of timing on hemin intervention.

Collectively, this work aims to provide valuable insights into the fundamental biology and therapeutic potential of novel strategies for the treatment of AMI through heme metabolism.

CHAPTER 2: REGULATORY CONTEXT FOR HEMIN AS A DRUG

2.1 INTRODUCTION

Hemin presents a promising therapeutic strategy for the treatment of injury/disease beyond its original indication in porphyria, however, pharmacological characterization of the drug has been limited. Hemin was first granted market approval by the United States Food and Drug Administration (U.S. FDA) in 1983 for the treatment of porphyria—a rare disorder characterized by the harmful accumulation of heme precursors due to defects in heme synthesis [163]. Since its market approval in porphyria, hemin has shown potential for therapeutic repurposing, including in the pre-clinical treatment of acute myocardial infarction (AMI) as a substrate/inducer of the enzyme, heme oxygenase-1 (HMOX1) [17,18]. In male mice subjected to AMI by permanent left anterior coronary artery ligation, hemin prophylaxis (20 $mg \bullet kg^{-1}$ i.p.) attenuates left ventricular fibrosis and preserves ejection fraction [164]. Similarly, hemin prophylaxis also reduces infarct size and oxidative stress (75$umol \bullet kg^{-1}$ / 48.9$mg \bullet kg^{-1}$ i.p.), and preserves cardiac contractility and relaxation (50$umol \bullet kg^{-1}$ / 32.6$mg \bullet kg^{-1}$ i.p.) in rat models of cardiac ischemia-reperfusion injury [9,17]. Yet, clinical translation of hemin remains limited to porphyria.

Comprehension of a drug's pharmacologic profile in health and disease strengthens our ability to treat patients effectively, to identify therapeutic opportunities or limitations, and to predict and prevent adverse side effects. For instance, understanding hemin's pharmacokinetics can shed light on interindividual variations in drug responses, such as those associated with GT repeats in the HMOX1 promoter [89]. Characterization of hemin's pharmacokinetics and pharmacodynamics (including its effects on endogenous heme regulation) can also guide optimal dosing strategies and improve drug safety in relation to AMI-induced changes in heme metabolism. However, requirements for the pre-clinical and clinical characterization of biologics approved under the U.S. FDA's Orphan Drug Act in 1983 (such as hemin) differed significantly from current

standards. This presents fundamental gaps in our collective understanding of hemin pharmacology in health and disease as well as knowledge barriers to clinical translation in future applications.

In contrast to market approval by the U.S. FDA in 1983, hemin's approval for the treatment of porphyria in Canada was granted in 2018. Federal regulatory agencies such as Health Canada and the U.S. FDA review pharmacological evidence submitted by drug sponsors/developers to ensure the safety and efficacy of new and repurposed pharmaceuticals prior to market approval. The evidence within such regulatory submissions and reviews can offer unique insights into a drug's strengths, weaknesses, and underlying mechanisms of action, yet are often overlooked as valuable sources of pharmacological information for research and drug development [165]. This evidence can also hold significant value as information reported in regulatory documents is often more extensive than that disclosed in the primary medical literature [166–170]. As a result, traditional sources of pharmacological information (like the primary medical literature) can sometimes fail to provide comprehensive overviews of all drug-related data, including negative findings or adverse events relevant to researchers, patients, clinicians, and the general public. However, whether regulatory submission documents for hemin's approval by Health Canada provide pharmacological characterization relevant to its further development or repurposing in new therapeutic interventions remains unclear.

In the present study, we review the current clinical and pre-clinical understanding of hemin using information extracted from the primary and regulatory literature—including regulatory submission documents obtained from Health Canada following hemin's market approval in 2018. Focusing specifically on the drug's pharmacodynamic effects on heme regulation and cardiomyocytes, potential risks associated with hemin use, considerations for therapeutic translation from pre-clinical to clinical settings, and knowledge related to cardiac injury/AMI thus far, we present a comprehensive review of current knowledge related to hemin's biopharmaceutical properties, pre-clinical/clinical pharmacokinetics, and pharmacodynamics. Ultimately, this case study seeks to improve the collective understanding of hemin pharmacology and enhance the potential for future pre-clinical and clinical successes in heme-modulating therapeutics.

2.2 MATERIALS AND METHODS

A formal request for the public release of regulatory documents pertaining to hemin for injection (Panhematin) was submitted by Eadie, A.L. to Health Canada's Information Science and Openness Division on July 21st, 2021; this request included the release of all information related to clinical studies in adults, paediatric patients, effectiveness studies, safety studies, Phase I, Phase II, and Phase III trials. Regulatory submission documents were subsequently released by Health Canada in June 2022 (Fig.2.1; https://clinical-information.canada.ca/ci-rc/item/212276). Additional information relating to hemin's (Panhematin's) original approval by the U.S. FDA in 1983 was extracted from the administration's Orphan Drugs Designations and Approvals database (https://www.accessdata.fda.gov). Information from the Drugs@FDA database (https://www.accessdata.fda.gov/scripts/cder/daf/) —including letters, correspondences, labels, memorandums, and regulatory reviews linked to hemin's original approval— required an official Freedom of Information Act request and were therefore not readily available. Data from the European Medicines Agency was similarly unavailable. All regulatory documents pertaining to this study were read by a single author (ALE) and the information contained within was extracted by hand. All other pre-clinical and clinical hemin studies were located through Google Scholar using the search terms 'hemin', 'hemin for injection', 'hematin', 'Panhematin', 'heme arginate', and/or 'Normosang'.

2.3 RESULTS

2.3.1 Overview of hemin in the treatment of porphyria

Hemin is a biologic heme surrogate indicated for the treatment of recurrent attacks of acute intermittent porphyria [171,172]. Available as a sterile, lyophilized black powder for reconstitution prior to i.v. administration (Panhematin; 1-4mg/kg/day for 3-14 days) or as a sterile solution complexed with arginine (Normosang; 3mg/kg/day for 4 days), hemin is produced from outdated human red blood cells subjected to viral inactivation through acetone (organic solvent), heat (with buffer), and acetic acid

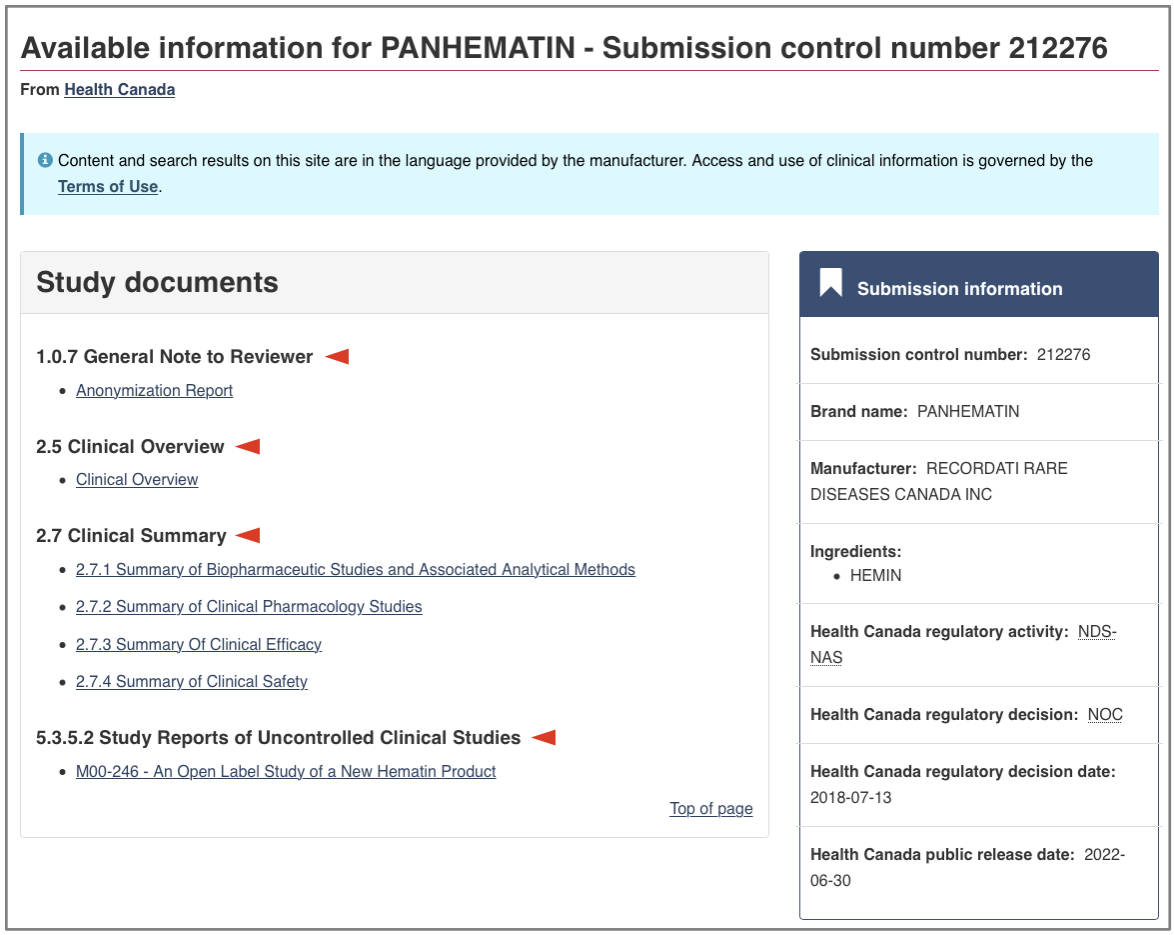

Figure 2.1 Panhematin submission documents obtained from Health Canada's clinical-information online portal (https://clinical-information.canada.ca/ci-rc/item/212276).

exposure [173]. In porphyria, hemin administration limits the rate of endogenous heme synthesis in the liver—reducing the harmful accumulation of defective heme precursors [174]. This effect is purportedly mediated by the inhibition of heme-synthesizing enzyme δ-aminolevulinic acid synthase-1 (ALAS1), however such a mechanism of action has yet to be confirmed: according to packaging documents reviewed by the FDA and Health Canada (dated May 2020) "*the exact mechanisms by which [hemin] produces symptomatic improvement in patients with acute episodes of the hepatic porphyrias has not been elucidated*" [171,173,175].

2.3.2 Regulatory history of hemin development

To provide a brief overview of hemin's regulatory history, major milestones were compiled from the available Health Canada and FDA documentation and concatenated in a timeline (Fig.2.2). On September 27th 1982, Abbott Laboratories submitted the original Biologics License Application (BLA) for Panhematin (hemin for injection) to the U.S. FDA [176]. Panhematin was subsequently approved for the treatment of acute intermittent porphyria on July 20th 1983 and was granted status as the first orphan drug under the U.S. Orphan Drug Act [176]. Since porphyria affects a relatively small patient population, FDA approval was based solely on the information published from 5 open-label studies [177–181] involving 99 patients, and 15 publications on an additional 15 patient case reports [171]. In the 5 open-label studies, 85.5% of patients treated with 3-4mg hemin/kg bodyweight once or twice daily demonstrated improvement in porphyria symptoms and pain reduction, with all patients demonstrating normalization of urinary aminolevulinic acid and porphobilinogen levels [177–181]. All patients within the open-label studies had been previously diagnosed with porphyria and hemin treatment did not exceed 13 days.

In 2000, the FDA required Abbott Laboratories to withdraw Panhematin from the market and perform an open-label noncomparative study to confirm drug safety after moving manufacturing to a new facility [171,182]. Hemin was only available to patients

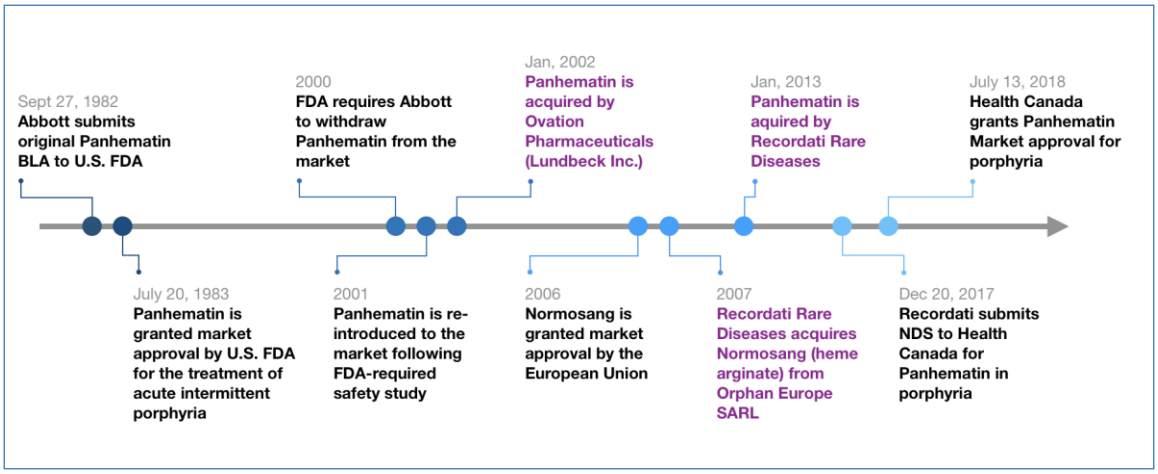

Figure 2.2 Timeline for the approval of hemin (Panhematin) compiled from available Health Canada and FDA documentation. Major milestones are presented. Milestones relating to the acquisition of Panhematin are highlighted in purple. BLA, Biologics License Application; FDA, Food and Drug Administration; NDS, New Drug Submission. Created with Vizzlo.

through enrollment in a noncomparative, multi-center, open-label compassionate use study during this time (n=130 patients) [171,182]. Placebo controls were not included in Panhematin studies for porphyria due to the ethical implications involved in denying patients treatment for neurologically life-threatening complications.

Following the completion of the open-label noncomparative safety study (n=124 patients completed), the FDA concluded that Panhematin manufactured at Abbott's new facility was safe and re-introduced the drug commercially in 2001 [171,182]. In January 2003, Ovation Pharmaceuticals (since renamed Lundbeck Inc.) acquired Panhematin from Abbott Laboratories [176]. Panhematin was subsequently acquired by Recordati Rare Diseases Inc. in January 2013 [176].

On December 20th 2017, Recordati Rare Diseases submitted a formal proposal (New Drug Submission) to Health Canada for the review and approval of Panhematin in the treatment of acute intermittent porphyria [171]. Panhematin was granted market approval for "*the amelioration of recurrent attacks of acute intermittent porphyria (AIP) temporally related to the menstrual cycle in susceptible women, after initial carbohydrate therapy is known or suspected to be inadequate*" on July 13th 2018 [171,172]. Similar to its original approval by the FDA in 1983, Panhematin's approval by Health Canada was also evaluated on the basis of 5 open-label studies in patients with porphyria [177–181], in addition to case reports from the aforementioned compassionate-use study [182], and an observational study [174] investigating patient-reported outcomes (a summary of clinical studies and case reports supporting Panhematin's evaluation by Health Canada is provided in Table 2.1.) [171,175]. Collectively, clinical studies evaluated by Health Canada included a total of 258 individuals administered hemin (249 with porphyria, 9 healthy volunteers; 58 males : 135 females : 65 N/A; Table 2.1). Participants within the studies were administered a variety of hemin dosing regimens, with a maximum of 13 days consecutive dosing (3mg•kg^{-1}) and an overall dose range between 1-8mg•kg^{-1} •day^{-1} of hemin (Table 2.1).

Table 2.1 Summary of Hemin Dosing in Clinical Studies

Clinical Studies and Case Reports Supporting Panhematin's Evaluation by Health Canada						
Study	Study Drug	Species	Study Population (healthy volunteers/ porphyria)	Dose and Route of Administration ($mg \bullet kg^{-1}$)	Duration (days)	Sex, No. (M/F)
Watson *et al.,* 1978 [177]	Hematin	Human	Porphyria (n=15)	4.0 i.v. (b.i.d. – q.d.)	1-6	4 M / 11 F
Pierach *et al.,* 1980 [178]	Hematin	Human	Porphyria (n=57)	4.0 i.v.	N/A	N/A
McColl *et al.,* 1981 [179]	Hematin	Human	Porphyria (n=8)	4.0 i.v. (b.i.d. – q.d.)	3-5	2 M / 6 F
Lamon *et al.,* 1979 [180]	Hematin	Human	Porphyria (n=12)	1.8-3.7 i.v./oral	3-30 (interval N/A)	3 M / 9 F
Lamon *et al.,* 1977 [181]	Hematin	Human	Porphyria (n=7)	3.0 i.v.	3-13	N/A
Dhar *et al.,* 1975 [212]	Hematin	Human	Porphyria (n=4)	4.2. i.v. (q.d.), 4.1-6.0	1, 2-4	1 M /3 F
Peterson *et al.,* 1976 [203]	Hemin in solution	Human	Porphyria (n=1)	3.6 i.v. (q.d.), 2.5 i.v. (b.i.d)	1, 2	1 F
Dhar *et al.,* 1978 [200]	Hemin in solution	Human	Porphyria (n=1)	6.1 i.v.*, 12.2 i.v. (overdose)	1, 1	1M
McColl *et al.,* 1979 [204]	Hemin in solution	Human	Porphyria (n=1)	4.0 i.v. (q.d.), 4.0 i.v. (b.i.d)	3, 3	1 F
Morris *et al.,* 1981 [205]	Hemin in solution	Human	Porphyria (n=1)	3.0 i.v. (b.i.d)*	1	1 F
Petersen and Pierach, 1984 [206]	Hemin in solution	Human	Porphyria (n=1)	4.0 i.v. (b.i.d)	6 doses monthly for 4 months	1 F
Khanderia, 1986 [207]	Panhematin	Human	Porphyria (n=1)	4.0 i.v.	1	1 F

Bissel, 1988 [211]	Panhematin	Human	Porphyria (n=8)	1.2 (q.d) – 1.3 i.v. (b.i.d)*	N/A	1 M / 7 F
Green and Ts'ao, 1990 [208]	Panhematin	Human	Porphyria (n=1)	4.0 i.v. (q.d.), 4.0 i.v. (b.i.d)	3, 4	N/A
Anderson and Collins, 2006 [182]	Panhematin	Human	Porphyria (n=130)	1.3-4.8 i.v.*	Various	37 M / 93 F
Bonkowsky *et al*., 1971 [174]	Hematin	Human	Porphyria (n=1)	3.8 i.v., accidental subcu, i.v. (b.i.d) *	3	1 F
Simionatto *et al*., 1988 [202]	Hematin	Human	Healthy volunteers (n=9)	4.0 i.v.	1	9 M
Other Clinical Studies						
Tokola *et al*., 1986 [191]	Heme arginate	Human	Healthy volunteers (n=4)	3.0 i.v.	1	1 M / 3 F
Ruifrok *et al*., 2011 (NCT00483587) [197]	Normosang	Human	NSTEMI (n=10)	3.85 i.v.*	1	8 M / 2 F
	Placebo		NSTEMI (n=5)	N/A	1	3 M / 2 F
Andreas *et al*., 2018 [195]	Normosang (pre-surgery)	Human	Aortic valve replacement (n=16)	1-3.0 i.v.	1	6 M / 10 F
	Placebo	Human	Aortic valve replacement (n=8)	N/A	1	3 M / 5 F
Total: 20 studies	**Panhematin/Hematin:** 12 studies **Normosang/ Heme arginate:** 3 studies **Hemin in solution:** 5 studies **Placebo:** 2 studies	**Human:** 20 studies	**Porphyria:** 240 patients **NSTEMI:** 10 patients **Aortic valve replacement:** 16 patients **Healthy:** 13 volunteers	**Range** ~1-8 mg•kg^{-1}	**Maximum consecutive dosing:** 13 days at 3.0 mg•kg^{-1}	**Total:** **M:** 73 **F:** 150 **N/A:** 65

***** Original dose was reported in total mg; dose in mg•kg^{-1} was therefore determined using an assumed mass of 65kg (worldwide average).

To date, neither Recordati nor previous market authorization holders in the U.S. have sponsored any clinical trials involving Panhematin following the drug's original approval [171]. Thus, pharmacological evidence submitted in support of Panhematin's most recent market authorization by Health Canada in 2018 has not increased significantly since its 1983 approval by the U.S. FDA.

2.3.3 Pharmaceutical comparison of Panhematin to Normosang

In 2007, Recordati Rare Diseases acquired Orphan Europe SARL—the manufacturer of a similar hemin product for the treatment of porphyria: heme arginate (Normosang) [183,184]. Although Recordati's acquisition of Normosang predated the company's procurement of Panhematin by six years, primary literature describing the use of Normosang were explicitly excluded from Recordati's search of safety-related case reports used to support Panhematin's approval by Health Canada [185]. The rationale underlying this decision remains unclear, given that pharmacological evidence for Normosang could provide orthogonal insights into Panhematin's pharmacology or mechanisms of action.

Prior to Panhematin's approval in July 2018, no clinical hemin products were available for use in Canada—though exceptions were made under the country's Special Access Program for Panhematin (lyophilized hemin) and Normosang (heme arginate) [183,184]. Similar to Panhematin, Normosang shares hemin as its active pharmaceutical ingredient and suppresses the production of heme precursors in porphyria. However, the two products differ in their preparation and are not considered pharmaceutically equivalent [151,186]. Normosang is provided as a solution of 250mg hemin (diluted in 0.9% NaCl before injection), and includes 96% ethanol and propylene glycol as excipients [171]. Normosang additionally complexes hemin with arginine to improve hemin stability in solution and reduce the risk of phlebitis (inflammation of the vein at the site of injection), a common risk associated with hemin administration [151]. In contrast, Panhematin is provided as a lyophilized powder (reconstituted in sterile water before injection) containing 350mg hemin, 335mg sorbitol, and 240mg sodium carbonate (dissolution of hemin in sodium carbonate produces hematin) [151]. Panhematin is

currently approved for use in the U.S. and Canada, whereas Normosang (now produced by Recordati Rare Diseases following the manufacturer's acquisition of Orphan Europe SARL in 2007) is approved for use in Europe, Japan and Russia [183,184]. To date, there are no clinical trials comparing the efficacy of Panhematin and Normosang [183].

2.3.4 Hemin pharmacokinetics

Information made available from Health Canada submission documents regarding the pharmacokinetics of hemin (in health and disease) was limited. According to submission documents, no clinical pharmacology studies have been conducted by Recordati Rare Diseases to date [171]. Instead, pharmacokinetic and pharmacodynamic data submitted in support of the company's Health Canada submission of Panhematin was collected from original trials and the primary literature [171].

According to primary literature cited within Panhematin's Health Canada submission documents: following i.v. infusion, hematin binds to hemopexin (the serum heme transporter) or albumin for transportation to the liver where it is subsequently catabolized by hepatic heme oxygenases [171,180,187,188]. How hematin (or hemin in general) is intracellularly imported is unclear. Like heme, hematin is then cleared through the hepatic pathway in bile or urine [187]. In patients with porphyria, hematin metabolism follows a two-compartment clearance model comprised of a rapid initial phase followed by a slower second phase [187]. According to documents submitted by Recordati Rare Diseases to Health Canada in support of Panhematin, "*other aspects of human pharmacokinetics have not been defined*" [173]. Similarly, "*clinical data for subjects aged 65 and over was not sufficient to determine whether they respond differently from younger subjects"* [173]. Human data is also cited as insufficient to establish the presence or absence of Panhematin-associated risk during pregnancy, although limited anecdotal evidence has suggested safe use [173,189,190]. However, reproduction studies with Panhematin in pre-clinical models have not been conducted to date and it remains unclear whether hemin is capable of crossing the placental barrier.

Information regarding hemin pharmacokinetics with acute and chronic dosing was similarly limited in primary literature (beyond that cited in Panhematin's submission to

Health Canada). However, a small study was performed by Tokola *et al.* in 1986 (3 years after Panhematin's FDA approval), wherein plasma concentrations of infused hemin (3mg•kg^{-1} i.v., single dose) were measured in healthy volunteers over 48h (1 male, 3 females; ages 26 – 50) [191]. In this study, hemin levels declined exponentially across all patients, with a mean elimination half-life of 10.8h. Comparatively, total plasma clearance did not differ significantly from symptomless patients with porphyria included in the same study (2 males, 2 females; ages 30 – 45), however n-values were low. Thus, more pharmacokinetic sampling is still necessary to characterize the effects of patient diversity (e.g. different ages and comorbidities) on hemin pharmacokinetics.

Although information related to hemin pharmacokinetics in humans is limited, pre-clinical animal models can provide valuable insights into how a drug is physiologically processed. Understanding hemin's pharmacokinetics in animal models is also important to facilitate therapeutic repurposing and dose optimization in pre-clinical models beyond porphyria. Thus, hemin pharmacokinetics derived from animal studies in the primary literature (i.e. outside the studies cited in Panhematin's submission to Health Canada) were also analyzed. In healthy male mice, hemin administered intravenously exhibits an LD_{50} of 56.3mg hemin•kg^{-1} (single dose) over 14 days, with a lowest lethal dose in mice and rats occurring at 30mg hemin•kg^{-1} i.v. [151]. Intraperitoneally, hemin exhibits an LD_{50} of nearly double (112.5mg hemin•kg^{-1}; single dose) in healthy male mice, indicating significant differences in drug uptake between intravenous and intraperitoneal administration [151]. Comparatively, male mice administered hemin orally at a dose of 5000mg•kg^{-1} exhibit no observed adverse effects over 14 days, indicating low oral hemin bioavailability and an inefficient strategy for therapeutic hemin delivery [151]. Hemin toxicity in female murine models remains to be understood, however, plasma clearance and distribution has been measured in a single study of female rhesus monkeys (n=3) [192]. In this study, each of three monkeys were assigned a unique dosing regimen, with hemin doses ranging from 2.6—9.8mg•kg^{-1} i.v. and total plasma elimination half-life ranging from 2.2h to 7.0h [192]. To measure hemin-iron distribution, one monkey was administered a single injection of 2.4 mg•kg^{-1} Fe^{59}-labelled hemin. At 21h post-injection, 48.2% of injected radioactivity was observed in the liver, with 4.8% measured in plasma, 2.0% in the intestine, 1.6% in the kidneys, 1.3% in vertebrae, 1.2%

in the lungs, 0.5% in the spleen, 0.4% in the heart, 0.2% in the sternum, and 0.1% in red blood cells; 34.2% of the remaining radioactivity was distributed across other tissues to lesser extents [192]. It remains unclear whether this distribution is reflective of hemin uptake or the uptake of free radiolabelled iron from hemin catabolism. Given that hemin undergoes significant metabolism by the liver, alternate strategies of hemin delivery/packaging—such as nanoparticle encapsulation—may be required to maximize therapeutic efficacy in non-hepatic diseases.

2.3.5 Hemin pharmacodynamics

Within Panhematin's Health Canada submission documents, characterization of hemin's pharmacodynamic effects focused primarily on the suppression of porphyria symptoms and urinary heme-precursor level normalization (i.e. aminolevulinic acid and porphobilinogen) [177–181], however, additional insights were obtained from regulator-approved product information sheets for both Panhematin and Normosang [175,193]. As previously discussed, the precise mechanism by which hemin suppresses symptoms of acute porphyria has yet to be elucidated and hemin's holistic effects on heme regulatory enzyme expression remain unclear [171,175]. However, hemin has been associated with increased iron and serum ferritin, phlebitis, as well as transient, mild anticoagulant effects [175,193]. As a result, it is recommended that physicians monitor iron and ferritin levels in patients receiving multiple hemin doses; iron chelation therapy is also recommended if iron/ferritin levels are elevated, however the levels at which its use should be considered are not defined (and whether it has been necessary in regular clinical use is not clear) [175]. To overcome challenges described by Recordati as "poor venous access" associated with hemin injections, large veins or central venous catheters have been recommended to reduce the risk of phlebitis with intravenous administration [173,193]. Whether phlebitis is prevalent in murine models remains to be determined, however, the resulting poor venous access may present challenges to repeated intravenous hemin injections administered via tail vein and should be taken into consideration in pre-clinical modeling. As hemin has exhibited transient, mild anticoagulant effects when added to blood clots *ex vivo*, its use has been contraindicated with concurrent anticoagulant

therapy in patients with porphyria [175,194]. However, hemin's mild anticoagulant effects could prove beneficial in the context of AMI, wherein anticoagulant therapy is already standard-of-care.

The pharmacodynamic effects of hemin on the heart (or myocytes) remain even less clear as clinical biopsies are not easily obtainable and studies involving pre-clinical models and pharmacodynamics focus almost exclusively on HMOX1 induction alone. However, two clinical studies investigating the effects of hemin on cardiac injury outcomes (not included within Panhematin's regulatory submission documents) were uncovered. In a randomized, placebo-controlled, safety and feasibility study from the primary literature, patients scheduled for conventional aortic valve replacement received either placebo (n=8), 1mg•kg^{-1} (n=7) or 3mg•kg^{-1} (n=9) heme arginate i.v. 24h pre-surgery (NCT02314780) [195]; patient sex was not listed. Following hemin administration, HMOX1 protein was dose-dependently increased (up to 3.4-fold) in atrial appendage samples compared to placebo-treated controls. HMOX1 mRNA was also dose-dependently increased in the right ventricle and peripheral blood mononuclear cells following hemin administration. In July 2007, an open-label, randomized Phase I/II trial (NCT00483587) evaluating the safety and efficacy of hemin (single high dose, 250mg i.v.) in patients (n=8 males, 2 females) with non-ST-elevation myocardial infarction (NSTEMI; within 3h of hospitalization) was initiated (in addition to standard of care treatment) [196]. Despite completion of the study in February of 2010, results of the study remain unregistered with clinicaltrials.gov and unpublished in primary peer-reviewed journals [196]. However—using the study's clinicaltrials.gov ID (NCT00483587), we were able to trace the unregistered/unpublished clinical trial results to the 2011 doctoral thesis of the principal investigator's student [197]. In NSTEMI patients from the clinical trial, hemin administration did not increase plasma ferritin, bilirubin, or HMOX1 mRNA expression/protein activity in peripheral blood mononuclear cells at 1, 2, 3, or 7 days when compared to placebo. Standard biochemical tests (e.g. electrolyte, inflammation, and blood tests) did not differ significantly between patients receiving placebo or hemin, and no adverse effects on the heart, kidney, or liver were detected following hemin administration (by ultrasound/echocardiography or clinical blood test). To date, no further information pertaining to this study has been released.

Given that a clinical trial in AMI has already been attempted (despite the absence of pre-clinical supporting evidence within the primary literature at the time and limited characterization of the drug's pharmacology), information regarding hemin's effects on the heart in health and disease is urgently required.

Although patient samples can provide valuable information regarding hemin's effects on the human heart, the collection of cardiac biopsies is invasive, requires highly-trained personnel, and provides only a brief snapshot of the mechanisms underlying hemin pharmacodynamics. Thus, preclinical animal models are currently necessary to provide temporal and systemic insights into the effects of hemin on cardiac signaling pathways of therapeutic interest. Yet, translating the relevance of pharmacological outcomes from animal models to humans requires the determination of interspecies hemin dose equivalence. Interspecies dose equivalence is often determined by adjusting for differences in body mass (i.e. $mg \bullet kg^{-1}$)—however, this method of calculation does not incorporate differences in species' pharmacokinetics (e.g. metabolism and clearance). As a result, current FDA guidelines recommend the extrapolation of Human Equivalent Doses using body surface area (e.g. mg/m^2) via the allometric scaling algorithm detailed in the FDA's *Guidance Document for Estimating the Maximum Safe Starting Dose in Initial Clinical Trials Table-1: Conversion of Animal Doses to Human Equivalent Doses Based on Body Surface Area*—with exceptions for non-traditional drugs (e.g. vaccines) or routes of administration (e.g. intraocular, topical, etc.) [198]. Herein, human doses are normalized from animal doses (and *vice versa*) by species-specific body surface area-conversion factors (BSA-CF), which relate to the species' metabolic rates [198]. Determining species dose equivalence from ranges already prescribed in the clinic (using BSA-CF) minimizes the risk of insufficient dosing or toxicity when repurposing pre-existing drugs in animal models, and can help to inform researchers whether dosing strategies in animals may be translatable within a well-tolerated range in humans. In porphyria patients, a daily dose of 1-4 $mg \bullet kg^{-1}$ hemin is recommended, equating to a calculated Human Equivalent Dose of 6.2-24.8$mg \bullet kg^{-1}$ hemin in rats and 12.3-49.2$mg \bullet kg^{-1}$ in mice [198]. To provide a summary of hemin dosing in pre-clinical animal models of health, cardiac ischemia-reperfusion injury, and AMI within the present

review—and how such ranges relate to the calculated Human Equivalent Doses for that particular species, pre-clinical studies are documented in Table 2.2.

2.3.6 Clinical considerations and risks

Understanding the potential risks associated with hemin use is necessary for the proper prevention and management of adverse events in drug repurposing. Although no adverse events were detected following administration of a single dose of hemin post-NSTEMI, hemin or HMOX1 induction—like any therapeutic intervention—can cause serious side effects if misused or used in the wrong context. Several cases of hemin overdoses have been reported in patients with porphyria (Table 2.3), resulting in liver failure/transplant without indication of iron overload in explanted tissue (19mg hemin•kg^{-1} body weight), acute liver failure with hyperbilirubinemia and anemia (~23mg•kg^{-1} over two days), hyperbilirubinemia with marked increase in aspartate aminotransferase (indicator of liver damage; ~30mg•kg^{-1}), and renal failure (19mg•kg^{-1}) [187,193,199–201]. A case of hemin-mediated overdose (~38mg•kg^{-1}) resulting in double liver transplant and patient death has also been referenced within a separate study by Frei *et al*., 2012 [199]. However, the referenced fatality is cited as a personal communication from Dr. Ulrich Stölzel of Chemnitz, Germany (dated April 2010) for which no supporting literature—such as a copy of the personal communication, peer-reviewed publication, or medical examiners' report—could be found, despite our best efforts [199]. According to Frei *et al*., 2012, information regarding any comorbidities or other potential circumstances underlying the patient's death are not available—thus, it remains unclear whether hemin was the sole factor contributing to death [199]. Given the severity of the patient's outcome, however, this study has been included in the present review (Table 2.3). Solubilizing agents and excipients were not attributed to the adverse effects of any of the aforementioned overdose cases as all solubilizers used to dilute hemin remained within daily recommended limits [199]. Although overdoses represent an extreme level

Table 2.2 Summary of Hemin Dosing in Pre-Clinical Models of Cardiac Health, Ischemia-Reperfusion Injury, and AMI

Study	Species (Pre-clinical Model)	Treatment	Dose and Route of Administration ($mg \bullet kg^{-1}$)		Dosing Interval(s)	Sex, No. (M/F)
			Dose Administered	Human Equivalent Dose*		
Sears & Huser, 1966 [192]	Rhesus monkey (Healthy)	Hematin	2.60-9.80 i.v	0.84-3.16	Various	3 F
Clark *et al*., 2000 [9]	Rat (IR-injury)	Hemin	48.89 i.p.	7.88	24h pre-IR	M
Lakkisto *et al*., 2009 [17]	Rat (IR-injury)	Hemin	32.60 i.p.	5.26	24h pre-IR	M
Shan *et al*., 2019 [164]	Mouse (AMI)	Hemin	20.00 i.p	1.62	1d pre- to 7d post-AMI, *dieb. alt*	M
Total: 4 studies	Monkey, rat (2), mouse Healthy, IR-injury (2), AMI	Hematin (1), Hemin (3)	**Range:**			F=3 M=unknown
			Monkey: 2.60-9.80 i.v **Rat:** 32.60-48.89 i.p. **Mouse:** 20.00 i.p.	~1-8 $mg \bullet kg^{-1}$	From single dose to 5 doses *dieb alt.*	

*Human Equivalent Dose was determined using the FDA's *Guidance For Industry Table-1: Conversion of Animal Doses to Human Equivalent Doses Based on Body Surface Area* [198]. Red cells are used to indicate a Human Equivalent Dose of hemin above the clinically recommended 1-4$mg \bullet kg^{-1}$ approved for the treatment of porphyria in humans. Green cells are used to indicate a Human Equivalent Dose of hemin within the recommended 1-4$mg \bullet kg^{-1}$.

Table 2.3 Summary of Documented Clinical Overdoses

Study	Study Drug	Species	Study Population (healthy volunteers/ porphyria)	Dose and Route of Administration ($mg \bullet kg^{-1} \bullet day^{-1}$)	Duration (days)	Sex, No. (M/F)	Outcome
Recordati Rare Diseases Product Information Sheet for Normosang [193]	Normosang	Human	Porphyria	30.0 i.v.[a]	1	1 M	Hyperbilirubinemia with increased aspartate aminotransferase
Kostrzewska *et al*., 1991 [201]	Heme arginate	Human	Porphyria	23.0 i.v.[b]	2	1 M	Hyperbilirubinemia and anemia
Frei *et al*., 2012 [199]	Heme arginate	Human	Porphyria	19.0 i.v.	1	1 F	Acute liver failure requiring urgent transplantation
Personal communication from Ulrich Stölzel,2010. Referenced by Frei *et al*., 2012 [199]	Heme arginate	Human	Unknown	38.5 i.v.[c]	1	N/A	Acute liver failure, double liver transplant, and subsequent death
Dhar *et al*., 1978 [200]	Hematin	Human	Porphyria	12.2 i.v.	1	1 M	Transitory renal failure

[a] Original dose was reported as '10X higher than recommended', therefore dose in $mg \bullet kg^{-1}$ was determined by multiplying the clinically recommended dose of Normosang by 10.
[b] Original dose was reported as '3000mg over 2 days', therefore dose in $mg \bullet kg^{-1}$ was determined using an assumed mass of 65kg (worldwide average).
[c] Original dose was reported as '2500mg', therefore dose in $mg \bullet kg^{-1}$ was determined using an assumed mass of 65kg (worldwide average).

of hemin administration in patients with a pre-existing heme disorder (distinct from regulated safety studies), they may provide valuable insights into potential risks associated with frequent hemin administration.

HMOX1 (the enzyme by which hemin canonically confers cytoprotection through its induction) can also cause adverse side effects when overexpressed. In the hearts of otherwise healthy mice, chronic (transgenic) HMOX1 overexpression causes spontaneous development of cardiac dysfunction after 1 year [107]. Although chronic HMOX1 overexpression in transgenic mice attenuates isoproterenol-induced cardiac dysfunction in parallel cohorts, it also exacerbates cardiac dysfunction induced by transverse aortic constriction [107,108]. Additionally, HMOX1 has been negatively implicated in cases of chronic metabolic inflammation, wherein hepatic and macrophagic HMOX1 deletion elicits resistance to inflammation and diet-induced insulin resistance in mice [109]. Thus, further investigation into the precise pathophysiological contexts in which HMOX1 induction (and by extension, hemin) confer cytoprotective—rather than adverse—effects remains necessary. Whether the state of heme metabolism (e.g. heme content and heme-regulatory enzyme expression) can inform/predict when HMOX1 will be cytoprotective also requires further investigation.

2.4 DISCUSSION

Using information extracted from the primary and regulatory literature, we explore the history of hemin development, review the current clinical and pre-clinical understanding of hemin pharmacology, and highlight potential insights for the advancement of therapeutic hemin repurposing. Although information related to hemin pharmacokinetics and pharmacodynamics/mechanisms-of-action was limited (evidence submitted in support of Panhematin's most recent market authorization by Health Canada in 2018 had not significantly increased since 1983), documents submitted to Health Canada for Panhematin approval revealed valuable insights into hemin dosing strategies that can be used towards pre-clinical modeling in AMI and inform future clinical studies. Within clinically-recommended doses for porphyria, hemin is safe for consecutive daily use in humans for up to at least 13 days (i.v. in patients with porphyria) [181,191,202].

Although the effects of once-daily hemin dosing over a longer duration remain to be understood, this finding introduces promising evidence that repeated hemin administration may be safe for chronic use (such as that required for the treatment of AMI). Meanwhile, insights gathered from pharmacokinetic characterizations and case studies on hemin overdoses in patients highlight markers of hemin toxicity and potential management strategies to reduce adverse events. Preliminary evidence from the primary literature also demonstrates hemin safety when administered within the clinically-recommended range for porphyria early post-AMI [197], as well as hemin's capacity to induce HMOX1 in the human heart (when administered intravenously) pre-aortic valve replacement surgery [195]. In mice administered i.p. hemin pre-AMI (and for 7 days *dieb. alt*) at a Human Equivalent Dose within the recommended i.v. range for porphyria, left ventricular function and remodeling were also improved [164,195]. Thus, preliminary evidence suggests a promising safety and efficacy profile for hemin repurposing (within the clinically-recommended range for porphyria) for the treatment of AMI. Whether hemin remains effective when treatment is initiated post-AMI (and how long post-AMI it might be effective) has yet to be determined. Given heme's prominent role in oxygen transport and ATP production, the potential impact of AMI and chronic hemin administration on endogenous heme regulation in the heart also requires further characterization.

In the present case study, we present a summary of clinical studies submitted in support of Panhematin's 2018 Health Canada approval for the treatment of porphyria. Within Panhematin's submission documents to Health Canada, 17 studies investigating hemin use in humans were used to support Panhematin's approval for porphyria—of which, 8 studies (~47%) included only one patient [200,203–209] and only one study was conducted within the past 33 years [182]. Total daily hemin ranged from 1-8mg•kg^{-1} i.v. (without overdose). Clinical studies used to support Panhematin's approval for porphyria also demonstrated inconsistencies in the inclusion of fundamental patient and dosing descriptions, with 3 clinical studies failing to indicate patient sex [n=65 patients] [181,208,210], 5 clinical studies failing to indicate the exact dose of hemin administered [n=141] [174,182,200,205,211], and 4 clinical studies failing to define precise dosing schedules/duration [n=78] [178,180,206,211]. Failure to describe fundamental patient

characteristics and dosing regimens in clinical studies reduces researchers' ability to effectively apply pharmacological findings to new drug applications and fails to do justice to the contribution of patients and volunteers. Thus, review of regulatory submission documents (such as in the present case study) can help to reiterate the importance of including fundamental patient and dosing information for secondary studies, new insights into drug repurposing, and systematic reviews.

Collectively, information gathered from the primary and regulatory literature related to hemin pharmacology highlights valuable insights for the advancement of therapeutic hemin repurposing. Yet, information regarding hemin's effects on endogenous heme regulation and mechanisms of cytoprotection in the heart, the therapeutic potential and potential limitations of hemin's efficacy when administered post-AMI (or in other indications), and its potential effects on other organs remain to be characterized. Ultimately, fundamental questions regarding hemin pharmacology in health and disease still require answers in order to better inform therapeutic strategies for hemin repurposing/translation and optimize hemin dosing.

CHAPTER 3: RESCUE OF MYOCARDIAL FUNCTION BY HEMIN INTERVENTION POST-INFARCTION

3.1 INTRODUCTION

Current strategies for the treatment of acute myocardial infarction (AMI) are limited and novel therapeutic interventions are required to prevent heart failure. AMI occurs when the coronary arteries supplying the heart become occluded, resulting in progressive cardiac cell death, metabolic stress, inflammation, fibrosis, and compromised function. Surgical and pharmacological interventions have significantly decreased the incidence of recurrent AMI, however the cumulative stress is not entirely resolved and morbidity and mortality remain high [62]. Due to delayed presentation or anatomically inaccessible occlusions, many patients are not reperfused and so invariably experience worse clinical outcomes [62,63]. Thus, pharmacological targeting of novel molecular pathways capable of eliciting myocardial rescue is necessary.

Elevating levels of heme oxygenase-1 (HMOX1) confers robust cardioprotection in pre-clinical models of AMI and ischemic reperfusion injury by promoting neovascularization, reducing oxidative stress, inflammation, and fibrosis, thus improving cardiac function and survival [8–13]. HMOX1 catabolizes free heme—the functional group by which oxygen is transported in proteins such as hemoglobin, myoglobin or cytochromes involved in ATP production—into biliverdin, carbon monoxide, and free iron (sequestered by ferritin heavy chain, FTH1) [14]. Together, heme by-products exert potent antioxidant, anti-inflammatory, and vasodilatory effects [14,16,160]. Yet, translational investigations into HMOX1 induction for post-AMI therapy are limited and typically focus on the enzyme alone or its immediate by-products, without consideration for temporal changes in HMOX1 or heme substrate bioavailability.

As a heme surrogate and potent inducer/substrate of HMOX1, hemin could be a viable pharmacological strategy for the treatment of AMI [17,18]. Hemin was first approved for therapeutic use by the United States Food and Drug Administration (U.S. FDA) in 1983 [163]. However, the requirements for pre-clinical and clinical

characterizations of biologics differed significantly from current standards, leaving fundamental gaps in pharmacological understanding. Hemin remains a clinically-approved orphan drug for the treatment of porphyria but has also been used to elicit anti-inflammatory, anti-oxidant, and pro-survival properties in a variety of experimental pre-clinical settings [17,18]. In isolated rat hearts subjected to ischemic-reperfusion injury, hemin administered 24h in advance—albeit at a dose above the prescribed human therapeutic equivalent range—preserved cardiac contractility and relaxation [9]. In rat models of AMI, hemin administered at a therapeutic human equivalent dose reduced infarct size, mitochondrial damage, oxidative stress, and increased fractional shortening (although it is unclear whether treatment was initiated before or after injury) [17]. Still, it remains uncertain whether hemin is truly capable of improving cardiac function within the clinically-approved human equivalent dose range of tolerability or whether such treatment is effective when initiated post-AMI.

It also remains unclear how cardiac heme content or its rate-limiting enzymes are impacted by either AMI or hemin. Although heme content is reportedly elevated in end-stage heart failure patients, how heme metabolism is altered prior to advanced injury is not well-characterized [19]. Heme is essential to cellular respiration due to the oxygen-carrying capacity of its iron core and is synthesized by the rate-limiting δ-aminolevulinic acid synthases (ALAS1 and ALAS2). Free heme is generally considered to be a noxious agent in ischemic tissue, though its negative effects may be over-generalized by the study of iron overload and ferroptosis [54,70]. As a result, heme catabolism is regulated by two genetically distinct isoenzymes: the heme- and stress-inducible HMOX1 and the constitutive HMOX2. A further understanding of heme metabolism, and its potential to be an agent of therapy (or molecular liability) is a distinct interest for translational pharmacology.

Here we show that heme content and heme regulatory enzyme expression are temporally dyssynchronous in the peri-infarct left ventricle post-AMI. We also show that hemin confers protection *in vitro* and *in vivo*, however its effectiveness is dependent on the timing of therapeutic intervention. These findings suggest that hemin could attenuate AMI-induced myocardial dysfunction but that further investigation is still required to

understand the time-dependent and cardiomyocyte-independent mechanisms likely mediating this cardioprotection.

3.2 MATERIALS AND METHODS

3.2.1 Study Design

The objective of the present study was to evaluate the translational potential of hemin as a novel treatment for AMI and to provide a holistic characterization of the resulting changes in heme regulation using a permanent coronary ligation mouse model. The study's sample sizes were determined using previously established surgery mortality rates. Mice were pathogen-free and were randomly assigned to their respective experimental groups. Animal studies were reported in compliance with the ARRIVE guidelines on reporting *in vivo* experiments.

3.2.2 Animal Care

All experimental procedures were approved by the University of Guelph Animal Care and Use Committee and were conducted in accordance with the guidelines of the Canadian Council on Animal Care. All experiments were conducted on 8-9 week old male CD-1 mice (~35g body weight; Charles River Laboratory International Inc.). Mice were acclimatized to the local institution for a minimum of 1 week prior to experiments. Mice were housed 1-3 per cage in a 12h-light/dark cycle facility (lights on at 8h:00) at the University of Guelph and were provided food and water *ad libitum*.

3.2.3 Surgical AMI Model

Mice were anesthetized with an isoflurane:oxygen mix (2%:100%), intubated, and mechanically ventilated (Harvard Apparatus) at a tidal volume of 300ul and at a rate of 150 breaths/min. Body temperatures were maintained at 37ºC using a water-lined heating pad, 100W heating lamp, and a TH-5 rectal probe thermometer (Physiotemp Instruments

LLC). Under sterile conditions, a para-sternal thoracotomy was performed between the 2nd and 3rd ribs to expose the left anterior descending coronary artery (LAD). The LAD was ligated directly inferior to the left atria using 7-0 polypropylene thread. Infarction was confirmed by blanching of the myocardium. The ribs and skin were sutured using 5-0 silk thread. Sham surgeries were performed identically to AMI surgery with exception to LAD occlusion. All surgeries were performed between 12h:00 and 17h:00 and animals were carefully monitored for post-surgical complications. Animals which displayed abnormalities or complications following surgery, such as pain, infection or excess bleeding, were removed from the study and not randomized to treatment. A polymodal analgesia protocol was used in accordance with the institutional animal utilization protocol to ensure adequate peri-operative pain alleviation that included pre/post-operative (24-48hrs) meloxicam following anesthetic plane lidocaine and bupivacaine given at the site of AMI and sham surgeries. Meloxicam dosing/frequency or buprenorphine could be adjusted or given as required and/or with veterinarian advisement as part of routine post-operative care.

3.2.4 Hemin Treatment

Hemin for injection was prepared fresh daily by dissolving 16.30mg hemin (Sigma Aldrich Cat# 51280) into 675ul 0.1M NaOH and buffered with 825ul 0.1M potassium phosphate monobasic to a pH of 7.4. Hemin was administered intraperitoneally at a volume of $3ul \cdot g^{-1}$ body weight (32.6mg $hemin \cdot kg^{-1}$ body weight). Hemin dosage was calculated using the U.S. FDA Guidance Document for Estimating the Maximum Safe Starting Dose in Initial Clinical Trials to convert the human dose of hemin recommended in the treatment of porphyria (1-4mg $hemin \cdot kg^{-1} \cdot day^{-1}$) to a Human Equivalent Dose in mice (12.3-49.2 $mg \cdot kg^{-1}$ body weight) [198].

Hemin stock for cell culture (5mM) was prepared by dissolving hemin in dimethyl sulfoxide (DMSO; Amresco Cat# N182) and by sonicating for 60min. Hemin stocks in DMSO were stored at 4°C (protected from light) for up to 4 months and were sonicated for 15min before each use.

3.2.5 Echocardiographic Analysis

Echocardiographic analysis was performed using the Vevo2100 system equipped with the 40MHz MS550D ultrasound transducer (VisualSonics Inc.). Mice were anesthetized with an isoflurane:oxygen mix (1.0-1.5%:100%) and were maintained at 37ºC throughout data collection using an electric heating pad and a TH-5 rectal probe thermometer. All measurements were performed using the VisualSonics Cardiac Package. Two-dimensional images of the left ventricle were obtained from the long-axis view such that the ventricle chamber was observed from the apex to the aortic outflow tract. Long-axis M-mode (1D) images were analyzed using the LV-trace function. Long-axis B-mode (2D) images were analyzed using the 2D area calculation.

3.2.6 Hemodynamic Analysis

Mice were anesthetized with an isoflurane:oxygen mix (2%:100%) and a 1.2F catheter (Scisense Inc. Cat# FTS-1211B-0018) was inserted into the left ventricle via the right carotid artery. Body temperatures were maintained at 37ºC. Pressures were digitized at a sampling rate of 2000Hz and recorded using iWorx® analytic software (Labscribe2). Following baseline pressure recordings, animals were exsanguinated and 10mL 1X phospho-buffered saline (PBS) was perfused through the right carotid artery to wash out blood from the tissue. Tissues were harvested and rinsed in 1X PBS to further remove any remaining blood. Hearts were divided into atria, septum, right ventricle, and left ventricle (subdivided into infarct and peri-infarct areas demarcated by the blanched infarct tissue). Tissues were then flash-frozen in liquid nitrogen and stored at -80ºC.

3.2.7 Histological Visualization of Myocardial Remodeling

Following hemodynamic analysis, animals designated for planimetry of coronary artery perfusion were gently infused with ~100ul Alexa Fluor® 488 (green; LAD) and 568 (red; right coronary artery and circumflex)-conjugated GS-IB4 isolectin ($10ug \cdot ml^{-1}$;

Thermo Fisher Scientific) into the respective coronary artery—above or below the LAD ligature—using a 31G, 1ml tuberculin syringe.

Animals designated for myocardial fibrosis imaging were exsanguinated after hemodynamic analysis and perfused with 10mL of 1X PBS, 10mL of 0.5M potassium chloride (KCl), and 10mL of 10% buffered formalin (VWR Cat# 89370-094) via the right carotid artery. Hearts were excised and stored in 10% buffered formalin for 24h. Hearts were subsequently transferred to 70% ethanol until tissue processing/paraffin embedding. Transverse sections (5um) of the paraffin-embedded hearts were obtained from the mid-papillary region and were stained with picrosirius red (500ml of saturated picric acid solution and 0.5g of Direct Red 80; Sigma Aldrich Cat# 88-89-1 and Cat# 2610-10-8) to visualize myocardial fibrosis (red). Images were acquired using a Pannoramic® Midi II digital slide scanner (3D Histech).

Hearts from animals assigned to myocardial necrosis imaging were immediately excised following hemodynamic analysis and were sliced into 1mm transverse sections along the mid-papillary region. To visualize the infarct (white) and peri-infarct (red) regions, heart slices were submerged in 1% triphenyltetrazolium chloride (TTC) solution at 37°C for 15min and 10% buffered formalin for 1.5h before being photographed.

3.2.8 Tissue Lysate Preparation

Powdered tissues (10-15mg) were homogenized on ice in fresh NP-40-based lysis buffer (120ul; 1% NP-40, 20mM Tris pH 7.4, 5mM EDTA, 10mM $Na_4P_2O_7$, 100mM sodium fluoride, ddH_2O) with activated sodium orthovanadate, a protease inhibitor cocktail (Sigma-Aldrich Cat# P8340), and a phosphatase inhibitor cocktail (Calbiochem Cat# 524628) at a volumetric ratio of 100:1:1:1. Samples were placed on ice for 30min prior to centrifugation at 2000 relative centrifugal force (rcf) for 2min at 4°C. The supernatant was transferred to a fresh microcentrifuge tube and centrifuged at 1200 rcf for 30 min at 4°C. The supernatant was then transferred to a fresh microcentrifuge tube using a $28^{1/2}$-gauge insulin syringe to shear any DNA in the remaining sample. Total protein content was measured by bicinchoninic acid assay (BCA; Thermo Scientific Cat# 23225).

3.2.9 Heme/Hemin Quantification

Tissue heme/hemin content was measured by commercial heme content assay (BioVision Inc. Cat#K672) using a Synergy H4 Hybrid Reader (Biotek) as per the manufacturer's instructions. Tissue lysates were diluted between 1:100 and 1:3500 in ddH_2O and were measured in triplicate. Optical density/absorbance at 570nm was acquired in Kinetic Mode at 2min intervals for 2h. Sample heme content was interpolated from the 6-point hemin standard curve at the point of max linearity. Samples with elevated or erratic heme content were interrogated for residual tissue blood contaminating hemoglobin via Western Blot and samples above two standard deviation distances from the median hemoglobin value were excluded from analysis.

3.2.10 Western Blotting

Tissue lysates were boiled at 99ºC for 5min in 4X Laemmli Buffer with DTT. Samples (8-25ug•lane^{-1}) and ladder (Bio-Rad Cat# 1610375EDU) were separated via SDS–polyacrylamide gel electrophoresis (Bio-Rad Cat# 5671095) and transferred to nitrocellulose membrane (Bio-Rad Cat#1620112) for immunoblotting. To ensure equal protein loading and uniform protein transfer, membranes were reversibly stained with MemCode (Thermo Fisher Scientific Cat# 24580) before probing. Membranes were then blocked in 5% milk for 45min and incubated in primary antibody (Table 3.1; 1:1000 in 1% skim-milk in tris-buffered-saline-tween (TBS-T) with sodium azide) at 4ºC overnight. Membranes were washed in 1X TBS-T and subsequently incubated in either goat anti-rabbit (Santa Cruz Biotechnology Cat# 2054) or goat anti-mouse (Santa Cruz Biotechnology Cat# 2055) horseradish peroxidase-conjugated secondary antibody (1:2000 in 5% milk for 2h). Signal was detected by enhanced chemiluminescence (Thermo Fisher Scientific Cat# 34076) and digital imaging (Bio-Rad Cat# 1708280). Densitometric quantification was performed using Image Lab software (Bio-Rad) and values were obtained by measuring the target band relative to the respective total lane protein.

Table 3.1 List of Primary Antibodies

Target	Supplier	Catalog #
HMOX1	Enzo Life Sciences	ADI-SPA-895-F
FTH1	Cell Signaling Technology	4393S
ALAS1	Bio-Rad Laboratories	VMA00203KT
ALAS2	Santa Cruz Biotechnology	Sc-166739
HIF1α	R&D Systems	AF1935
Ph-NFkB Ser536	Cell Signaling Technology	3033S
NFkB	Cell Signaling Technology	8242S
Ph-Nrf2 Ser40	Abcam	Ab76026
Nrf2	Abcam	Ab89443
Hemoglobin-α	Proteintech	14537-1-AP

HMOX1, heme oxygenase-1; FTH1, ferritin heavy chain; ALAS1, aminolevulinic acid synthase-1; ALAS2, aminolevulinic acid synthase-2; HIF1α, hypoxia inducible factor 1α; NFkB, nuclear factor kappa-B; Nrf2, nuclear factor erythroid 2-related factor-2.

3.2.11 Cell Culture

H9C2 left ventricular cardiomyoblasts (American Type Culture Collection Cat# CRL-1446) were expanded from frozen stocks in Dulbecco's Modified Eagle Medium-High Glucose (DMEM-HG; Gibco Cat# 11965-092) supplemented with 10% fetal bovine serum (FBS; Seradigm Cat# 1400-500). Cells were seeded for 80% next-day confluency at either $1.50x10^4$ cells•well^{-1} for cell viability assays or $2x10^5$ cells•35mm plate^{-1} for immunoblotting. Cells were subsequently differentiated by FBS deprivation for 5-6 days and media was renewed as indicated (Figures 3.3A, 3.4) [117]. Cells were maintained at 37ºC in a humidified atmosphere of 95%:5% air/CO_2. All experiments were initiated at least one passage after recovery from cryogenic storage and cells did not exceed 19 passages.

Differentiated H9C2 cells were harvested by rinsing the cells with cold 1X PBS and scraping the cells in fresh NP-40-based lysis buffer. Samples were set on ice for 30 minutes before sonicating for 10 seconds (20kHz, 30% amplitude). Total protein concentrations were quantified by BCA assay.

3.2.12 Cell Viability Assay

H9C2 cells were seeded in a 96-well plate containing 100ul media•well^{-1} and differentiated as previously described. H_2O_2 (Sigma-Aldrich Cat# 323381) was freshly diluted to 0.1M in sterile 1X PBS. N-Acetyl-L-Cysteine (NAC; Amresco Cat# 0108-25G) was prepared as a 3mM stock in sterile 1X PBS (stored at 4°C for up to 3 months). Hemin, vehicle (DMSO), H_2O_2, and NAC were further diluted in media immediately before exposure to cells. Cell viability was measured using resazurin sodium salt (0.3mg•ml^{-1}; Thermo Scientific Cat# R12204). Cells were incubated with resazurin (10% volume) at 37ºC for 3h. Absorbance was measured using a Synergy H4 Hybrid Reader at 560/590nm excitation/emission. Cell viability was determined by subtracting the absorbance of media-only controls from treated cells and normalizing values to the mean survival of untreated controls.

3.2.13 Statistics

Values presented are expressed as mean ± SD. Graphical and statistical analyses were completed using GraphPad (Prism 6, GraphPad Software Inc.). For comparison between two groups, an unpaired Student's t-test was used. For comparison between three or more groups, a One-Way Analysis of Variance (ANOVA) and Tukey's multiple comparisons test were used. Kruskall-Wallis and Dunn's multiple comparisons tests were performed for non-parametric data. Significance was set at $P<0.05$ ($^{*}P < 0.05$, $^{**}P < 0.01$, $^{***}P<0.001$; $^{****}P<0.0001$). Outliers were identified by ROUT method (Q=1%).

3.3 RESULTS

3.3.1 AMI causes progressive LV remodeling and reduction in hemodynamic function in mice

The effect of AMI on left ventricular remodeling and hemodynamic function is shown in Fig.3.1. AMI resulted in an immediate discoloration (blanching) of the downstream left ventricle (Fig.3.1A), an area with limited overlap between left anterior descending (LAD) and circumflex/right coronary artery (CircFlx/RCA) perfusion (Fig.3.1B, i and ii). TTC staining of the infarct (white) and peri-infarct (red) myocardium revealed necrosis restricted to LAD-perfused tissue 3 days post-AMI (Fig.3.1B, iii) with progressive infarct expansion and thinning detected by picrosirius red scar matrix staining at 4 weeks post-AMI (Fig.3.1B, iv).

AMI reduced both systolic and diastolic hemodynamic function (Fig.3.1C). A reduction in systolic cardiac function was rapid and sustained, by measure of maximum left ventricular pressures (iv), the maximum rate of left ventricular contraction (dP/dt Max; v), dP/dt at 40mmHg left ventricular pressure (vi), and systolic blood pressure (ii) from 3 days to 4 weeks post-AMI compared to sham hearts. Diastolic function was also impaired by measure of elevated end diastolic pressures between 3 days and 4 weeks post-AMI (viii), while rate of relaxation (dP/dt Min; vii) and diastolic blood pressure (iii)

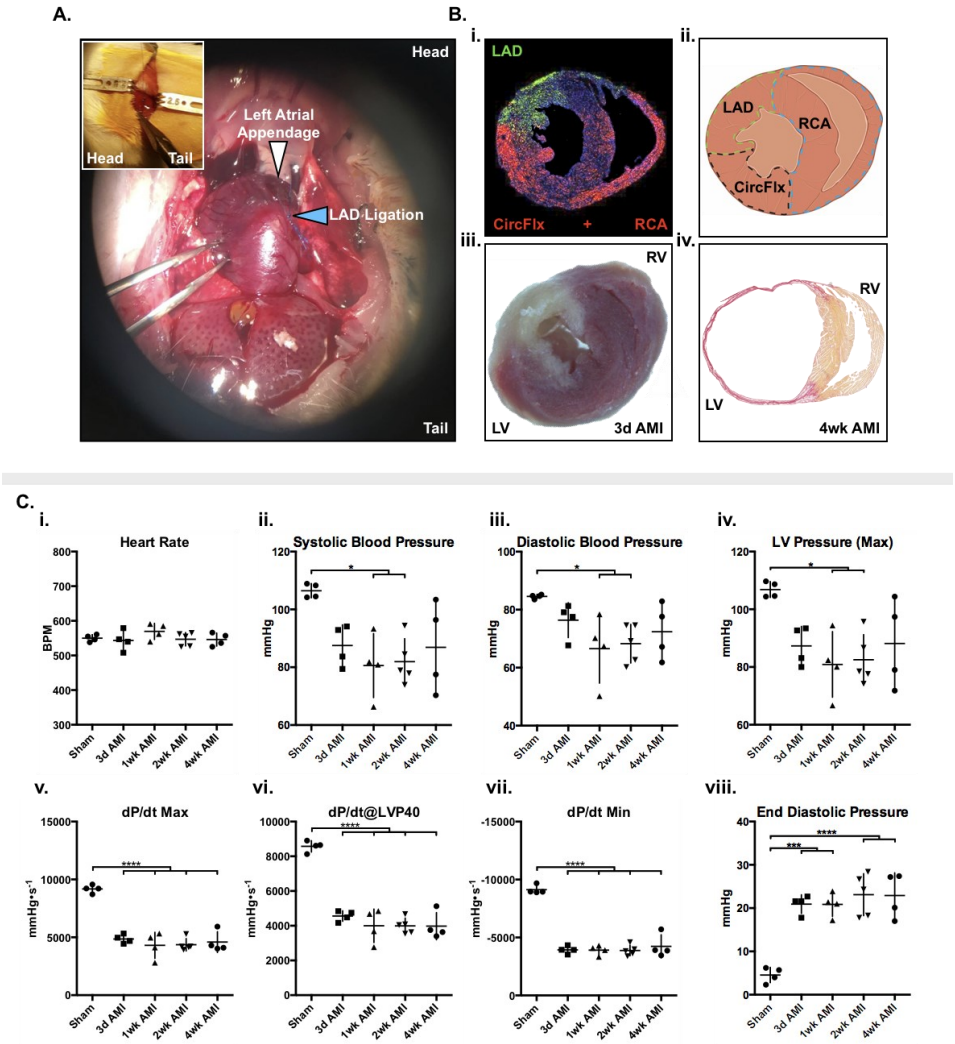

Figure 3.1 Physiological adaptation to left ventricle remodeling in an experimental model of acute myocardial infarction progression. (A) Inset: Minimally invasive parasternal thoracotomy exposing the LAD between ribs 2 and 3 for ligation. Point of LAD ligation inferior to the left atrial appendage (image taken at time of collection). **(B)** Planimetry of LAD perfusion **(i-ii)** and progressive infarct expansion in myocardial cross-sections post-AMI **(iii-iv)**. **i.** Injection of conjugated isolectin via restricted intracoronary catheterization indicates limited overlap (yellow) between LAD (Alexa Fluor®488 green), and circumflex/right coronary artery (RCA; Alexa Fluor®594 red) perfusion. Nuclei are counterstained with DAPI (blue). **ii.** Illustrated map of approximate areas perfused by the LAD, RCA and circumflex. **iii.** Triphenyltetrazolium chloride (TTC) staining of infarct (white) and peri-infarct (red) myocardium reveals necrosis restriction to LAD-perfused tissue 3d post-AMI. **iv.** Picrosirius red-stained heart reveals infarct expansion (red scar) and thinning 4 weeks post-AMI. **(C)** Hemodynamic function in mice 3 days, 1 week, 2 weeks, and 4 weeks post-AMI, and sham. **i.** Heart rate. **ii.** Systolic blood pressure. **iii.** Diastolic blood pressure. **iv.** Maximal left ventricular (LV) pressure. **v.** Maximal values of the first derivative of LV pressure. **vi.** Values of the first derivative of LV pressure at 40mmHg LV pressure. **vii.** Minimal values of the first derivative of LV pressure. **viii.** LV end diastolic pressure.

were both reduced. Heart rate remained unchanged during hemodynamic analysis post-AMI (i).

3.3.2 Heme content and heme regulatory enzyme expression are temporally dyssynchronous in the peri-infarct LV post-AMI and are not predictive of hemodynamic function

To examine the progressive relationship between AMI and heme regulation in viable left ventricular tissue, the peri-infarct regions of the left ventricles were collected at 3 days, 1 week, 2 weeks, and 4 weeks post-AMI for investigation (Fig.3.2). Compared to sham, heme content in the peri-infarct left ventricle was erratic post-AMI with large confidence intervals, yet was significantly elevated at 2 weeks post-AMI (Fig.3.2A). HMOX1 was significantly elevated at 3 days post-AMI before rapidly returning to baseline by 1-2 weeks, the same time peak heme content was observed. HMOX1 levels were dyssynchronous with heme content in the peri-infarct left ventricle (Fig.3.2A/B). FTH1, however, was temporally synchronized with heme content and increased significantly to peak at 2 weeks post-AMI (Fig.3.2C), similar to peak heme content. To investigate whether temporal changes in heme content could be accounted for by changes in rate-limiting heme synthesis enzymes instead, ALAS1 and ALAS2, were measured (Fig.3.2D, E). ALAS1 and ALAS2 demonstrated isoform switching in the peri-infarct heart: ALAS1 levels decreased significantly (Fig.3.2D) whilst ALAS2 increased significantly by 2 and 4 weeks post-AMI (Fig.3.2E). Total ALAS (i.e. the relative sum of their densities) did not differ significantly between AMI and sham (Fig.3.2F). Peri-infarct heme content nor rate-limiting enzyme expression correlated with any parameters of hemodynamic function (data not shown). Taken together, AMI progressively alters myocardial heme content without lasting compensatory induction of HMOX1, with changes in FTH1 and ALAS isoform switching suggesting a more complex reactionary or adaptive molecular shift in heme metabolism regulation.

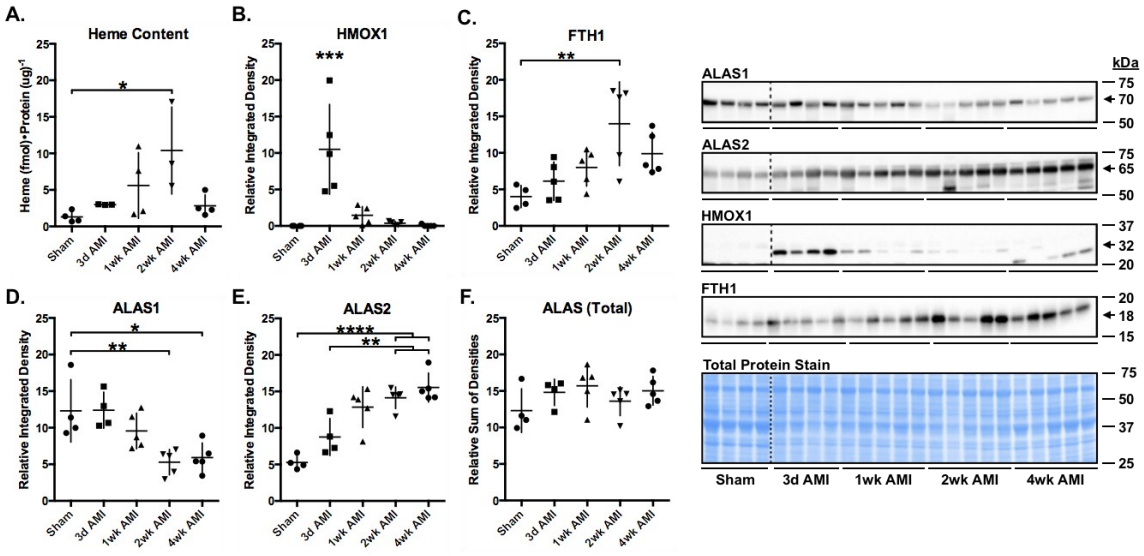

Figure 3.2 Heme content is increased with acute myocardial infarction progression without concordant changes in heme regulatory enzyme expression. Peri-infarct LVs were collected at 3 days, 1 week, 2 weeks and 4 weeks post-AMI and compared to sham LVs. **(A)** Heme content; excluding samples with potential red blood cell contamination (high hemoglobin levels). **(B-F)** Densitometric analysis of heme regulatory enzyme expression with representative Western Blots and total protein stain; dashed lines indicate cropped lanes within the same blot. **(B)** HMOX1, **(C)** FTH1, **(D)** ALAS1, and **(E)** ALAS2 relative integrated densities. **(D-E)** ALAS1 and ALAS2 undergo isoform switching with AMI progression. **(F)** Total ALAS levels remain unchanged.

3.3.3 Pharmacodynamic characterization of hemin exposure *in vitro* and *in vivo* reveals increased HMOX1 and altered ALAS

To examine the effects of hemin in cardiomyocytes directly, H9C2 cells were differentiated into cardiomyotubules by serum deprivation and exposed to a dose response of: 1, 2.5, 5, 10, or 25uM hemin, or vehicle (volume equivalent to 25uM hemin) for 24h (Fig.3.3A). An *in vitro*, physiologically tolerable hemin concentration was determined by survival (i-ii). Survival was significantly reduced in cells exposed to either 10uM or 25uM hemin after 24h (vehicle administration did not affect cell viability). The maximum tolerable dose without toxicity was 2.5uM hemin. Exposure to 2.5uM hemin for 24h increased HMOX1, FTH1 and ALAS2 expression in differentiated H9C2 cells, however ALAS1 expression remained unchanged.

To investigate the effects of hemin *in vivo*, healthy mice were administered a single dose of hemin ($32.6 mg \cdot kg^{-1}$) or vehicle i.p. (Fig.3.3, B-H) and tissues were collected after 2h, 4h, 8h, 12h, 24h, or 48h. HMOX1 induction was detected in the heart (both left and right ventricles), liver, kidneys, and lungs of healthy mice at 8h post-hemin (Fig.3.3B). HMOX1 remained unchanged in the brain and spleen. Left ventricular heme content and FTH1 were not significantly altered by hemin at this dose (Fig.3.3C and E). Left ventricular HMOX1 was increased significantly, peaking from 8-12h before returning to near-control levels at 48h post-hemin (Fig.3.3D). ALAS1 and ALAS2 demonstrated isoform switching similar to that observed in the peri-infarct heart (Fig.3.3, F and G). Left ventricular ALAS1 was significantly decreased from 4-8h post-hemin, while ALAS2 was significantly elevated at 8h, returning to baseline by 48h. Total left ventricular ALAS remained unchanged with hemin administration (Fig.3.3H). Exogenous hemin induces HMOX1 as expected without altering FTH1 and also induces the ALAS isoform switching observed during infarction. These data suggest that elevated heme is a driver of ALAS isoform switching but that concomitant multifactorial stress or cell-specific responses in the infarct are responsible for the variable expression in HMOX1 and FTH1, and not the elevated heme content *per se*.

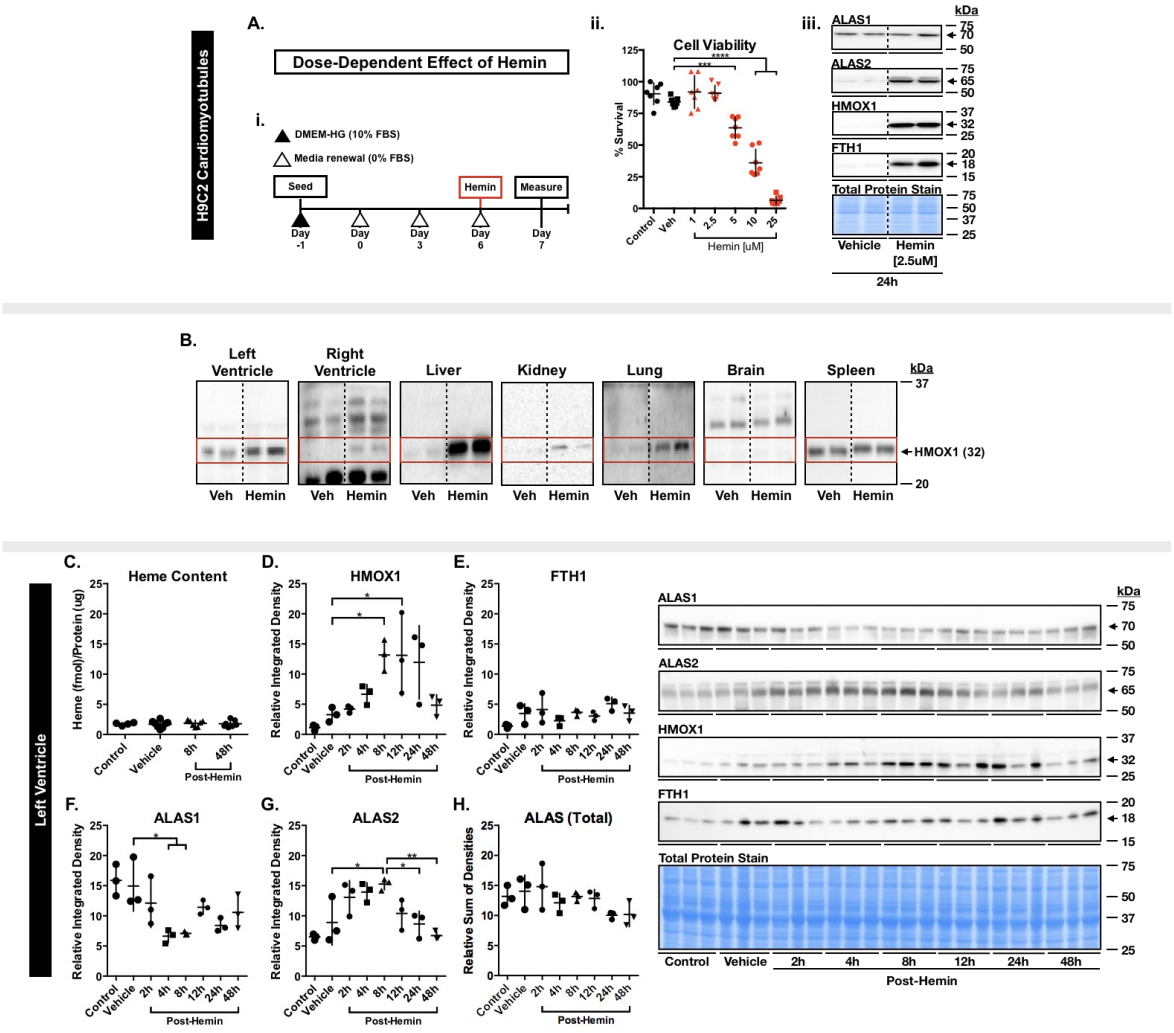

Figure 3.3 Pharmacokinetic and pharmacodynamic characterization of hemin exposure *in vitro* and in healthy mice. (A) Dose-dependent effects of hemin on differentiated H9C2 left ventricular cardiomyotubule viability and heme regulatory enzyme expression. **i.** Outline of H9C2 differentiation and 24h hemin exposure. **ii.** Resazurin cell viability assay. **iii.** Heme regulatory enzyme expression in differentiated H9C2 cells exposed to 2.5uM hemin or vehicle for 24h. Dashed lines indicate cropped lanes within the same blot. **(B-H)** Healthy mice were administered a single dose of i.p. hemin [32.6mg•kg^{-1}] or vehicle. Tissues were collected after 2h, 4h, 8h, 12h, 24h, or 48h. **(B)** Representative Western Blots of HMOX1 protein expression in the heart, liver, kidney, lung, brain, and spleen at 8h post-hemin or vehicle administration. **(C-D)** Heme content and heme regulatory enzyme expression in the left ventricle with representative Western Blots. **(C)** Heme content. **(D)** HMOX1, **(E)** FTH1, **(F)** ALAS1, and **(G)** ALAS2 relative integrated densities. **(F-G)** ALAS1 and ALAS2 undergo isoform switching with hemin. **(H)** Total ALAS levels remain unchanged.

3.3.4 Hemin treatment confers cytoprotection to cardiomyotubules against oxidative injury, when administration is initiated prophylactically but not interventionally

To investigate whether hemin was capable of protecting cardiomyocytes directly, H9C2 cardiomyotubules were treated with hemin either 24h pre- or 1h post-H_2O_2-mediated injury (Fig.3.4). H_2O_2 LD_{75} was first interpolated from differentiated H9C2 survival following exposure to either 650, 800, or 900uM H_2O_2 for 24h (Fig.3.4 A and B, ii). Approximate LD_{75} was interpolated as 500uM H_2O_2 in the pre-injury model and 850uM H_2O_2 in the post-injury model. Susceptibility to H_2O_2 injury was significantly increased when media was renewed prior to H_2O_2 (pre-injury model timeline) compared to simultaneous media renewal with H_2O_2 (post-injury model timeline; possibly due to the fresh presence of media antioxidants). Both pre- and post-injury models were performed simultaneously within the same plate for direct comparison. H9C2 cardiomyotubules were treated with either 300uM NAC antioxidant reference control, or 1, 2.5, or 5uM hemin either 24h pre- or 1h post-H_2O_2. Cell survival was significantly improved with 5uM hemin pre-H_2O_2 (Fig.3.4A, iv and v). Comparatively, pre-treatment with NAC did not reduce H_2O_2-mediated cell death. Treatment with NAC post-H_2O_2 significantly attenuated cell death, whereas hemin treatment did not (Fig.3.4B, iv and v). These data show that hemin preconditions cells to cytoprotection prior to an oxidant injury but does not offer post-conditioning survival benefits to cells after an oxidant injury. This could be limiting to the practical clinical application of hemin as a pharmacological intervention after the occurrence of a myocardial infarction.

3.3.5 Prophylactic hemin (pre-AMI) improves left ventricular function, as does interventional administration (post-AMI) of hemin to a lesser extent

To evaluate whether hemin could confer cardioprotection *in vivo*, mice were administered a single dose of hemin (32.6mg•kg^{-1}, i.p.) daily, beginning either 3h pre-AMI (prophylactic- initiated dosing regimen) or 2h post-AMI (interventional dosing regimen) and continued until 28 days post-AMI (Fig.3.5A). Echocardiography revealed interventional hemin significantly attenuated reduced left ventricle fractional shortening,

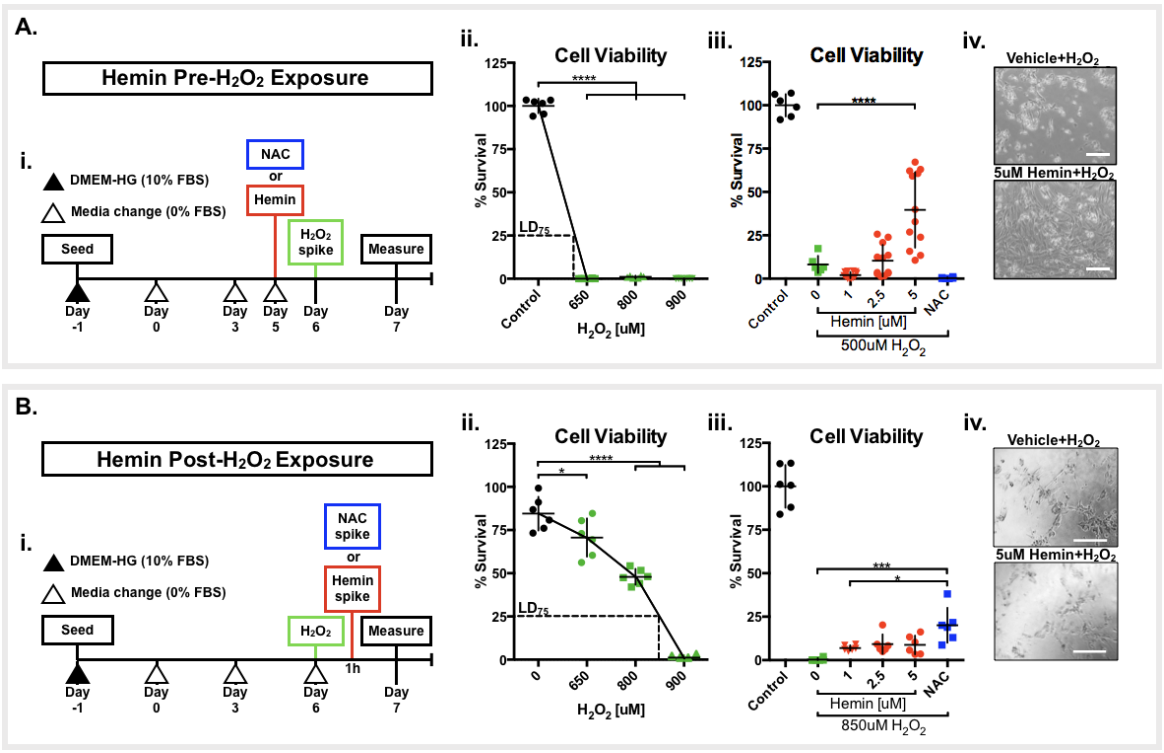

Figure 3.4 Hemin treatment *in vitro* confers cytoprotection to H9C2 cardiomyotubules in a time-dependent manner. (A) Dose-dependent effects of hemin treatment pre-H_2O_2 on differentiated H9C2 left ventricular cardiomyotubule viability. **i.** Outline of H9C2 differentiation and pre-H_2O_2 injury model timelines. **ii.** Resazurin cell viability assay in H9C2 cells exposed to 650uM, 800uM, or 900uM H_2O_2 for 24h. **iii.** Outline of H9C2 differentiation and treatment 24h pre-H_2O_2 exposure (500uM, 24h). **iv.** Resazurin cell viability assay in H9C2 cells treated with 1uM, 2.5uM, or 5uM hemin, or 300uM N-Acetyl-L-Cysteine (NAC), 24h pre-H_2O_2 (500uM, 24h). **v.** Representative images of H9C2 cells treated with vehicle or 5uM hemin 24h pre-H_2O_2. **(B)** Dose-dependent effects of hemin treatment post-H_2O_2 on differentiated H9C2 cardiomyotubule viability. **i.** Outline of H9C2 differentiation and post-H_2O_2 injury model timelines. **ii.** Resazurin cell viability assay in H9C2 cells exposed to 650uM, 800uM, or 900uM H_2O_2 for 24h. **iii.** Outline of H9C2 differentiation and treatment 1h post-H_2O_2 exposure (850uM, 24h). **iv.** Resazurin cell viability assay in H9C2 cells treated with 1uM, 2.5uM, or 5uM hemin, or 300uM N-Acetyl-L-Cysteine (NAC), 1h post-H_2O_2 (850uM, 24h). **v.** Representative images of H9C2 cells treated with vehicle or 5uM hemin 1h post-H_2O_2.

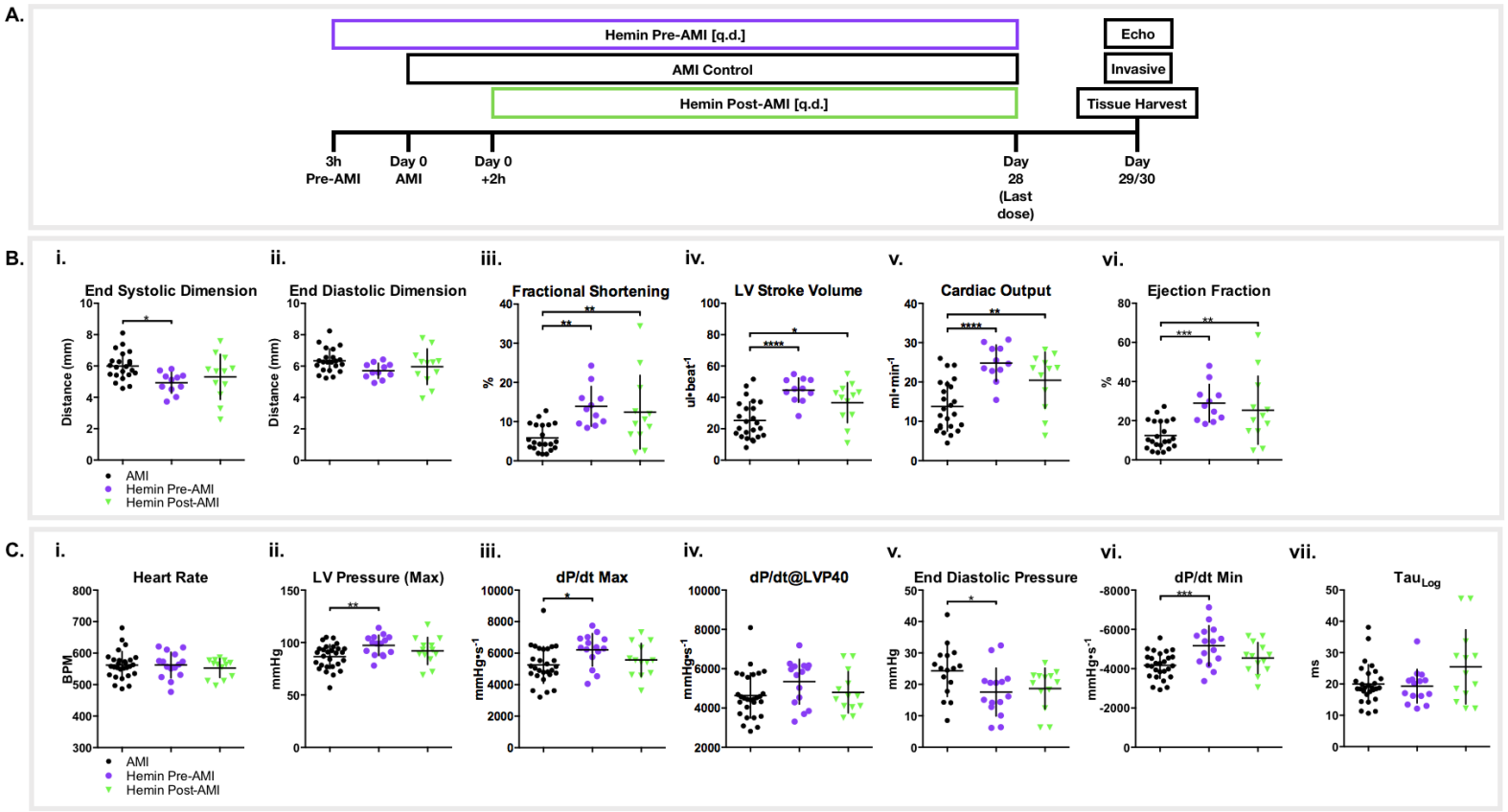

Figure 3.5 Hemin improves left ventricular function when administration is initiated prophylactically (pre-AMI) versus interventionally (post-AMI). Mice were administered a once-daily dose of i.p. hemin [32.6mg•kg^{-1}] for 28d, with the first dose initiated either 3h pre- or 2h post-AMI, and were compared to vehicle-treated AMI controls. **(A)** Experimental outline. **(B)** Left ventricular (LV) echocardiography. **i.** End systolic dimension. **ii.** End diastolic dimension. **iii.** Fractional shortening. **iv.** Stroke volume. **v.** Cardiac output. **vi.** Ejection fraction. **(C)** Hemodynamic function. **i.** Heart rate. **ii.** Maximal LV pressure. **iii.** Maximal values of the first derivative of LV pressure. **iv.** Values of the first derivative of LV pressure at 40mmHg LV pressure. **v.** LV end diastolic pressure. **vi.** Minimal values of the first derivative of LV pressure. **vii.** Tau_{Log}.

stroke volume, cardiac output, and ejection fraction observed post-AMI (Fig.3.5B, iii-vi). Hemin initiated prophylactically also attenuated reduced left ventricle fractional shortening, stroke volume, cardiac output, and ejection fraction in addition to reducing left ventricle end systolic dimensions (Fig.3.5B). Neither prophylactic nor interventional hemin significantly affected end diastolic dimensions (Fig.3.5B, ii).

Hemodynamic analysis (Fig.3.5C) revealed prophylactic hemin treatment significantly attenuated reductions in (ii) maximal left ventricle pressure, (iii) dP/dt Max, (vi) dP/dt Min, and reduced end diastolic pressure observed post-AMI (v). Interventional hemin administration did not improve measures of hemodynamic function. Neither prophylactic nor interventional hemin administration significantly altered (i) heart rate, (iv) dP/dt at 40mmHg left ventricular pressure, or (vii) Tau_{Log}. Taken together, the benefits for hemin (as measured by echocardiography) suggest improved structural remodeling of the heart independent of the time of treatment initiation. Yet, preservation of contractile performance was only significantly improved when hemin administration was initiated in advance of myocardial injury. As such, a preservation of myocardial performance by hemin is plausible but limited in its postconditioning benefits.

3.3.6 Interventional hemin administration does not alter cardiac heme content or ALAS switching in the peri-infarct heart but prolongs elevated cytoprotective HMOX1 and FTH1

To evaluate the long-term effects of hemin treatment and investigate whether the left ventricle was capable of a lasting expression of HMOX1 beyond 3 days post-AMI, peri-infarct left ventricles were collected from mice administered hemin from 5-28 days post-AMI as outlined in Fig.3.5A. Left ventricles were collected at the end of the study, 24hrs after the last dose. Interventional hemin administration did not alter cardiac heme content (Fig.3.6A) but did maintain significantly elevated HMOX1 (Fig.3.6B) and FTH1 (Fig.3.6C) levels similar to what was observed in the natural course of AMI (Fig.3.2C). ALAS1 and ALAS2 switching was not reversed nor altered by hemin post-AMI (Fig.3.6, D and E). These data suggest that while hemin does not elevate total heme content, it

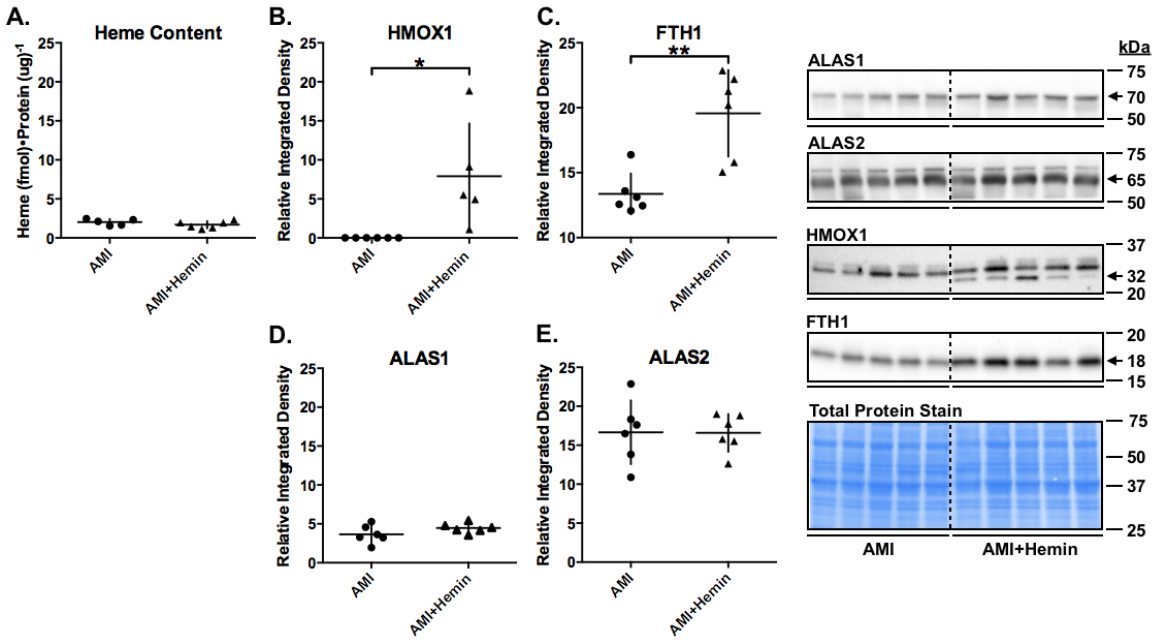

Figure 3.6 Interventional hemin administration does not alter cardiac heme content or ALAS switching in the peri-infarct heart but adaptively perpetuates elevated HMOX1 and FTH1. Peri-infarct left ventricles were collected from mice administered a once-daily dose of i.p. hemin [32.6mg•kg^{-1}] for 23d, with the first dose initiated 5d post-AMI, and were compared to vehicle-treated AMI controls. **(A)** Heme content. **(B-E)** Densitometric analysis of heme regulatory enzyme expression with representative Western Blots and total protein stain; dashed lines indicate cropped lanes within the same blot. **(B)** HMOX1, **(C)** FTH1, **(D)** ALAS1, and **(E)** ALAS2 relative integrated densities. **(D-E)** ALAS1 and ALAS2 maintain isoform switching with hemin post-AMI.

could be capable of extending the duration of cytoprotection derived in part from both the elevated expression of HMOX1 and FTH1.

3.4 DISCUSSION

In the present study, we characterize the broader regulation of cardiac heme metabolism in response to hemin, AMI, or both, and investigate the therapeutic efficacy of hemin with respect to timing of administration for the first time. Here, we show that heme content and heme regulatory enzyme expression are temporally dyssynchronous in the peri-infarct heart, which is unexpected given that heme is a principal driver of HMOX1 expression. Heme content increased post-AMI without proportional changes in HMOX1 nor in concert with heme-synthesizing enzyme expression (ALAS1, ALAS2), suggesting it may be regulated by factors beyond its canonical catabolic and anabolic enzymes. Only FTH1 was observed to coincide directly with heme levels post-AMI, perhaps so as to maintain cardiac iron homeostasis. The induction of HMOX1 was early, short-lived, and driven by the initial infarction stress. This was followed in parallel by progressive switching between dominant ALAS isoforms (i.e. decreased ALAS1 and increased ALAS2). In the healthy heart and cardiomyotubule culture, hemin exposure also elicited ALAS isoform switching. Chronic hemin administration post-AMI did not alter peri-infarct heme content or reverse isoform switching. In cell culture, hemin attenuated H_2O_2-mediated cell death when treatment was initiated prophylactically, demonstrating a capacity to directly confer cytoprotection to cardiomyotubules. However, cytoprotection was not conferred when hemin treatment was initiated simultaneously with- (data not shown) or post-H_2O_2 injury. Hemin treatment significantly improved left ventricular cardiac output and ejection fraction when initiated either pre- or post-AMI, yet improvements to systolic and diastolic hemodynamic function were only observed in mice administered hemin prior to AMI. Collectively, elevated cardiac heme content is associated with injury but does not appear to be a driver of heart failure since early hemin administration showed marked benefit *in vitro* and *in vivo*.

In contrast to previous reports suggesting increased ALAS2 contributes to human ischemic heart failure by the overproduction of heme, our findings suggest it is not likely

the primary contributor to increased heme content post-AMI [19]. In the peri-infarct heart, we show that ALAS2 induction peaked while heme content was abating. In H9C2 cardiomyotubules and healthy mice, we also show that hemin induced ALAS2, confirming that it does not lead—but rather follows—elevated heme content. ALAS2 has been previously reported as translationally regulated by iron content via iron regulatory protein-2 (IRP2) in erythroid cells (where it is the predominant isoform), though it remains unclear whether this mechanism is conserved in cardiomyocytes [120]. In the presence of free iron, the repressive IRP2 is released from the iron-responsive element within ALAS2 mRNA, thus enabling translation [120]. FTH1—an essential cytoprotectant in the prevention of ferroptosis, Fenton-reaction oxidative stress and iron overload—is similarly regulated by free iron [213,214]. Here we show that FTH1 follows a similar pattern to ALAS2 in response to hemin in H9C2 cardiomyotubules, in proportion to elevated heme content post-AMI, and was further elevated by hemin treatment post-AMI. Interestingly, we also show that ALAS2 induction is juxtaposed by a proportional reduction in ALAS1 in the peri-infarct and hemin-treated hearts. Previous studies show that overexpression of ALAS2 in proliferating H9C2 cardiomyoblasts significantly decreases ALAS1 protein levels, yet ALAS1 gene expression is alleged to be unchanged in the peri-infarct heart, suggesting that it is also regulated translationally [19]. In liver, ALAS1 can be directly regulated post-translationally via hemin-mediated carbonylation and subsequent inhibition [215,216]. Hence, the general consensus for classifying ALAS1 as a housekeeping gene is untenable. Increased heme content may not result from ALAS at all, but could be attributed to the release of free heme from tissue damage, hemolysis, or intracellular hemoproteins via autophagolysosomal or other proteolytic processes [133]. Post-AMI, reactive oxygen species are increased in the peri-infarct heart which could modify hemoprotein stability to that end. Unchecked reactive oxygen species also damage mitochondria: the site of heme synthesis and a major source of hemoproteins. The mechanisms underlying heme regulation are still emerging and have shown stimulus, cell-specific, age, and species differences that make mechanistic conclusions limited [217–219]. Thus, the regulation of the labile pool of heme in the heart is complex with transcriptional, translational, proteolytic, autophagic, transport, and compartmentation all requiring further study.

Curiously, increased heme content in the peri-infarct heart is also unmatched by concomitant induction of HMOX1. Increased heme content without a proportional induction of HMOX1 has been previously shown in end-stage human failing hearts, however the source of this dyssynchrony had not been investigated [19]. This is surprising given that heme is considered the canonical inducer of HMOX1 for regulating heme homeostasis. Originally, we hypothesized that post-AMI HMOX1 dyssynchrony stemmed from a developed inability to sustain cardiac HMOX1 induction long-term. However, HMOX1 levels were increased after 4 weeks of hemin treatment post-AMI and without evidence of heme or hemin accumulation in the peri-infarct heart. HMOX1 is canonically induced through the free heme-dependent displacement of transcriptional repressor Bach1 (undetectable in our models) and the subsequent binding of transcription factors HIF1α (hypoxia), NFkB (inflammation), or Nrf2 (oxidative stress) [44,48,83,220,221]. Whether these transcription factors are temporally and spatially expressed in concert with HMOX1 post-AMI is not fully characterized. In rats, LAD coronary artery ligation increases downstream HIF1α protein expression within 6h and out to 7 days post-AMI, however HIF1α is narrowly localized to the left ventricular area-at-risk and peri-infarct border respectively [222]. Nrf2 protein is significantly elevated in the whole hearts of mice subjected to 5:5min of LAD ichemia:reperfusion preceding 24h permanent ligation, however the upregulation of HMOX1 is attenuated with increased Nrf2 in those same hearts [223]. We were unable to detect HIF1α or phosphorylated Nrf2 in our models. NFkB is upregulated in concert with proinflammatory and hypoxic or oxidative signaling, yet its temporal expression in the peri-infarct heart diverges from peak cytokine levels characterized in the literature, suggesting it is more dependent on redox mechanisms of activation [224]. Peak levels of pro-inflammatory cytokines and macrophage infiltration are detected between 3h and 3 days post-AMI in the infarcted myocardium—the same period in which we observe HMOX1 levels peak in the peri-infarct heart post-AMI [224]. However, we observe that phosphorylated NFkB levels are maximally induced in the peri-infarct heart between 1 and 2 weeks post-AMI, temporally diverging from HMOX1 expression (Fig.3.7, Supplemental). As such, it is unclear which transcriptional regulators mediate the *in vivo* transactivation of the HMOX1 promoter.

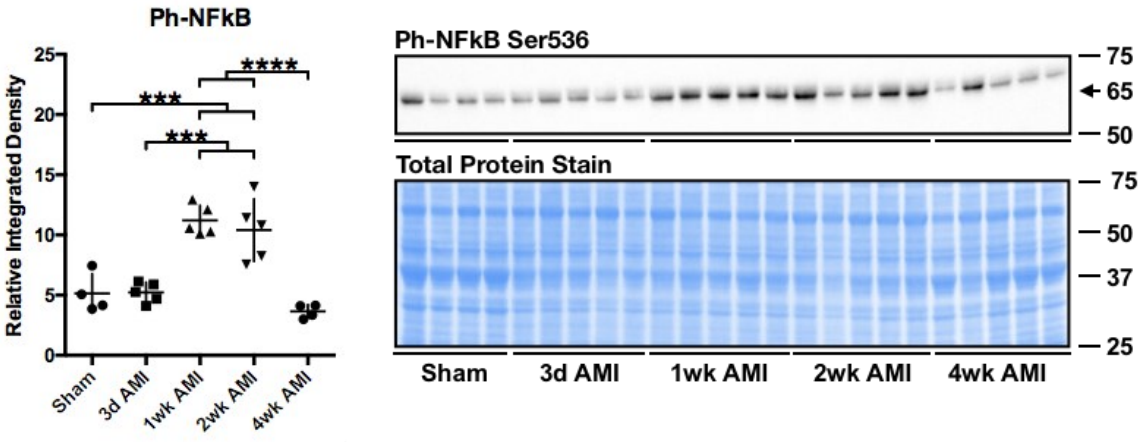

Figure 3.7 Transient Ph-NFkB levels post-AMI. Peri-infarct LVs were collected at 3 days, 1 week, 2 weeks and 4 weeks post-AMI and Ph-NFkB Ser536 levels were compared to sham LVs.

The exact mechanisms underlying the discrepant peri-infarct heme regulatory enzyme expression and heme content require further investigation.

The initial timing of hemin administration significantly impacts its effectiveness in AMI—even when staggered by as little as 5h between prophylactic and interventionall treatment groups. The canonical mechanism of hemin cytoprotection is the HMOX1-mediated increase of biliverdin and carbon monoxide, which serve as buffers against reactive oxygen species and inflammation in ischemic injury [147,149]. Unlike experimental HMOX1 peptides or gene vectors typically used in HMOX1-designed therapy, additional steps exist for the hemin-mediated induction of intracellular HMOX1, such as intracellular transport, nuclear uptake and HMOX1 translation. In the present study, we show the earliest indication of left ventricular HMOX1 induction occurs between 4 and 8h post-hemin in healthy mice, suggesting that more rapid methods of hemin delivery might be necessary to improve cardiac outcomes post-AMI.

In contrast to prophylactic hemin administration, hemin post-AMI does not improve left ventricular hemodynamic function despite improved parameters measured by echocardiography. These findings suggest that the ventricle's shape is maintained when hemin treatment is initiated post-AMI but that contractile performance was not. Post-AMI, cardiomyocyte survival and extracellular matrix remodeling determine the shape of the left ventricular chamber. *In vitro*, we show that hemin improves H9C2 cardiomyotubule survival, but not when administered after oxidative injury. *In vivo*, the timing of hemin administration is relative to the expanding infarct zone, with hemin post-AMI potentially conferring prophylactic-like effects on survival to cardiomyocytes located further from the infarct border or to fibroblasts remodeling the scar. Previous work has established a long-term benefit of HMOX1 regulating cardiac myofibroblast conversion and fibroblast proliferation when therapy is initiated pre-AMI [11,13,141]. In hepatic myofibroblasts, hemin has also been shown to reduce proliferation and collagen I expression, yet it is unclear whether this mechanism is conserved post-AMI in cardiac myofibroblasts [225]. Thus, histological assessment of left ventricular shape, cardiomyocyte survival, fibrosis and integrity are needed.

HMOX1 is characterized as a heme-sensitive, stress-inducible cytoprotective enzyme, yet in the present study, we show that its induction is short-lived in the peri-

infarct heart, despite increased heme content and a capacity for hemin-mediated induction post-AMI. Whether HMOX1 induction and the progressive heme regulatory changes observed in the peri-infarct heart are adaptive or maladaptive remains to be understood but could provide further insight into when hemin treatment initiation may be most effective post-AMI. Previous studies have suggested that increasing heme content may be maladaptive in ischemic injury and suggested that ALAS2 overexpression increased cardiac heme content and oxidative stress to exacerbate AMI in mice [19,226]. However, ALAS2 overexpression was also associated with significantly higher cardiac heme content than AMI controls at 4 weeks post-AMI—a result that was not observed with daily hemin administration in the present study and may be indicative of heme overload in the ALAS2 overexpression model [226]. Although endogenous ALAS2 and heme content correlate with injury in mouse models of AMI and in human heart failure, this may not be an underlying cause of AMI and heart failure progression. Treatment dose and interval of administration with regard to the regulation of endogenous molecular mechanisms of action are critical considerations in pharmacological development and are important factors to consider when investigating whether a treatment strategy is part of an adaptive response to, or exacerbating, cardiac injury.

Whether the induction of cardiac HMOX1 elicited by hemin is the sole mechanism by which protection is conferred to the heart in AMI remains to be understood. An alternative mechanism of hemin-mediated cytoprotection may result from hemin's inhibition of Bach1. Although most commonly recognized as the transcriptional repressor of HMOX1, Bach1 has also been identified as a transcriptional repressor of human FTH1, ferritin light chain, and antioxidants such as thioredoxin reductase-1 and NADP(H) quinone (oxido)reductase [227]. Thus, hemin-mediated release of Bach1 from these genes could potentially confer protection via anti-ferroptotic and anti-antioxidant effects. Another potential mechanism of hemin-mediated cytoprotection stems from recent evidence suggesting that free heme functions as an alarmin [54,117]. Alarmins, or danger-associated molecular patterns (DAMPs), are endogenous molecules released from damaged or dying cells that can promote sterile inflammatory responses when sensed by extracellular pattern recognition receptors on other cells. Heme purportedly functions as a DAMP through the activation of toll-like receptor 4 (TLR4), a transmembrane protein

involved in mediating innate immune responses by initiating pro-inflammatory cytokine production [228]. In mouse peritoneal macrophages, heme increased the levels of tumor necrosis factor-α, however this response did not occur in macrophages from TLR4$^{-/-}$ mice or in macrophages lacking the TLR4 adaptor protein, Myd88 [228]. Whether heme-mediated increases in tumor necrosis factor-α result from direct binding to TLR4 or are affected indirectly through second messengers—such as reactive oxygen species or NFkB—is unclear. It also remains to be understood whether exogenous hemin activates different mechanisms than endogenous heme to regulate heme metabolism. Thus, a direct comparison of heme regulatory enzyme expression between cardiomyocytes endogenously overexpressing heme synthesizing enzymes and cardiomyocytes exposed to exogenous hemin is required.

Careful consideration of experimental design and methodology is needed to advance hemin and other HMOX1-targeted therapeutics closer to clinical translation. In pre-clinical AMI models, heme content and heme regulatory enzyme expression are often measured in the whole heart or ventricle—if indicated at all. In the present study, we show that heme content and heme regulatory enzyme expression differ in AMI between the left ventricular infarct (Fig.3.8, Supplemental) and peri-infarct zones, highlighting the importance of sectioning the heart by regions to prevent signal overlap. In pre-clinical studies, HMOX1 induction is often used as a sole surrogate marker for increased heme content, yet we show that heme content and HMOX1 can be dyssynchronous, highlighting the importance of measuring heme content, anabolism (ALAS1/2) and catabolism (HMOX1). Reconciling the origins of increased heme content without proportional changes in heme regulatory enzyme levels is complex. While it is likely heme is endogenously sourced from within the myocardium due to its elevated requirements for oxygen transport and energy production, risk of mis-interpretation is possible from the presence of exogenous blood in processed tissues or methods reliant upon indirect iron assessments that have unstable chemistry. Hence, we used a direct heme catabolism assay and cross-verified our samples for errant hemoglobin protein contamination to mitigate these challenges. Consideration of clinically translatable treatment strategies in pre-clinical models of pharmacological AMI intervention are also needed to advance novel therapies closer to the clinic. In the present study, non-pharmacy

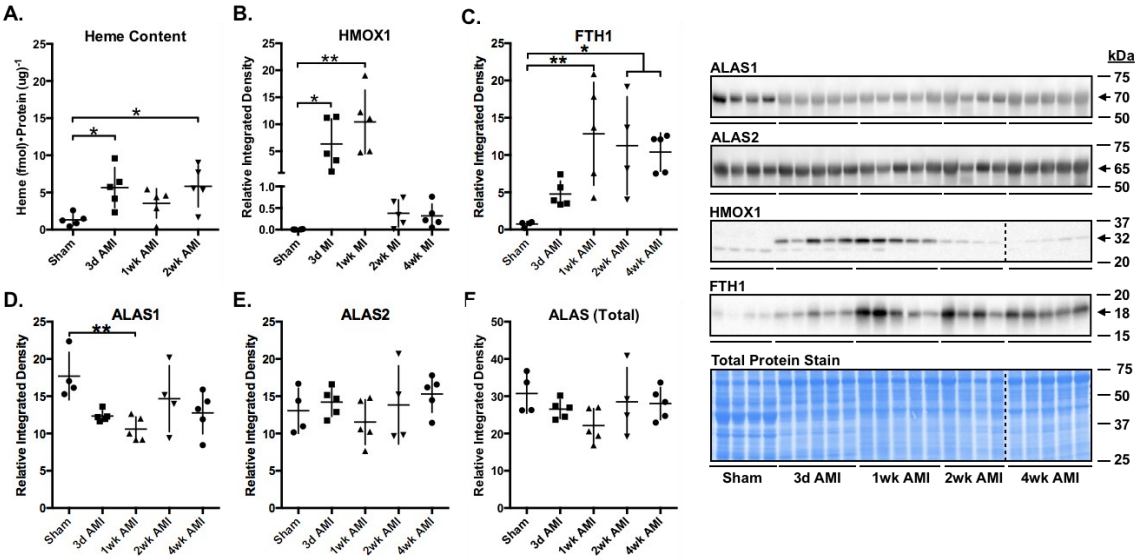

Figure 3.8 Heme regulation is altered in the infarcted left ventricle. LV infarcts were collected at 3 days, 1 week, 2 weeks and 4 weeks post-AMI and compared to sham LVs. **(A)** Heme content (4 week samples were not included due to low n-values). **(B-F)** Densitometric analysis of heme regulatory enzyme expression with representative Western Blots and total protein stain; dashed lines indicate cropped lanes within the same blot. **(B)** HMOX1, **(C)** FTH1, **(D)** ALAS1, and **(E)** ALAS2 relative integrated densities. **(F)** Total ALAS levels.

grade hemin was administered due to the challenges involved in acquiring pharmacy-grade orphan drugs for research. Although delivered intravenously in patients, hemin was delivered intraperitoneally in the present study to reduce the risk of accidental intramuscular injection associated with repetitive tail vein injections. Fundamental gaps still exist in understanding how different routes of administration may affect hemin uptake, peak concentrations and metabolism, thus, further studies comparing their pharmacokinetics are necessary.

The pharmacological effects of hemin require further investigation using pre-clinical models that better reflect patient demographics. Here, we modeled AMI in young, male mice, yet the incidence of AMI is increased in humans after 65 years of age in both males and females [3]. Age reduces drug clearance and elimination by the liver—the primary site of hemin's first-pass metabolism—and could drastically impact hemin pharmacokinetics [229]. Despite the use of hemin in older patients with porphyria, the degree of this impact is unclear and future studies comparing clinical markers, such as serum ferritin and biliverdin, to hemin clearance in aged models could help to determine optimal hemin dosing in older patients. Although age is a critical consideration for clinical translatability, age also reduces the chance of survival post-AMI, thus making aged mice unideal first models in which to evaluate the therapeutic effects of hemin post-AMI. Information regarding the impact of biological sex on cardiac heme regulation and the benefits of HMOX1 induction is similarly limited. Our current understanding of heme metabolism is predominantly derived from studies in males and thus presented a larger foundation of information from which to perform the present study. In chick embryo liver cells, testosterone and estradiol reportedly increase porphyrin content and testosterone is additionally associated with increased hematocrit in humans [230,231]. Increased ALAS activity is also shown in chick livers exposed to progestational contraceptives and the use of estrogens in porphyria patients is not recommended due to their potential to indirectly stimulate ALAS activity by inducing cytochrome hemoprotein synthesis [232,233,175]. Yet, how these hormones differ in their regulation of heme synthesis and catabolism in the heart is not clear. Similar to HMOX1 protein trends observed in male mice in the present study, infarct zone HMOX1 mRNA is significantly elevated in female mice 1 day post-AMI and progressively declines until 7 days post-AMI [234]. In female rats

administered 30 mg•kg^{-1} hemin i.p. for 2 days prior to cardiac ischemia-reperfusion injury, hemin reportedly reduced infarct size [10]. However, further investigation into sex-dependent differences in heme regulation is required to improve the development of HMOX1-targeting interventional therapeutics for both males and females.

Many challenges still need to be overcome before hemin can be translated to the clinic. The effects of drugs like hemin on heme regulation as a whole, beyond just HMOX1 induction, must be taken into consideration. Pre-clinical studies must reflect clinical realities, such as the need for post-AMI interventions and models that reflect minimal patient demographics, such as sex or age. A greater understanding of hemin pharmacokinetics and pharmacodynamics is long overdue. Even so, our data provide important foundational information to further advance our understanding of therapeutically targeting heme metabolism in AMI.

CHAPTER 4: EXPLORING THE EFFECTS OF HEMIN ON LATE MYOCARDIAL INFARCTION INTERVENTION

4.1 INTRODUCTION

Acute myocardial infarction (AMI) occurs when coronary arteries supplying oxygenated blood to the myocardium become occluded, causing ischemia with progressive cardiac tissue necrosis, inflammation, fibrosis, and compromised function. Current therapeutic strategies for the treatment of AMI have significantly reduced the incidence of recurrent AMI, yet despite advances in surgical and pharmacological AMI interventions, morbidity and mortality remain high [4–6,62]. Invariably, many patients will experience worse clinical outcomes due to delayed clinical presentation or ineligibility for reperfusion therapy [62,63,235–237]. Thus, novel pharmacological strategies for the treatment of AMI are necessary.

Rescue and recovery of ischemic myocardium are mediated through five principle mechanisms: cell survival, inflammation, neovascularization, extracellular matrix remodeling, and adaptive contractility [238]. In AMI, low oxygen availability (hypoxia) from coronary artery occlusion impairs cardiac ATP production, increases oxidative stress and apoptosis, and results in the progressive loss of viable contractile tissue via necrosis and necroptosis [20,24]. Loss of contractile tissue reduces the heart's capacity to properly contract and deliver oxygenated blood to the rest of the body for its essential functions. Cardiomyocyte stress and cell death also results in the release of chemokines and pro-inflammatory cytokines—essential modulators of inflammation and macrophage recruitment post-AMI [24,25]. Although critical for initiating the remodeling (wound-healing) phase of AMI progression through the stimulation of myofibroblast proliferation/differentiation, inflammation can also exert deleterious effects through the propagation of reactive oxygen species production and negative extracellular remodeling if left unresolved [25]. Thus, timely resolution of inflammation is also required for effective myocardial repair and recovery. In response to the loss of cardiac tissue and increased hemodynamic stress, surviving cardiomyocytes in the peri-infarct heart compensate for contractile dysfunction by undergoing hypertrophic remodeling—adding

additional sarcomeric units to maintain contractile performance and reduce ventricular wall stress [28]. However—as the oxygen demands of hypertrophying cardiomyocytes rise to meet the increased mechanical load, collateral neovascularization becomes crucial to ensure a sufficient supply of oxygen and nutrients to the myocardium and avoid decompensatory heart failure [30,31]. Thus, simultaneous compensatory hypertrophy in surviving cardiomyocytes (with commensurate neovascularization) are required to maintain cardiac output [36]. Stabilization of the infarcted ventricular wall is also critical to preventing ventricular deformation and hemorrhagic ventricular rupture, and occurs through the replacement of necrotic myocardial tissue with fibrotic scar tissue [26,32]. Following the initial AMI injury, rapid fibroblast proliferation is stimulated by increased hemodynamic load (from loss of viable cardiomyocytes), mechanotransduction, and cytokine accumulation, resulting in the production of extracellular matrix proteins such as fibrin, fibronectin, and collagens I and III [33,34]. However, the continued production of extracellular matrix proteins also presents risks to cardiac contractility—reducing the heart's ability to stretch and fill with blood due to the excessive deposition of extracellular matrix and subsequent stiffening of the ventricle wall [35]. Given the complex nature of an AMI, a pleiotropic strategy capable of therapeutically targeting cardiomyocyte survival, contractility, extracellular matrix remodeling, neovascularization, and inflammation may be necessary to augment myocardial recovery post-AMI.

One novel strategy with pleiotropic potential to address these five major mechanistic pathways is the elevation of heme oxygenase-1 (HMOX1). HMOX1 is the stress-inducible enzyme responsible for the catabolism of heme—the prosthetic group responsible for oxygen binding in proteins such as hemoglobin, myoglobin, myeloperoxidase, and cytochromes involved in ATP production. Through HMOX1, free heme is catabolized into three metabolic byproducts: biliverdin (a potent antioxidant), carbon monoxide (a potent anti-inflammatory and vasodilator via cyclic guanosine monophosphate), and free iron (sequestered by ferritin)—which together exert pleiotropic cytoprotective effects [147,149]. Elevating HMOX1 levels in pre-clinical models of AMI and ischemic-reperfusion injury has been shown to significantly improve cardiomyocyte survival, neovascularization, inflammation resolution, extracellular remodeling, and

cardiac function [12,141]. Yet, translational investigations into HMOX1 for post-AMI therapy are limited and often fail to consider the bioavailability of the enzyme's substrate, heme.

In recent years, hemin has emerged as a potential pharmacological strategy for the treatment of AMI through its ability to serve as both HMOX1 inducer and substrate. Hemin is a clinically-approved orphan drug indicated for the treatment of porphyria (a rare disease characterized by defects in heme synthesis), but has also demonstrated promise for drug-repurposing in pre-clinical models of AMI and cardiac ischemia-reperfusion injury [9,17,18,164] [Chapter 3: Fig.3.5]. As a heme surrogate, hemin serves as both substrate/inducer to HMOX1, and—like heme—is catabolized by HMOX1 into equimolar quantities of biliverdin, carbon monoxide, and free iron. Through previous work, we have shown that hemin is capable of conferring cardioprotection in pre-clinical models of AMI [Chapter 3], yet hemin administration displayed greater benefit with earlier intervention. These findings suggest that hemin could be used to attenuate AMI-induced myocardial dysfunction, however the limits of its efficacy require further investigation. Given that 15-20% of patients experiencing AMI present late to the clinic (i.e. >12h after initial symptom onset)—a phenomenon significantly associated with worse clinical outcomes—whether hemin remains capable of conferring any benefit to the heart in models of late-presenting AMI is a topic of significant interest [235,236,239].

In the present study, we investigate the effects of delayed hemin intervention, exploring whether hemin has any capacity to attenuate adverse AMI outcomes in pre-clinical models of AMI when treatment is initiated late post-permanent-occlusion-AMI. Surprisingly, hemin significantly improved cardiac contractility and relaxation when treatment was initiated late (5 days) post-AMI—parameters that were not improved in prior analysis of hemin intervention immediately post-AMI. Improvements in cardiac function were not associated with differences in fibrotic remodeling as would be expected from reduced cell death or inflammation—raising the question of how hemin might confer cardioprotection in late AMI intervention. Using 3D engineered human cardiac tissues, we show for the first time that hemin is capable of increasing cardiac contractile force and rates of relaxation directly—apparently independent of Ca^{2+} flux. We also show for the first time that hemin significantly increases the ATPase activity of cardiac

myofilaments obtained from healthy mice administered i.p. hemin, and post-translationally alters myofilament protein phosphorylation.

Collectively, these findings suggest that hemin may exert inotropic benefits to the heart through altered ATPase activity and conformational changes to cardiac myofilaments. Thus—while early hemin interventions can potentially impact all five major mechanisms of myocardial recovery, late-presenting AMI may yet benefit from at least one major mechanism: augmented contractility.

4.2 MATERIALS AND METHODS

4.2.1 Study Design

The objective of the present study was to explore whether hemin mediates cardioprotective effects through additional molecular mechanisms post-AMI—beyond the direct canonical effects conferred by hemin's metabolic by-products. The study was performed using three primary models: 1) the permanent coronary artery ligation mouse model of AMI, 2) 3D engineered human cardiac tissues, and 3) isolated myofilaments.

4.2.2 Animal Care

Animal studies were reported in compliance with the ARRIVE guidelines on reporting *in vivo* experiments. All experimental procedures were approved by the University of Guelph Animal Care and Use Committee and were conducted in accordance with the guidelines of the Canadian Council on Animal Care. Mice were acclimatized to the local institution for a minimum of 1 week prior to experiments and were housed 1-3 per cage in a 12h-light/dark cycle facility (lights on at 8h:00). All mice were pathogen-free and were randomly assigned to their respective experimental groups. Food (Envigo Cat# 7004) and tap water were provided *ad libitum*.

4.2.3 Surgical AMI Model

Surgical experiments were conducted on 8-9 week old male CD-1 mice (~35g body weight; Charles River Laboratory International Inc.). Mice were anesthetized with an isoflurane:oxygen mix (2%:100%), intubated, and mechanically ventilated (Harvard Apparatus) at a tidal volume of 300ul and at a rate of 150 breaths/min. Body temperatures were maintained at 37ºC using a water-lined heating pad, 100W heating lamp, and a TH-5 rectal probe thermometer (Physiotemp Instruments LLC). Under sterile conditions, a para-sternal thoracotomy was performed between the 2nd and 3rd ribs to expose the left anterior descending coronary artery (LAD). The LAD was ligated directly inferior to the left atria using 7-0 polypropylene thread. Infarction was confirmed by blanching of the myocardium. The ribs and skin were sutured using 5-0 silk thread. All surgeries were performed between 12h:00 and 17h:00, and animals were carefully monitored for post-surgical complications. Animals that displayed abnormalities or complications following surgery (such as pain, infection, or excess bleeding) were removed from the study and not randomized to treatment. A polymodal analgesia protocol was used in accordance with the institutional animal utilization protocol to ensure adequate peri-operative pain alleviation that included pre/post-operative (24-48hrs) meloxicam following anesthetic plane lidocaine and bupivacaine given at the site of AMI and sham surgeries. Meloxicam dosing/frequency or buprenorphine could be adjusted or given as required and/or with veterinarian advisement as part of routine post-operative care.

4.2.4 Echocardiographic Analysis

Echocardiographic analysis was performed using the Vevo2100 system equipped with the 40MHz MS550D ultrasound transducer (VisualSonics Inc.). Mice were anesthetized with an isoflurane:oxygen mix (1.0-1.5%:100%) and were maintained at 37ºC throughout data collection using an electric heating pad and a TH-5 rectal probe thermometer. All measurements were performed using the VisualSonics Cardiac Package. Two-dimensional images of the left ventricle were obtained from the long-axis view such that the ventricle chamber was observed from the apex to the aortic outflow

tract. Long-axis M-mode (1D) and B-mode (2D) images were analyzed using the LV-trace function and 2D area calculation, respectively.

4.2.5 Hemodynamic Analysis and Tissue Harvest

Mice were anesthetized with an isoflurane:oxygen mix (2%:100%) and a 1.2F catheter (Scisense Inc. Cat# FTS-1211B-0018) was inserted into the left ventricle via the right carotid artery. Body temperatures were monitored with a rectal probe and an insulating under-body warming pad was used to ensure maintenance between 36-37ºC during acquisition. Pressures were digitized at a sampling rate of 2000Hz and recorded using iWorx® analytic software (Labscribe2). Following baseline pressure recordings, animals were exsanguinated and 10mL 1X phospho-buffered saline (PBS) was perfused through the right carotid artery to wash out blood from the tissue. Tissues were harvested and rinsed in 1X PBS to further remove any remaining blood. Hearts were divided into atria, septum, right ventricle, and left ventricle (subdivided into infarct and peri-infarct areas demarcated by the blanched infarct tissue). Tissues were then flash-frozen in liquid nitrogen and stored at -80ºC.

4.2.6 Histological Visualization of Myocardial Remodeling

Animals designated for myocardial fibrosis imaging were exsanguinated after hemodynamic analysis and perfused with 10mL of 1X PBS, 10mL of 0.5M potassium chloride (KCl), and 10mL of 10% buffered formalin (VWR Cat# 89370-094) via the right carotid artery. Hearts were excised and stored in 10% buffered formalin for 24h. Hearts were subsequently transferred to 70% ethanol prior to tissue processing/paraffin embedding. Transverse sections (5um) of the paraffin-embedded hearts were obtained from the mid-papillary region and were stained with picrosirius red (500ml of saturated picric acid solution and 0.5g of Direct Red 80; Anachemia Cat# 70995-360 and Alfa Aesar Cat# B21693) to visualize myocardial fibrosis (red). Images were acquired using a Pannoramic® Midi II digital slide scanner (3D Histech) and were codified for double-blinded analysis.

Images were analyzed using the quantitative HALO® tissue analysis software (Indica Labs; Area Quantification Module v.2.4.2). Total collagen was calculated as the percent-area of red-stained tissue (collagen fibers) relative to total heart area (i.e. the sum of red and yellow tissue in both the septum and ventricles). Hearts were excluded from total collagen analysis if the tissue was not wholly intact (as a consequence of embedding/sectioning processes)

Infarct size was calculated as the percent-perimeter of left ventricular free wall occupied by red-stained collagen fibers relative to the total left ventricular free wall perimeter. Infarct perimeter was defined herein as any section of the left ventricular free wall in which wall thickness was composed of 50% collagen. Left ventricular free wall perimeters were measured by manual HALO® annotation. Hearts were excluded from infarct size analysis if the infarct had been severed during tissue processing.

Infarct thickness was measured using the straight-ruler annotation tool and was calculated as the average of three measurements of left ventricular wall thickness (per heart) along varying regions of the infarct zone. Straight-ruler annotations were placed at 90° angles perpendicular to the infarct; annotations were not placed in regions of the ventricle in which free wall folding occurred (an artifact of tissue embedding/sectioning). To exclude empty spaces between tissues from analysis, infarct thickness was measured using distances in red and yellow (tissue) pixels.

Images for collagen subtype analysis were acquired under polarized light using a semi-confocal Zeiss Observer Z.1 microscope. The ratio of collagen I to collagen III was measured as the area of red/orange birefringent fibers (collagen I) relative to the area of green (collagen III) birefringent fibers, within the infarct zone; ratios were calculated as the average measurement of three areas (per heart) along varying regions of the infarct zone.

4.2.7 Neonatal Rat Cardiomyocyte (NRCM) Isolation

NRCMs were generously provided by Dr. Purvi Trivedi from the Department of Biochemistry at Dalhousie University (when available as overage to established

protocols/procedures) and in accordance with the Canadian Council on Animal Care's Three Rs principle on reducing animal use in research.

NRCMs were isolated from 2 day-old Sprague-Dawley rat pups; pregnant mothers were obtained from Charles River Laboratory International Inc. and neonatal pups were sacrificed by decapitation. Neonatal rat hearts (n=18) were excised and placed in a petri dish containing cold 1X phospho-buffered saline (PBS; Corning Cat# 20-030-CV). Atria and non-cardiac tissue were removed from each heart and an incision was made in each heart to remove any blood remaining within the ventricles. Ventricles were then minced in fresh PBS. Subsequent steps were performed in a Labconco® Biological Safety Cabinet under sterile conditions.

Minced hearts were transferred to a T-25 cell culture flask (Corning) with a pasteur pipette and PBS (17ml) containing freshly prepared, sterile-filtered (0.22µm) collagenase type 2 (2% w/v; Worthington Biochemical Co.), DNase I (0.5% w/v; Worthington Biochemical Co.), and trypsin (2% w/v; Worthington Biochemical Co.). The flask was incubated at 37ºC on a rotary shaker for 20min to allow for tissue dissociation. Dissociated hearts were then transferred to a tube and were centrifuged at 800rpm for 1 minute at room temperature. The supernatant was discarded and dissociated hearts were gently re-suspended in plating media (Dulbecco's Modified Eagle Medium [DMEM]/F12 Medium; [Sigma-Aldrich Cat# D6421] supplemented with 10% fetal bovine serum [FBS; Sigma-Aldrich], 15% horse serum, 1% penicillin-streptomycin [Corning Cat# 30-002-CI], and 50µg•ml^{-1} gentamycin [Corning Cat# 30-005-CR]). The cell suspension was transferred to a fresh 50ml tube over a 100µm cell strainer (BD Falcon) and triturated. The cell filtrate was then transferred to a T-25 flask for differential plating and incubated at 37ºC for 1h. NRCMs suspended in the media were transferred to a new T-25 flask without disrupting the bottom surface of the flask (fibroblast layer), and were incubated for an additional 1h at 37ºC. The supernatant was then transferred to a sterile 15ml tube and centrifuged at 1000rpm for 2 minutes at room temperature. The supernatant was aspirated and the remaining NRCM pellet was diluted in 18ml plating media.

Viable cells were counted by hemocytometer and 0.4% Trypan Blue solution (Amresco Cat# K940-100ml). NRCMs were seeded at $2x10^6$ cells•$35mm^{-1}$ Primaria™ plate (Corning) and were incubated at 37ºC for 24h prior to treatment.

4.2.8 Adult Mouse Cardiomyocyte (AMCM) Isolation

AMCMs were generously provided by Adithi Pisapathi from the Department of Biochemistry at Dalhousie University (when available as overage to established protocols/procedures) and in accordance with the Canadian Council on Animal Care's Three Rs principle on reducing animal use in research.

AMCMs were isolated from 8 week old male C57/B6 wild-type mice using a Langendorff enzymatic digestion protocol. Mice were administered heparin (200ul heparin in 200ul saline per 35g mouse, i.p., DIN# 02264315) and sacrificed by intraperitoneal sodium pentobarbital injection (0.8ml, 65mg•kg^{-1}). Each heart was rapidly excised with the ascending aorta intact and was transferred to a petri dish containing ice-cold perfusion buffer (pH 7.4; 120.4 mM NaCl, 14.7mM KCl, 0.6mM KH_2PO_4, 0.6mM Na_2HPO_4, 1.2mM $MgSO_4$-$7H_2O$, 10mM sodium HEPES, 4.6mM $NaHCO_3$, 20mM taurine, 10mM butadiene monoxime, 5.5mM D-glucose anhydrous). Hearts were transferred to a second petri dish containing ice-cold perfusion buffer for further rinsing.

Hearts were then quickly connected to a Langendorff perfusion apparatus and secured via clamp and suture thread. After 5min, the flow rate of oxygenated perfusion buffer through the apparatus was adjusted to 4ml•min^{-1} and buffer was exchanged for collagenase solution (2.4mg•ml^{-1} collagenase II, Worthington Biochemical Co., Lot # 45d15719; 12.5uM $CaCl_2$). The apparatus was switched to 'recirculating mode' after an additional 5min. After 20-22min (once the heart had softened), ventricular tissue was separated from the rest of the heart and transferred to a petri dish containing collagenase perfusate. Ventricles were finely shredded into a homogenous suspension and poured into a small beaker. Shredded ventricles were stirred thoroughly until dissociated.

The dissociated cell suspension was then filtered through a 100um filter into a 50ml conical tube and centrifuged at 500rcf for 45s at room temperature. Supernatant was discarded and 15ml of C1 solution (100uM $CaCl_2$ in modified perfusion buffer containing

2.4mg•ml^{-1} FBS and 50uM $CaCl_2$) was added to the AMCM pellet. AMCMs were then gently re-suspended, oxygenated and left to settle for 10min. Supernatant was discarded and cells were re-suspended in C2 solution (400uM $CaCl_2$ in modified perfusion buffer). Cells were re-oxygenated and left to settle for 10min. Cells were then re-suspended in C3 solution (900uM $CaCl_2$ in modified perfusion buffer), re-oxygenated, and left to settle for 10min. Cells were finally re-suspended in oxygenating AMCM media (10ml; Minimum Essential Media-Hanks' Balanced Salts Solution [MEM-HBSS; Sigma Cat# M1018], 10% FBS, 10mM butadiene monoxime, 0.1g•L^{-1} streptomycin [Sigma-Aldrich Cat# S9137], 0.1g•L^{1} penicillin [Sigma-Aldrich Cat# P3032], 2mM glutamine, 5mM taurine, and 2mM carnitine).

Cell viability was examined by hemocytometer and 0.4% Trypan Blue solution. Cells were then aliquoted (280ul per microcentrifuge tube) and centrifuged at 500rcf for 5min at room temperature. Supernatant was discarded and AMCM pellets were stored at -80°C.

4.2.9 Cell Culture

H9C2 left ventricular cardiomyoblasts (American Type Culture Collection Cat# CRL-1446) were expanded from frozen stocks in Dulbecco's Modified Eagle Medium-High Glucose (DMEM-HG; Gibco Cat# 11965-092) supplemented with 10% fetal bovine serum (FBS; Seradigm Cat# 1400-500). Cells were seeded for 80% next-day confluency at 2x10^5 cells•35mm plate^{-1} and were subsequently differentiated into quiescent cardiomyotubules by complete FBS deprivation. Media was changed to DMEM-HG with 0% FBS (differentiation media) 24h after cell plating, and was subsequently renewed with fresh differentiation media every 72h thereafter. Experimental conditions were initiated on the 6th day of differentiation. Cells were maintained at 37ºC in a humidified atmosphere of 95%:5% air/CO_2. All experiments were initiated at least one passage after recovery from cryogenic storage and cells did not exceed 19 passages.

Differentiated H9C2 cells were harvested for whole lysate analysis by rinsing the cells with cold 1X PBS and scraping the cells in fresh NP-40-based lysis buffer (30ul per 35mm plate; 1% NP-40, 20mM Tris pH 7.4, 5mM EDTA, 10mM $Na_4P_2O_7$, 100mM

sodium fluoride, ddH_2O) with activated sodium orthovanadate, protease inhibitor cocktail (Sigma-Aldrich Cat# P8340), and phosphatase inhibitor cocktail (Calbiochem Cat# 524628) at a volumetric ratio of 100:1:1:1. Samples were transferred to a microcentrifuge tube and set on ice for 30 minutes before sonicating for 10 seconds (20kHz, 30% amplitude). Total protein content was measured by bicinchoninic acid assay (BCA; Thermo Scientific Cat# 23225).

4.2.10 Hemin Treatment

Hemin for *in vivo* use was prepared fresh daily by dissolving 16.30mg hemin (Sigma Aldrich Cat# 51280) into 675ul 0.1M NaOH and buffered with 825ul 0.1M potassium phosphate monobasic to a pH of 7.4. Hemin was administered intraperitoneally at a volume of $3ul \cdot g^{-1}$ body weight (32.6mg $hemin \cdot kg^{-1}$ body weight). Hemin dosage was calculated using the U.S. FDA Guidance Document for Estimating the Maximum Safe Starting Dose in Initial Clinical Trials to convert the human dose of hemin recommended in the treatment of porphyria (1-5mg $hemin \cdot kg^{-1} \cdot day^{-1}$) to a Human Equivalent Dose in mice (12.3-61.5 $mg \cdot kg^{-1}$ body weight) [198].

Hemin stock solution for *in vitro*, *ex vivo*, 3D engineered human cardiac tissue exposure [5mM] was prepared by dissolving hemin in dimethyl sulfoxide (DMSO; Amresco Cat# N182) and by sonicating for 60min. DMSO vehicle controls did not exceed 0.1% final cell culture solution volume. Hemin stocks in DMSO were stored at 4°C (protected from light) for up to 4 months and were sonicated for 15min before each use.

4.2.11 Preparation of Isoproterenol

Isoproterenol stock for *in vitro* and *ex vivo* exposure was prepared fresh daily by dissolving 0.248mg of (-)-isoproterenol hydrochloride (-20°C; Sigma Millipore Cat# 16504-100mg) in 1ml ddH_2O. Subsequent dilutions were prepared in 1X PBS and placed on ice until use. Isoproterenol stock for 3D engineered human cardiac tissue exposure (Thermo Fisher Scientific Cat# J61788.14) was similarly prepared in ddH_2O.

4.2.12 Tissue Lysate Preparation (Whole Lysate)

Powdered tissues (10-15mg) were homogenized on ice in fresh NP-40-based lysis buffer (120ul; 1% NP-40, 20mM Tris pH 7.4, 5mM EDTA, 10mM $Na_4P_2O_7$, 100mM sodium fluoride, ddH_2O) with activated sodium orthovanadate, a protease inhibitor cocktail (Sigma-Aldrich Cat# P8340), and a phosphatase inhibitor cocktail (Calbiochem Cat# 524628) at a volumetric ratio of 100:1:1:1. Samples were placed on ice for 30min prior to centrifugation at 2000 rcf for 2min at 4°C. The supernatant was transferred to a fresh microcentrifuge tube and centrifuged at 1200 rcf for 30 min at 4°C. The supernatant was then transferred to a fresh microcentrifuge tube using a $28^{1/2}$-gauge insulin syringe to shear any DNA in the remaining sample. Total protein concentrations were quantified by BCA assay.

4.2.13 Myofilament Isolation

Myofilaments isolated for the purpose of myosin ATPase analysis were collected from fresh (never frozen) tissues unless explicitly specified, and were isolated on the day of ATPase analysis. Myofilaments isolated for the purpose of Western Blotting and phospho-staining were prepared from fresh or frozen samples. Buffers for myofilament isolation were prepared as described in Table 4.1.

Tissues collected for myofilament isolation were excised and rinsed in 1ml ice-cold 1X PBS. Whole mouse hearts were cut into 4 equal pieces to facilitate homogenization. Tissues were then transferred to a 1ml glass Kimble mortar (Cat# 885450-0020) containing 250ul-1ml ice-cold K60 buffer (Table 4.1, 60mM KCl, 30mM imidazole at pH 7.0, and 2mM $MgCl_2$, with freshly added protease [Sigma-Aldrich Cat# P8340] and phosphatase [Calbiochem Cat# 524628] inhibitor cocktails at a volumetric ratio of 100:1:1). Cells collected for myofilament isolation were similarly processed: cells were rinsed in PBS and harvested in ice-cold K60 before transfer to a Kimble mortar. Samples were gently homogenized on ice with a glass Kimble pestle until tissues or cells became dissociated and insoluble white myofilaments were visible (Fig.4.1A). Samples were then transferred to a fresh 1.5ml microcentrifuge tube and placed on ice.

Table 4.1 Preparation of stock K60 buffer for myofilament isolation

Reagent	**Supplier** (Cat#)	**[Stock]**	**[Final]**	**200ml**
ddH_2O	—	—	—	187.6ml
KCl	Alfa Aesar (7447-40-7)	2M	60mM	6ml
Imidazole, pH7.0	Sigma Aldrich (I5513-5G)	1M	30mM	6ml
$MgCl_2$	Sigma Aldrich (M1028-100ml)	1M	2mM	0.4ml

Add protease and phosphatase inhibitor cocktails to K60 buffer before use (1:1:100).

Approximately 4.5ml K60 buffer is required per tissue/cell sample.

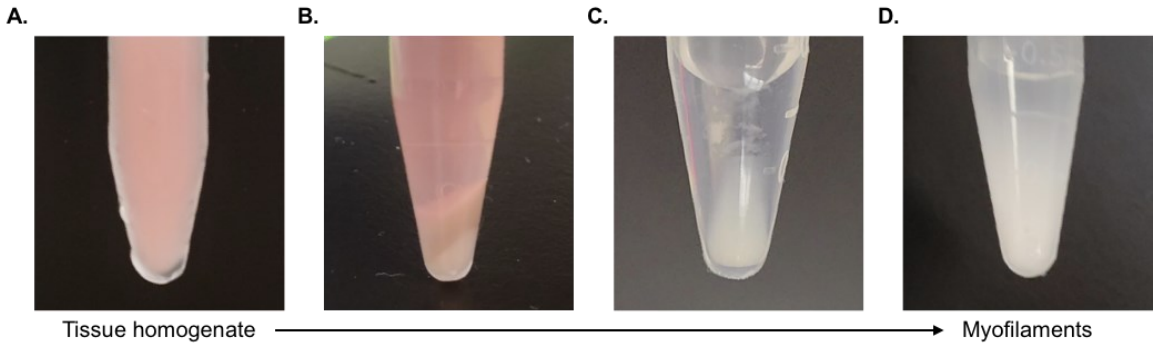

Figure 4.1 Myofilament isolation. (A) Cardiac tissue homogenate. **(B)** Crude myofilament pellet following first centrifugation. **(C)** Myofilament pellet following K60-Triton incubation, re-suspension in K60 buffer, and subsequent centrifugation. **(D)** Isolated myofilaments re-suspended in K60 buffer following final washing**.**

Once all samples had been homogenized, myofilament lysates were centrifuged at 14,000 rcf for 15min at 4°C (Fig.4.1B). Supernatant was discarded and the remaining pellet (white with red-brown cap) was resuspended by gentle pipetting in 1ml K60 buffer supplemented with 1% Triton X100 (v/v; Sigma Aldrich Cat# T9284-100ML). Samples were then placed on ice through perforated styrofoam or aluminum foil to separate microcentrifuge tube brims from ice water (so as to avoid contamination). Samples were tilted to a 45° angle within the ice box to maximize K60-Triton mixing. Ice boxes containing samples were then transferred to a shaker plate and left to shake at 150 RPM for 45min until insoluble filaments became completely white. Samples were then centrifuged at 1100rcf for 15min at 4°C. Supernatants were discarded and white myofilament pellets were washed by resuspension in 0.5ml cold K60 buffer.

Samples were centrifuged once again at 1100 rcf for 15min at 4°C (Fig. 4.1C). This wash-and-centrifugation step was repeated three times. After the fourth wash and centrifugation, supernatants were discarded and myofilaments (white pellets) were re-suspended in 250ul K60 buffer (Fig. 4.1D).

Myofilament protein content was measured by BCA assay using a 1-in-10 dilution in ddH_2O. Due to myofilament insolubility, adherence and mass, samples and pipette tips were primed to ensure accurate pipetting. Myofilament samples were vortexed and the desired volume was immediately aspirated into the pipette tip. Myofilaments were allowed to adhere to the inner wall of the pipette tip before returning the aspirant to its original microcentrifuge tube. Vortexing and aspiration were repeated three times to ensure thorough coating of myofilaments along the inside walls of the pipette tip. Samples were then vortexed and aspirated a final time before being immediately transferred into the chosen analytical container. Pipette tips were discarded between technical replicates from the same sample.

Myofilaments for Western Blotting and phospho-staining were stored at -80°C until further use, while those isolated for myosin ATPase assays were placed on ice in microcentrifuge tubes.

4.2.14 Myosin ATPase Activity Assay

In accordance with the Canadian Council on Animal Care's Three Rs principle on reducing animal use in research, myofilament protocol optimization was performed using tissues harvested from ongoing mouse experiments under established animal utilization protocols where those tissues were not being used by other investigators (e.g. skeletal diaphragm muscle, tibialis, soleus).

An overview of the myosin ATPase activity assay protocol (adapted from Pyle *et al.* 2012 [240] & Simpson *et al.* 2008 [241], and modified from Carter and Karl 1982 [242]) is provided in Figure 4.2. Briefly, myofilaments (50ug or as indicated) were incubated in ATP buffers with increasing concentrations of free Ca^{2+} (0.000847-124uM, derived from $CaCl_2$) to initiate ATPase activity. The reaction was then quenched with 10% trichloroacetic acid (TCA) and the production of inorganic phosphate was measured at optical density 630nm following the addition of developing agent (0.5% $FeSO_4$ and 1% ammonium molybdate in 1M H_2SO_4). Inorganic phosphate levels were interpolated from a standard curve of K_2HPO_4 under similar conditions. All myosin ATPase activity assays were performed within 8h of myofilament isolation.

All solutions were prepared in thoroughly cleaned and dried containers to prevent reagent contamination (special care was extended to bottle caps, outer bottle threading, and magnetic stirrer rods as well). Activating solution (5L stock; also known as pCa^{2+} 4.0 solution) was prepared as described in Table 4.2 (in the order of reagents listed) and the pH was adjusted to 7.0 with 2M potassium hydroxide. Relaxing solution (5L stock; also known as pCa^{2+} 9.0 solution) was prepared as described in Table 4.3 (in order of reagents listed) and the pH was adjusted to 7.0 with 2M potassium hydroxide. Both activating and relaxing stock solutions were immediately aliquoted into 15ml and 50ml tubes over ice, and were stored at -80°C for a maximum of 5 years (solutions were made in large volumes to reduce variability between assays within a given study). Solution aliquots were thawed early and exclusively on ice on the day of use (to prevent Na_2ATP decay). Standard phosphate curves were prepared by dissolving K_2HPO_4 in ddH_2O (20ml stocks were stored at 4°C for a maximum of 6 months).

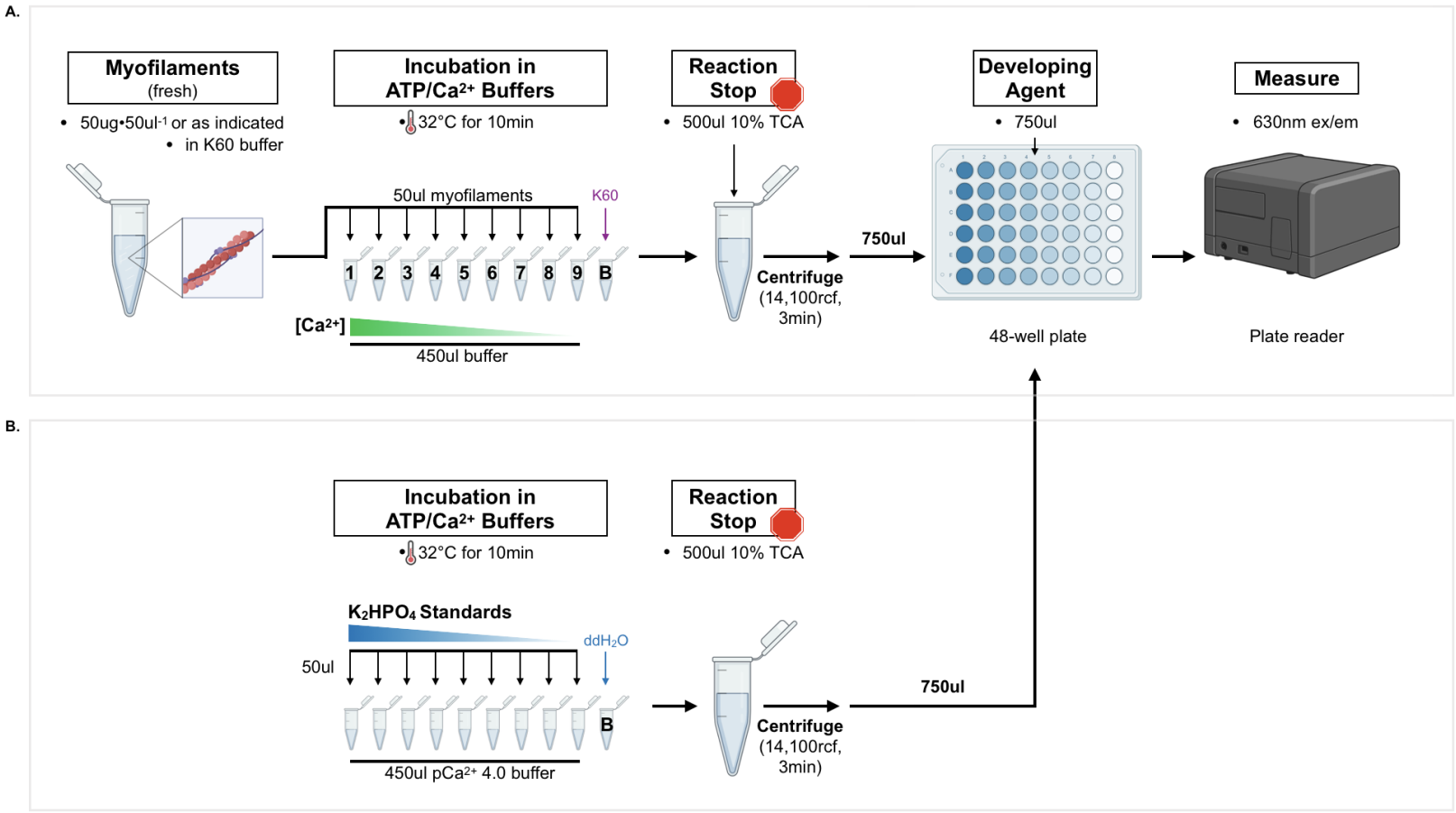

Figure 4.2 Myosin ATPase assay protocol. (A) Fresh myofilaments (50ug or as indicated) were incubated in ATP buffers (450ul) with increasing concentrations of free Ca^{2+} (0.847nM-124uM, derived from $CaCl_2$) to initiate ATPase activity. Reactions were quenched with 10% trichloroacetic acid (TCA) and the production of inorganic phosphate was measured at optical density 630nm following the addition of developing agent (0.5% $FeSO_4$ and 1% ammonium molybdate in 1M H_2SO_4). Inorganic phosphate levels were interpolated from a **(B)** standard curve of K_2HPO_4 prepared under similar conditions. Created with BioRender.com.

Table 4.2 ATPase assay Activating Solution (pCa^{2+} 4.0)

Reagent	Supplier (Cat#)	[Stock]	[Final]	1L	Notes
ddH_2O	—	—	—	921.25ml	—
KCl	Alfa Aesar (7447-40-7)	2M	23.5mM	11.75ml	Muscle relaxant and salt buffer
$MgCl_2$	Sigma Aldrich (M1028-100ml)	1M	5mM	5ml	Buffer and source of Mg^{2+}
EGTA, pH 7.0	Amresco (0932-100G)	0.1M	2mM	20ml	Free Ca^{2+} dissociation rate-limiter
Imidazole, pH7.0	Sigma Aldrich (I5513-5G)	1M	20mM	20ml	Ion buffer
$CaCl_2$	Thermo Scientific (349 615 000)	0.1M	2.2mM	22ml	Source of free Ca^{2+}
Na_2ATP	Sigma (A3377-5g)	551.1g/n	3.2mM	1.76g	Source of ATP

Adjust final pH to 7.0 with 2M KOH

Table 4.3 ATPase assay Relaxing Solution (pCa^{2+} 9.0)

Reagent	**Supplier** (Cat#)	**[Stock]**	**[Final]**	**1L**
ddH_2O	—	—	—	941.85ml
KCl	Alfa Aesar (7447-40-7)	2M	26mM	13ml
$MgCl_2$	Sigma Aldrich (M1028-100ml)	1M	5.1mM	5.1ml
EGTA, pH 7.0	Amresco (0932-100G)	0.1M	2mM	20ml
Imidazole, pH7.0	Sigma Aldrich (I5513-5G)	1M	20mM	20ml
$CaCl_2$	Thermo Scientific (349 615 000)	0.1M	4.9uM	49ul
Na_2ATP	Sigma (A3377-5g)	551.1g/n	3.2mM	1.76g

Adjust final pH to 7.0 with 2M KOH

Developing agent stock solution (25ml; or more as needed) was prepared by adding 22.8ml of 18M H_2SO_4 (18M H_2SO_4 stock obtained from Sigma Aldrich, Cat# 258105-500ml) to 22.2ml ddH_2O in an Erlenmeyer flask (a magnetic stirrer was added prior to H_2SO_4 to avoid splashing). The flask was loosely covered with aluminum foil and placed on a heat-resistant surface. The flask was then allowed to cool at room temperature for 10min until it was no longer hot from the exothermic reaction but was still warm (to facilitate reagent dissolution in subsequent steps). Once the flask had slightly cooled, 5g of ammonium molybdate (Thermo Scientific Cat# 43206.14) was added. Importantly, the flask ***was not*** re-covered with aluminum foil, as condensation from ammonium molybdate solution interacts with silicates in aluminum foil and erroneously activates the developing agent. In a fume hood, the flask was swirled gently until ammonium molybdate was dissolved and the solution was clear, colourless and cool. The stock solution was then transferred to a 100ml bottle, wrapped in foil to reduce long-term light exposure, and stored at room temperature until use or expiration (indicated by a faint blue color change). A small bottle—without foil lining under its cap—was used to store the stock solution to extend its shelf life by minimizing the air pocket within. On the day of use, 0.25g ferrous sulfate (Sigma Aldrich Cat# 215422-5G) and 5ml developing agent stock solution were added to a bottle containing 45ml ddH_2O (Table 4.4; 770ul of fresh developing agent was prepared for each sample/standard replicate). The fresh developing agent was then swirled gently until ferrous sulfate was dissolved. The container of fresh developing agent was wrapped in foil and placed at room temperature until later use.

On the day of experimentation, fresh myofilaments were extracted and subjected to protein quantification as previously described. Myofilament samples were diluted to a final concentration (unless otherwise stated) of $50ug \bullet 50ul^{-1}$ in stock K60 buffer (diluent volumes varied by sample to meet $50ug \bullet 50ul^{-1}$). At least 550ul diluted myofilament sample was required to perform the activity assay in full.

For each myofilament sample/phosphate standard, ten microcentrifuge tubes (1.5ml) were placed on ice and labelled numerically 1-through-9, with the 10^{th} tube labelled as ‘blank’. Thawed activating (pCa^{2+} 4.0) and relaxing (pCa^{2+} 9.0) stock solutions were then added together to each tube in varying proportions as outlined in

Table 4.4 Preparation of fresh Developing Agent for myosin ATPase assay

Reagent	**Supplier** (Cat#)	**[Stock]**	**[Final]**	**50ml**
ddH_2O	—	—	—	45ml
Ferrous sulfate	Sigma Aldrich (215422-5G)	—	0.5% w/v	0.25g
Ammonium molybdate, H_2SO_4	—	10% v/v	1%, 1M	5ml

A minimum of 770ul of fresh developing agent was prepared for each sample/standard replicate

Table 4.5, yielding a pre-calculated amount of free Ca^{2+} in 450ul mixed solution per tube.{For example, 400ul of activating solution (pCa^{2+} 4.0) and 50ul of relaxing solution (pCa^{2+} 9.0) were added to tube #2 to yield a final concentration of 10.8uM free Ca^{2+}. If more than three myofilament samples were included for ATPase activity measurement, 15ml tubes were used to prepare individual stock solution mixtures instead before aliquoting 450ul into corresponding microcentrifuge tubes}. Free Ca^{2+} levels were previously elucidated (computationally) by Patton *et al.* 2004 [243] to account for changes in release kinetics from $CaCl_2$ relative to its surrounding buffer components and maintain a steady free Ca^{2+} level (Table 4.5).

Microcentrifuge tubes containing Ca^{2+} solutions were vortexed and briefly spun, ensuring all contents had pooled at the bottom. Tubes were then incubated in a heating block at 32°C for 3min. To activate the ATPase reaction, myofilament samples ($50ug \bullet 50ul^{-1}$) were added to each of their ten respective Ca^{2+} solution tubes using the previously described pipette-tip primed pipetting technique. Myofilaments were added to each tube at exactly 30s intervals and each reaction was incubated with gentle shaking (300rpm) for precisely 10min at 32°C. Standard dilutions of K_2HPO_4, ddH_2O and K60 blanks were similarly added to their respective Ca^{2+} solution tubes and incubated. Special care was made to ensure that all myofilament sample, standard, and blank was added directly to solution and did not splash along the inner tube walls. Following 10min of incubation, reactions were immediately quenched with 500ul 10% TCA (w/v; Sigma Aldrich Cat# T6399-250g) and tubes were centrifuged at 14,100rcf for 3min at room temperature. Quenched reaction solution (750ul) was transferred to a 48-well plate (Corning Cat# CA62406-195) and phosphate levels were detected by adding 750ul fresh developing agent. Absorbance was measured using a Synergy H4 Hybrid Reader at 630nm excitation/emission. Phosphate production was determined by subtracting the absorbance of blank controls from samples and interpolating unknown concentrations from the K_2HPO_4 standard curve.

Table 4.5 Preparation of Ca^{2+} gradients for myosin ATPase assay

Tube	**Activating Solution, pCa^{2+} 4.0** (ul)	**Relaxing Solution, pCa^{2+} 9.0** (ul)	**Free Ca^{2+}** (uM)
1	450	0	124
2	400	50	10.8
3	350	100	2.03
4	300	150	0.951
5	275	175	0.71
6	250	200	0.544
7	225	225	0.424
8	100	350	0.112
9	0	450	0.000847
Blank	0	450	0.000847

4.2.15 Western Blotting

Tissue lysates and myofilaments were boiled at 99ºC for 5min in 4X Laemmli Buffer with 1M DTT (9:1). Samples (8-25ug•lane^{-1}) and ladder (Bio-Rad Cat# 1610375EDU) were separated via SDS–polyacrylamide gel electrophoresis (Bio-Rad Cat# 5671095) and transferred to nitrocellulose membrane (Bio-Rad Cat# 1620112) for immunoblotting. To ensure equal protein loading and uniform protein transfer, membranes were reversibly stained with MemCode (Thermo Fisher Scientific Cat# 24580) before probing. Membranes were then blocked in 5% milk for 45min and incubated in primary antibody (Table 4.6; 1:1000 in 1% skim-milk in tris-buffered-saline-tween [TBS-T] with sodium azide; 1:5000 for GAPDH) at 4ºC overnight. Membranes were washed in 1X TBS-T and subsequently incubated in either goat anti-rabbit (Invitrogen Cat# 31460) or goat anti-mouse (Bio-Rad Cat# 1705047) horseradish peroxidase-conjugated secondary antibody (1:2000 in 5% milk for 2h). Signal was detected by enhanced chemiluminescence (Thermo Fisher Scientific Cat# 34076) and digital imaging (Bio-Rad Cat# 1708280). Densitometric quantification was performed using Image Lab software (Bio-Rad) and values were obtained by measuring the target band relative to the respective total lane protein.

4.2.16 Phosphoprotein Staining

Gel electrophoresis was performed as previously described, with exception to the quantity of myofilament protein loaded (8-13ug•lane^{-1}) and the addition of a phosphoprotein standard ladder (PeppermintStick ladder, Invitrogen Cat# P27167). PeppermintStick ladder (8ul•lane^{-1}) was prepared fresh daily by adding 3ul of ladder to 9ul 4X Laemmli Buffer with 1M DTT and boiling for 5min. Upon the completion of electrophoresis, gels were rinsed with ddH_2O and removed from their casings. Stacking lanes were trimmed from the gel and discarded. Gels were then submerged into a glass container filled with ddH_2O. Water was discarded and the gel was immersed in fresh fixative solution (100ml; 80ml ddH_2O, 100ml methanol, and 20ml glacial acetic acid) with a lid seal (to control vapours). The gel was incubated in fixative at room

Table 4.6 List of validated primary antibodies and suppliers

Target	Supplier	Catalog #
HMOX1	Enzo Life Sciences	ADI-SPA-895-F
FTH1	Cell Signaling Technology	4393S
GAPDH	Origene	TA802519

HMOX1, heme oxygenase-1; FTH1, ferritin heavy chain; GAPDH, glyceraldehyde 3-phosphate dehydrogenase.

temperature—with gentle agitation—for at least 30min, after which the fixative was renewed for another 30min to ensure SDS removal (gels could remain in fixative overnight before proceeding to subsequent steps). Following the second incubation in fixative, gels were rinsed and completely submerged in ddH_2O three times for 10min each with gentle agitation. Water was discarded and gels were stained with Pro-Q™ Diamond phosphoprotein stain (Invitrogen Cat# P33300) while protected from light for 90min. All subsequent steps were performed with the gel protected from light.

After 90min of staining, used Pro-Q™ Diamond solution was transferred to 50ml tubes. Tubes were wrapped in foil and used Pro-Q™ Diamond was stored at 4°C for future experiments. Gels were gently washed three times in 100ml Pro-Q™ Diamond Phosphoprotein Gel Destaining Solution (Invitrogen Cat# P33310) for 30min. Gels were then washed twice with 100ml ddH_2O for 5min.

For phosphoprotein imaging, gels were transferred to a translucent cover sheet and then onto a clean ChemiDoc MP transilluminator (Bio-Rad). Gels were imaged via Image Lab using the built-in Pro-Q™ Diamond UV excitation protocol. Densitometric quantification was performed using Image Lab software (Bio-Rad) and values were obtained by measuring the target band relative to the density of actin in its respective lane.

4.2.17 Coomassie Gel Staining

Coomassie stain (0.25%) was prepared by adding 0.5g Coomassie Brilliant Blue R-250 (Amresco Cat# 0472-25G), to a solution of 100ml methanol, 20ml glacial acetic acid, and 80ml ddH_2O. Coomassie stain was added directly to gels following phosphoprotein imaging and was incubated on a shaker plate overnight at 50rpm. Coomassie stain was discarded and the dark purple gels were rinsed five times with ddH_2O. To remove background staining, gels were subsequently incubated in fixative solution for 1.5h on a shaker plate. Fixative was renewed and gels were incubated for an additional 30min until backgrounds became clear and colorless. Gels were rinsed in ddH_2O and transferred to a translucent cover sheet, then to a White Light Conversion

Screen (Bio-Rad) inserted into a Bio-Rad ChemiDoc MP Imaging System. Gels were imaged via Image Lab using the default colorimetric imaging protocol.

4.2.18 Formation of 3D Engineered Human Cardiac Tissues

Hemin's effects on cardiac force generation and calcium handling were assessed using TARA Biosystems' BioWire II organoid-on-a-chip platform, as previously described ([244]; Figure 4.3). Briefly, 3D engineered human cardiac tissues were prepared by mixing 100,000 human induced-pluripotent stem-cell (hiPSC)-derived cardiomyocytes (iCell Cardiomyocytes^2-01434, Fujifilm Cellular Dynamics Inc. Cat# R1017, female donor) and 10,000 normal human ventricular cardiac fibroblasts (Lonza Bioscience Cat# CC-2904, mixed male and female donors) in a hydrogel of fibrin (Sigma-Aldrich), collagen (Sigma-Aldrich), and Matrigel (Corning). Cell/hydrogel mixture (2ul, 110,000 cells) was then seeded into each microwell of a custom polystyrene sheet containing two flexible wires fabricated from a poly(octamethylene maleate [anhydride] citrate) (POMaC) polymer; microwells were coated in 0.5ul of 25 IU•mL^{-1} thrombin (Sigma Aldrich) prior to seeding and POMaC wires were secured in parallel along either end of the microwells with adhesive glue. Polystyrene sheets were inserted into a 10cm culture dish/stimulation chamber. Following 15min of cell/hydrogel gelation at 37°C in the custom polystyrene sheet, 15mL of Induction 3 Medium (StemPro-34 complete media, 20mM HEPES, 1% GlutaMAX, 1% penicillin-streptomycin, Life Technologies; 213ug•mL^{-1} 2-phosphate ascorbic acid, Sigma Aldrich) was added to the chamber. Aprotinin (10uM; Sigma Aldrich) was subsequently added to the chamber media and cells/hydrogel were incubated at 37°C (5% CO_2).

After 7 days in culture, hiPSC-derived cardiomyocytes and cardiac fibroblasts self-organized into 3D cylindrical/trabecular cardiac tissues, and—with hydrogel compaction—were suspended between the POMaC wires. Cardiac tissues were then matured through exposure to a 7 week electrical conditioning stimulation protocol in customized chambers containing parallel carbon electrodes. Electrical stimulation was performed in an environmental chamber (37°C, 5% CO_2**)** using biphasic pulses (2ms duration) at twice the excitation threshold (i.e. the minimum voltage required to

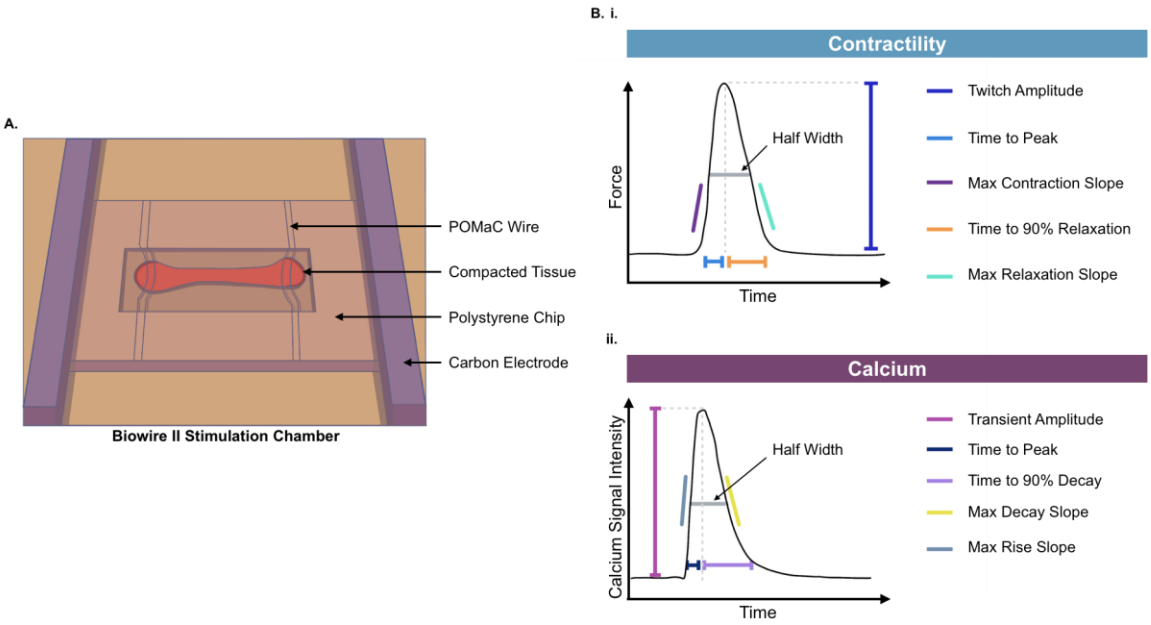

Figure 4.3 Schematic of TARA Biosystems' Biowire II platform for 3D engineered human cardiac tissues. (A) Illustration of the Biowire II stimulation chamber used to measure cardiac tissue **(B) i.** contractility by POMaC wire deflection and **ii.** calcium transients by Fura-4F-AM 340/380nm intensity. Adapted from Tara Biosystems**.**

depolarize a tissue; equal to 4V during maturation). Stimulation started at 1Hz and was increased by 0.1Hz per day to a maximum of 6Hz. Media was renewed weekly during the stimulation protocol.

Following the 7 week electrical conditioning protocol, engineered cardiac tissues were subjected to quality control evaluation. Tissues were discarded if 1) a positive force-frequency relationship was not observed, 2) abnormal post-rest potentiation occurred after resuming stimulation (i.e. a significant increase in force was observed after restarting stimulation, followed by a gradual yet significant decrease in force from baseline), or 3) a spontaneous beat rate was observed. All tissues were subjected to inotropic stimulation (isoproterenol) following compound testing as an additional quality control check.

4.2.19 Image-Based Contractility Measurements

The contractility of engineered cardiac tissues was measured by tracking POMaC wire deflection as a function of time [244]. POMaC wires were illuminated using 350nm excitation and cardiac tissues were electrically stimulated at twice the excitation threshold (1.5V). Videos of the contracting tissues were acquired at a rate of 100 frames per second using a Zyla 4.2 sCMOS camera (Andor Technology) with a 470 nm emission filter and NIS-Elements Advanced Research software (Nikon Instruments Inc, Edgewood, New York). Videos were analyzed using proprietary software to track POMaC wire location. POMaC pixel movements were converted to force as previously described [244]. Once pixel movements were converted to force, parameters of contractility including maximal twitch amplitude, time constants, and rates of contraction and relaxation were derived.

4.2.20 Calcium Transient Recording

To measure the relative change of intracellular calcium concentrations in engineered cardiac tissues, tissues were incubated in Krebs-Henseleit buffer (Millipore Sigma Cat# K3753; supplemented with 20mM $NaHCO_3$ and 1.8mM $CaCl_2$) containing

5uM Fura-4F-AM (Thermo Scientific Cat# F14175) for 45min. After 45min incubation, cardiac tissues were transferred to supplemented Krebs-Henseleit buffer without Fura-4F-AM for 15min prior to the start of compound testing.

Calcium transients were alternatingly recorded at 340nm and 380nm excitation using a CoolLED PE340 Illumination System for ratiometric calcium imaging, and emissions were recorded at 510nm using an Andor Zyla 4.2 high-performance camera (100 frames per second). Recordings were collected and averaged from 8 unique (POMaC-proximal) regions of interest in each engineered cardiac tissue.

Calcium measurements are presented as fold changes in the ratio of background-subtracted 340/380nm emission signals and were acquired from the same cardiac tissues used to measure contractility.

4.2.21 Compound Testing in 3D Engineered Human Cardiac Tissues

The dose- and time-dependent effects of hemin on engineered human cardiac tissue contractility were first investigated using a force transducer. Tissues were placed in a perfusion bath (1cm x 5cm, 600 ul) of Krebs-Henseleit buffer (supplemented with 20mM $NaHCO_3$ and 1.8mM $CaCl_2$; 37°C with 5%CO_2 aeration; 4ml•min^{-1}) and POMaC wires on one end of each tissue were subsequently cut and attached to a Kronex Technologies Model-AE801 force transducer. The opposite end of each tissue was attached to a micromanipulator and immobilized. To convert strain into a voltage signal, the force transducer was connected to a Wheatstone bridge amplifier in half-bridge mode (Transbridge 4M). Signals were recorded at 10kHz using Axoscope software (Molecular Devices) and were digitized using a Digidata 1322A instrument (Molecular Devices). The force transducer was calibrated prior to experimentation with standards of known mass and a voltage-force relationship of 104uN•mV^{-1}. Tissues were incubated in the perfusion bath for 30min prior to experimentation under field stimulation of 1Hz.

To investigate the time-dependent effects of hemin on tissue contractility using the force transducer, 5uM hemin was prepared in supplemented Krebs-Henseleit buffer and perfused across a single 3D engineered human cardiac tissue (N=1) for 10-30min. Similarly, the dose-dependent effects of hemin on tissue contractile force were examined

by sequentially perfusing hemin at increasing concentrations (1-10uM) across a second 3D engineered human cardiac tissue (N=1; 30min incubation per dose), before adding 10nM isoproterenol.

To measure the effects of hemin on image-based measurements of contractility and calcium transients as previously described (sections 4.3.18-19), cardiac tissues were incubated in an environmental chamber (37°C, 5%CO_2) containing supplemented Krebs-Henseleit buffer. Tissues were incubated in the environmental chamber for 15min before mixing 1/3 of the Krebs-Henseleit buffer volume (6ml total) in each polystyrene well twice by pipette (so as to equilibrate tissues to shear stress induced by the compound testing procedure). Baseline contractility (POMaC wire deflection) and calcium transients (Fura-4F-AM) were then recorded for 30s, 10min after pipetting.

Hemin [10uM final] was added to cardiac tissues (N=6) by dilution in tissue buffer and was mixed twice by pipetting 1/3 of the total buffer volume. Vehicle (DMSO) was similarly added to separate cardiac tissues (N=4). Contractility and calcium transients were recorded for 30s at 10min and 20min post-hemin/vehicle administration. After 20min post-administration, isoproterenol (10nM) was added to hemin-exposed cardiac tissues and contractility and calcium transients were once again recorded for 30s. Contractility and calcium measurements were normalized by dividing their values in the presence of hemin by the same tissue's respective baseline values. Contractility and calcium measurements were further normalized to 10, 20, or 30min vehicle controls measured on the same day. This was accomplished by subtracting the combined mean vehicle control values from those of each hemin/isoproterenol-exposed tissue.

4.2.22 Statistics

Values presented are expressed as mean ± SD. Graphical and statistical analyses were completed using GraphPad (Prism 6, GraphPad Software Inc.). For comparison between two groups, an unpaired Student's t-test was used. For comparison between three or more groups, a One-Way Analysis of Variance (ANOVA) and Tukey's multiple comparisons test were used. Kruskall-Wallis and Dunn's multiple comparisons tests were

performed for non-parametric data. Significance was set at $P<0.05$ ($^{*}P < 0.05$, $^{**}P < 0.01$, $^{***}P<0.001$; $^{****}P<0.0001$). Outliers were identified by ROUT method (Q=1%).

4.3 RESULTS

4.3.1 Hemin improves cardiac contractility with delayed administration post-AMI (5-28 day hemin)

To evaluate whether hemin could confer cardioprotection *in vivo* when the initiation of treatment was delayed, mice were administered a single dose of hemin ($32.6mg•kg^{-1}$, i.p.) daily, beginning 5d post-AMI (late interventional dosing regimen) and continued until 28 days post-AMI (Figure 4.4A). Echocardiography revealed that late hemin intervention significantly reduced left ventricular end-systolic and diastolic dimensions (Fig.4.4B, i, ii), but did not affect (iii) fractional shortening, (iv) left ventricular stroke volume, (v) cardiac output, or (vi) ejection fraction compared to AMI controls. Left ventricular echocardiography differed markedly between mice administered hemin 5-28d post-AMI and mice administered hemin pre- and early post-AMI (Chapter 3 Fig.3.5B), with earlier hemin interventions resulting in improved left ventricular fractional shortening, stroke volume, cardiac output, ejection fraction, and end-systolic dimensions (prophylactic administration only) but not end-diastolic dimensions. These data suggest that late hemin intervention can attenuate left ventricular dilatation caused by AMI but does not improve echocardiographic measures of cardiac output or ejection fraction.

Hemodynamic analysis (Fig.4.4C) revealed that late interventional hemin treatment significantly attenuated AMI-induced reductions in left ventricular (iii) dP/dt Max, (iv) dP/dt at 40mmHg, (vi) dP/dt Min, and reduced (v) end-diastolic pressures; late hemin intervention did not affect (i) heart rate or (ii) maximal left ventricular pressures compared to AMI controls. Together, hemodynamic and echocardiographic analysis of late hemin intervention indicate significant improvements to left ventricular contractility, relaxation, diastolic pressures, and suggest some improvement in structural remodeling of the heart, post-AMI. These findings are curious since hemin intervention early post-AMI

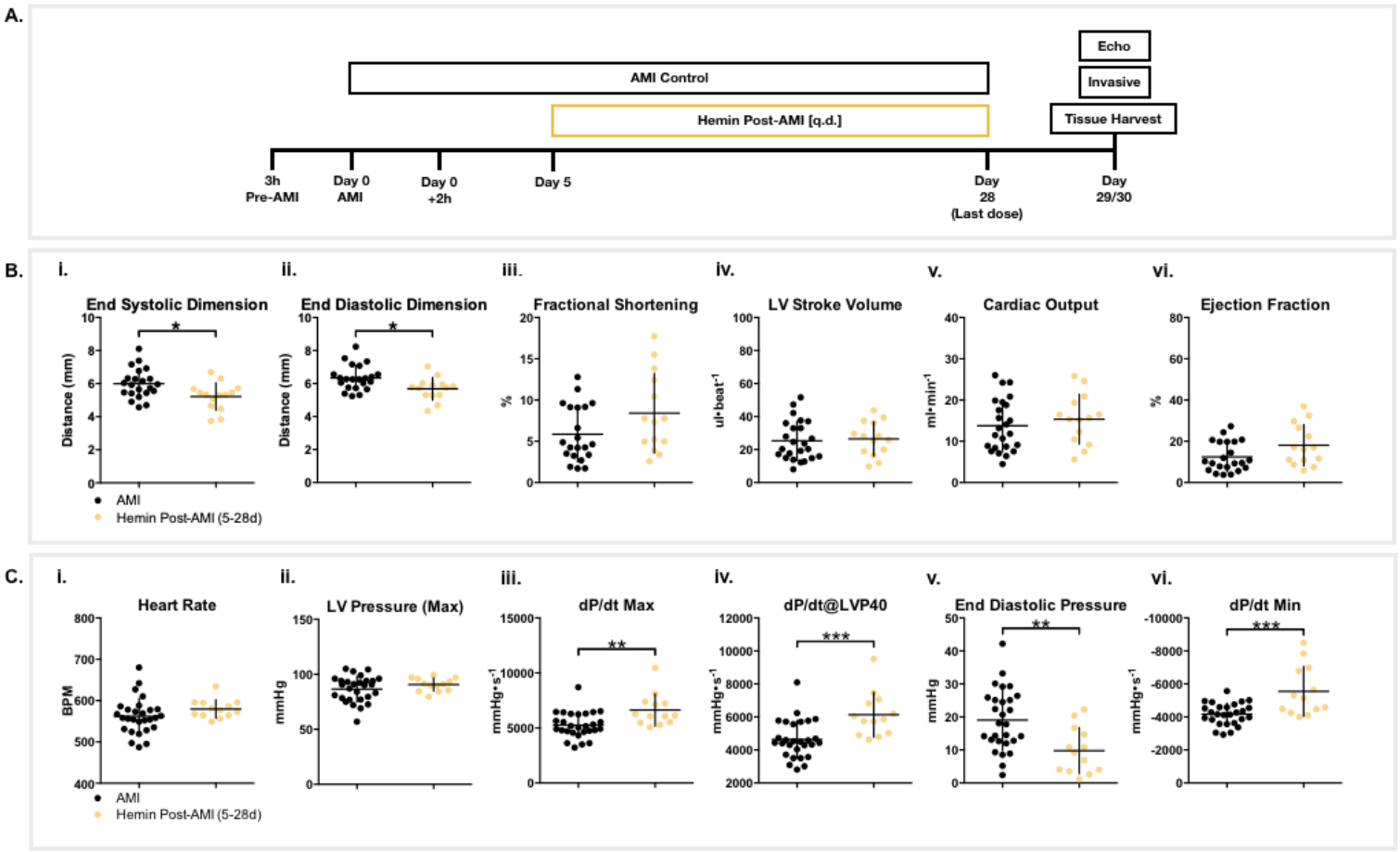

Figure 4.4 Hemin improves left ventricular contractility when administration is initiated late post-AMI. Mice were administered a once-daily dose of i.p. hemin [32.6mg•kg^{-1}] for 23d, with the first dose initiated 5d post-AMI, and were compared to vehicle-treated AMI controls. **(A)** Experimental outline. **(B)** Left ventricular (LV) echocardiography. **i.** End systolic dimension. **ii.** End diastolic dimension. **iii.** Fractional shortening. **iv.** Stroke volume. **v.** Cardiac output. **vi.** Ejection fraction. **(C)** Hemodynamic function. **i.** Heart rate. **ii.** Maximal LV pressure. **iii.** Maximal values of the first derivative of LV pressure. **iv.** Values of the first derivative of LV pressure at 40mmHg LV pressure. **v.** LV end diastolic pressure. **vi.** Minimal values of the first derivative of LV pressure.

(2h-28d post-AMI; Chapter Fig.3.5C) did not significantly improve hemodynamic indices of left ventricular contractility or relaxation. This suggests that hemin's effects on cardiac function may be dependent on molecular events occurring within the first 5 days post-AMI.

4.3.2 Hemin-mediated inotropy is not associated with improvements in fibrotic remodeling when therapeutic administration is delayed (5-28 day hemin)

Improvements in hemodynamic function can result from attenuated adverse cardiac remodeling. To investigate whether delayed hemin intervention could improve myocardial remodeling late post-AMI, hearts from mice administered hemin ($32.6 mg \bullet kg^{-1}$, i.p) once-daily from 5-28d post-AMI were stained with picrosirius red and compared to AMI controls (Fig.4.5A, B). Compared to AMI controls, hemin administration late post-AMI did not significantly alter infarct size (Fig.4.5B, i; P=0.22), thickness (Fig.4.5B, ii; P=0.29), or total collagen from the LV, RV, and septal wall (Fig.4.5B, iv; P=0.47). Similar results were also observed in mice administered hemin from 2h-28d post-AMI (Fig.4.5B, i, ii, iv).

To examine whether hemin late post-AMI might have impacted the infarct's biomechanical stability or composition, birefringent collagen I (stiff subtype) and III (pliable subtype) were measured in picrosirius red-stained left ventricles under polarized light (Fig.4.5A, iii, B, iii). However, the ratio of collagen I (red/orange) to III (green) abundance was also not significantly altered by hemin treatment late (P=0.74) or early post-AMI (P=0.14; Fig.4.5B, iii). Thus, these data show that overall infarct formation and collagen composition did not differ between treated and untreated groups.

Biomechanical infarct stability was also considered in post-mortem analysis of cardiac rupture in mice that survived initial AMI surgery but did not survive out to 28d post-AMI. (Fig.4.5C). Autopsies were performed on all mice that did not survive the 28d post-AMI period, and death by cardiac rupture was identified by a breach in the left ventricular wall as well as the presence of pooled blood within the cardiothoracic cavity. In AMI controls, 40% of all mortalities resulted from left ventricular rupture (Fig.4.5C,

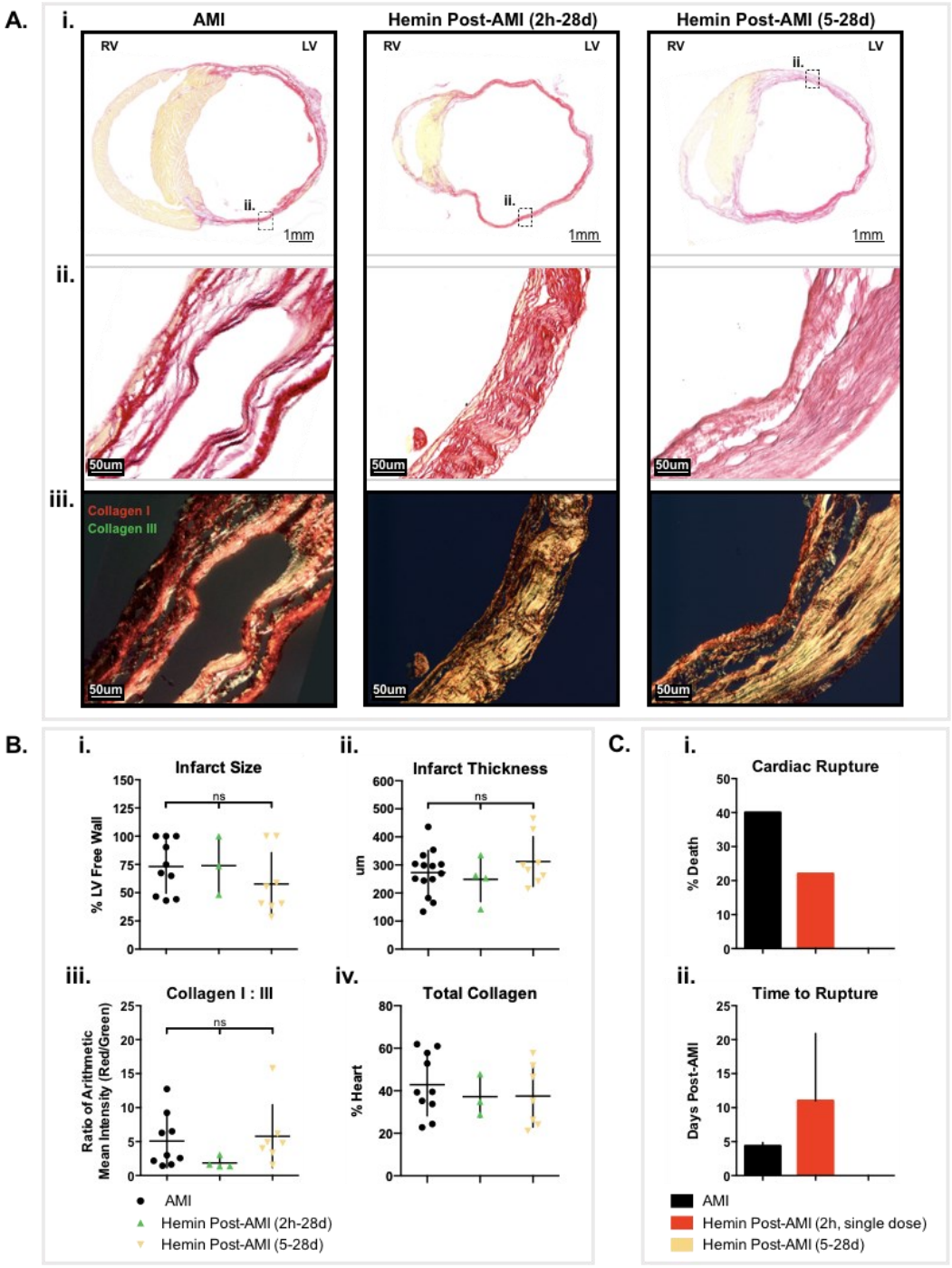

Figure 4.5 Hemin-mediated inotropy is not associated with improvements in fibrotic remodeling. Hearts were collected from mice administered i.p. hemin [32.6mg•kg^{-1}] once-daily from 2h-28d or 5d-28d post-AMI (or as a single dose 2h post-AMI), and were compared to vehicle-treated AMI controls. **(A)** Representative PSR-stained hearts. **i.** Whole heart. **ii.** Magnified region of the infarcted left ventricle. **iii.** Infarcted left ventricle under polarized light. **(B)** Quantification of **i.** infarct size, **ii.** thickness, **iii.** collagen I (red/orange):III (green) ratio, **iv.** and total cardiac collagen. **(C)** Post-mortem analysis of the **i.** incidence and **ii.** time to death by cardiac rupture.

i). No deaths by cardiac rupture were observed in mice administered hemin from 5-28d post-AMI; however, this observation is likely the result of survival bias, given that all mortality by cardiac rupture occurred within the first 5 days post-AMI (Fig.4.5C, i, ii). Interestingly, deaths by cardiac rupture in mice administered a single dose of hemin (n=19; 32.6mg•kg^{-1}, i.p) at 2h post-AMI were fewer (20%; Fig.4.5C, i) and delayed by 5 days on average compared to AMI controls (ii). Taken together, these data suggest that hemin-mediated improvements in hemodynamic function may be independent of infarct remodeling or biomechanical stability.

4.3.3 Hemin increases contractile force in 3D-engineered human cardiac tissues without concurrent changes in Ca^{2+} amplitude

To determine whether hemin was capable of increasing cardiac contractility/relaxation directly (independent of infarct remodeling or prophylactic cytoprotection), 3D-engineered human cardiac tissues were exposed to hemin using the Tara Biosystems' Biowire II platform (Fig.4.6). Time and dose-dependent effects of hemin were first investigated in a pilot study by connecting engineered cardiac tissues to a force transducer (Fig.4.6A). Exposure to 5uM hemin increased cardiac tissue contractile force by ~32% compared to peak untreated baseline control after 10min exposure (Fig.4.6A, i). After 15min of hemin exposure, contractile force was increased by ~50% above peak baseline. Contractile force was further elevated after 30min hemin exposure, increasing ~64% above peak baseline. To investigate the dose-dependent effects of hemin on contractile force, 3D-engineered human cardiac tissues were sequentially exposed to 1, 5, and 10uM hemin for 30 minutes at each dose (Fig.4.6A, ii). Contractile force was not visibly increased following exposure to 1uM hemin, but was increased ~1.6-fold from baseline peaks with 5uM hemin and ~2.1-fold from peak baseline with 10uM hemin. Subsequently, exposure to 10nM isoproterenol increased contractile force by ~8-fold compared to peak baseline, indicating that cardiac tissue contractile reserve had not been completely expended with hemin exposure. Ultimately, these data demonstrate for the very first time that hemin is capable of directly increasing contractile force in human cardiac tissue.

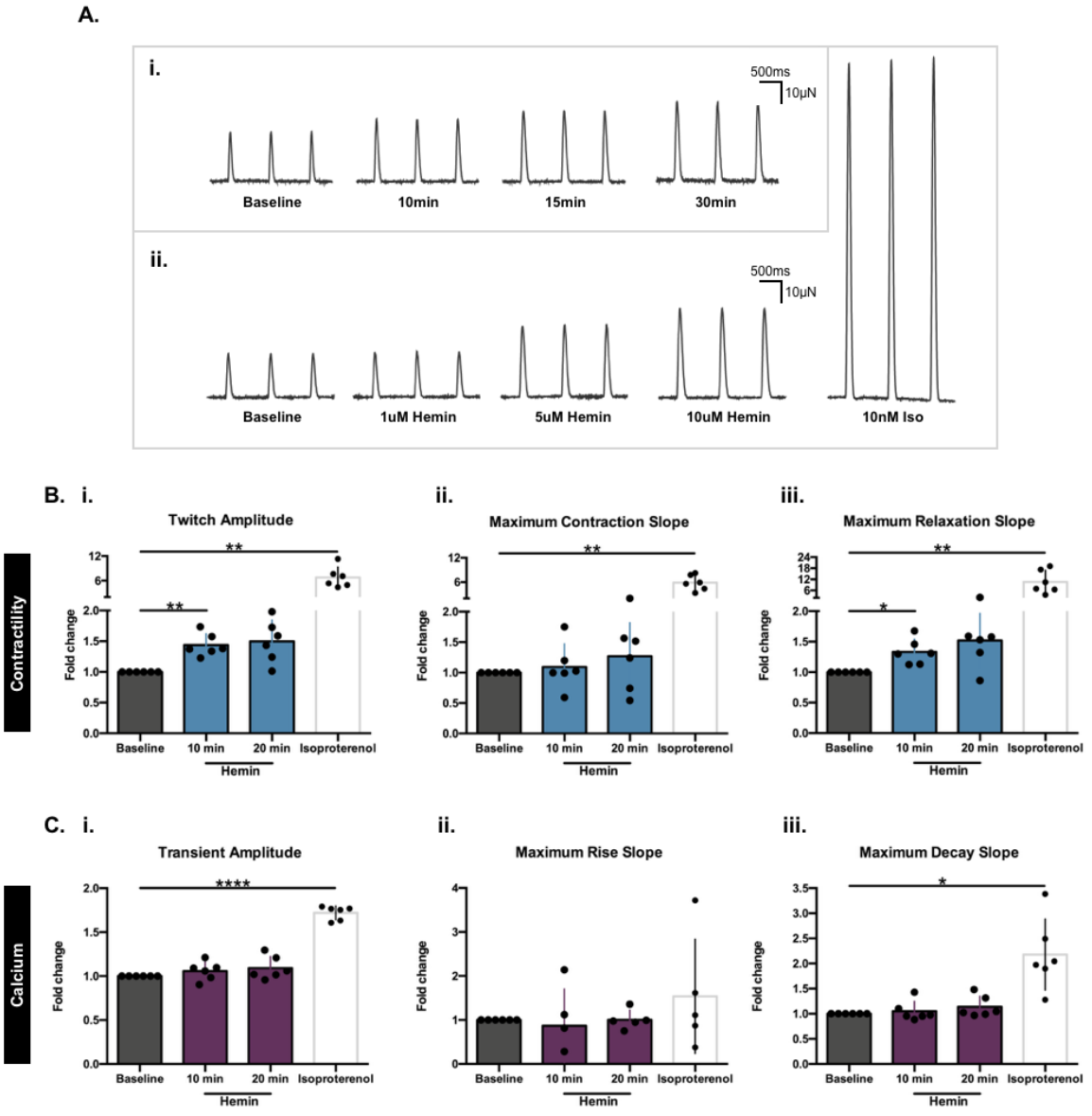

Figure 4.6 Measurement of contractility and calcium transients in hemin-exposed 3D-engineered human cardiac tissues using the Biowire II Platform. (A) Representative force tracings of hemin-exposed cardiac tissues **i.** over time (5uM hemin) and **ii.** with increasing hemin concentrations compared to isoproterenol controls (30min). **(B)** Contractile function in cardiac tissues at baseline, and following 10-20min of hemin (10uM), then isoproterenol alone (10nM). **i.** Twitch amplitude. **ii.** Maximum contraction slope. **iii.** Maximum relaxation slope. **(C)** Simultaneous measurement of Ca^{2+} transients (Fluo-4 dye fluorescence). **i.** Transient amplitude. **ii.** Maximum rise slope. **iii.** Maximum decay slope. **(B-C)** All tissues were normalized to their respective baseline values.

To measure the effects of hemin on contractility and calcium transients (image-based measurements), 3D-engineered human cardiac tissues were exposed to either vehicle (DMSO) or 10uM hemin (followed by 10nM isoproterenol) on the Biowire II deflection platform (Fig.4.6B,C). Contractility and calcium transients in hemin-exposed tissues were normalized by subtracting the mean values of time-matched vehicle controls, as well as by normalizing hemin-exposed tissues to their respective (untreated) baseline values. Vehicle controls did not differ significantly from baseline (data not shown). Measurements of contractility and calcium transients were obtained from each tissue at baseline, 10 and 20min of hemin/vehicle exposure (although 30min hemin demonstrated the largest force increase in transducer pilot studies, a 20min timepoint was ultimately selected to comply with the manufacturer's recommendations for Fluo-4 use). Cardiac tissues were exposed to 10nM isoproterenol immediately following 20min hemin measurements as part of tissue quality control assessments.

Twitch amplitude was significantly increased in 3D-engineered human cardiac tissues following 10min hemin (10uM) exposure, with amplitudes of all tissues remaining above baseline after 20min hemin (Fig.4.36, i). Similar effects were also observed on maximum relaxation slope, with hemin significantly increasing rates of cardiac tissue relaxation compared to baseline following 10min exposure. (Fig.4.6B, iii). Relaxation rates in all but one cardiac tissue remained elevated above baseline after 20min hemin. Hemin exposure did not significantly alter maximum rates of contraction in engineered cardiac tissues (Fig.4.6B, ii), however, exposure to 10nM isoproterenol significantly increased (i) twitch amplitude, (ii) maximum contraction slopes, and (iii) maximum relaxation slopes as expected.

Despite significant increases in twitch amplitude in hemin-exposed tissues, concomitant increases in calcium transient amplitude were not observed at any time following hemin exposure (Fig.4.6C, i). Calcium (ii) maximum rise and (iii) decay slopes also remained unchanged following hemin exposure. In contrast, isoproterenol exposure significantly increased (i) calcium transient amplitude and (iii) maximum decay slopes in engineered cardiac tissues, but did not alter (ii) calcium maximum rise slopes compared to baseline. Together, these data suggest that hemin-mediated increases in cardiac contractility (and rates of relaxation) may be independent of calcium transients.

Additional time-dependent measurements of contractility and calcium transients in 3D-engineered human cardiac tissues exposed to hemin were also collected (Fig.4.7). Times to peak twitch amplitude, 50% relaxation, and 90% relaxation (Fig.4.7A, i-iii)—as well as corresponding times to peak calcium fluorescence, 50% calcium decay, and 90% calcium decay (Fig.4.7B, i-iii)—were not altered by hemin exposure at any timepoint. In contrast, times to 90% relaxation (Fig.4.7A, iii), 50% calcium decay (Fig.4.7B, ii), and 90% calcium decay (Fig.4.7B, iii) were significantly reduced with isoproterenol—matching concomitant contraction/rise and relaxation/decay rates and thresholds for tissue quality control. Half-width duration (an indicator of potential arrhythmia risk similar to that of QT prolongation; Fig.4.7A, iv and Fig.4.7B, iv) was not altered by 10uM hemin exposure at 10 or 20min. Collectively, this data suggests that calcium flux typical of inotropes is not the likely mechanism by which hemin elicits increased contractile force and rates of relaxation. Importantly, this data also suggests that hemin does not negatively alter or disturb calcium handling.

4.3.4 Myofilament protein phosphorylation is not visible from whole, hemin-treated cardiac lysates

In an attempt to resolve the potential mechanism(s) underlying hemin's effects on cardiac contractility, we investigated whether hemin-mediated inotropy might occur through alterations in intrinsic myofilament signaling rather than calcium flux. Post-translational modification of myofilament proteins (such as by phosphorylation) can lead to changes in cardiac contractility independent of altered calcium transients. To investigate whether hemin-mediated increases in cardiac contractility could be attributed to modified myofilament protein phosphorylation, whole (i.e. unfractionated; NP-40 buffer-processed) lysates were collected from control and hemin-treated peri-infarct hearts, neonatal rat cardiomyocytes (NRCMs), and differentiated H9C2 cardiomyotubules (Fig.4.8A). Samples were subsequently separated by SDS-PAGE and gels were imaged using a nonspecific phosphoprotein stain (ProQ Diamond; Fig.4.8, i) and Coomassie Blue total protein stain (Fig.4.8A, ii). Major myofilament proteins were not visible in whole peri-infarct heart, neonatal rat cardiomyocytes, or H9C2

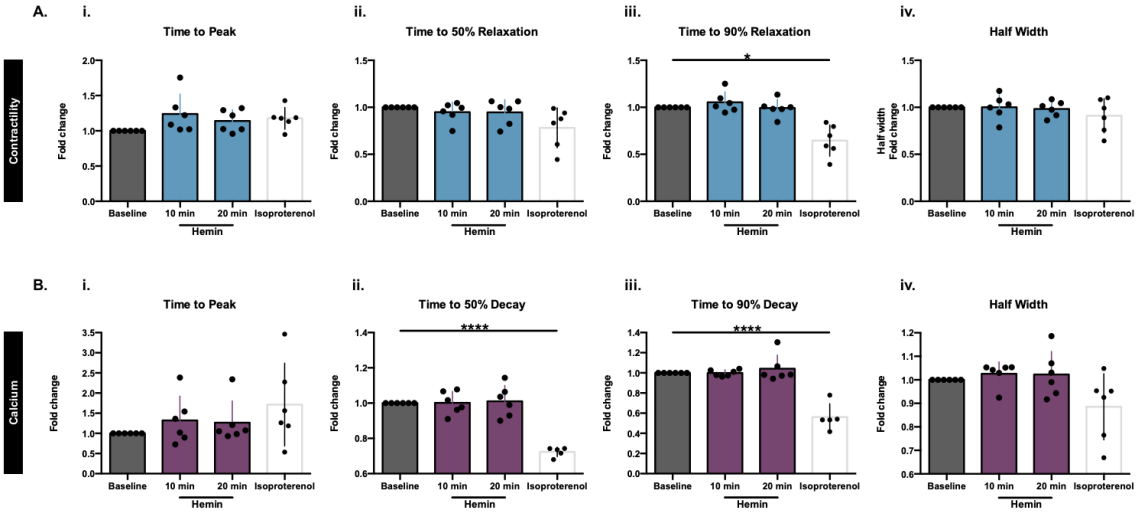

Figure 4.7 Additional measurements of contractility and calcium transients in 3D-engineered human cardiac tissues using the Biowire II Platform. (A) Contractile function in cardiac tissues at baseline, and following 10-20min of hemin (10uM), then isoproterenol alone (10nM). **i.** Time to peak amplitude. **ii.** Time to 50% relaxation. **iii.** Time to 90% relaxation. **iv.** Half width. **(B)** Simultaneous measurement of Ca^{2+} transients (Fluo-4 dye fluorescence). **i.** Time to peak transient amplitude. **ii.** Time to 50% decay. **iii.** Time to 90% decay. **iv.** Half width. **(A-B)** All tissues were normalized to their respective baseline values.

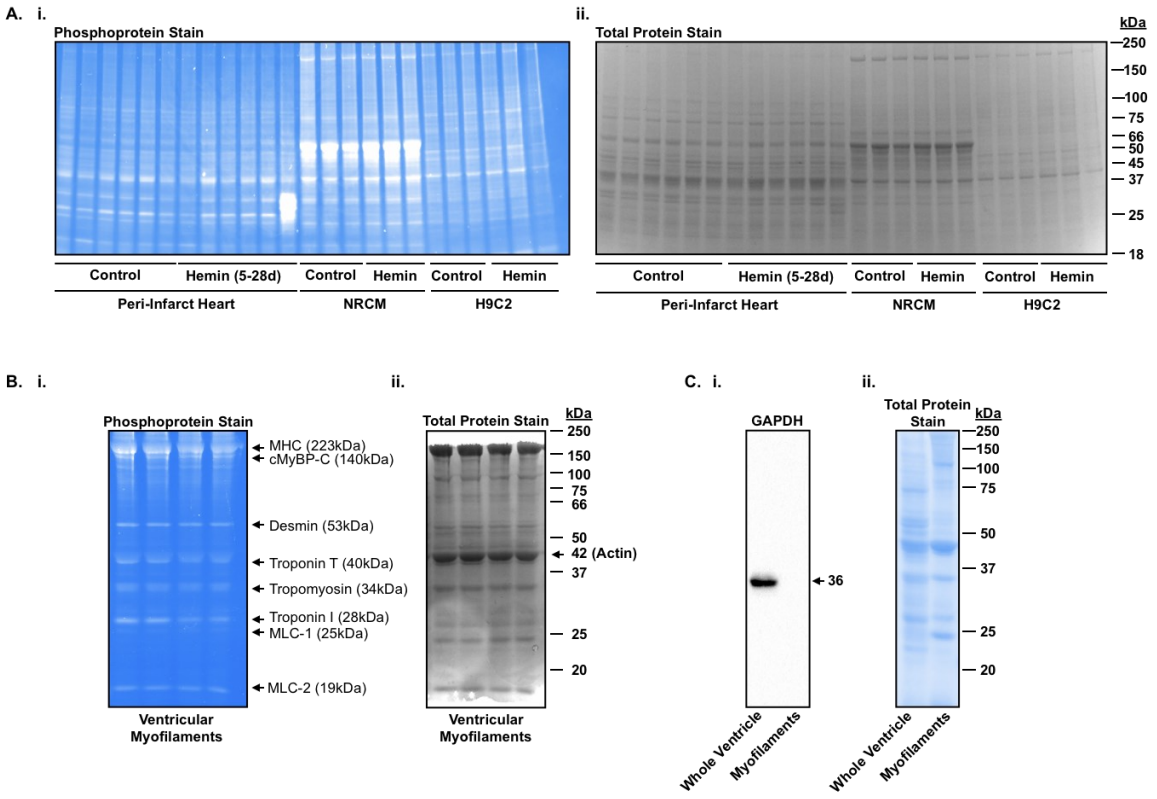

Figure 4.8 Major myofilament proteins are not visible from whole, hemin-treated cardiac lysates. (A) Whole lysates derived from peri-infarct hearts, neonatal rat cardiomyocytes (NRCM), and differentiated H9C2 cardiomyotubules were separated by SDS-PAGE and stained with **i.** ProQ Diamond phosphoprotein stain or **ii.** Coomassie Blue. Peri-infarct hearts were collected from mice administered a once-daily dose of i.p. hemin [32.6mg•kg^{-1}] for 23d, with the first dose initiated 5d post-AMI, and were compared to vehicle-treated AMI controls. NRCM and H9C2 cells were exposed to 2.5uM hemin for 24h (doses sufficient to induce HMOX1). **(B)** Ventricular myofilaments isolated from mouse hearts were separated by SDS-PAGE and stained with **i.** ProQ Diamond phosphoprotein stain or **ii.** Coomassie Blue. Major myofilament proteins are indicated on both panels. **(C)** Representative **i.** Western Blot (GAPDH) and **ii.** total protein stain (MemCode) of whole lysate and isolated myofilaments from mouse RV.

cardiomyotubule lysates following phosphoprotein or Coomassie Blue staining (Fig.4.8A). No significant differences in total peri-infarct heart protein phosphorylation were observed between hemin-treated (5-28d hemin post-AMI, once-daily, 32.6mg•kg^{-1} i.p.) and control mice post-AMI (Fig.4.8, i). Total protein phosphorylation was also measured in isolated neonatal rat cardiomyocytes to reduce the risk of diluting any potential change in cardiomyocyte-specific phosphorylation with non-myocyte cardiac cells (Fig.4.8A). However, hemin (2.5uM, 24h) also did not significantly alter total protein phosphorylation in neonatal rat cardiomyocytes compared to vehicle controls (DMSO; Fig.4.8A, i). To investigate whether changes could be observed in matured, homogeneous cells, total protein phosphorylation was further measured in differentiated H9C2 cardiomyotubules but also remained unchanged with hemin (2.5uM, 24h) exposure compared to vehicle controls (DMSO; Fig.4.8A, i).

Although major myofilament proteins were not readily detectable from whole, hemin-treated cardiac lysates, they were identifiable with myofilament extraction. Myofilaments isolated from the ventricles of healthy mice and separated by SDS-PAGE demonstrate distinct banding differences in ProQ Diamond phosphoprotein staining (Fig.4.8B, i), Coomassie Blue staining (Fig.4.8B, ii), and total protein nitrocellulose staining (MemCode; Fig.4.8C, ii) compared to whole lysates, indicating differences in protein composition. Myosin heavy chain (MHC), cardiac myosin binding protein-C (cMyBP-C), desmin, troponin T (TnT), tropomyosin (TM), troponin I (TnI), and myosin light chains 1 and 2 (MLC-1, MLC-2) were readily detectable by myofilament phosphoprotein staining (Fig.4.8B, i) and identified through reference studies [245,246]. Actin was similarly identified by Coomassie Blue staining (Fig.4.8B, ii) [245,246].

To confirm that processed samples were composed primarily of myofilaments, whole ventricle lysates and isolated ventricular myofilament fractions were probed for GAPDH (glyceraldehyde 3-phosphate dehydrogenase)—one of the most highly abundant proteins in the cytoplasm (Fig.4.8C). Compared to whole lysate derived from healthy mouse right ventricle, GAPDH was undetectable in myofilament fractions isolated from healthy mouse right ventricle (Fig.4.8C, ii), suggesting that myofilament samples were low in cytoplasmic protein contamination.

4.3.5 Myofilaments are readily isolated from adult mouse cardiomyocytes but not proliferative or differentiated H9C2 cardiomyotubules

Myofilaments isolated from fresh tissues were also required for the development/optimization of an in-house assay investigating the acute effects of hemin on cardiac myosin ATPase activity. Due to logistical challenges limiting the availability of fresh cardiac tissue, myofilament extraction was first attempted at smaller scales in isolated adult mouse cardiomyocytes (contractile; AMCMs) and H9C2 cells (Fig.4.9). Similar to whole hearts, myofilaments were readily isolated from AMCMs (280ul, equal to 80% confluence on a 35mm dish) and major myofilament proteins were identifiable by phosphoprotein staining (Fig.4.9A)—indicating that myofilament extraction from cells was possible at smaller volumes.

As fresh cardiac tissue was still required for AMCM myofilament isolation, myofilament extraction was subsequently attempted using immortalized H9C2 cardiomyoblasts (Fig.4.9B). However, no difference was observed between whole H9C2 lysates and myofilament-processed fractions (Fig.4.9B), indicating that myofilaments were not readily extracted from H9C2 cardiomyoblasts. To investigate whether myofilaments could be extracted from mature H9C2 cells, myofilament isolation was also attempted in differentiated H9C2 cardiomyotubules (Fig.4.9C). Again, no difference was observed between whole lysate and myofilament-processed fraction staining (Fig.4.9C), indicating that myofilaments were not readily extracted from H9C2 cardiomyotubules. This line of investigation into myofilament isolation from cell culture was thus ended, with the results deemed too insensitive for resolving hemin's underlying mechanisms of action on cardiac contractility.

4.3.6 Myofilaments are readily isolated from mouse diaphragm muscle but phosphorylation is not altered with acute hemin exposure *ex-vivo*

While unable to extract myofilaments from H9C2 cells, alternate sources of fresh muscle—such as mouse diaphragm muscle—were initially used to investigate the effects of hemin on myofilament phosphorylation and in the development/optimization of an

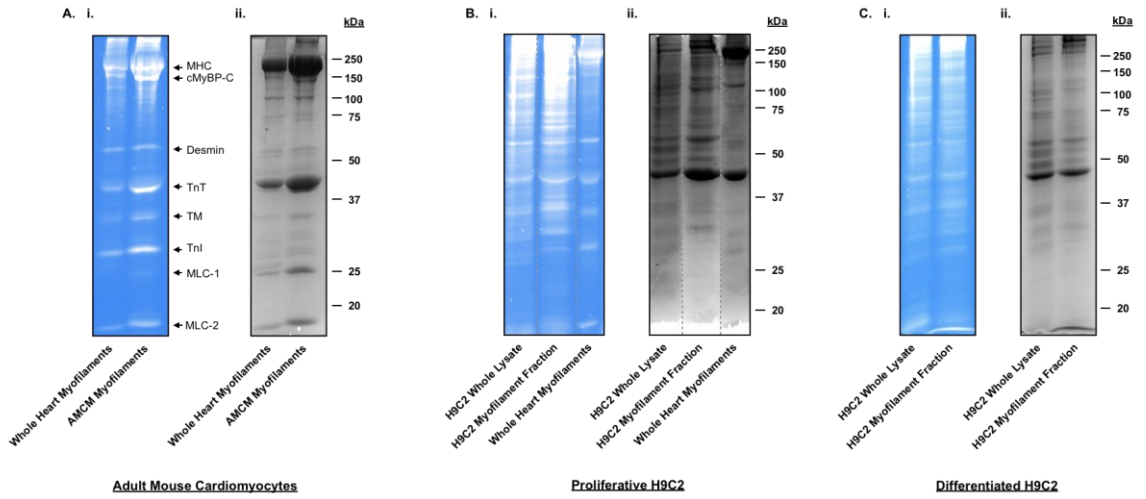

Figure 4.9 Myofilaments are readily isolated from adult mouse cardiomyocytes but not proliferative or differentiated H9C2 cardiomyotubules. (A) Adult mouse cardiomyocytes (AMCM), **(B)** proliferative H9C2 cardiomyoblasts, and **(C)** differentiated H9C2 cardiomyotubules were subjected to myofilament isolation, and were compared to whole lysate controls or myofilaments isolated from whole mouse hearts **(A-C)**. Samples were separated by SDS-PAGE and gels were stained with **i.** ProQ Diamond phosphoprotein stain or **ii.** Coomassie Blue. Major myofilament proteins are indicated in panel **(A)**. Dashed lines indicate cropped lanes within the same blot.

assay to measure myosin ATPase activity. Diaphragm performance can also enhance cardiopulmonary function [247]; as such, we took the opportunity to investigate whether hemin-mediated changes in diaphragm myofilament phosphorylation might offer a partial explanation for improved cardiac performance. To first determine whether major myofilament proteins were readily detectable from diaphragm muscle, myofilaments were isolated from the diaphragms of healthy mice left over from another study (in accordance with 3R principles and Animal Use protocols), separated by SDS-PAGE, and imaged using phosphoprotein and Coomassie Blue gel stains (Fig.4.10A). Cardiac myofilaments were used as a reference marker to identify major myofilament proteins. Similar to isolated cardiac myofilaments, major myofilament proteins were readily detectable in myofilament fractions extracted from (skeletal) diaphragm muscle (Fig.4.10A).

To assess whether hemin might be capable of directly altering major myofilament protein phosphorylation, fresh mouse diaphragm muscles (n=7) were collected and sectioned into two equal pieces: one half of each muscle was submerged in either 10nM isoproterenol or 10uM hemin in PBS for 10min while the second half was submerged in the corresponding vehicle control (Fig.4.10B). Myofilaments were then extracted, separated by SDS-PAGE, and imaged using phosphoprotein and Coomassie Blue gel stains (Fig.4.10B, representative images). Although there was some data to suggest that hemin may influence the phosphorylation of myofilament proteins (such as TnI; Fig.4.10B, i), the degree of variability between samples, their quantitation, and given that phosphorylation alone does not necessarily determine muscle contractility, we determined that this approach was not sensitive or reliable enough to draw conclusions from its results. Similar results were also observed in tibialis muscle exposed to isoproterenol, hemin, or matching vehicle control (data not displayed in representative image).

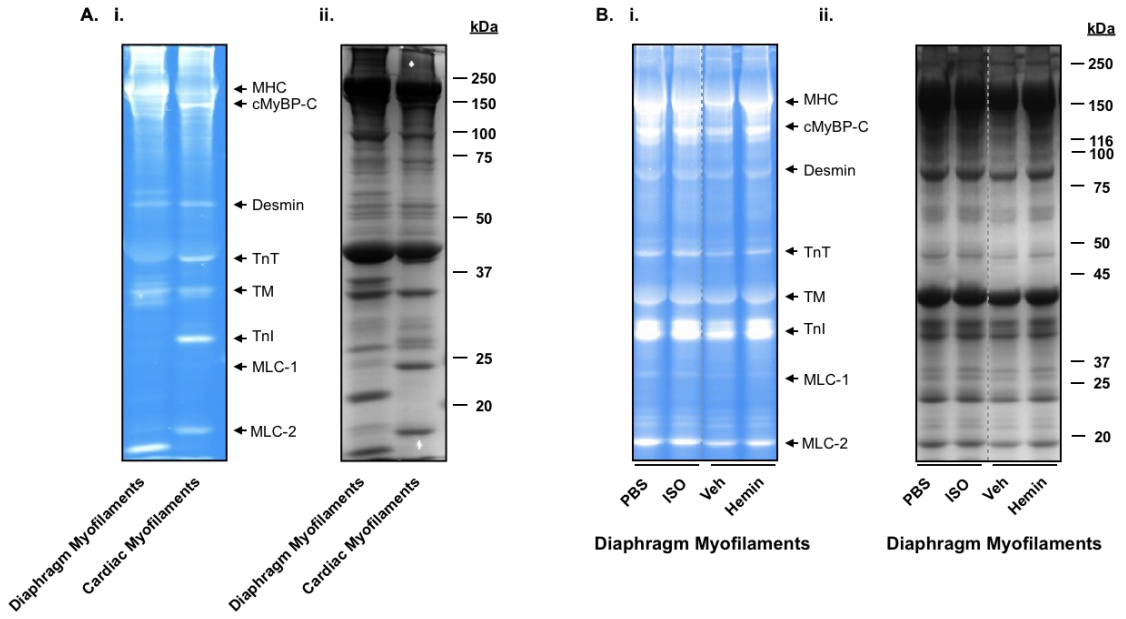

Figure 4.10 Phosphorylation of major myofilament proteins in skeletal muscle bathed in hemin or isoproterenol. (A) Myofilaments isolated from mouse diaphragm muscle and heart were separated by SDS-PAGE and stained with **i.** ProQ Diamond phosphoprotein stain or **ii.** Coomassie Blue. **(B)** Fresh diaphragm muscle from mice was collected and sectioned into two equal pieces: one half of each muscle was submerged in either 10nM isoproterenol or 10uM hemin in PBS for 10min while the second half was submerged in the corresponding vehicle control. Samples were separated by SDS-PAGE and gels were stained with **i.** ProQ Diamond phosphoprotein stain or **ii.** Coomassie Blue. Dashed lines indicate cropped lanes within the same blot.

4.3.7 Myosin ATPase activity assay validation using diaphragm and cardiac tissue-isolated myofilaments

Myosin ATPase is responsible for the hydrolysis of myosin-bound ATP into ADP and free phosphate (P_i), causing myosin heads to convert to a high-energy 'cocked' conformation. Subsequent release of free phosphate from myosin heads initiates cardiomyocyte contraction through a conformational 'power stroke' before releasing ADP and restarting the cycle of contraction. In terms of both sensitivity and specificity associated with myocyte performance, the myosin ATPase assay is the current gold standard for the measurement of functional myofilament alteration. To investigate whether hemin-mediated increases in cardiac contractility could be caused by changes to myosin ATPase activity, a myosin ATPase activity assay was performed by adapting the protocols of Pyle *et al.* 2012 and Simpson *et al.* 2008 [240,241], as well as Carter and Karl 1982 [242] to instruments available within our laboratory (requiring scaled-down chemistry). Method development, validation and optimization of the myosin ATPase activity assay were performed using both diaphragm and cardiac-derived myofilaments (Fig.4.11, 4.13, 4.14).

Myosin ATPase activity was measured via free phosphate production and was first examined in mouse diaphragm myofilaments (50ug) exposed to either pCa^{2+} 4.0 (124uM Ca^{2+}) or pCa^{2+} 9.0 (0.87nM Ca^{2+}) ATPase buffers and developing agent (Fig.4.11A). As expected, diaphragm-isolated myofilaments exposed to pCa^{2+} 4.0 (124uM Ca^{2+}) ATPase buffer produced higher levels of free phosphate compared to myofilaments exposed to pCa^{2+} 9.0 (0.87nM Ca^{2+}; the presence of free phosphate was indicated by a blue colour change in solutions containing developing agent). Concentration-dependent detection of free phosphate levels was also confirmed using K_2HPO_4 standards (K_2HPO_4 readily dissociates into free phosphate in ddH_2O; Fig.4.11B). These findings indicated that free phosphate was detectable in a concentration-dependent manner and that myofilament isolation did not abolish [Ca^{2+}]-dependent myosin ATPase activity.

To ensure that the developing agent reacted specifically with phosphate-containing standards—and not myofilament isolation and ATPase activity assay buffer

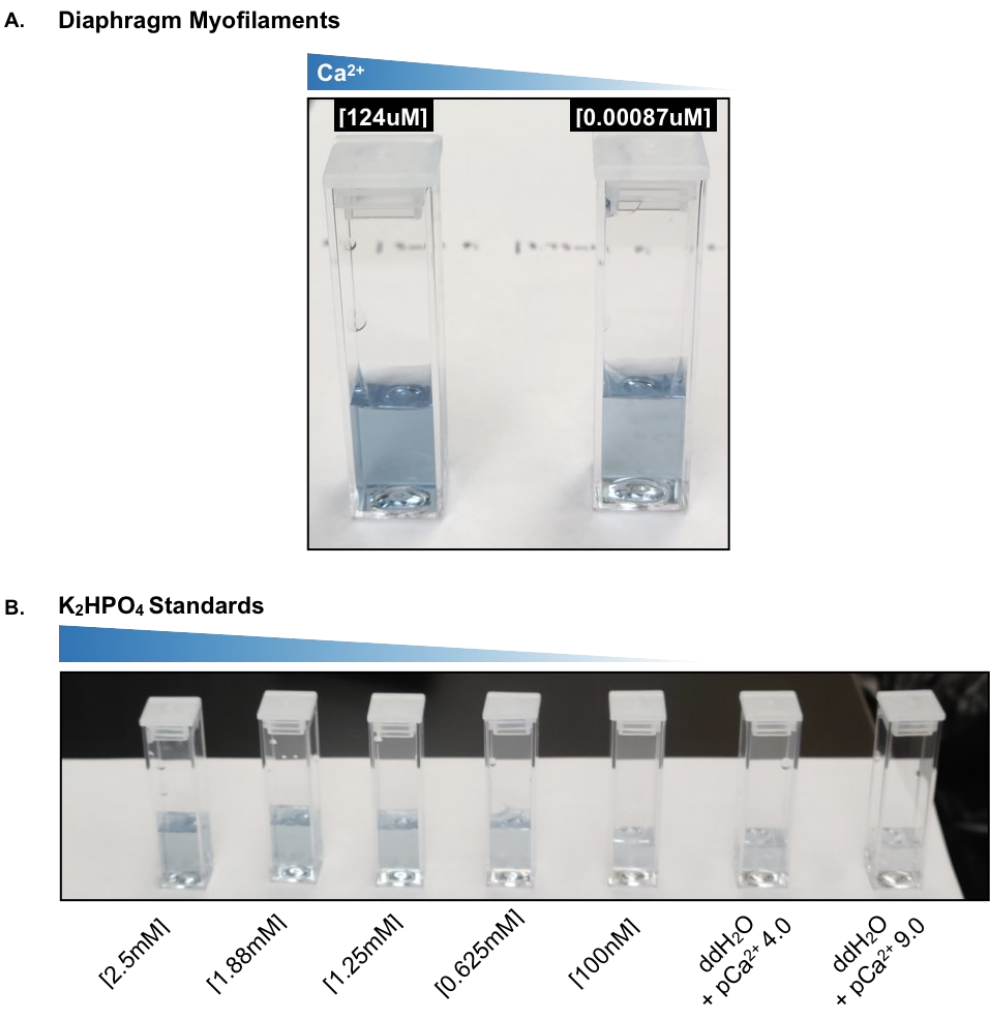

Figure 4.11 Concentration-dependent detection of free phosphate levels in myosin ATPase activity assays and K_2HPO_4 standards. (A) Ca^{2+}-dependent production of free phosphate in isolated myofilaments (50ug) exposed to either pCa^{2+} 4.0 (124uM Ca^{2+}) or pCa^{2+} 9.0 (0.87nM Ca^{2+}) ATPase buffers and developing agent. Myofilaments were isolated from a single mouse diaphragm. **(B)** Developer-mediated detection of free phosphate derived from K_2HPO_4 (2.5mM, 1.88mM, 1.25mM, 0.625mM, and 100nM) in pCa^{2+} 4.0 compared to ddH_2O controls in pCa^{2+} 4.0 and 9.0 ATPase buffers.

components, K_2HPO_4 [10mM], activating solution (pCa^{2+} 4.0), KCl [2M], $MgCl_2$ [1M], EGTA [0.1M], imidazole [1M], $CaCl_2$ [0.1M], and 10% TCA stock solutions were incubated with ddH_2O and developing agent at a ratio of 1:1:2 for 10 min (Fig.4.12). Developing agent did not react with myofilament isolation or ATPase activity assay buffer components. Importantly, the developing agent did not react with ATP-containing activating solution (pCa^{2+} 4.0), indicating specificity to free-phosphate; developing agent did, however, react with activating solution if mistakenly prepared using decayed Na_2ATP (data not shown; decay elicited by Na_2ATP storage at 4°C instead of -20°C, and monitored for using ATP-developing agent controls).

To determine optimal phosphate standard curve dilutions for myosin ATPase activity assay use, K_2HPO_4 standards (10nM-10mM) were incubated in pCa^{2+} 4.0 (124uM Ca^{2+}) ATPase buffer, developing agent, and measured at optical density 630nm in a 96-well plate (300ul) (Fig.4.13). Cardiac myofilaments (8.2ug and 82ug) were similarly incubated in pCa^{2+} 4.0 ATPase buffer and developing agent for comparison (Fig.4.13A). Following 10min exposure to pCa^{2+} 4.0 ATPase buffer, mouse cardiac myofilaments are typically expected to produce ~200nM phosphate•min^{-1}•mg^{-1} (~150-175nM phosphate•min^{-1}•mg^{-1} more than when exposed to 0.112uM Ca^{2+}: the second lowest [Ca^{2+} gradient] [246,248]. However, differences in free phosphate levels below 100uM K_2HPO_4 were not detectable using a 96-well plate reader, indicating a lower limit of differential detection of ~10uM K_2HPO_4 (Fig.4.13A). Although cardiac myofilament optical densities were situated above the lower limit of phosphate differential detection when exposed to maximal [calcium] ATPase buffer (124uM Ca^{2+}; Fig.4.13A), it remained unclear whether the 96-well plate reader was sensitive enough to detect differences in myosin ATPase activity along a full calcium gradient (124uM-0.87nM Ca^{2+}), let alone any subtle differences mediated by hemin. To examine whether increased exposure to developing agent could increase phosphate standard curve optical densities above the lower limit of differential detection, optical densities of K_2HPO_4 standards were measured following 10min (standard), 60min, 120min, and 900min incubation with developing agent (Fig.4.13B). Optical densities between phosphate standards exposed to developing agent for 10min, 60min, or 120min did not vary significantly (Fig.4.13B). Exposure to developing agent for 900min markedly increased all phosphate standard

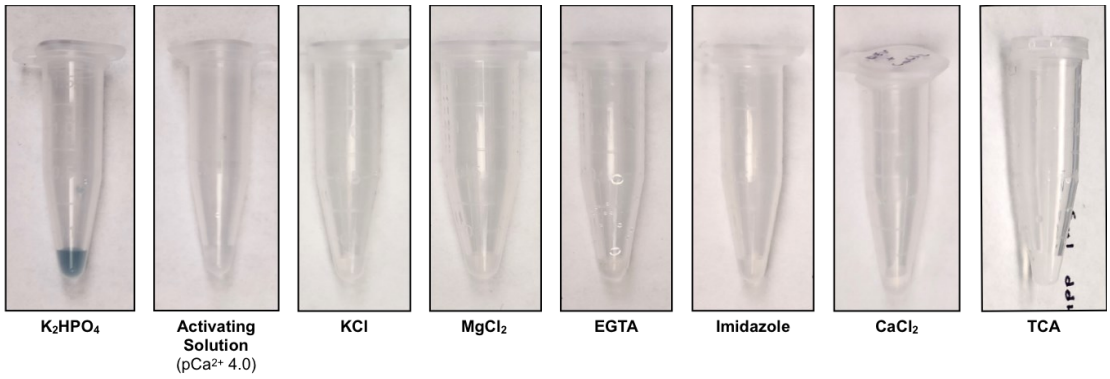

Figure 4.12 Measurement of developing agent specificity to phosphate-containing standards compared to myofilament isolation and ATPase activity assay buffer components. K_2HPO_4 [10mM], activating solution (pCa^{2+} 4.0), KCl [2M], $MgCl_2$ [1M], EGTA [0.1M], Imidazole [1M], $CaCl_2$ [0.1M], and 10% TCA stock solutions were incubated with ddH_2O and developing agent at a ratio of 1:1:2 for 10 min.

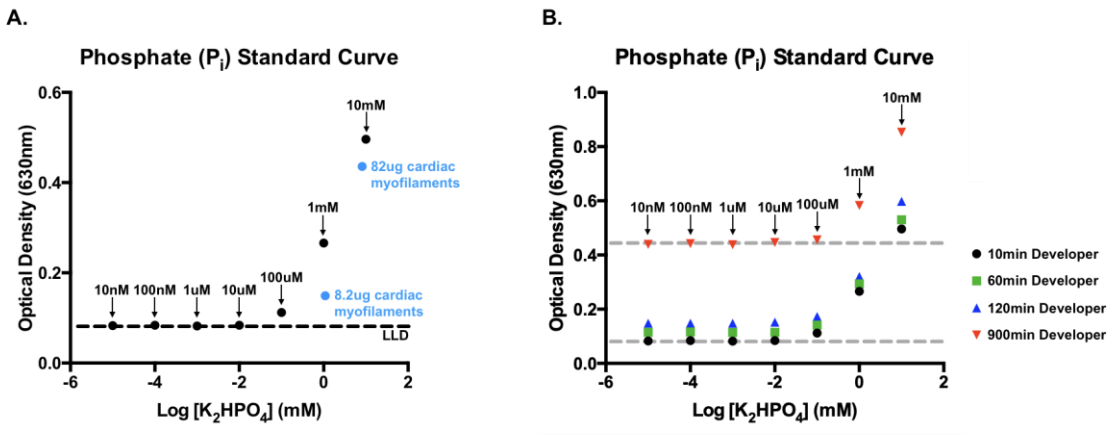

Figure 4.13 Optimization of K_2HPO_4 standard curves and developing agent exposure. **(A)** K_2HPO_4 standards (10nM-10mM) were incubated in pCa^{2+} 4.0 (124uM Ca^{2+}) ATPase buffer, developing agent, and measured at optical density 630nm in a 96-well plate (300ul). Cardiac myofilaments (8.2ug and 82ug) were similarly incubated in pCa^{2+} 4.0 ATPase buffer and developing agent for comparison. Differences in free phosphate levels below 100uM K_2HPO_4 were not detectable (LLD, lower limit of differential detection). **(B)** Optical densities of K_2HPO_4 standards were measured following 10min, 60min, 120min, and 900min incubation with developing agent.

optical densities compared to lower exposure times, however, lower limits of differential detection between 10nM and 100uM K_2HPO_4 standards remained unchanged (Fig.4.13B). Together, these data suggest that extending developing agent exposure cannot improve the assay's lower limits of differential phosphate detection. A similar experiment was also performed by exposing diaphragm myofilaments (50ug) to pCa^{2+} 4.0 ATPase buffer for 10min (standard), 15min, or 30min before quenching reaction mixtures with TCA, however optical densities were variable and did not increase more than 0.05 OD (optical density).

4.3.8 Optimization of myosin ATPase activity measurement in isolated cardiac myofilaments by pathlength extension

Inability to detect subtle changes in phosphate levels between standard curve dilutions and myofilament production limits the confidence with which we might be able to detect hemin-mediated changes in myosin ATPase activity. To examine whether increasing sample solution heights (i.e. extending the optical pathlength through solution) could improve phosphate signal intensity and [phosphate] discrimination, ATPase activity/signal intensity was measured in mouse cardiac myofilaments exposed to either pCa^{2+} 4.0 (124uM Ca^{2+}) or pCa^{2+} 9.0 (0.87nM Ca^{2+}) ATPase buffers in different containers (10.5ml quartz cuvette, 48-well plate, BioCell, and 96-well plate) (Fig.4.14). Cardiac myofilaments (50ug) were obtained from a single mouse to minimize sample variability. Stopped reaction solutions (750ul) were added to developing agent (750ul) in a standard 10.5ml quartz cuvette (10mm pathlength) and incubated for 10min at room temperature. Developed sample optical densities (630nm) for pCa^{2+} 4.0 (124uM Ca^{2+}) and pCa^{2+} 9.0 (0.87nM Ca^{2+})-exposed myofilament fractions were immediately measured in the cuvettes. Developed myofilament samples were subsequently transferred to and measured in a 48-well plate (1.5ml), BioCell (1ml), and 96-well plate (300ul) within 5min. All measurements were performed using a Synergy H4 Hybrid Plate Reader. Cuvette and BioCell plate reader adaptors were implemented as required. Optical densities were consistently higher in pCa^{2+} 4.0 (124uM Ca^{2+})-exposed cardiac myofilaments than those exposed to pCa^{2+} 9.0 (0.87nM Ca^{2+}) across all containers

A.

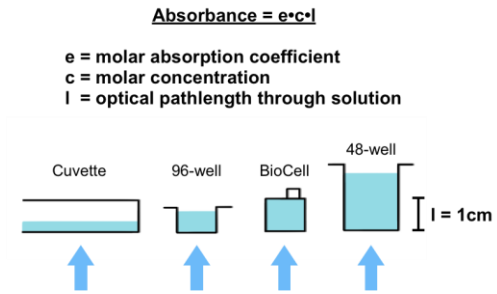

B.

	Optical Density (630nm)		
	pCa^{2+} 4.0 (High Ca^{2+})	pCa^{2+} 9.0 (Low Ca^{2+})	ΔOD
Cuvette	0.127	0.114	0.013
96-well	0.201	0.162	0.039
BioCell	0.277	0.223	0.054
48-well	0.359	0.277	0.082

Figure 4.14 Optimization of myosin ATPase activity signal intensity in isolated cardiac myofilaments by pathlength extension. (A) The effect of container size and solution height (optical pathlength) on sample absorbance. As the optical pathlength of a sample is extended, sample absorbance is also increased (Beer Lambert Law). **(B)** The effect of extending optical pathlengths through solution on ATPase activity assay signal intensity in mouse cardiac myofilaments (50ug) exposed to either pCa^{2+} 4.0 (124uM Ca^{2+}) or pCa^{2+} 9.0 (0.87nM Ca^{2+}) ATPase buffers. Stopped reaction solutions (750ul) were added to developing agent (750ul) in a standard 10.5ml quartz cuvette (10mm pathlength) and incubated for 10min at room temperature. Developed sample optical densities (630nm) were immediately measured in the cuvettes. Developed samples were subsequently transferred to and measured in a 48-well plate (1.5ml), BioCell (1ml), and 96-well plate (300ul).

(Fig.4.14B), indicating Ca^{2+}-dependent myosin ATPase activity. Differences in optical density (OD) between pCa^{2+} 4.0 and pCa^{2+} 9.0-exposed myofilaments were also increased with container depth/solution height, indicating that elongating optical pathlengths through solution could artificially increase instrument sensitivity to potentially subtle [phosphate] changes. Thus, subsequent myosin ATPase activity assays were conducted using a dedicated Genesys 150 UV-VIS vertical cuvette spectrophotometer (pathlength = 1.5cm; high sensitivity).

4.3.9 Hemin increases maximal myosin ATPase activity and alters protein phosphorylation in the cardiac myofilaments of healthy mice

To investigate whether hemin-mediated increases in cardiac contractility could be caused by changes to myosin ATPase activity, healthy mice were administered a single dose of i.p. hemin [32.6mg•kg^{-1}] (n=8) or vehicle control (sham; n=7). At 4h post-injection (the first timepoint in which hemin-mediated changes to heme regulatory enzyme expression can be observed in healthy mouse hearts; Chapter 3 Fig.3.3F), left ventricles were collected and flash-frozen (Fig.4.15). Myofilaments were subsequently isolated from the left ventricles and incubated (25ug) in ATP buffers with increasing concentrations of free Ca^{2+} (followed by developing agent). The production of inorganic phosphate (indicating ATPase activity) was interpolated from a standard curve of K_2HPO_4 prepared under similar conditions.

Left ventricular myosin ATPase activity increased with free Ca^{2+} in both sham and hemin-treated mice (Fig.4.15A), however, ATPase activity was significantly higher in hemin-treated mice than in sham controls (from 0.424-124uM free Ca^{2+}). Importantly, hemin significantly increased maximal ATPase activity in the cardiac myofilaments of healthy mice—with max myosin ATPase activity surpassing sham controls by 10.4%. Thus—not only did hemin increase the efficacy of myosin ATPase-mediated free phosphate production *in vivo*, but it did so at a dose shown to confer cardioprotection both pre- and post-AMI [Chapter 3 Fig.3.5; Fig.4.4]. Notably, hemin also increased myofilament sensitivity to Ca^{2+} (Fig.4.15A), indicated by a leftward shift in the entire hemin-treated ATPase activity curve. Given that hemin mediated an increase in both

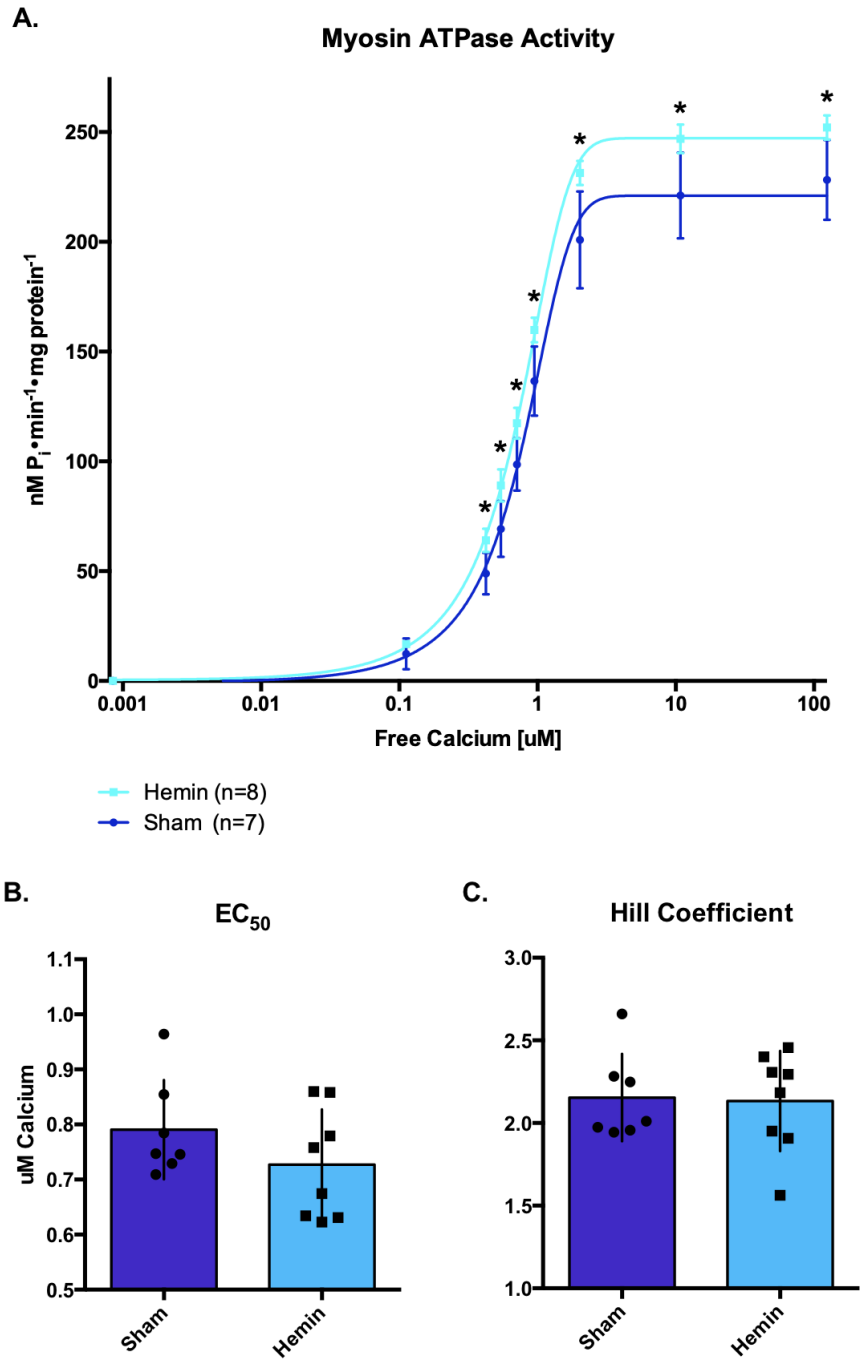

Figure 4.15 Hemin increases maximal ATPase activity in the cardiac myofilaments of healthy mice. Healthy mice were administered a single dose of i.p. hemin [32.6mg•kg^{-1}] (n=8) or vehicle control (sham; n=7), and at 4h post-injection, left ventricles were collected and flash-frozen. Myofilaments were subsequently isolated from the left ventricle and incubated in ATP buffers with increasing concentrations of free Ca^{2+}. The production of inorganic phosphate (indicating ATPase activity) was interpolated from a standard curve of K_2HPO_4 prepared under similar conditions. **(A)** Myosin ATPase activity. Significant differences between hemin and sham are denoted by '*'. **(B)** EC_{50}. **(C)** Hill coefficient.

maximal ATPase activity and Ca^{2+} potency, average EC_{50} values (i.e. concentrations of free Ca^{2+} needed to generate 50% ATPase activation) unsurprisingly did not differ significantly between sham and hemin-treated groups (Fig.4.15B). Similarly, no significant differences were observed in Hill coefficients between sham and hemin-treated groups (Fig.4.15C). Thus, hemin did not significantly modify Ca^{2+} cooperativity. Taken together, hemin increases maximal ATPase activity in the cardiac myofilaments of healthy mice (as well as the potency with which Ca^{2+} elicits an ATPase response), suggesting that treatment may result in modified myofilament protein interactions.

To further explore the molecular mechanisms underlying hemin's inotropic effects, left ventricular myofilaments (10ug) isolated from the previous experiment (Fig.4.15) were separated by SDS-PAGE and stained for myofilament protein phosphorylation (Fig.4.16). Compared to sham controls, hemin significantly reduced the phosphorylation of cMyBP-C, desmin, troponin T, and MLC-2 (Fig.4.16); phosphorylation of tropomyosin, troponin I, and MLC-1 did not differ significantly between the two groups. Thus, altered myofilament phosphorylation following *in vivo* administration could account for hemin-mediated increases in myosin ATPase activity. Collectively, these data reveal a novel potential mechanism underlying hemin-mediated cardioprotection (through altered post-translational myofilament modification and increased ATPase activity).

4.3.10 A preliminary investigation into other mechanisms underlying hemin-mediated protection in the heart (future directions)

It remains to be understood whether hemin potentially mediates its cardioprotective benefits through other (non-canonical) molecular/cellular actions post-AMI. For example, previous work by Tomczyk *et al.* 2017 has suggested an important role for HMOX1 in suppressing pro-inflammatory splenic monocytes [234]. In Tomczyk *et al.* 2017, HMOX1 deletion results in greater circulation of pro-inflammatory spleen-derived ($Ly6C^{Hi}$) monocytes in mice post-AMI. Surprisingly, HMOX1 deletion—and the resulting pro-inflammatory $Ly6C^{Hi}$ monocyte induction—significantly improved left ventricular function and reduced the incidence of cardiac rupture within the first 5 days

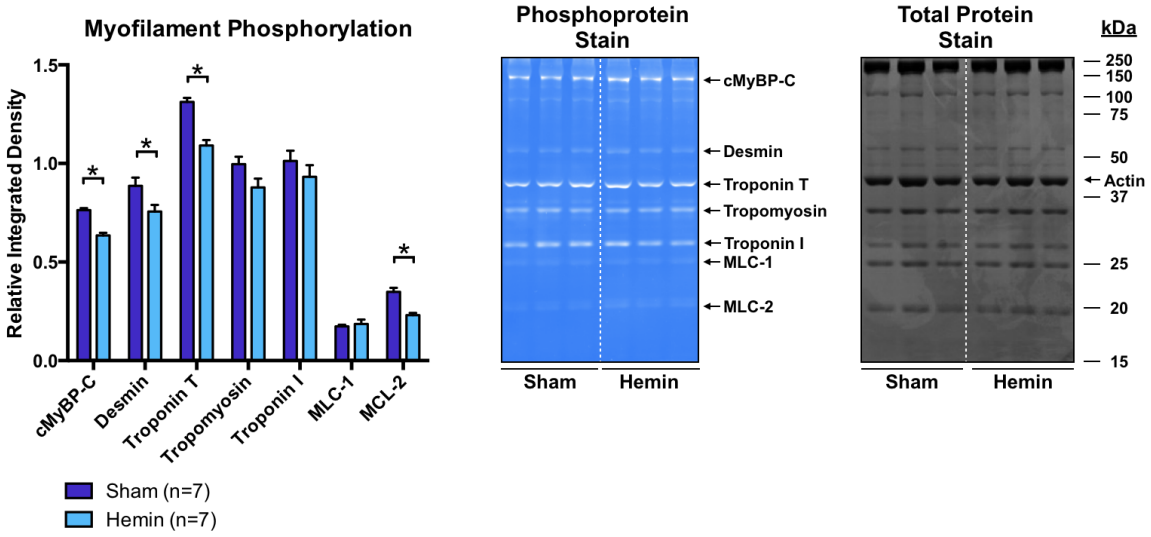

Figure 4.16 Hemin administration alters cardiac myofilament phosphorylation in healthy mice. Healthy mice were administered a single dose of i.p. hemin [32.6mg•kg^{-1}] or vehicle control (sham). At 4h post-injection, left ventricles were collected and flash-frozen. Myofilaments were subsequently isolated, separated by SDS-PAGE and stained with ProQ Diamond phosphoprotein stain and total protein stain (Coomassie Blue). Major myofilament proteins were quantified and are indicated on the representative gel images.

post-AMI compared to HMOX1$^{+/+}$ controls. However from 7-21 days post-AMI, HMOX1 deletion resulted in a more potent decline in left ventricular function than in the surviving HMOX1$^{+/+}$ controls. As a preliminary investigation into hemin's potential to confer cardioprotective benefits through a splenic mechanism, spleens were collected from mice administered a once-daily dose of i.p. hemin [32.6mg•kg^{-1}] for 23d, with the first dose initiated 5d post-AMI, and were compared to vehicle-treated AMI controls (Fig.4.17A); infarcts, livers, and kidneys were also collected (Fig.4.17B). Interestingly, we show that chronic hemin administration post-AMI increases HMOX1 levels in the infarcted region of the heart, the liver, and kidneys (Fig.4.17B), with a notable exception to the spleen (Fig.4.17A). In the spleens of hemin-treated mice, HMOX1 levels were significantly reduced compared to AMI controls, despite increased FTH1 expression (suggesting increased hemin-derived iron uptake). HMOX1 is highly expressed in the spleen and its resident monocytes/macrophages due to their roles in recycling erythrocytes. Thus, a hemin-mediated decrease in HMOX1 levels in the spleen could plausibly indicate supressed pro-inflammatory monocyte/macrophage production similar to that observed by Tomczyk *et al.* 2017 [234]. As such, investigation into whether hemin confers cardioprotective benefits through macrophage modulation and cardiac trafficking may be warranted in future studies.

4.3 DISCUSSION

In the present study, we explored the effects of delayed hemin intervention on cardiac outcomes post-AMI and identified a novel mechanism by which hemin confers benefit. Improvements to cardiac contractility post-AMI can stem from a variety of factors, such as increased cardiomyocyte survival and remodeling (e.g. hypertrophy), resolution of myocardial inflammation, reductions in adverse fibrotic remodeling, and/or enhanced myofilament activity/interactions. Here, we showed that hemin therapy initiated late (5 days) post-AMI significantly improves left ventricular contractility—bereft of benefit to fibrotic remodeling (suggesting that hemin modifies cardiac function directly, not by altering infarct size or remodeling). Improvements to left ventricular contractility with delayed hemin intervention were surprising, given the 5-day period

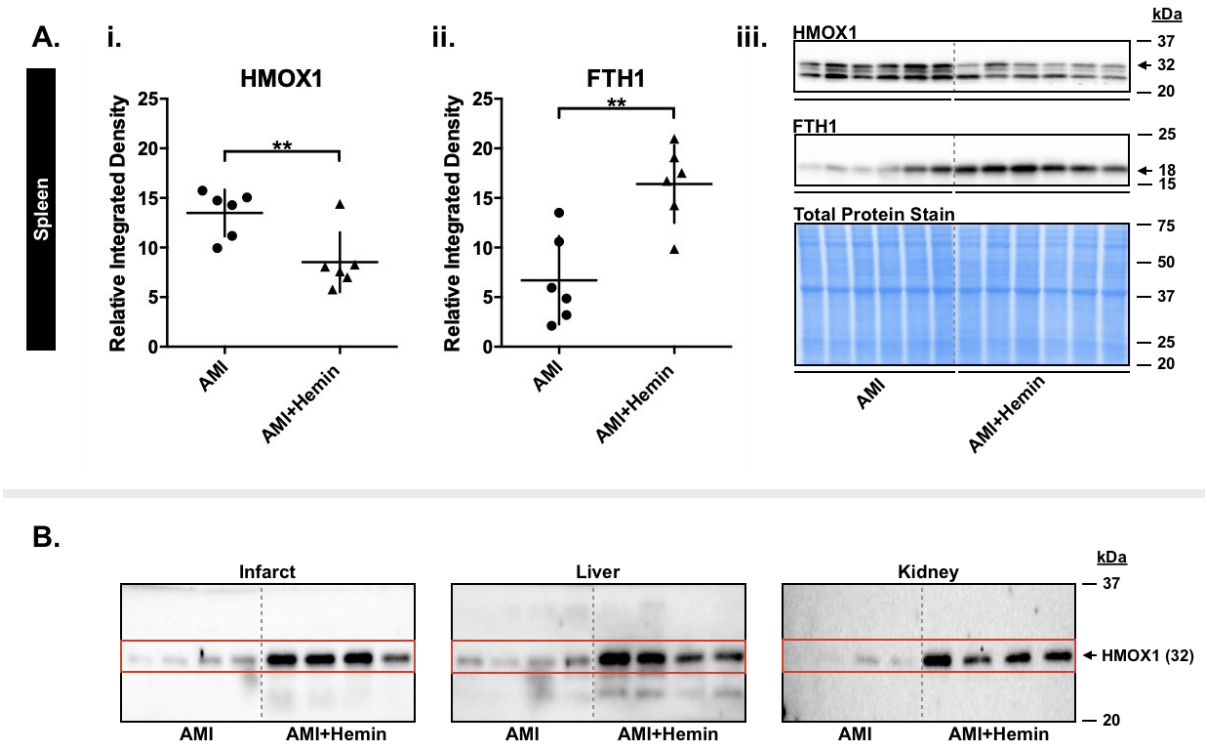

Figure 4.17 Hemin induces FTH1 but decreases HMOX1 levels in the spleen post-AMI. Spleens, infarcts, livers, and kidneys were collected from mice administered a once-daily dose of i.p. hemin [32.6mg•kg-1] for 23d, with the first dose initiated 5d post-AMI, and were compared to vehicle-treated AMI controls. **(A)** Densitometric analysis of **i.** HMOX1 and **ii.** FTH1 expression with **iii.** representative Western Blots and total protein stain; dashed lines indicate cropped lanes within the same blot. **(B)** Representative Western Blots of HMOX1 protein expression in the infarcted region of the myocardium, liver, and kidney following hemin 5-28d post-AMI compared to vehicle-treated AMI controls.

enabled AMI-induced injury to cumulatively progress without intervention. Using 3D-engineered human cardiac tissues, we established that hemin is capable of directly increasing contractile force and rates of relaxation. Hemin-mediated increases in contractility were also not associated with changes in Ca^{2+} transients, suggesting that elevated Ca^{2+} flux may not be the mechanism by which hemin alters contractile force and relaxation. Interestingly, hemin administration *in vivo* significantly increased maximal myosin ATPase activity and Ca^{2+} sensitivity in myofilaments isolated from the left ventricles of healthy mice. Increases in myosin ATPase activity and Ca^{2+} sensitivity were also associated with reductions in cMyBP-C, desmin, troponin T, and MLC-2 phosphorylation—presenting a potential Ca^{2+}-independent mechanism for increased cardiac contractility. These mechanisms could account, at least in part, for improved left ventricular contractility observed with delayed hemin intervention post-AMI, though further study is warranted. Ultimately, these data establish hemin as a novel cardiac inotrope with retained benefits—even in late intervention.

Clinically, 15-20% of patients experiencing AMI are classified as late presenters (i.e. present to the clinic more than 12h after infarction)—a phenomenon significantly associated with worse clinical outcomes [235,236,239,249]. Thus, understanding the temporal limitations of a novel therapeutic strategy has important implications for this patient population [62,63,235–237]. Here we show that hemin initiated late post-AMI significantly improves hemodynamic indices of left ventricular contractility and relaxation. Hemin late post-AMI also preserves left ventricular dimensions (as measured by echocardiography), but does not improve cardiac output, ejection fraction, or maximal left ventricular pressure. In earlier work characterizing the effects of hemin treatment from 2h-28d post-AMI, we established that hemin treatment initiated early post-AMI did not significantly improve hemodynamic indices of left ventricular contractility or relaxation but did improve cardiac output and ejection fraction [Chapter 3]. Interestingly, hemin's differential effects on contractility occur at a time of heme dyssynchrony in the peri-infarct heart, wherein heme content is progressively increased post-AMI without a concomitant increase in the heme- and stress-inducible HMOX1 or the heme-synthesizing (ALAS) enzymes [Chapter 3]. In this prior work, we showed that peri-infarct HMOX1 is rapidly induced by 3 days post-AMI without proportional changes in

heme content [Chapter 3]. By 7 days post-AMI, heme levels rise while HMOX1 returns to sham-like levels—a pattern that is also reflected in HMOX1 mRNA (with HMOX1 downregulation beginning 4 days post-AMI) [Chapter 3, [234]]. Whether this period of heme dyssynchrony (between day 1 and day 3 post-AMI) is linked directly to factors influencing cardiac contractility between early (2h) and late (5 day) post-AMI remains unclear, however, further investigation is warranted to advance our understanding of hemin's effects on contractility post-AMI and its therapeutic limitations.

Although the differential mechanism(s) responsible for hemin-mediated improvements in contractility and relaxation with late (but not early) post-AMI intervention remain unclear, parallels have been reported with HMOX1 deletion [234]. HMOX1 whole-body knockout significantly improves left ventricular function in mice within the first 5 days post-AMI, however, functional decline is worsened from 7-21 days post-AMI compared to $HMOX1^{+/+}$ controls [234]. In $HMOX1^{-/-}$ mice, adverse outcomes in late post-AMI ventricular function are credited to the enhanced migration of $Ly6C^{hi}$ (inflammatory) monocytes from the spleen to the infarcted heart, suggesting that splenic monocytes are likely beneficial early (but not late) post-AMI [234]. In the present study, we show that HMOX1 levels are significantly decreased in the spleens of mice administered hemin from 5-28d post-AMI, despite increasing splenic FTH1 and HMOX1 levels in the heart, liver and kidney. HMOX1 is normally highly expressed in the spleen due to its resident monocytes/macrophages and their roles in erythrocyte recycling. Thus, further investigation into whether hemin is capable of conferring cardioprotective benefits by suppressing pro-inflammatory splenic monocyte/macrophage production and cardiac trafficking is needed.

Fibrotic stabilization of the infarcted ventricular wall is essential to reducing the risk of hemorrhagic ventricular rupture, however, excessive fibrosis also impairs cardiac contractility by stiffening the chamber walls. Hemin has previously been shown to reduce fibroblast proliferation in hepatocytes [225] and HMOX1 confers long-term benefits through the regulation of cardiac myofibroblast conversion/proliferation when upregulated pre-AMI [11,13,141]. In the present study, late hemin intervention was not associated with improvements in fibrotic remodeling. As such, initiating hemin treatment 5 days post-AMI may be too late to attenuate cardiac fibrosis. Interestingly, deaths by

cardiac rupture in mice administered a single dose of hemin at 2h post-AMI during a comparative pilot study were fewer and delayed by 5 days on average compared to AMI controls. No deaths by cardiac rupture were observed in mice administered hemin from 5-28d post-AMI, however, this observation is likely the result of survival bias, given that all mortality by cardiac rupture in untreated controls occurred within the first 5 days post-AMI. Taken together, these data suggest that hemin-mediated improvements in contractility occur independently of infarct remodeling or biomechanical stability.

To date, endogenous carbon monoxide remains the most direct link between hemin and contractility. Carbon monoxide is one of three metabolites released from hemin catabolism and serves as a potent vasodilator in smooth muscle, however, the physiological impact of carbon monoxide on cardiac muscle is less well-known. In smooth muscle, carbon monoxide stimulates the production of cyclic guanosine monophosphate (cGMP) through soluble guanylate cyclase, thus activating cGMP-dependent protein kinase G [95,250]. In turn, protein kinase G inhibits intracellular Ca^{2+} influx via L-Type channels [251] and stimulates myosin phosphatases to drive vasorelaxation [95]. In isolated rat tail arteries, incubation with dissolved carbon monoxide induces concentration-dependent relaxation—as does hemin (independent of nitric oxide) [250]. Similar results are also observed in cardiac muscle. In strips of rat myocardium (atria), exogenous carbon monoxide baths reduce cardiac contractile force and maximal velocities of contraction and relaxation, and in H9C2 cells, carbon monoxide significantly decreases intracellular Ca^{2+} in normoxia and ischemia via L-Type Ca^{2+} channel inhibition [252,253]. Thus, previous reports of carbon monoxide-induced changes in cardiac contractility (i.e. carbon monoxide-induced relaxation) suggest that it is not the primary mediator of increased cardiac contractility observed in the present study.

Cardiac contractility can be enhanced by a variety of mechanisms, including 1) increasing cytosolic calcium levels/transients, 2) heightening myofilament calcium-sensitivity, 3) modifying myofilament conformation for mechanical advantage, or combinations thereof. Here we show for the first time that hemin is directly capable of improving contractility in cardiac tissues (independent of infarct remodeling or signs of prophylactic cytoprotection), however, increases in cardiac contractility and relaxation

were not associated with concomitant changes in calcium transients. We also show for the first time that *in vivo* hemin administration in healthy mice significantly increases cardiac myofilament sensitivity to calcium. Cardiac myofilaments are the central apparatus responsible for force generation in the heart and are activated by a transient influx of calcium into the cytoplasm—driving cardiomyocyte shortening, muscle contraction, and ejection of blood from the ventricles. To activate contraction, calcium binds to the major myofilament protein, troponin C (situated on the thin/actin filament), resulting in conformational changes to the protein's shape [254,255]. This change in shape results in the displacement of troponin I (the myosin ATPase-inhibiting subunit of the troponin hetero-trimer) and its mechanical lever/tropomyosin-link, troponin T [254,255]. In turn, troponin I displacement results in the disinhibition of the helical protein, tropomyosin—exposing sites for myosin binding along the thin filament [254,255]. Following tropomyosin displacement, ATP bound to myosin (thick filament) heads is hydrolyzed by myosin ATPase, producing ADP and P_i; in turn, myosin heads adopt the high-energy 'cocked' conformation whereby P_i is subsequently released from myosin, resulting in sarcomere shortening and muscle contraction [255]. Calcium reuptake by the sarcoplasmic reticulum and the release-and-replacement of ADP with ATP triggers myosin dissociation from actin, initiating relaxation and preparing myofilaments for the next contraction cycle [254,255]. Here we show for the first time that hemin increases myosin ATPase activity in cardiac myofilaments (a surrogate marker for enhanced muscle contraction). Hemin-mediated increases in myosin ATPase activity were not associated with changes in Hill coefficients—a measure of cooperative ligand-binding (in this context, Ca^{2+}-binding) through the steepness of the ATPase-calcium relationship. Under normal physiological conditions, a Hill coefficient of ~2.0 is expected in cardiac myofilaments as the binding of a single Ca^{2+} ion to troponin C cooperatively elicits the formation of approximately two actin-myosin cross-bridges. In turn, two myosin ATPases are activated from the Ca^{2+} ion due to cooperative Ca^{2+}-mediated distortions in the troponin and tropomyosin complexes. Hill coefficients of ~2.0 were observed for both sham and hemin myofilament groups. Thus, hemin-mediated increases in maximal myosin ATPase activity are not caused by altered cooperativity between calcium binding and myosin ATPase production of free phosphate.

Enhancements to cardiac contractility can also be produced through the post-translational modification of myofilament proteins and their capacity to confer mechanical advantage (e.g. conformationally changing the position of myosin heads in greater proximity to actin or augmenting ATPase activity). Cardiac myofilaments are rapidly and reversibly regulated through changes in the phosphorylation of several key proteins. The functional output of such changes results from not only the degree of myofilament protein phosphorylation, but also (dependent on which proteins are targeted) the specific amino acids affected and combinations therein. Here we report the novel findings that hemin significantly decreases the phosphorylation of cMyBP-C, desmin, troponin T, and MLC-2. Cardiac myosin-binding protein-C (cMyBP-C) is a myosin-associated myofilament protein located along the light meromyosin (tail) segment of the thick filament, and regulates the positioning of myosin heads relative to actin (thus influencing their interactions) [256]. Dephosphorylation of cMyBP-C has previously been shown to increase calcium sensitivity in cardiac myofilaments [257,258], yet it remains unclear which of the protein's amino acids may mediate these effects as up to 17 unique phosphorylation sites have been proposed [259]. Similarly, troponin T has four sites for phosphorylation—with only one shown to have any functional impact on myofilament activation (which is to decrease both cardiac myofilament sensitivity and myosin ATPase activity when phosphorylated) [260]. In a study by Monasky *et al*. 2012, transgenic p21-activated kinase-1 (Pak1) knockout mice exhibited increased phosphorylation of both cMyBP-C and troponin T (as well as an exacerbation in ischemic reperfusion injury) [257]. As an activator of protein phosphatase-2a, Pak1 overexpression also decreases cMyBP-C and troponin T phosphorylation (while increasing myofilament calcium sensitivity) [261]. We therefore postulate that hemin-mediated reductions in cMyBP-C and troponin T phosphorylation—as well as the subsequent increase in myofilament calcium sensitivity—could be attributed to Pak1 (although no direct ties to hemin have yet been reported). Thus, changes in myofilament calcium sensitivity, myocardial contractility, and potential mitigation of ischemic injury observed in the present study with hemin are consistent with previous reports of post-translational cMyBP-C and troponin T modification without hemin.

The functional impacts of differential desmin and myosin light chain-2 (MLC-2) phosphorylation are less clear. Changes in the phosphorylation of desmin (a key structural subunit of the intermediate filament linking sarcomeric boundaries/Z-bands to the plasma membrane) have also been linked to Pak1, although the functional impact has largely been restricted to structural stability of the myocardium and the impact on myofilament function remains unexplored [262,263]. Notably, the impact of myosin light chain-2 (MLC-2) dephosphorylation on myofilament function is also uncertain, with studies reporting that such a change can both decrease calcium sensitivity [264] and exert no impact on myofilament calcium responsiveness [265]. Some studies have connected Pak1 with MLC-2 regulation, though this work is associated with hearts subjected to ischemic reperfusion injury and it is not yet understood what impact Pak1 has on MLC-2 phosphorylation in a non-ischemic heart [257]. Ultimately, desmin modifications do not have a known link to acute myofilament function and MLC-2 dephosphorylation does not have a consistent connection with myofilament activation.

While changes to myofilament protein phosphorylation alone provide a sufficient mechanistic rationale for increased cardiac contractility, the risk of misinterpreting calcium's contribution is possible given potential technical limitations associated with the ratiometric calcium indicator, Fura-4F-AM. Unlike its Fura-2 predecessor (which was developed for high-sensitivity calcium detection: Log [Ca^{2+}] -8.0 to -6.0]), Fura-4F-AM was developed for high-intensity calcium detection (Log [Ca^{2+}] -6.5 to -4.0) and longer fluorescent signal duration [266]. Using 3D-engineered human cardiac tissues, we show that hemin increases contractile force after 10min exposure, but that contractile force is further increased at 15min—and again at 30min. Thus, Fura-4F-AM was selected for the present study given the prolonged times of hemin exposure. However, tissue transient amplitudes (calcium) in the present study are not increased in proportion to changes in twitch amplitudes (contractility) following isoproterenol exposure, suggesting potential limitations in the sensitivity of calcium detection. Increasing intracellular calcium concentrations as a means to augment cardiac contractility risks calcium overload, which exacerbates injury in the ischemic heart [267]. However, hemin's capacity to attenuate post-ischemic cardiac injury and myocardial dysfunction is not consistent with calcium-overload-induced exacerbation of ischemic injury [9,10,17,268]. Still, caution must be

exercised in concluding that intracellular calcium levels do not contribute in part to hemin-mediated increases in cardiac contractility.

The inotropic effects of hemin require further investigation in pre-clinical models of AMI and in models that better reflect patient demographics like age and sex. Here, we investigated the effects of hemin in young, male mice, yet the incidence of AMI is increased in humans after 65 years of age in both sexes [269]. Information regarding how biological sex and age might alter hemin's ability to increase cardiac contractility is currently limited. Maximal myosin ATPase activity is significantly higher in male cardiac myofilaments at baseline than in females, however, myosin ATPase activity increases with age in females (but not males) [246]. Additionally, calcium transient amplitude is significantly lower in female ventricular myocytes than in males (with amplitude decreasing with age in both sexes, similar to cooperative of Ca^{2+}-mediated ATPase activation) [246]. Thus, further investigation into the potential for sex-dependent differences in hemin-mediated inotropy is required to improve hemin as a therapeutic strategy post-AMI for both males and females.

Hearts undergo significant changes in myofilament organization/mechanical behavior and energy metabolism post-AMI [255], thus, it remains to be understood whether potential mechanisms underlying hemin-mediated inotropy identified herein in healthy tissues are conserved in infarcted hearts. Here we show that hemin increases contractility in 3D-engineered human cardiac tissues, as well as surrogate markers of increased contractility in cardiac myofilaments isolated from healthy hearts. Whether hemin-mediated changes in 3D-engineered human cardiac tissues and myofilaments from the present study translate directly to increased contractility in whole hearts post-AMI still requires further characterization as hemodynamic function post-hemin was not measured in healthy hearts. In male rats, 7 days of left coronary artery ligation significantly reduces the cumulative tension of left ventricular cardiomyocytes in response to calcium-mediated stimulation when compared to sham controls [270]. AMI also reduces myosin ATPase activity in left ventricular myofilaments isolated from rat hearts compared to sham controls in both males and females [271], though whether this is attributed to changes in myofilament post-translational modification, myocardial slippage, or salient reductions in ATP stores is not definitive. However, in the murine

myocardium, intracellular calcium concentrations peak near 1uM [272]. Our data show that at calcium concentrations of ~0.5uM and higher, myosin ATPase activation is significantly increased in cardiac myofilaments isolated from mice administered hemin. Thus, our results are consistent with whole heart data and further investigation into the functional impacts of hemin on whole heart contractility in healthy and infarcted hearts is reasonable. Measurement of hemin-mediated changes in cardiac contractility *in vivo* via isolated heart perfusion apparatus (e.g. Langendorff) could be a simple avenue to initiate further investigation into hemin's functional effects on whole hearts, however, the solubility of hemin in oxygenated perfusion buffer or buffers lacking heme/protein carriers should be considered.

Ultimately, hemin-mediated changes in myofilament protein dephosphorylation and calcium sensitivity provide a potential mechanistic explanation for increased cardiac contractility seemingly independent of calcium flux. However, more work is still necessary to identify which phosphorylation sites are affected by hemin exposure—either directly or via some intermediate signaling mechanism—and whether these findings translate to functional changes *in vivo* and with age/sex. Even so, this study marks a significant contribution to the field of hemin pharmacology through its identification as a novel cardiac inotrope.

CHAPTER 5: THERAPEUTIC DEVELOPMENT STRATEGIES UTILIZING HEME METABOLISM

5.1. INTRODUCTION

Elevating heme oxygenase-1 (HMOX1) levels in the heart has long been investigated as a potential strategy for the treatment of acute myocardial infarction (AMI), however successful clinical translation has yet to occur [12,68,147]. HMOX1 is the stress-inducible enzyme responsible for the catabolism of free heme—the functional group by which oxygen is transported in proteins such as hemoglobin, myoglobin, and cytochromes involved in ATP production. HMOX1 catabolizes free heme into carbon monoxide, biliverdin, and ferrous iron (sequestered by ferritin heavy chain [FTH1]) [14], which together elicit potent antioxidant, anti-inflammatory, neovascularizing, and vasodilatory effects [14–16,104]. In pre-clinical models of AMI, transgenic cardiac HMOX1 overexpression significantly reduces oxidative damage, inflammation, improves myocardial remodeling, and preserves hemodynamic function [12]. Similar benefits are also observed in cardiomyocytes *in vitro* and *in vivo* with viral HMOX1 overexpression, however these gene expression strategies are not translatable to the clinic [68,104]. These strategies also do not resolve endogenous from exogenous HMOX1 expression or heme regulatory pathway adaptation in myocardial cells.

As a heme surrogate and potent inducer/substrate of HMOX1, hemin has emerged as an alternate strategy for the treatment of AMI by virtue of HMOX1 induction. Hemin is a clinically-approved orphan drug indicated for the treatment of porphyria but has also demonstrated cardioprotection in pre-clinical models of AMI and cardiac ischemia-reperfusion injury [9,17,18,164][Chapter 3: Fig.3.5]. Though dose, timing and molecular mechanisms remain to be fully resolved, hemin therapy has been shown to attenuate mitochondrial damage, oxidative stress, infarct expansion, and preserve hemodynamic function in rat models of cardiac ischemia-reperfusion injury [17,18] and AMI [9,17]. We have also demonstrated that hemin confers cardioprotection in pre-clinical models of AMI [Chapter 3: Fig.3.5]; in mice subjected to permanent left anterior descending coronary artery ligation, i.p. hemin treatment initiated 3h pre-AMI or—surprisingly—2h

post-AMI significantly improves left ventricular fractional shortening, stroke volume, cardiac output, and ejection fraction [Chapter 3: Fig.3.5]. However, additional precision in hemin delivery (i.e. targeted delivery to the infarcted heart) and/or other options capable of shortening time-to-HMOX1-elevation may be required to further improve therapeutic outcomes.

In the present study, we sought to investigate the therapeutic potential of two novel strategies designed for more rapid targeted delivery of HMOX1 to the infarcted heart: the encapsulation of hemin into a nanoparticle shell (Niohemin), and the exogenous delivery of functional HMOX1 using a cell-penetrating peptide (HMOX1-CPP). Cell-penetrating peptides (CPPs) are short amino acid sequences (~10-20 amino acids in length) that enable linked proteins and other cargo—such as nucleic acids, pharmaceuticals, and nanoparticles—to move across cellular membranes without canonical receptor-ligand interactions [273]. Unlike other methods of increasing protein expression, CPPs enable the delivery of functionally active proteins (without the need for pre-emptive steps such as mRNA translation), thereby potentially increasing the speed at which a large increase in HMOX1 activity—and therefore cytoprotection—might be elicited. HMOX1-CPPs have been shown to elicit robust cytoprotection in several pre-clinical models of cardiac ischemic injury [274,275]. In a rat model of heart transplant, *ex vivo* intra-coronary HMOX1-CPP administration 15-18h prior to transplantation significantly reduced tissue apoptosis, total infarct area, and increased the overall 7d graft survival compared to untreated controls and CPP lacking HMOX1 activity [274]. In a rat coronary artery ligation model of ischemic reperfusion injury, HMOX1-CPP significantly reduced infarct size, serum TNF-α (tumor necrosis factor-α), and cardiac levels of NFkB (nuclear factor kappa-B) [275]. Importantly, the level of HMOX1 enzyme must be carefully titrated, as excesses or dysregulation can be associated with dysfunction in the cardiovascular system [107,108]. At present, it remains unclear whether HMOX1-CPP is capable of directly conferring protection to cardiomyocytes or demonstrates superiority over the provision of substrate (heme/hemin) alone at bioequivalent (endogenous) HMOX1 levels.

The delivery of hemin-containing nanoparticles also holds significant promise for the improvement of HMOX1 targeting. Drug-encapsulating nanoparticles offer several

benefits for colloidal drug delivery: for example, their small sizes (10-200nm) and the ability to modify the drug's exterior through customized nanocarrier shells can reduce drug clearance by the liver and kidneys. Nanocarrier shells can also be tailored to improve drug solubility, stability, cellular uptake, or prolong drug circulation times by facilitating the evasion of first-pass metabolism and providing barriers between drugs and external degradation factors—thus increasing drug bioavailability [276]. Further, nanocarrier shells can be designed to control drug delivery to specific regions of the body to increase therapeutic efficacy and reduce off-target effects via active and/or passive targeting. In active targeting, nanocarrier surfaces are modified through decoration with receptor-specific ligands, antibodies, or peptides with affinities for specific cells or tissues to direct drug delivery [277]. These surfaces can also be modified with radiolabels, fluorescent dyes, or contrast agents such as iodine or gold to enable pharmacokinetic visualization *in vivo* [278]. While elegant, active-targeting modifications have substantial regulatory limitations due to formulation complexity. In contrast, passive therapeutic targeting takes advantage of the unique features within the target tissue's microenvironment to achieve precision drug delivery; for instance, nanoparticles designed for susceptibility to sheer stress have been used to target stenotic and atherosclerotic vasculature [279], and pH-sensitive nanoparticles have been used to target the acidic microenvironments of tumors and infarcted myocardium [277,280–282]. As a result, encapsulation of hemin within a nanoparticle shell could increase the drug's bioavailability and accumulation at the site of injury—thus increasing the drug's therapeutic efficacy compared to current hemin formulations.

In the present study, we developed a hemin-encapsulating nanoparticle, called Niohemin. Niohemin is the first hemin-encapsulating nanoparticle of record using the novel niosome-class nanocarrier. Niosomes are nano-sized vesicles used for the delivery of drugs, nucleic acids, and proteins. These vesicles can be uni- or multilamellar in structure, as well as biodegradable [283]. Unlike liposomes which are self-assembled from neutral or charged phospholipids, niosomes require energy for synthesis and are constructed from uncharged non-ionic surfactants (such as polyethylene glycol and Tween) [283]. Due to the amphiphilic materials used for their synthesis, niosomes are also capable of accommodating both hydrophilic and lipophilic drugs [283]. Although

liposomes such as Doxil (liposomal doxorubicin hydrochloride) and Shingrix (liposome-encapsulated recombinant varicella-zoster virus glycoprotein E) have received market approval by the U.S. Food and Drug Administration, niosomes have yet to enter the market for drug-delivery. However, niosomes are generally considered more stable and cost-effective, with superior safety and tolerability profiles than their liposome counterparts [283].

To advance our collective understanding of nano-encapsulated hemin using the novel niosome platform, we begin to characterize Niohemin's physical properties, its therapeutic potential in cardiomyocytes, and its pharmacodynamic effects relative to hemin. Here we perform preliminary proof-of-concept tests investigating whether Niohemin may release hemin in an extracellular acidic micromilieu (mirroring the acidic shift anticipated in the heart's surrounding environment post-AMI). We show for the first time that niosome-encapsulated hemin directly confers cytoprotection to cardiomyotubules against oxidative injury *in vitro* and at a lower concentration than hemin alone, despite equivalent HMOX1 induction. These findings suggest that the pharmacokinetics and/or pharmacodynamics between hemin and hemin released from niosomes differ and that efficacy is not dependent on peak HMOX1 levels alone. We also present preliminary *in vitro* evidence suggesting that Niohemin nanodrug-release kinetics may be affected by an acidified environment. Additionally, we show that HMOX1-CPP confers pre-emptive cytoprotection against oxidative injury in cardiomyotubules compared to bioequivalent amounts of hemin, but that supplementation with hemin substrate together may be therapeutically incompatible. These findings also provide important preliminary insights into the pharmacodynamic differences between HMOX1 enzyme and substrate in cardiomyotubules. Collectively, these findings provide valuable insights into the therapeutic potential (and possible limitations) of two emerging strategies designed to target heme metabolism through HMOX1 induction in the infarcted heart.

5.2 MATERIALS AND METHODS

5.2.1 Study Design

The objective of the present study was to evaluate the therapeutic potential of two experimental approaches targeting heme metabolism: the delivery of hemin within a synthetic nanoparticle shell (Niohemin) and the direct elevation of functional HMOX1 enzyme conjugated to a cell-penetrating peptide.

5.2.2 HMOX1 Cell-Penetrating Peptide (HMOX1-CPP) for Therapy

Soluble human HMOX1-CPP was generously provided as a gift by Dr. Ian Alwayn from the Atlantic Centre for Transplantation Research at Dalhousie University and Department of Transplant Surgery, Universiteit Leiden.

Production of the HMOX1-CPP is described in detail by Venkatachalam *et al.* 2017 [150] and Livingstone 2012 [284]. Briefly, DNA fragments from a template including the enhanced green fluorescent protein (EGFP) gene pEGFP-C1 (Clontech Laboratories) were amplified by polymerase chain reaction (PCR) using forward primers containing the oligonucleotide sequences for cell-penetrating peptide, endonuclease sites *Nhe*I and *Eco*RI, reverse primers containing the sequence for endonuclease site *Hind*III (Table 5.1) and Phusion Hot Start Taq Polymerase (Finnzymes Reagents). EGFP-CPP PCR products were subsequently purified and inserted into pET-28b(+) expression plasmids (Novagen) containing a kanamycin resistance gene, T7 promoter, and 6X histidine tags. DNA fragments from a plasmid pINCY (Open Biosystems) template containing the cDNA sequence for human HO-1 (HMOX1 gene) were also amplified by PCR to produce the sequence for soluble HMOX1 (lacking the last 23 amino acids at the protein's C-terminus; Table 5.1).

EGFP was excised from the pET-28b(+)-EGFP-CPP expression vector using *Eco*RI and *Hind*III endonucleases (Promega) and remaining DNA fragments containing pET-28b(+)-CPP were subsequently purified by gel purification kit (Qiagen). DNA fragments of soluble human HMOX1 were ligated into the place of EGFP to generate an

Table 5.1 Primer sequences of oligonucleotides used for HMOX1-CPP production

Target		Primer Sequence (5'–3')
CPP, endonuclease sites *Nhe*I and *Eco*RI	F1	AAGCTAGCGGCTATGCTCGCGCTGCTGCTCGCCAGGCTCGCGCT GGTGAATTCCGCCACCATGGTGAGCAAGGGCG
	R1	GGCAAGCTTCTTGTACAGCTCGTCCATGCC
Soluble human HMOX1	F1	TAGAATTCATGGAGCGTCCGCAACCCGAC
	R1	AAATAAGCTTTCAAGCCTGGGAGCGGGTGTTGAGTGG

CPP, cell-penetrating peptide; HMOX1, heme oxygenase-1

HMOX1-CPP expression plasmid. HMOX1-CPP expression plasmids were then inserted into *Escherichia coli* (Rosetta [DE3] pLysS strain; Novagen) to produce recombinant HMOX1-CPP protein and plated onto Luria Broth agar (EMD Chemicals) containing 50μg•mL^{-1} kanamycin and 34μg•mL^{-1} chloramphenicol (Sigma). Transformed bacterial pellets were collected and lysed by buffer composed of PBS (Sigma-Aldrich), 20mM imidazole (Sigma-Aldrich), 20mM anhydrous NaH_2PO_4 (Sigma-Aldrich), 500mM NaCl (Sigma-Aldrich), and Complete Mini Protease Inhibitors without EDTA (Roche Diagnostics). Lysates were subsequently sonicated and centrifuged at 20,000rpm for 20min. To isolate target HMOX1-CPP (bookended by 6x histidine tags), supernatant was loaded onto a 1mL HisTrap™ HP column (high histidine-affinity nickel Sepharose column; GE Healthcare Bio-Sciences) and run on gravity feed at a speed of 0.5mL•min^{-1}. Columns were subsequently washed with 50mL lysis buffer and eluted with buffer composed of PBS, 500mM imidazole, 20mM anhydrous NaH_2PO_4, 500mM NaCl, and Complete Mini Protease Inhibitors without EDTA. Elutions were performed at a speed of 0.5mL•min^{-1} and eluate was added to a PD-10 desalting size exclusion chromatography column (GE Healthcare Bio-Sciences). Protein concentrations of desalted HMOX1-CPP solutions were determined by Bradford assay and samples were subsequently stored with glycerol (10% v/v) at -80°C.

HMOX1-CPP enzymatic activity was previously confirmed by bilirubin production assay and independently cross-validated by co-incubation with hemin at Dalhousie Medicine New Brunswick (co-incubation generates a rapid and visible colour change in hemin from black to yellow-green which is quantifiable by absorbance spectroscopy at 670nm).

5.2.3 Cy5.5 for HMOX1-CPP Imaging

Cy5.5-labelled HMOX1-CPP was prepared by adding 1.0mg of HMOX1-CPP to a 1.0mg stock tube of Cy5.5 monofunctional reactive dye (General Electric Cat# Q15408) under sterile conditions. Cy5.5-labelled HMOX1-CPP was then mixed well by pipette, left undisturbed at room temperature for 1h, and stored at -80°C until required.

5.2.4 Cy5.5 Conjugation for Niosome/Niohemin Incorporation

Cy5.5 monofunctional reactive dye for niosome/Niohemin imaging was prepared by adding 192.3ul dimethyl sulfoxide (DMSO; Amresco Cat# N182) to the 1.0mg stock Cy5.5 tube and mixing well by pipette. Cy5.5 was then transferred (in-full) to a separate 1.5ml microcentrifuge tube containing 1.0mg 1-octadecylamine, protected from light and mixed well by pipette. The tube was subsequently incubated at room temperature for 1h, undisturbed, to allow for Cy5.5 conjugation. Following incubation, 40ul Cy5.5-octadecylamine was transferred to a fresh 1.5ml microcentrifuge tube and 500ul PBS was added; the remaining Cy5.5-octadecylamine was stored at 4°C, protected from light.

5.2.5 Nanoparticle-Encapsulated Hemin (Niohemin) Synthesis

Niohemin synthesis was performed over three multi-day sequences: 1) hemin conjugation for drug loading (EDC-coupling reaction), 2) niosome preparation, and 3) gold nanocluster synthesis (Fig.5.1-5.4).

To conjugate hemin for Niohemin synthesis, 2mL DMSO was added to 13.1mg of hemin powder (Sigma Aldrich Cat# 51280) in a 15ml tube, followed by 5mg N, N'-dicyclohexylcarbodiimide ($C_{13}H_{22}N_2$; Alfa Aesar Cat# A10973) and 2.5mg N-hydroxysuccinimide ($C_4H_5NO_3$; Alfa Aesar Cat# A10312) to initiate 1-ethyl-3-(3-dimethylaminopropyl) carbodiimide (EDC) coupling. Next, 5.4mg of 1-octadecylamine ($CH_3[CH_2]_{17}NH_2$; Alfa Aesar Cat# L15458) and 2.25ml DMSO were added to the 15ml tube, vortexed, and centrifuged at 100 rcf for 1min (room temperature) to settle crystals. Without disturbing the crystals, 200ul of octadecylamine-conjugated-hemin supernatant was transferred to a fresh 15mL tube wrapped in aluminum foil (protected from light). Remaining supernatant was stored at -20°C in 200ul aliquots for future use as required.

DMSO was removed from octadecylamine-conjugated hemin by sublimation. An aliquot of 200ul conjugated-hemin (15ml tube) was first wrapped in foil and placed (uncapped) in a styrofoam tube holder. The uncapped tube and holder were transferred to a glass freeze-drier holding unit where a rubber top and vacuum connector were firmly attached. The connector opening was covered in parafilm before storing the holding unit

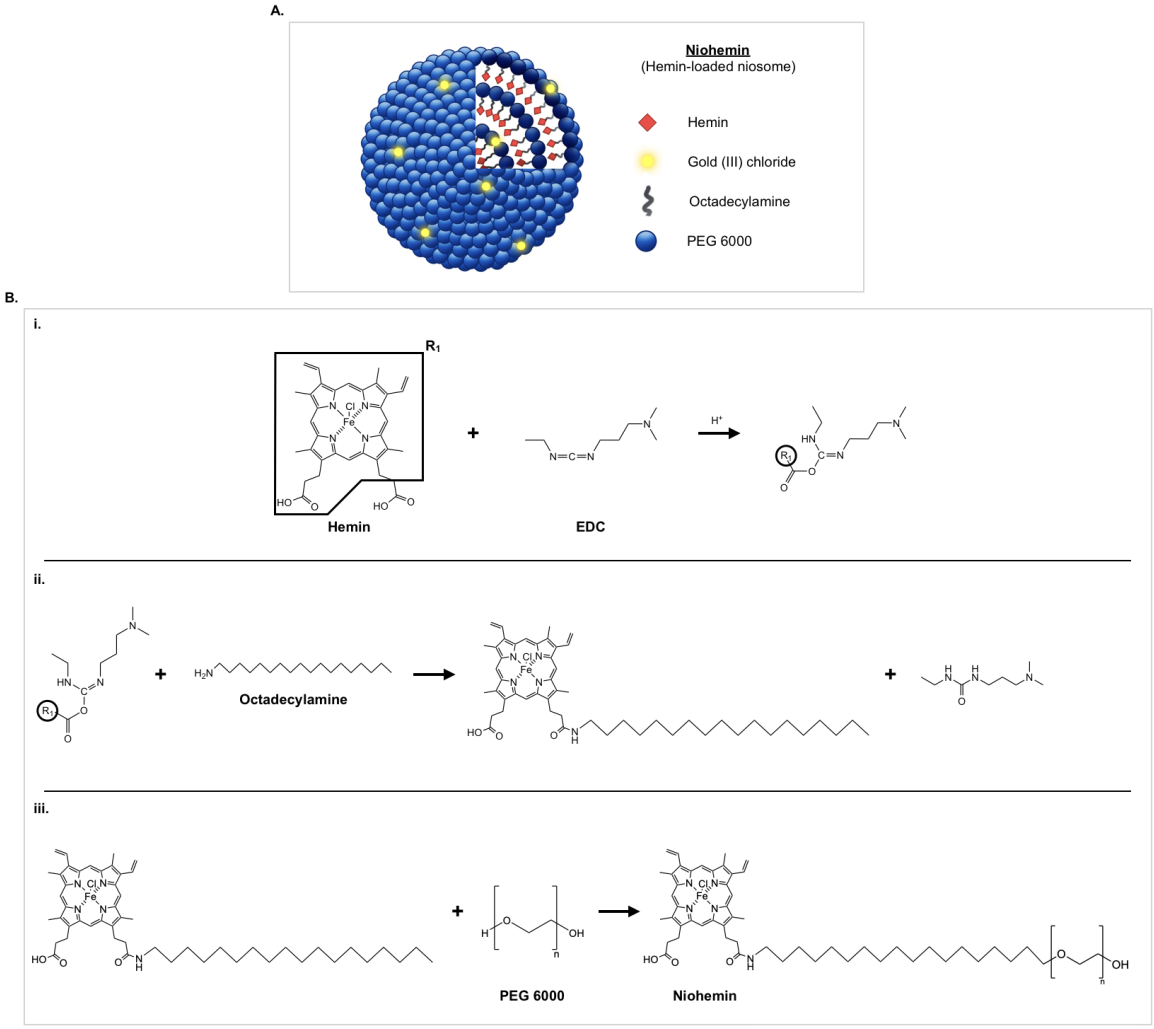

Figure 5.1 Niohemin synthesis. (A) Illustration of niohemin and its constituent components. **(B)** Conjugation of hemin to the hydrophobic octadecylamine tail and PEG 6000 (polyethylene glycol) niosome shell via 1-ethyl-3-(3-dimethylaminopropyl) carbodiimide (EDC)-coupling reaction. **i.** EDC previously generated by the reaction of N, N'-dicyclohexylcarbodiimide and N-hydroxysuccinimide couples to the carboxyl group located along hemin's carbon-13 sidechain, **ii.** permitting conjugation of the carboxyl intermediary to octadecylamine. **iii.** Sonication of lyophilized hemin-octadecylamine with PEG 6000 in Tween-80 incorporates hemin into the synthetic niosome membrane.

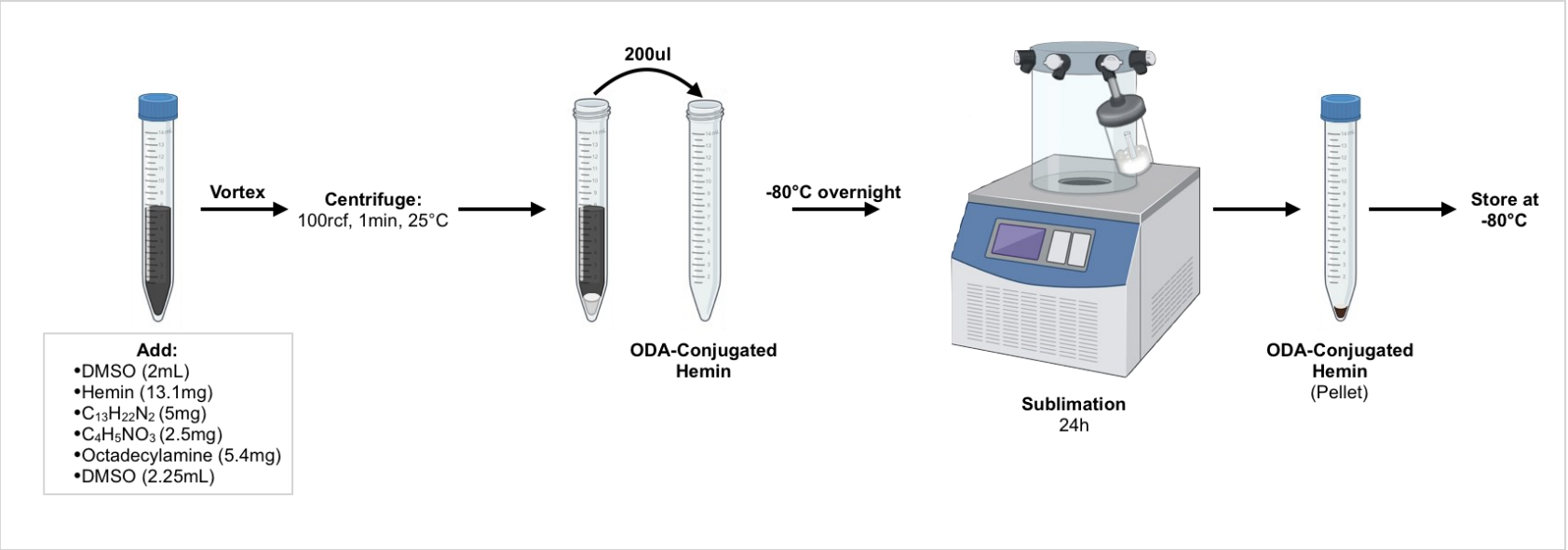

Figure 5.2 Hemin conjugation protocol for Niohemin loading. Illustration of the first step involved in Niohemin synthesis. ($C_{13}H_{22}N$, dicyclohexylcarbodiimide; $C_4H_5NO_3$, hydroxysuccinimide; DMSO, dimethyl sulfoxide; ODA, octadecylamine).

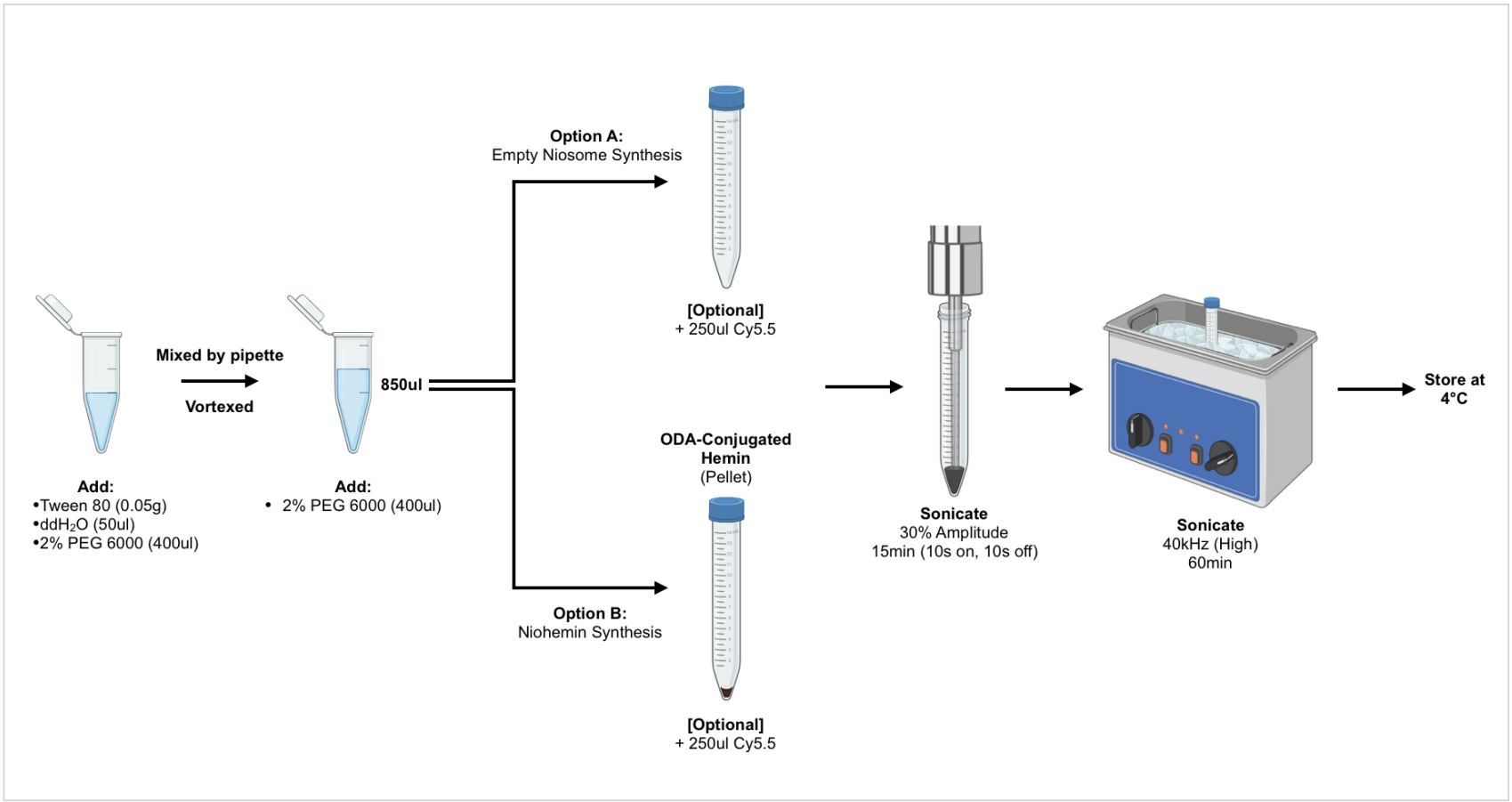

Figure 5.3 Niosome synthesis protocol. Illustration of the second step involved in Niohemin/niosome synthesis: generation of the PEG 6000 shell. (ODA, octadecylamine).

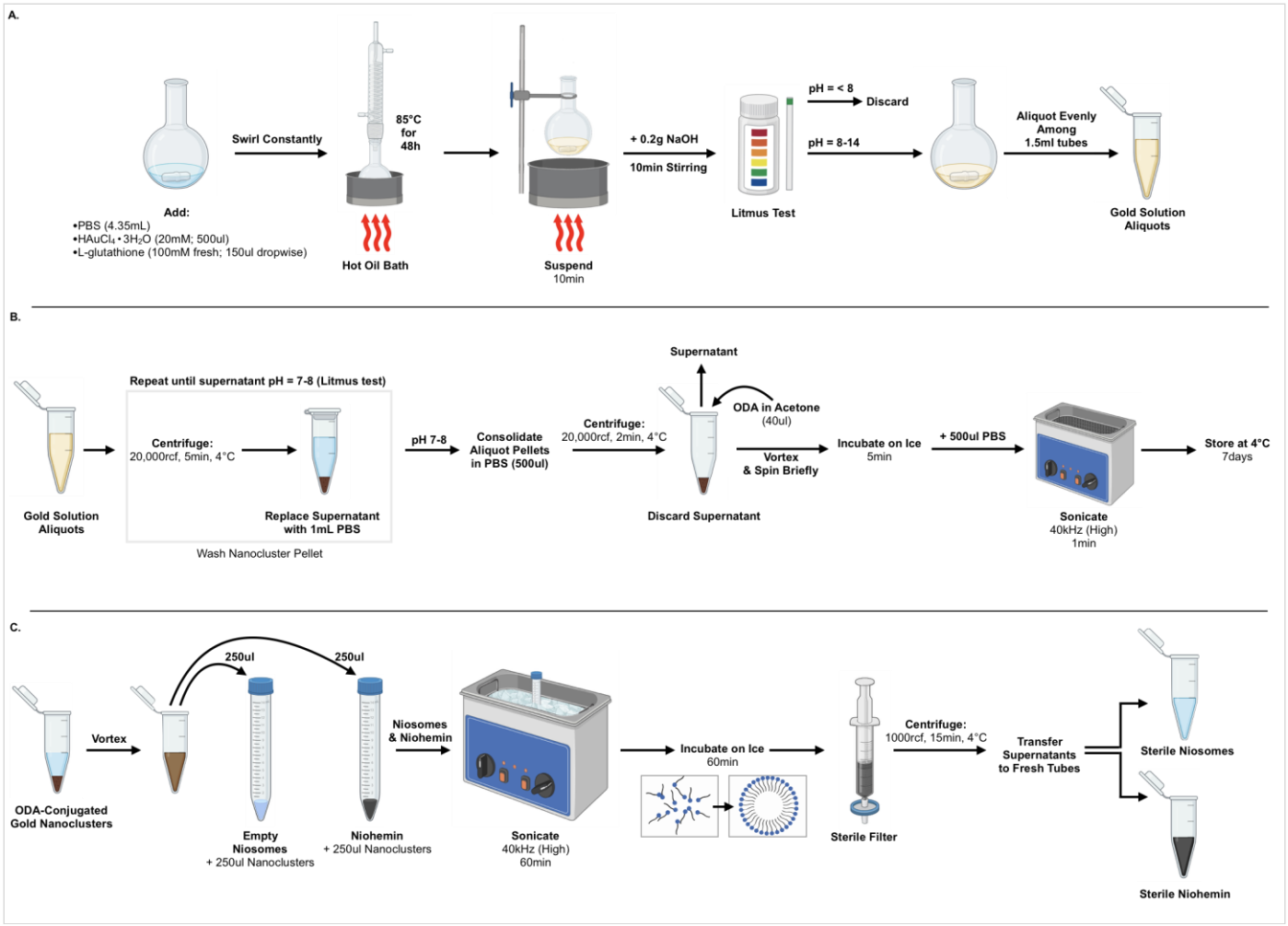

Figure 5.4 Gold nanocluster synthesis and incorporation into niosomes/Niohemin protocol. Illustration of the third and final step involved in Niohemin/niosome synthesis. **(A)** Preparation of gold (III) chloride trihydrate for octadecylamine conjugation. **(B)** Conjugation of gold to octadecylamine. **(C)** Integration of gold nanoclusters into niosomes/Niohemin. (ODA, octadecylamine; PBS, phospho-buffered saline).

overnight at -80°C to prevent falling ice crystal contamination. Following overnight storage at -80°C, the frozen holding unit containing an uncapped octadecylamine-hemin aliquot was rapidly secured to a FreeZone$^{2.5}$ (Labconco) freeze-drying vacuum unit to prevent sample thawing. Aliquots were sublimated for 24h (until DMSO had evaporated and conjugated hemin was converted into a brown solid). Following sublimation, suction pressure was relieved, and hemin was rapidly capped and stored at -80°C. The vacuum unit, cooling coils and hoses were then cleaned thoroughly to prevent damage or digital sensor errors.

To synthesize niosomes for hemin loading, 0.05g Tween 80 (Amresco Cat# M126-1L) was added to a 1.5mL microcentrifuge tube using a pipette tip, followed by 50ul ddH_2O. For niosome layer stability, 400ul of 2% PEG 6000 (polyethylene glycol; EMD Millipore Cat# PX1286L-4; 0.2g in 10mL PBS) was then added. Without disposing of the pipette tip used for PEG 6000 (to minimize the loss of viscous Tween), the tube's contents were mixed vigorously by pipetting, collecting any residual Tween by rinsing down the inner tube walls. The tube was then vortexed for 15s. While retaining the same pipette tip, another 400ul of 2% PEG 6000 was added. Tween 80, ddH_2O, and 2% PEG 6000 were similarly added to a second 1.5mL microcentrifuge tube for the preparation of empty Niosome controls.

Niosomes (850ul) prepared as no-drug (empty) controls were then transferred to a fresh 15ml tube, whereas niosomes (850ul) prepared for hemin loading were added directly to sublimated octadecylamine-hemin (15ml tube; prepared previously) and thereafter referred to as Niohemin. Niosomes and Niohemin synthesized for the purpose of Cy5.5-labelled imaging were similarly prepared, however 250ul PBS-diluted Cy5.5-octadecylamine (described in Section 5.2.4) was also added to each 15ml tube.

Tubes containing niosomes and Niohemin (labelled or unlabelled) were then placed on ice and probe-sonicated for 15min (30% amplitude, pulse: 10s on, 10s off). Tubes were sonicated again for 60min (40kHz, High), protected from light, in a sonic waterbath (Branson 3800) containing 50% ice and 50% water. To incorporate gold nanoclusters additionally into niosomes, nanoclusters were vortexed and 250ul was immediately added to sonicated niosome-containing tubes. Tubes were then sonicated

(40kHz, High) in a sonic ice-water bath for 1h and left undisturbed on ice for 1h minimum to allow for Nio-reformation. Ice was replaced as necessary and niosomes/Niohemin were stored at 4°C, protected from light, until required.

To synthesize gold nanoclusters for niosome/Niohemin integration, 4.35mL of PBS was first added to a 50-100mL round-bottomed flask (RBF). Next, 500ul of 20mM gold (III) chloride trihydrate ($HAuCl_4 \bullet 3H_2O$; Sigma-Aldrich Cat# 520918-1G; 4.7mg into 597ul PBS; vortexed) was added to the RBF (remaining gold [III] chloride trihydrate was stored at 4°C, protected from light). Freshly prepared L-glutathione-reduced (150ul of 100mM; Sigma-Aldrich Cat# 64251-5g; 9.8mg into 318ul PBS; mixed by pipette) was then added drop-wise (while swirling) to the RBF. L-glutathione (an antioxidant) reduces gold for nanocluster formation and—once added to the RBF—must be swirled continuously until indicated. To facilitate swirling, a magnetic stirrer bar (measuring 2cm specifically) was gently added to the RBF (in order to prevent the contents from splashing along the upper inner sides of the flask).

To overcome the catalytic energy barriers involved in gold nanocluster formation, heat was applied to the RBF via oil bath (J-kem Scientific, 50-500mL; set to 85°C). The oil bath was positioned on an active magnetic stirrer plate within a fume hood, underneath a suspended cold-water glass condensing unit. At 30°C oil temperature, the RBF was secured to the condensing unit and lowered to the bottom of the bath, ensuring that the oil level met or surpassed the height of the flask's contents. To prevent the evaporation of PBS from within the flask, a constant flow of pressurized cold water was passed through the condensing unit, ensuring that PBS did not accumulate higher than the flask's neck. Once the oil bath had reached 85°C, the RBF was left for exactly 48h. After 48h, the RBF was removed from the condensing unit and suspended above the hot oil bath for at least 10min (still stirring). Excess oil was then wiped from the flask and a color change (pale yellow) was confirmed in the RBF's contents. The flask's contents were not permitted to cool to room temperature until after the addition of NaOH. One pellet of NaOH (0.20g; EMD Millipore Cat# SX0590-3) was added to the suspended RBF and dissolved by magnetic stirring (5-10min). The pH of the RBF's contents was then measured by Litmus paper (VWR Chemicals BDH® Cat# BDH35309.606) to confirm a pH range between 8-14; if pH was below 8, the flask's contents were discarded

and the protocol was restarted as a critical quality assurance confirmation for gold nanocluster formation. The RBF contents were then divided evenly between 1.5ml tubes and centrifuged at 20,000 rcf for 5min at 4°C to maximize nanocluster precipitation. Successful gold nanocluster formation was indicated by the precipitation of a brown pellet. If pellets were absent, the protocol was restarted from the beginning as a critical quality assurance confirmation. Tubes containing pellets could subsequently be stored at 4°C overnight—protected from light exposure—as an optional stopping point before proceeding.

To reduce the pH of gold nanocluster solution to biologically appropriate levels, tubes were first removed from 4°C and centrifuged at 10,000 rcf for 1min. The supernatant (yellow-brown) was subsequently discarded and replaced by 1mL PBS (per tube). Insoluble gold nanoclusters were then mixed by pipette and centrifuged at 20,000 rcf for 2min at 4°C. The supernatant was once again discarded, replaced by 1mL PBS, and mixed by pipette. Nanocluster washing by PBS was repeated until supernatant pH measured between 7-8 on Litmus paper. Once at pH 7-8, all supernatants were discarded and nanocluster pellets were consolidated into a total of 500ul PBS.

In a fresh 1.5ml microcentrifuge tube, 2.6mg of 1-octadeyclamine and 500ul HPLC-grade acetone were added and vortexed until dissolved. The tube containing gold nanoclusters in PBS was then centrifuged at 20,000 rcf for 2min at 4°C. The supernatant was discarded and immediately replaced with 40ul of 1-octadecylamine solution; remaining 1-octadecylamine solution was discarded. Nanoclusters were then vortexed, briefly spun down by tabletop mini-centrifuge (until no solution remained on the inner tube wall), and placed on ice for 5min before adding an additional 500ul PBS. Nanoclusters were placed in the sonic water bath on High (40kHz) for 1min, forming a brown and slightly viscous solution. Octadecylamine-conjugated gold nanoclusters were then stored at 4°C, protected from light, for 7 days.

Gold nanoclusters were incorporated into niosomes/Niohemin for the purpose of future *in vivo* imaging and pharmacokinetic studies by magnetic resonance imaging or Raman microscopic analysis. To incorporate gold nanoclusters into niosomes/Niohemin, nanoclusters were vortexed and 250ul was immediately added to previously-sonicated

Nio-containing tubes. Tubes were then sonicated (40kHz, high) in a sonic ice-water bath for 1h and left undisturbed on ice for 1h minimum to allow for Nio-reformation.

To prepare empty niosomes/Niohemin for dynamic light scattering (DLS), spectral quantification, and cell culture use, the following steps were performed in a biosafety cabinet under sterile conditions. Niosomes and Niohemin were transferred to 10mL syringes and sterile-filtered (0.2um; Thermo Scientific Cat# 723-9920; using separate filters for each) into new 1.5ml microcentrifuge tubes; tubes were then centrifuged at 1000 rcf for 15min at 4°C to pellet unreacted hemin/gold. Under sterile conditions, supernatants were subsequently transferred to new 1.5ml microcentrifuge tubes on ice, protected from light, before proceeding immediately to DLS. Sterile niosomes and Niohemin were stored thereafter at 4°C.

5.2.6 Dynamic Light Scattering (DLS)

Nanoparticle size and acute stability were measured by DLS (Zetasizer Nano ZSP, Malvern Instruments). To a fresh microcuvette (Malvern Instruments Cat# ZEN0040; 173° backscatter), 80ul of sterile-filtered PBS (0.2um) was added and verified for the absence of air bubbles. Nanoparticles/samples were gently mixed by pipette before transferring 1ul to the microcuvette containing PBS. Microcuvette contents were mixed gently by pipetting immediately before analysis.

Microcuvettes were inserted into the Zetasizer Nano ZSP and settings were selected as: polystyrene latex/PEG (refractive index = 1.590) for the measured material, water as the dispersant, and the temperature was set to 25°C. The initial equilibrium time was set to 60s to ensure that DLS was not residually impacted by transportation to the instrument. Three independent readings (each consisting of 33 internal replicates) were obtained—in succession—per sample. Equilibrium time between readings was set to 30s to detect potential particle aggregation over time.

5.2.7 Spectral Quantification of Hemin Loading

The quantity of hemin encapsulated within niosomes (Niohemin) was determined by spectral absorption scanning (Synergy H4 Hybrid Reader, Biotek; 200-800nm wavelength range). Briefly, the optical density of Niohemin (100ul; 10ul Niohemin diluted into 90ul PBS) was measured and compared against hemin standards (2.5-500uM), empty niosomes, and vehicle controls (DMSO, PBS) at 390nm. Hemin content was then calculated using the following equation:

$$\frac{Absorbance\ of\ Hemin\ at\ 390nm}{Absorbance\ of\ 10\%\ v/v\ Niohemin\ at\ 390nm} = \frac{[Hemin]}{[10\%\ v/v\ Niohemin]}$$

Example:

$$\frac{0.690\ Optical\ Density}{2.239\ Optical\ Density} = \frac{50uMHemin}{[10\%\ v/v\ Niohemin]}$$

$$\downarrow 3.0862 = \frac{50uMHemin}{[10\%\ v/v\ Niohemin]}$$

$$\downarrow \frac{50uMHemin}{3.0862} = [10\%\ v/v\ Niohemin] = 162.011uM$$

$$\downarrow Niohemin = 162.011uM \times 10$$

$$= 1620uM\ hemin\ equivalence$$

5.2.8 Hemin Formulation for Cell Culture

Hemin stock solution [5mM] was prepared by dissolving hemin (Sigma Aldrich Cat# 51280) in dimethyl sulfoxide (DMSO; Amresco Cat# N182) and by sonicating for 60min. DMSO vehicle controls did not exceed 0.1% in the final cell culture media

volume. Hemin stocks in DMSO were stored at 4°C (protected from light) for up to 4 months and were sonicated for 15min before each use.

5.2.9 Cell Culture

H9C2 left ventricular cardiomyoblasts (American Type Culture Collection Cat# CRL-1446) were expanded from frozen stocks in Dulbecco's Modified Eagle Medium-High Glucose (DMEM-HG; Gibco Cat# 11965-092) supplemented with 10% fetal bovine serum (FBS; Seradigm Cat# 1400-500). Cells were seeded to achieve ~80% next-day confluency at either $1.50x10^4$ cells•well^{-1} for cell viability assays or $2x10^5$ cells•35mm plate^{-1} for immunoblotting and immunocytochemistry. Cells were subsequently differentiated by FBS deprivation for 5-6 days and media was renewed as indicated (Figures 5.8, 5.14). Cells were maintained at 37ºC in a humidified atmosphere of 95%:5% air/CO_2. All experiments were initiated at least one passage after recovery from cryogenic storage and cells did not exceed 19 passages.

To investigate the effects of pH on Niohemin kinetics *in vitro*, differentiated H9C2 cardiomyotubules were exposed to pH-modified Earle's Balanced Salt Solution (EBSS) media. pH was modified using HCl under aseptic conditions, and was measured both pre- and post-cell exposure (although no differences were observed).

Differentiated H9C2 cells were harvested by rinsing the cells with cold 1× PBS and scraping the cells in fresh NP-40-based lysis buffer. Samples were set on ice for 30 minutes before sonicating for 10 seconds (20kHz, 30% amplitude). Total protein concentrations were quantified by BCA assay.

5.2.10 Cell Viability Assay

H9C2 cells were seeded in a 96-well plate containing 100ul media•well^{-1} and differentiated as previously described. H_2O_2 (Sigma-Aldrich Cat# 323381) was freshly diluted to 0.1M in sterile 1× PBS. N-Acetyl-L-Cysteine (NAC; Amresco Cat# 0108-25G) was prepared as a 3mM stock in sterile 1× PBS (stored at 4°C for up to 3 months). Hemin, vehicle (DMSO), Niohemin, empty Niosomes, HMOX1-CPP, H_2O_2, and NAC

were further diluted in media immediately before exposure to cells. Importantly, hemin and HMOX1-CPP were kept separate until added to cells (to prevent *ex vivo* heme catabolism). Cell viability was measured using resazurin sodium salt ($0.3 mg \cdot ml^{-1}$; Thermo Scientific Cat# R12204). Cells were incubated with resazurin (10% volume) at 37ºC for 3h. Absorbance was measured using a Synergy H4 Hybrid Reader at 560/590nm excitation/emission. Cell viability was determined by subtracting the absorbance of media-only controls from treated cells and normalizing values to the mean survival of untreated controls.

5.2.11 Immunocytochemistry

Hoechst (19.98uM, 5min; Thermo Scientific Cat# 62249) or DAPI (EverBrite™ medium with DAPI; 30min; Biotium Cat# 23002), phalloidin-488 (164nM, 60min; Invitrogen Cat# A12379), and Lysotracker Green (75nM, 30min; Invitrogen Cat# L7526) were used to stain cells for immunocytochemistry. Cells were plated on 35mm glass-bottom dishes (Ibidi Cat#81158) and differentiated as previously described. Media was aspirated and cells were washed gently with 1ml ice-cold PBS, which was then aspirated and immediately replaced with 2% paraformaldehyde. Briefly, 2% paraformaldehyde was prepared by adding 2g paraformaldehyde (EMD Millipore Cat# PX0055-3) to heated ddH_2O (66.6mL; 60°C). NaOH (2N) was then added dropwise until the solution became clear and colorless. The solution was then removed from heat and topped to 100mL with PBS (33.3mL), before reducing the pH to 7.2 with HCl. Cells were fixed in 2% paraformaldehyde for 12min and were washed gently with 1× tris-buffered saline before aspiration. Cells used in conjunction with live-cell dyes (i.e. Lysotracker) were not fixed prior to staining and were instead washed—and imaged—in PBS (1mL).

Epifluorescent images were obtained by Zeiss Observer.Z1 (equipped with Apotome.2, X-Cite 120 LED, and Axiocam 506 mono). Super-resolution images were obtained by Zeiss LSM 900 Axio Observer (equipped with Airyscan 2). Fixed cells were coated in EverBrite antifade medium (Biotium Cat# 23001) prior to imaging.

5.2.12 Western Blotting

Tissue lysates were boiled at 99ºC for 5min in 4× Laemmli Buffer with DTT. Samples (8-25ug•lane^{-1}) and ladder (Bio-Rad Cat# 1610375EDU) were separated via SDS–polyacrylamide gel electrophoresis (Bio-Rad Cat# 5671095) and transferred to nitrocellulose membrane (Bio-Rad Cat#1620112) for immunoblotting. To ensure equal protein loading and uniform protein transfer, membranes were reversibly stained with MemCode (Thermo Fisher Scientific Cat# 24580) before immunoblotting. Membranes were then blocked in 5% milk for 45min and incubated in primary antibody (1:1000 in 1% skim-milk in tris-buffered-saline-tween [TBS-T] with sodium azide) at 4ºC overnight. Membranes were washed in 1× TBS-T and subsequently incubated in either goat anti-rabbit (Santa Cruz Biotechnology Cat# 2054) or goat anti-mouse (Santa Cruz Biotechnology Cat# 2055) horseradish peroxidase-conjugated secondary antibody (1:2000 in 5% milk for 2h). Signal was detected by enhanced chemiluminescence (Thermo Fisher Scientific Cat# 34076) and digital imaging (Bio-Rad Cat# 1708280). Densitometric quantification was performed using Image Lab software (Bio-Rad) and values were obtained by measuring the target band relative to the respective total lane protein.

5.2.13 Statistics

Values presented are expressed as mean ± SD. Graphical and statistical analyses were completed using GraphPad (Prism 6, GraphPad Software Inc.). For comparison between three or more groups, a One-Way Analysis of Variance (ANOVA) and Tukey's multiple comparisons test were used. Kruskall-Wallis and Dunn's multiple comparisons tests were performed for non-parametric data. Significance was set at $P<0.05$ ($^{*}P < 0.05$, $^{**}P < 0.01$, $^{***}P<0.001$; $^{****}P<0.0001$). Outliers were identified by ROUT method (Q=1%).

5.3. RESULTS

5.3.1 HMOX1-CPP localizes to the cytoplasm of cardiomyotubules *in vitro*

To confirm HMOX1-CPP was capable of cardiomyocyte entry/internalization, H9C2 cells were differentiated into cardiomyotubules by serum deprivation and exposed to 50ug•mL^{-1} Cy5.5-conjugated HMOX1-CPP for 24h before imaging (Fig.5.5). Epifluorescent imaging revealed widespread HMOX1-CPP localization to the cytoplasm region of H9C2 cells (Fig.5.5A), which was further corroborated by super-resolution imaging (Fig.5.5B). Super-resolution imaging also revealed HMOX1-CPP internalization, with Cy.5.5-HMOX1-CPP appearing below the nuclear—and within the F-actin—planes of focus (Fig.5.5B, v).

5.3.2 HMOX1-CPP exposure *in vitro* demonstrates increased HMOX1 levels, without concomitant induction of FTH1 at bioequivalent hemin doses

To examine the dose-dependent effects of HMOX1-CPP on cardiomyocyte HMOX1 and FTH1 levels, differentiated H9C2 cardiomyotubules were exposed to 0, 2.5, 25, or 100ug•mL^{-1} HMOX1-CPP for 24h (Fig.5.6). HMOX1 levels were significantly increased in cardiomyotubules exposed to 25 and 100ug•mL^{-1} HMOX1-CPP (Fig.5.6A), however FTH1 levels remained unchanged (Fig.5.6B).

To compare the effects of HMOX1 enzyme on FTH1 and HMOX1 to those of its substrate at bioequivalent doses, differentiated H9C2 cardiomyotubules were exposed to 2.5, 25, or 50ug•mL^{-1} HMOX1-CPP, 0.5, 1, or 2.5uM hemin, or vehicle (volume equivalent to 2.5uM hemin) for 24h (Fig.5.7). HMOX1 levels were equally elevated by exposure to 25ug•mL^{-1} HMOX1-CPP as they were by exposure to 2.5uM hemin; thus, HMOX1-CPP and hemin were deemed bioequivalent at these concentrations and timepoint. FTH1 in differentiated H9C2 cells was also elevated with hemin exposure but remained unchanged at bioequivalent (and higher) concentrations of HMOX1-CPP.

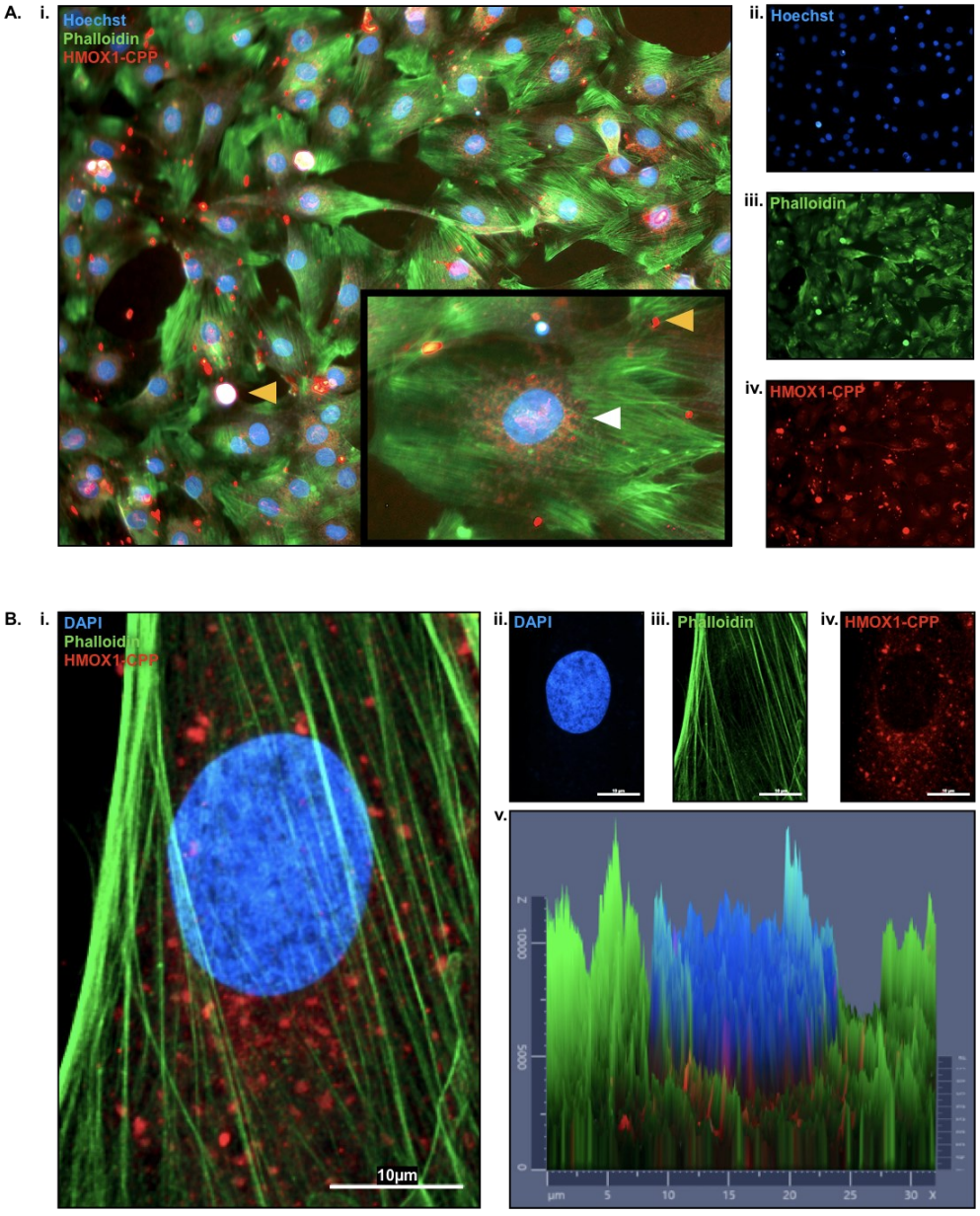

Figure 5.5 HMOX1-CPP localizes to the cytoplasm of differentiated H9C2 cardiomyotubules. (A) Differentiated H9C2 cardiomyotubules were administered Cy5.5-conjugated HMOX1-CPP (50ug•mL^{-1} for 24h), fixed, and imaged by epifluorescent microscopy. **i.** Composite image; inset: Magnified view of composite H9C2 cell containing Cy5.5-conjugated HMOX1-CPP (white arrowhead). External HMOX1-CPP aggregates are denoted by yellow arrowheads. **ii.** Hoechst (nuclei). **iii.** Phalloidin (F-actin). **iv.** Cy5.5. **(B)** Single-cell imaging by super-resolution microscopy. Cells were washed with an additional 2mL of PBS to reduce external HMOX1-CPP adherence. **i.** Composite image. **ii.** DAPI. **iii.** Phalloidin. **iv.** Cy5.5. **v.** 2.5-dimensionsal histogram of DAPI (blue), phalloidin (green), and Cy5.5-conjugated HMOX1-CPP localization by airyscan imaging.

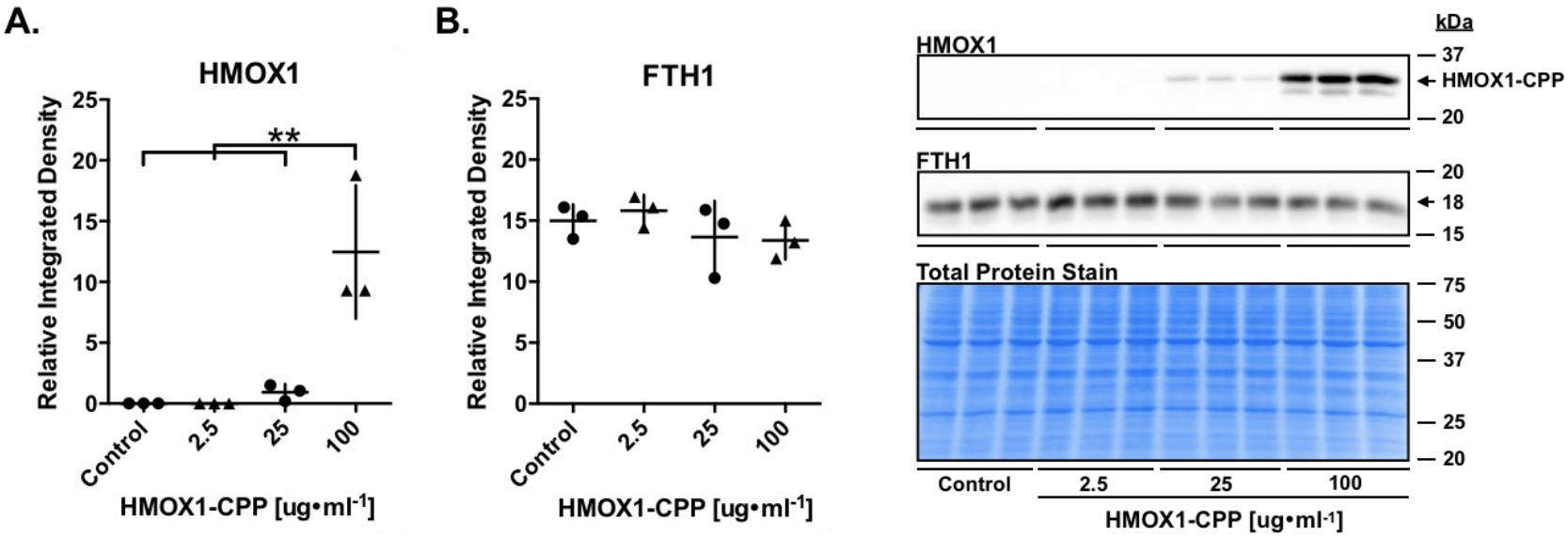

Figure 5.6 Pharmacodynamic characterization of HMOX1-CPP exposure *in vitro* demonstrates increased HMOX1 without concomitant induction of FTH1. Dose-dependent effects of 24h HMOX1-CPP exposure on heme regulatory enzyme expression in differentiated H9C2 cardiomyotubules. Densitometric analysis of **(A)** HMOX1 and **(B)** FTH1 with representative Western Blots and total protein stain.

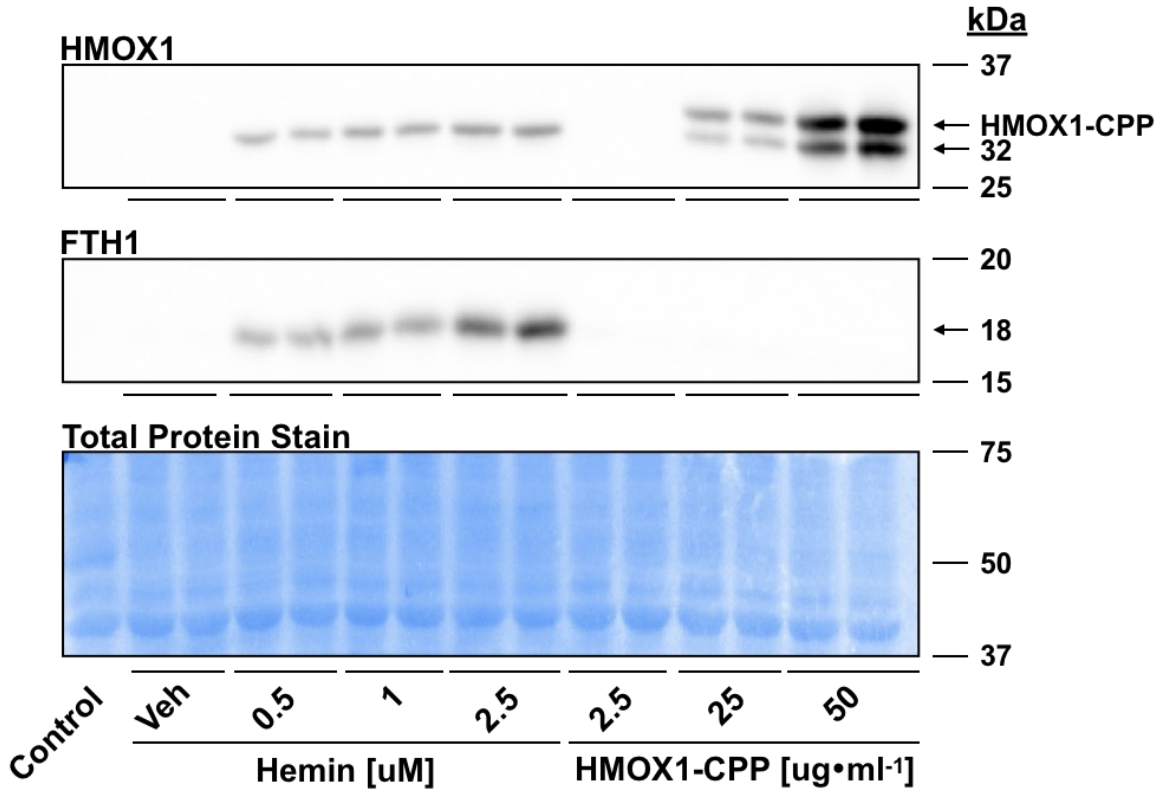

Figure 5.7 Hemin and bioequivalent HMOX1-CPP exert differential effects on heme regulatory enzyme expression *in vitro*. Representative Western Blots of HMOX1 and FTH1 protein expression in differentiated H9C2 cells exposed to hemin (0.5, 1, 2.5uM), corresponding vehicle (2.5uM DMSO), or HMOX1-CPP (2.5, 25, 50ug•mL^{-1}) for 24h. At 2.5uM hemin bioequivalency, HMOX1-CPP (25ug•mL^{-1}) did not result in increased FTH1 expression.

5.3.3 HMOX1-CPP treatment confers differential cytoprotection against oxidative injury compared to hemin in cardiomyotubules

To investigate whether HMOX1 enzyme was capable of protecting cardiomyocytes directly to the same degree as that induced by its native substrate, differentiated H9C2 cardiomyotubules were treated with HMOX1-CPP (2.5, 25, 50, or 100ug•mL^{-1}), hemin (1, 2.5, or 5uM), vehicle, or 300uM N-acetyl cysteine (NAC) antioxidant reference control, beginning 4h pre- or simultaneously with H_2O_2 (880uM, 24h)-mediated injury (Fig.5.8). Cell survival was significantly increased with 100ug•mL^{-1} HMOX1-CPP when administered 4h pre-H_2O_2 (Fig.5.8A, ii). Comparatively, pre-treatment with hemin or NAC did not attenuate H_2O_2-mediated cell death (vehicle administration did not affect cell viability).

Treatment with hemin (or vehicle) initiated at the same time as H_2O_2-mediated injury also failed to improve cell survival (Fig.5.8B, ii). In contrast, survival was significantly increased with 100ug•mL^{-1} HMOX1-CPP or NAC when administered simultaneously with H_2O_2. Cell survival was also significantly increased with 25ug•mL^{-1} HMOX1-CCP, although no improvement was observed with bioequivalent hemin (2.5uM). Although HMOX1-CPP (25ug•mL^{-1}) and hemin (2.5uM) elevated HMOX1 to similar levels after 24h (Fig.5.7), these data suggest that HMOX1-CPP-mediated cytoprotection may be attributed to other pharmacodynamic/pharmacokinetic mechanisms as well.

Collectively, these data show that HMOX1-CPP initiates cytoprotection against oxidative injury earlier than hemin. These data also suggest that HMOX1-CPP-mediated cytoprotection could be attributed to other pharmacodynamic/pharmacokinetic mechanisms (such as faster elevation of HMOX1 levels), as similar HMOX1 levels between HMOX1-CPP and hemin were not equal to similar cytoprotection.

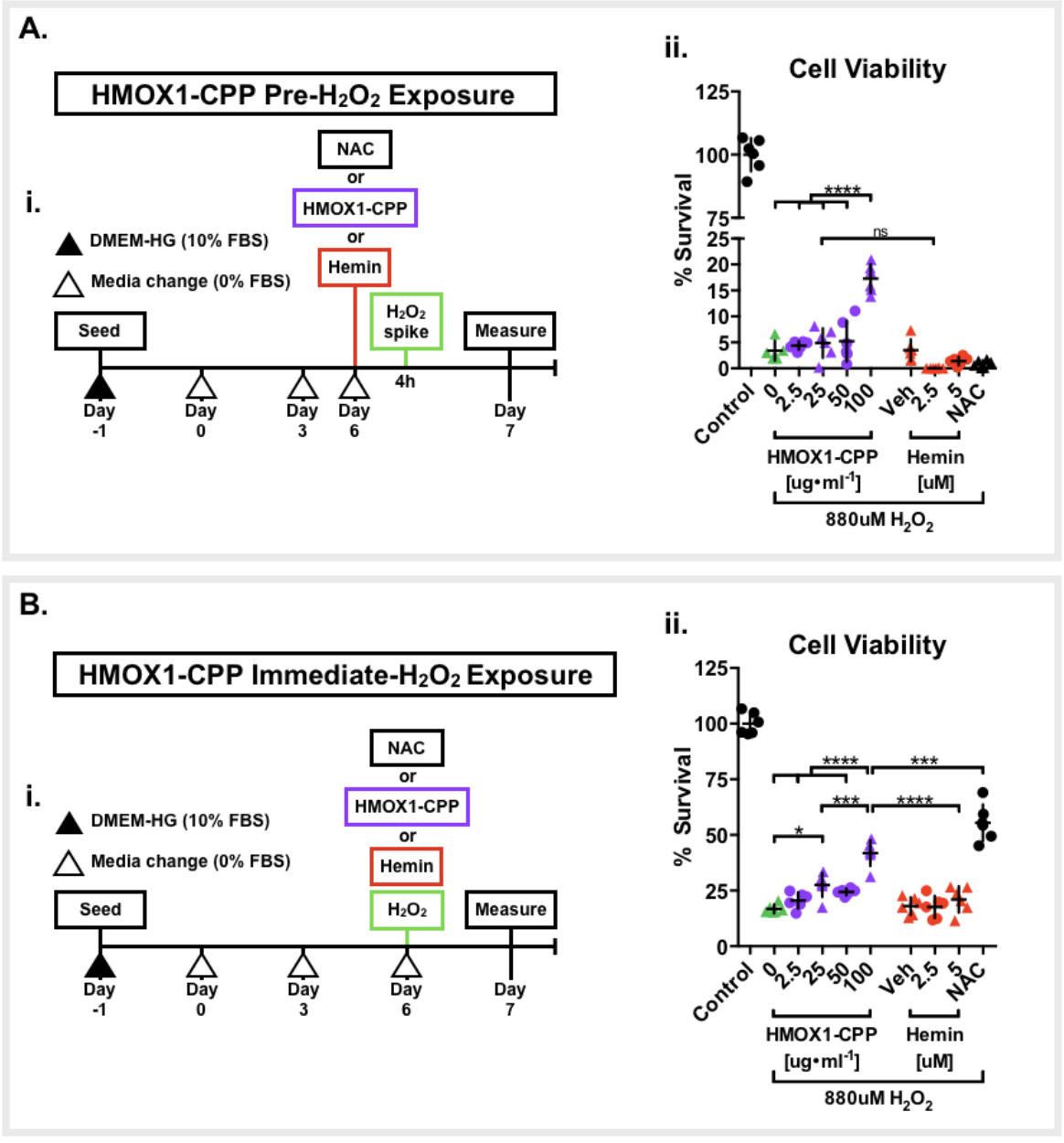

Figure 5.8 HMOX1-CPP treatment confers differential cytoprotection to H9C2 cardiomyotubules compared to bioequivalent hemin. (A) Dose-dependent effects of HMOX1-CPP and hemin treatment pre-H_2O_2 on differentiated H9C2 cardiomyotubule viability. **i.** Outline of H9C2 differentiation and treatment 4h pre-H_2O_2 exposure (880uM, 24h). **ii.** Resazurin cell viability assay in H9C2 cells treated with HMOX1-CPP (2.5, 25, 50, or 100ug•mL^{-1}), hemin (2.5uM or 5uM), or 300uM N-Acetyl-Cysteine (NAC), 4h pre-H_2O_2 exposure (880uM, 24h). **(B)** Dose-dependent effects of HMOX1-CPP and hemin treatment administered simultaneously with H_2O_2 on differentiated H9C2 cardiomyotubule viability. **i.** Outline of H9C2 differentiation and treatment with simultaneous H_2O_2 exposure (880uM, 24h). **ii.** Resazurin cell viability assay in H9C2 cells treated with HMOX1-CPP (2.5, 25, 50, or 100ug•mL^{-1}), hemin (2.5uM or 5uM), or 300uM N-Acetyl-Cysteine (NAC), with H_2O_2 exposure (880uM, 24h).

5.3.4 Simultaneous exposure to HMOX1-CPP and hemin at individually therapeutic concentrations decreases overall cell survival

To examine the dose-dependent effects of HMOX1 enzyme on survival and compare them to those of its substrate at independently therapeutic doses [Chapter 3: Fig.3.4A, iii], differentiated H9C2 cardiomyotubules were exposed to 2.5, 25, 100, or 200ug•mL^{-1} HMOX1-CPP, 5uM hemin, or vehicle for 24h (Fig.5.9). Survival was significantly reduced in cells exposed to a supra-therapeutic dose of 200ug•mL^{-1} HMOX1-CPP, and when exposed to 5uM hemin (vehicle administration did not affect cell viability). Thus, HMOX1-CPP demonstrates less toxicity than hemin in healthy cardiomyotubules at therapeutic concentrations.

To investigate the effects of adding HMOX1 enzyme to a heme-replete environment (such as that observed in the peri-infarct heart, Chapter 3: Fig.3.2), differentiated H9C2 cardiomyotubules were simultaneously administered 5uM hemin and increasing concentrations of HMOX1-CPP (2.5, 25, 100, or 200ug•mL^{-1}) for 24h (Fig.5.9). Cell death caused by 5uM hemin alone was significantly attenuated by simultaneous exposure to 2.5ug•mL^{-1} HMOX1-CPP. However, 100ug•mL^{-1} HMOX1-CPP exacerbated cell death and worsened survival beyond that of either enzyme or substrate on its own. Collectively, these data show that simultaneous exposure to HMOX1-CPP and hemin at individually therapeutic conditions decreases overall cell survival. This could limit the practical application of HMOX1-CPP as a pharmacological intervention for AMI as heme content is also increased in the peri-infarct heart [Chapter 3: Fig.3.2]. Additionally, it raises uncertainty as to the safety of using HMOX1-CPP as an antidote to heme-overload, which requires further exploration.

5.3.5 Characterization of Niohemin and its physical properties

Prior to evaluating the therapeutic potential of niosome-encapsulated hemin, Niohemin was first subjected to physicochemical analysis by spectral scanning and Dynamic Light Scattering (Fig.5.10). Spectral scanning was used to quantify hemin within the niosome (Fig. 5.10A). Hemin produces a characteristic absorption spectral

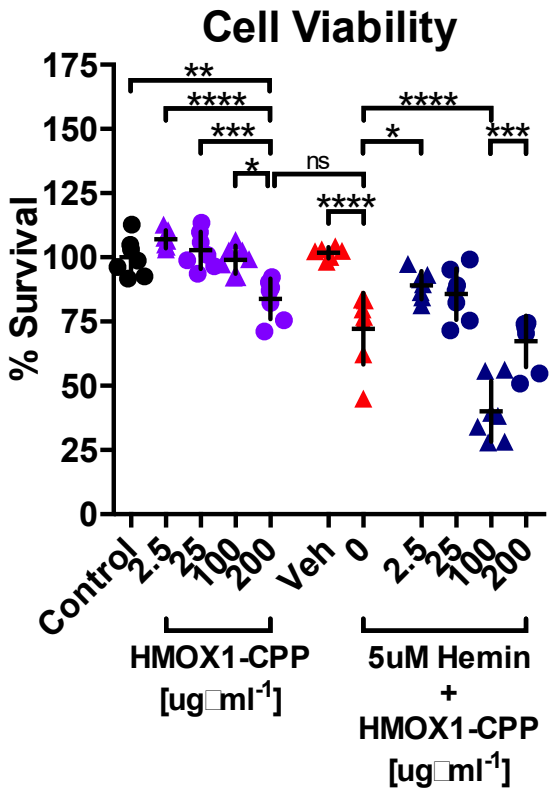

Figure 5.9 Simultaneous exposure to HMOX1-CPP and hemin at individually therapeutic concentrations decreases overall cell survival. Resazurin cell viability assay in differentiated H9C2 cells administered HMOX1-CPP (2.5, 25, 100, or 200ug•mL^{-1}), 5uM hemin, or 5uM hemin with HMOX1-CPP (2.5, 25, 100, or 200ug•mL^{-1}) for 24h.

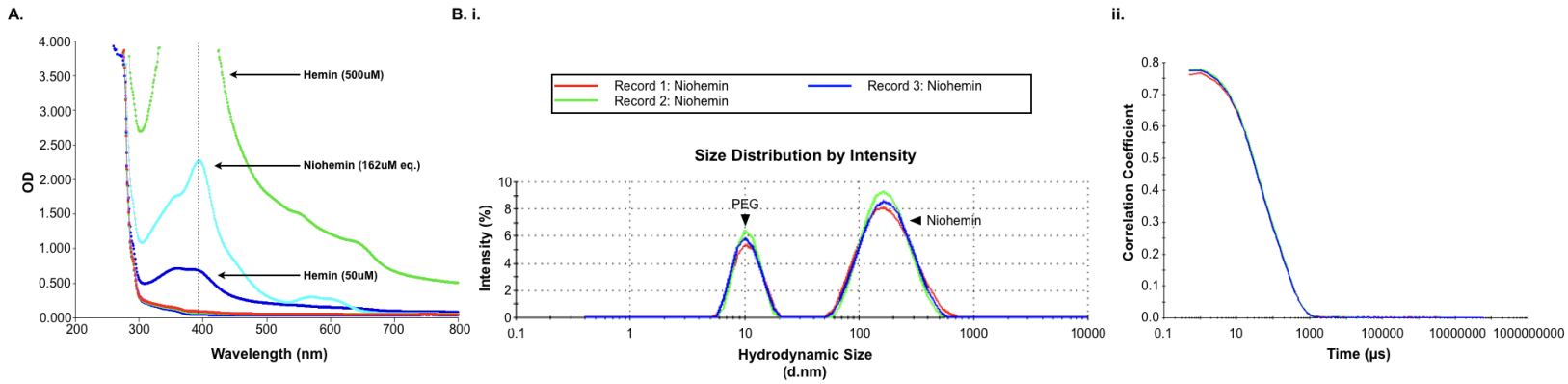

Figure 5.10 Characterization of Niohemin and its physical properties. (A) Representative absorption spectra for the quantification of hemin loading. The optical density of Niohemin (10% v/v in PBS) was measured and compared against hemin standards (2.5-500uM) at 390nm (dashed line) to calculate hemin content (162uM e.q.). Empty niosomes (162uM e.q. by volume), 2.5-5uM hemin, and vehicle controls (DMSO, PBS) were similarly measured for comparison (all optical densities below 0.250). **(B)** Measurement of Niohemin's hydrodynamic diameter (d.nm) by Dynamic Light Scattering. **i.** Representative size distribution of Niohemin (194.3d.nm, 73.7% intensity, PdI=1.000). **ii.** Correlogram of Niohemin measurements (records 1-3) over time.

peak at 390nm, thus, hemin loading within niosomes was obtained by comparing the optical density of diluted Niohemin to hemin standards (2.5, 5, 50, 500uM) at 390nm. Niohemin was calculated to have a spectral equivalency to 162uM hemin (hereafter referred to as a hemin-$[uM]_{eq}$). The optical densities of empty niosomes (scanned at an equivalent volume to Niohemin), 2.5-5uM hemin, and vehicle controls (DMSO, PBS) were similarly measured, however all demonstrated optical densities below 0.250.

Niohemin size was determined by Dynamic Light Scattering (Fig.5.10B). Also known as photon correlation spectroscopy, Dynamic Light Scattering measures Brownian motion (i.e. the random movement of suspended nanoparticles and macromolecules resulting from collisions between particles and their surrounding solvent) and relates this motion to particle size. As particle sizes decrease, Brownian motion (measured by fluctuations in light scattering patterns and variation in auto-correlation over time) is increased since smaller particles diffuse more rapidly through solvent than their larger counterparts. Dynamic Light Scattering revealed a heterogenous (PdI > 0.2) nanoparticle population within the Niohemin sample, composed of two distinct particle size populations/peaks (Fig.5.10.B,i). Niohemin (the principle group) encompassed 73.7% of the total particle population, whereas PEG6000 (the second group; ~10d.nm) constituted the remainder, indicating that future optimization of Niohemin preparation to good clinical practice standards may require a reduction in PEG6000 or size-exclusion chromatography purification. Niohemin size (hydrodynamic diameter) was determined as 194.3d.nm, indicating that niosome-encapuled hemin is classifiable as a nano-sized particle. Both Niohemin and PEG6000 size remained stable over time (Fig.5.10.B,i and ii), indicating that nanoparticles did not aggregate.

Empty niosomes were similarly investigated (Fig.5.11A). Niosomes encompassed 85.5% of the total particle population size (PdI = 0.683), measured 244.0d.nm, and remained size-stable over Dynamic Light Scattering recording. Like Niohemin, a ~10d.nm PEG6000 peak was also observed within the empty niosome sample; the PEG6000 peak was identified by measuring the size distribution of raw PEG6000 in PBS (Fig.5.11B; 15.54d.nm). These data establish that empty niosomes serve as appropriate nanocarrier controls alongside hemin-vehicle and hemin standard references.

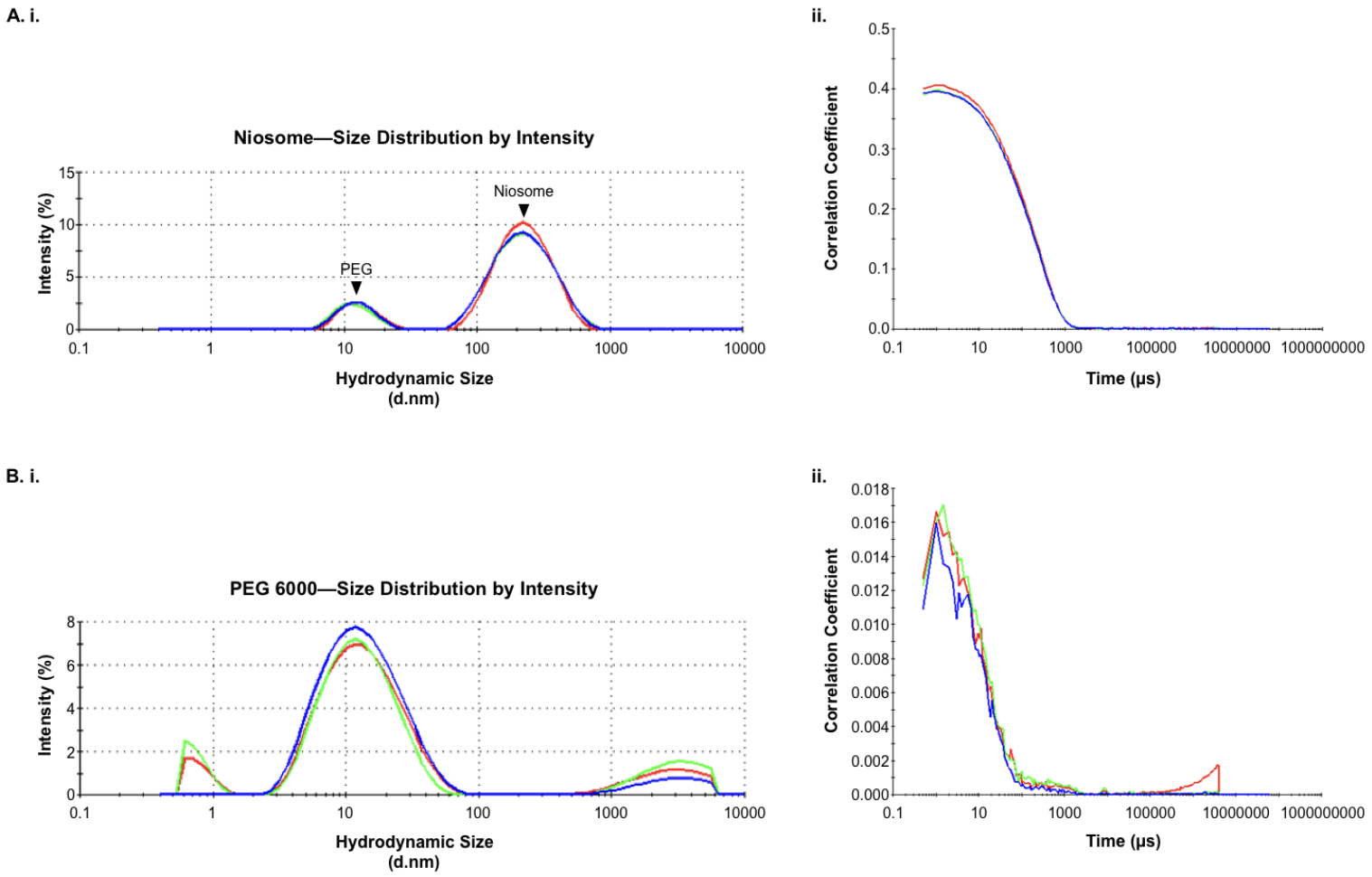

Figure 5.11 Measurement of empty niosomes and the identification of a PEG 6000 peak by Dynamic Light Scattering. (A) i. Representative size distribution of empty niosomes (244.0d.nm, 85.5% intensity, PdI=0.683). **ii.** Correlogram of niosome measurements (records 1-3) over time. **(B) i.** Representative size distribution of raw PEG 6000 in PBS (15.54d.nm, 92.6% intensity, PdI=0.326). **ii.** Correlogram of PEG 6000 measurements (records 1-3) over time.

5.3.6 Niohemin localizes to the cytoplasm and lysosomes of cardiomyotubules *in vitro*

To investigate whether Niosome-encapulated hemin was capable of cardiomyocyte entry/internalization, differentiated H9C2 cardiomyotubules were exposed to $[2.5uM]_{eq}$ Cy5.5-conjugated Niohemin for 24h (Fig.5.12). Epifluorescent imaging revealed widespread Niohemin localization to the cytoplasm region of H9C2 cells (Fig.5.12A), which was further corroborated by super-resolution imaging (Fig.5.12B). Niohemin was not observed to have entered the nucleus (Fig.5.12A, ii and iv; Fig.5.12B, i). Single live-cell imaging by super-resolution microscopy also revealed extensive co-localization between Niohemin and lysosomes (Lysotracker green; Fig.5.12B, iv), suggesting that lysosomes may play a role in Niohemin breakdown/catabolism. Super-resolution microscopy was also used as an orthogonal approach to measuring Niohemin diameter, with a single nanoparticle measuring 0.212um in diameter by microscopy (Niohemin measured 0.194d.nm by Dynamic Light Scattering). These nanopharmacokinetic data show agreement for nanoparticle size, size-preservation after cellular internalization to the cytoplasm (or lysosomal escape), and lysosomal interaction.

5.3.7 Pharmacodynamic characterization of Niohemin *in vitro*

To investigate the dose-dependent effects of niosome-encapsulated hemin on cell viability, HMOX1 and FTH1, differentiated H9C2 cardiomyotubules were exposed to Niohemin (0.5, 1, 2.5, 5, or 50uM eq.), empty niosomes, hemin (2.5 or 5uM) or vehicle for 24h (Fig.5.13). Cell viability was significantly reduced to near-zero levels in cardiomyotubules exposed to $[50uM]_{eq}$ Niohemin—this was not unexpected as hemin toxicity in healthy H9C2 cells begins at 5uM (Fig.5.13A). However, it is not clear whether the observed toxicity of $[50uM]_{eq}$ Niohemin was due to high hemin content or toxicity from the niosome shell ($[25uM]_{eq}$ niosome exposure also reduced cell viability to near-zero). No significant difference in cell viability was observed between 5uM hemin and equivalent Niohemin ($[5uM]_{eq}$), although a higher mean survival with Niohemin

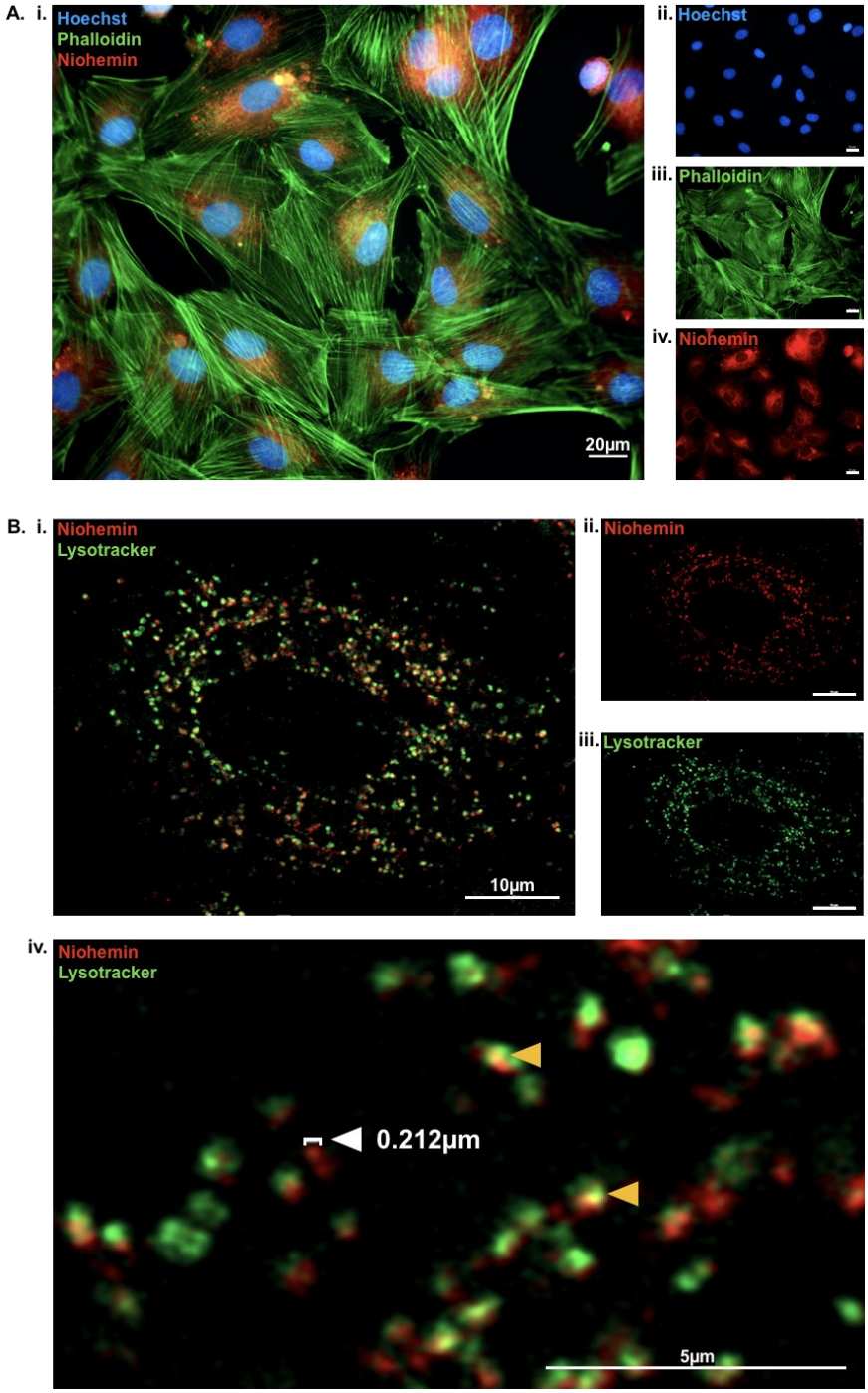

Figure 5.12 Cy5.5-Niohemin localizes to the cytoplasm and lysosomes. (A) Differentiated H9C2 cardiomyotubules were administered Cy5.5-conjugated Niohemin (2.5uM eq. for 24h) and imaged by epifluorescent microscopy. **i.** Composite image. **ii.** Hoechst (nuclei). **iii.** Phalloidin (F-actin). **iv.** Cy5.5. **(B)** Single live-cell imaging by super-resolution microscopy with Lysotracker Green (lysosomes). **i.** Composite image. **ii.** Cy5.5. **iii.** Lysotracker. **iv.** Magnified image of Cy5.5-conjugated Niohemin and Lysotracker composite. Measurement of Niohemin's diameter (0.212µm; white arrowhead). Yellow arrowheads denote representative examples of lysosome and Niohemin overlap.

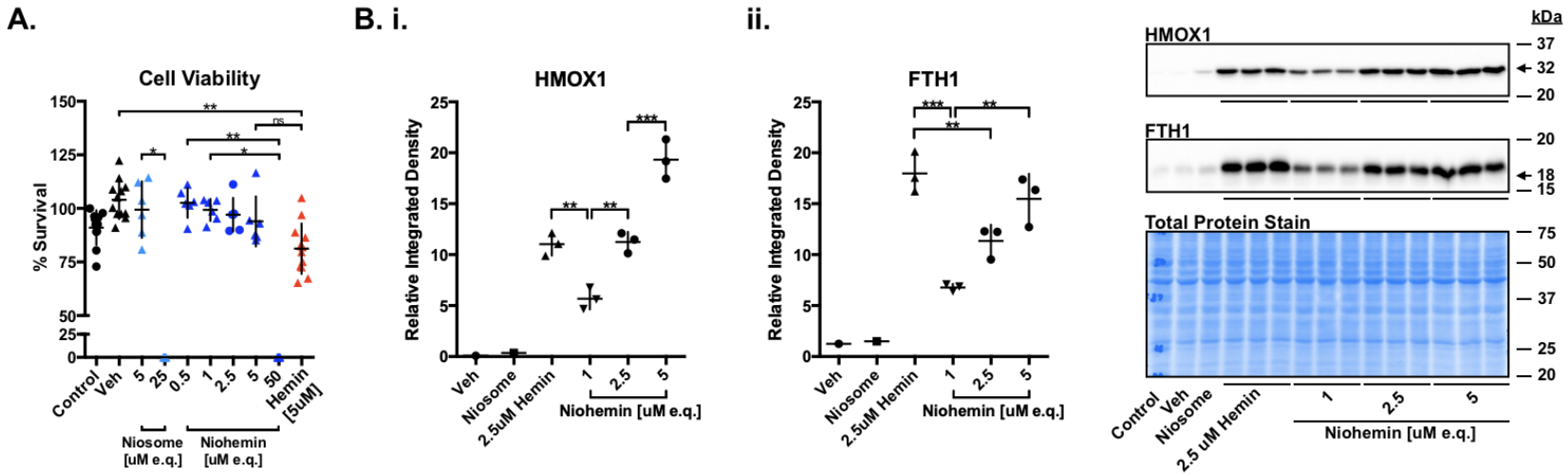

Figure 5.13 Pharmacodynamic characterization of hemin exposure *in vitro*. Dose-dependent effects of 24h Niohemin exposure on differentiated H9C2 cardiomyotubule **(A)** viability and **(B)** heme regulatory enzyme expression. **(A)** Resazurin cell viability assay in H9C2 cells treated with empty niosomes (5uM or 25uM e.q.), Niohemin (0.5uM, 1uM, 2.5uM, 5uM, or 50uM e.q.), or hemin (5uM). **(B)** Densitometric analysis of **i.** HMOX1 and **ii.** FTH1 with representative Western Blots and total protein stain.

suggests further investigation may be necessary to determine whether niosome-encapsulation attenuates hemin toxicity.

HMOX1 was significantly increased with Niohemin exposure, however HMOX1 elevation did not differ significantly between 2.5uM hemin and bioequivalent Niohemin ($[2.5uM]_{eq}$; Fig.5.13B,i). FTH1 was also significantly increased with Niohemin exposure. Interestingly, FTH1 induction by Niohemin ($[2.5uM]_{eq}$; Fig.5.13B,ii) was significantly less than that of bioequivalent hemin (2.5uM), despite both compounds elevating HMOX1 to the same degree. These findings suggest that the pharmacokinetics and/or pharmacodynamics between hemin and hemin released from niosomes are not identical.

5.3.8 Niohemin treatment confers cytoprotection against oxidative injury at a lower dose than hemin in cardiomyotubules

To investigate whether niosome-encapsulated hemin was capable of protecting cardiomyocytes to the same degree as hemin, differentiated H9C2 cardiomyotubules were treated with hemin (1, 2.5, or 5uM), equivalent Niohemin, empty niosomes, or 300uM NAC 16h pre-H_2O_2 (500uM, 24h)-mediated injury (Fig.5.14). Cell death was not attenuated by empty niosomes, but survival was significantly improved with 2.5 and 5uM eq. Niohemin (Fig.5.14B). Interestingly, cell survival was significantly preserved with 5uM hemin (to the same degree as $[5uM]_{eq}$ Niohemin), but not with 2.5uM hemin (which induces HMOX1 to identical levels as bioequivalent Niohemin). These data show that Niohemin confers cytoprotection against oxidative injury at a lower dose than hemin *in vitro*, suggesting that the pharmacokinetics and/or pharmacodynamics between hemin and hemin released from niosomes are different and may not be dependent on peak HMOX1 levels alone. These data also suggest that there might exist a saturable point of hemin (or Niohemin)-mediated cytoprotection, as $[2.5uM]_{eq}$ or $[5uM]_{eq}$ Niohemin demonstrated equal improvement in cardiomyotubule survival.

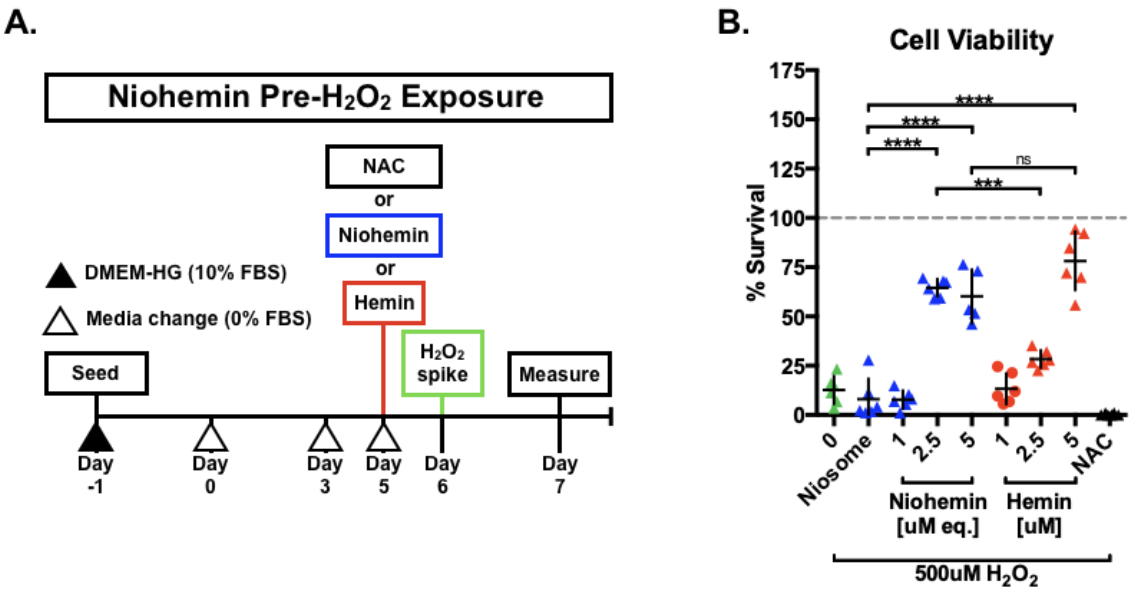

Figure 5.14 Niohemin treatment confers cytoprotection to H9C2 cardiomyotubules. Dose-dependent effects of Niohemin and hemin treatment pre-H_2O_2 on differentiated H9C2 cardiomyotubule viability. **(A)** Outline of H9C2 differentiation and treatment 16h pre-H_2O_2 exposure (500uM, 24h). **(B)** Resazurin cell viability assay in H9C2 cells treated with empty niosomes (5uM e.q.), Niohemin (1uM, 2.5uM, or 5uM e.q.), hemin (1uM, 2.5uM, or 5uM), or 300uM N-Acetyl-Cysteine (NAC), 16h pre-H_2O_2 exposure (500uM, 24h). Dashed lines indicate the mean survival of untreated controls not exposed to H_2O_2.

5.3.9 Qualitative evidence suggests pH differentially affects Niohemin pharmacokinetics *in vitro*

One of the principal advantages of nanomedicine is the ability to direct drug release to site-specific targets (such as by decorating the nanoparticle's surface with homing proteins or constructing the particle using materials that are modulated by the target site's micromilieu). In the present study, we sought to design a nanoparticle capable of directing hemin release to the heart—whose microenvironment undergoes ischemic acidification after AMI. To test this proof-of-concept, we examined whether a shift in media pH could affect markers of hemin release from its niosome shell (Fig.5.15). Differentiated H9C2 cardiomyotubules were exposed to $[2.5uM]_{eq}$ Niohemin in pH-modified or un-modified EBSS media for 24h (un-modified media=pH 7.20; acidic media=pH 6.80; basic media=pH 7.52). Controls were exposed to respective pH- or un-modified media only. The addition of Niohemin to cardiomytubules in basic media significantly increased HMOX1 expression. HMOX1 expression was also increased by the addition of Niohemin to cardiomyotubules in acidic media, albeit to levels significantly higher than with basic media. The modification of pH alone did not affect HMOX1 expression in either medium. Collectively, these data provide the first evidence that Niohemin release-kinetics could be modified in an acidified environment, however further work investigating Niohemin's Zeta potential (electrokinetic stability of colloidal dispersions) in modified pH is still required to validate these initial findings.

5.4 DISCUSSION

In the present study, we establish the therapeutic potential of two novel strategies designed for more rapid targeted delivery of HMOX1 to the infarcted heart: the exogenous delivery of functional HMOX1 using a cell-penetrating peptide (HMOX1-CPP) and the encapsulation of hemin into a nanoparticle shell (Niohemin). Here, we characterize the fundamental physicochemical, pharmacokinetic, and pharmacodynamic properties of HMOX1-CPP and Niohemin, and investigate their therapeutic efficacy in reference to hemin using cardiomyotubles. Collectively, we show that HMOX1-CPP and

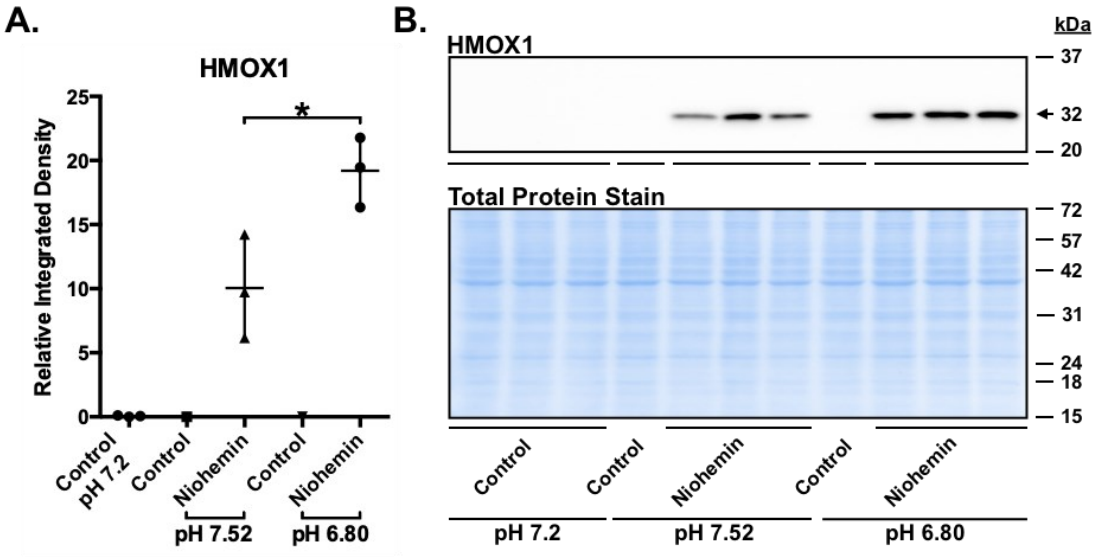

Figure 5.15 Qualitative evidence suggests pH differentially affects Niohemin pharmacokinetics *in vitro*. Differentiated H9C2 cardiomyotubules were exposed to 2.5uM e.q. Niohemin for 24h in pH-modified EBSS media (unmodified media=pH 7.2, basic media=pH 7.52, or acidic media=pH 6.80). Controls were exposed to pH- or un-modified media only. **(A)** Densitometric analysis of HMOX1. **(B)** Representative Western Blot and total protein stain.

Niohemin are readily internalized to the cytoplasm of differentiated cells and are directly capable of conferring cytoprotection to cardiomyotubules against oxidative injury. We further demonstrate that HMOX1-CPP confers cytoprotection more rapidly than hemin, but that simultaneous combination of the two therapeutics are likely incompatible. We also show for the first time that Niohemin confers cytoprotection directly to cardiomyotubules *in vitro*, and at a lower concentration than hemin alone—despite equivalent HMOX1 induction at 24h. Finally, we present preliminary evidence suggesting that Niohemin's nanodrug-release kinetics may be affected by an acidified environment *in vitro*, which—if further validated—could provide the fundamental evidence needed to proceed with *in vivo* exploration of pH-directed hemin therapy in an infarcted heart.

Distinguishing between drug internalization and cell surface adhesion/co-localization is a fundamental step in determining a drug's mechanism of action and provides essential information with which to advance pharmacokinetic characterization, and optimize therapeutic targeting and efficiency. Both HMOX1-CPP and Niohemin are readily internalized to the cytoplasm of differentiated cardiomyotubules. CPPs derived from modified human immunodeficiency virus transactivator of transcription (TAT) protein—such as the HMOX1-CPP described herein—enter cells independent of typical mechanisms of cellular internalization [273]. Clathrin-mediated endocytosis, caveolin-mediated endocytosis, and macropinocytosis act as the primary mechanisms by which TAT CPPs enter the cell [273], yet whether these mechanisms are conserved across all cell types (including cardiomyotubles) is not yet definitive. Although confocal microscopy indicates Niohemin internalization, the cellular mechanism(s) underlying cell entry also remain to be elucidated. Variations in nanoparticle design, size, composition, and cell-surface modifications can significantly alter how (and how readily) a niosome enters the cell and is subsequently processed—making pharmacokinetic characterization unique to each proprietary nanoparticle construct [285,286]. However, real-time tracing of Niohemin-Cy5.5 co-localization through the use of commercially available fluorescent protein fusion constructs for proteins such as Rab5a (the master regulator of endosome biogenesis [287]; e.g. CellLight Early Endosomes BacMam 2.0 tracer)—could be a simple avenue to initiate further investigations into the mechanism(s) underlying

Niohemin internalization. Once inside cardiomyotubules, Niohemin further co-localized to lysosomes (a fate also shared by liposomes and extracellular vesicles [288]). Whether interactions between Niohemin and the acidic lysosomal micromilieu (i.e.) are necessary for hemin release—or are simply the mechanism by which spent nano-carrier shells are degraded—requires further study. Thus, more work is still required to elucidate Niohemin's mechanisms of internalization and pharmacokinetics.

As expected, HMOX1-CPP exposure significantly increased HMOX1 levels in H9C2 cardiomyotubules. Interestingly, two HMOX1 bands were detected by Western Blot in HMOX1-CPP-exposed cardiomyotubules, whereas only one band was detected in cardiomyotubules exposed to hemin at bioequivalent HMOX1 levels. Using the same HMOX1-CPP herein, Venkatachalam *et al.* 2017 showed a similar pattern between purified HMOX1-CPP (34kDa) and recombinant HMOX1 peptide (32kDa) by gel electrophoresis—suggesting that the lower band observed in HMOX1-CPP-exposed cardiomyotubules may represent a CPP-cleaved HMOX1 [150]. However, we have yet to rule out other potential post-translational-type modifications to HMOX1-CPP that could account for this double-banding pattern. Previous studies have reported endogenous HMOX1 appearances across the range of 28-32kDa when measured by gel electrophoresis, attributing this to endogenous post-translational modifications such as the addition/cleavage of organelle-targeting sequences, degradation, and intracellular compartmentation [289]. Thus, HMOX1-CPP could be subjected to similar endogenous modification processes once inside the cell. Immunoprecipitation of HMOX1-CPP via its histidine tags—or simply a direct comparison between HMOX1-CPP and recombinant HMOX1 peptide in future experiments—could help to identify relevant modifications, compartmentation, or enzyme turnover/function in the safety and efficacy of this therapeutic approach. As the identity and activity of the lower HMOX1 band was uncertain, hemin bioequivalence was determined using the density of both bands; the pharmacodynamic and cytoprotective effects of HMOX1-CPP were also cross-verified at bioequivalence set to the upper HMOX1-CPP band alone (data not shown) for due diligence, and showed no variability to reported effects.

HMOX1-CPP provided a valuable opportunity to compare the therapeutic benefits/limitations (and underlying molecular differences) of two translational strategies

for HMOX1 elevation: enzyme delivery (HMOX1-CPP) and substrate-mediated induction (hemin). In contrast to hemin administration at the same timepoints, HMOX1-CPP significantly improved cardiomyotubule viability when administered 4h pre- or simultaneously with H_2O_2 exposure—demonstrating both direct prophylactic and immediate cytoprotection to cardiomyotubules. Hemin has previously been shown to confer cytoprotection in differentiated H9C2 cardiomyotubules when administered 24h pre-oxidative injury (Chapter 3) or 16h pre-oxidative injury (albeit at a lower degree of oxidative injury), suggesting that more time may be necessary for its benefits to take optimal therapeutic effect. Unlike HMOX1-CPP (which delivers a functionally active enzyme), hemin requires several steps to increase intracellular HMOX1 levels—such as mRNA transcription, translation, and protein folding. Further, HMOX1-mediated accrual of hemin's catabolic byproducts—biliverdin, carbon monoxide, and free iron—produces the primary mediators of hemin's antioxidant and anti-inflammatory effects. Thus, HMOX1-CPP may require less time to confer cytoprotection compared to hemin. However, it remains unclear whether the time at which bioequivalence was measured between HMOX1-CPP and hemin may also contribute to comparative differences in cytoprotection. Bioequivalence between HMOX1-CPP and hemin was measured at 24h exposure. A time-course study investigating whether this timepoint marked the peak, plateau, or clearance phase of intracellular HMOX1-CPP concentrations relative to hemin-induced HMOX1 (i.e. whether intracellular HMOX1-CPP was elevated prior to 24h) has yet to be performed. Whether differences in cytoprotection are attributable to differences in the rates of increased intracellular HMOX1 or conversion of heme/hemin into cytoprotective metabolites (i.e. time for accumulation to therapeutic effect/time to bioequivalence, levels of cytochrome P450 reductase to initiate HMOX1-mediated catabolism), peptide/hemin clearance, or cumulative HMOX1 activity remain uncertain. Thus, differences in cytoprotection between HMOX1-CPP and hemin could possibly be attributed to differences in both the rates of therapeutic HMOX1 elevation and total HMOX1 activity over a 24h period of analysis.

Interestingly, simultaneous exposure to HMOX1-CPP and hemin in healthy cardiomyotubules at individually therapeutic concentrations ($100ug \bullet ml^{-1}$ and 5uM respectively) decreased overall cell survival. Given that HMOX1-CPP offered no

commensurate induction of FTH1 in H9C2 cardiomyotubules, the rapid release of free iron from hemin substrate could be a contributing factor (though the exact cause is not yet known). FTH1 is one of two ferritin subunits, collectively serving as the primary site for intracellular iron storage. Proper iron storage is essential, as excess free iron can promote/propagate reactive oxygen species production via the Fenton reaction [70]. *In vitro,* FTH1 knockdown significantly increases intracellular iron content and reduces viability in otherwise healthy cells [290]. In contrast, FTH1 overexpression has been shown to reduce intracellular iron content, and improve overall cell viability in PC-12 (pheochromocytoma) cells exposed to the ROS-inducing compound, oxidopamine [290]. Thus, co-incubation of hemin and HMOX1-CPP at high doses may have resulted in iron-overload toxicity and subsequent cell death, however more work is necessary to rule out excess carbon monoxide production, free radical stress, and hyperbilirubinemia. Further investigation into the effects of hemin timing (e.g. after chronic HMOX1-CPP exposure/potential heme depletion) and dose-optimization may also be warranted.

Concurrent exposure to HMOX1-CPP and hemin might also model pathophysiological scenarios associated with AMI and heart failure. In the heart, heme levels are increased post-AMI (and in human heart failure); thus, modeling a heme/hemin-replete environment *in vitro* could help to identify issues associated with HMOX1-CPP intervention early on [Chapter 3, [19]]. Co-incubation of HMOX1-CPP and hemin could also provide foresight into overcoming potential challenges in long-term HMOX1 elevation. In transgenic mice, cardiac-specific HMOX1 overexpression induces spontaneous heart failure after 1 year (yet significantly reduces acute isoproterenol-mediated cardiac dysfunction) [107]. Whether chronic HMOX1 overexpression induces heart failure through the depletion of endogenous heme substrate remains to be understood, though hemin supplementation is a probable treatment strategy to be explored in that eventuality.

Further, we show for the first time that niosome-encapsulated hemin directly confers cytoprotection to cardiomyotubules against oxidative injury *in vitro* and at a lower concentration than hemin alone, despite equivalent HMOX1 induction at 24h. In differentiated H9C2 cardiomyotubules, both Niohemin and hemin conferred similar levels of cytoprotection when administered at $[5uM]_{eq}$ 16h pre-oxidative injury. Yet,

Niohemin also conferred the same degree of protection at $[2.5uM]_{eq}$ (despite identical HMOX1 induction after 24h between Niohemin and equivalent hemin), suggesting that hemin's efficacy is improved through niosome encapsulation and may not be dependent on peak HMOX1 levels alone. Interestingly, FTH1 levels were significantly higher in hemin-treated cells than Niohemin at $[2.5uM]_{eq}$ after 24h—further suggesting that differences in pharmacokinetics and/or pharmacodynamics between hemin and hemin released from niosomes could be responsible for differences in cytoprotection. Thus, niosome encapsulation might improve hemin-mediated cytoprotection through accelerated intracellular drug delivery. To characterize the differences between hemin's and Niohemin's pharmacokinetics/pharmacodynamics (and optimize cytoprotection), further studies comparing the time- and dose-dependent effects of both on heme regulatory enzyme expression will be required.

Preliminary evidence also suggests that Niohemin's nanodrug-release kinetics may be affected by an acidified environment *in vitro*. In its unencapsulated form, hemin is subjected to extensive first-pass metabolism by the liver—potentially limiting hemin delivery to the infarcted heart. However, increasing hemin dosage to overcome such limitations may risk potential off-target effects in other (non-cardiac) tissues [Chapter 3, Fig.3.3], as well as increased toxicity [Chapter 2, Table 2][200]. Thus, encapsulation of hemin into niosomes capable of pH-sensitive cargo release presents a potential strategy to improve hemin bioavailability by passively targeting drug delivery to the acidic extracellular milieu of ischemic cardiac tissue. Unlike cell membranes, niosomes are unable to actively maintain their surface charge in acidic pH. As a result, the niosome surface charge shifts from neutral to protonated at low pH, thus enhancing interactions with the net negatively-charged cell membrane. Though no differences between pH-modified media controls were observed at baseline in the present study, acidified media further increased Niohemin-mediated HMOX1 induction in H9C2 cardiomyotubules compared to more basic media. Further investigation into Niohemin's stability under various pH conditions—through imaging (i.e. transmission electron microscopy) and measurement of the electrical potential between the nanoparticle's surface and surrounding solvent (i.e. zeta potential) under controlled conditions will be clarifying in future studies and enhance the understanding of *in vivo* kinetics.

Nanoparticle-encapsulated hemin demonstrates promise as a therapeutic strategy in AMI intervention, but—with exception to a single study by Ben-Mordecai *et al*. 2017 characterizing liposome-mediated hemin delivery—little is known about hemin-loaded nanoparticles [291]. In the 2017 study, female mice administered 2mg lipid•kg^{-1} hemin-containing hyaluronan liposomes i.v. one day post-AMI (via left main coronary artery ligation) demonstrated significant reductions in left ventricular fibrosis and mass (suggesting attenuation of left ventricular hypertrophy) [291]. Female mice administered either raw hemin (2mg•kg^{-1}) or empty liposomes (10mg lipid•kg^{-1}) alone also showed similar reductions in left ventricular fibrosis and mass following AMI, however pharmacoequivalency of hemin loading in liposomes was not verified [291]. Further, female mice administered PE-rhodamine-infused liposomes at three days post-AMI revealed significant nanoparticle accumulation at the infarct zone 6h after injection. In contrast, liposome accumulation in the left ventricle was not observed following sham surgery and little (if any) liposome accumulation was observed in the lung, liver, or spleen relative to the infarct zone post-AMI [291]. A comparison between the effects of hemin and hemin-containing liposomes on cardiac HMOX1 was not performed. Though preliminary, the 2017 study does establish that *in vivo* hemin delivery by nanoparticle can confer cardioprotection acutely post-AMI.

Collectively, the present study provides valuable insights into the therapeutic potential (and possible limitations) of HMOX1-CPP and the novel Niohemin nanoparticle. Further characterization of HMOX1-CPP's and Niohemin's pharmacokinetic properties, therapeutic potential/limitations, and effects on heme/iron metabolism as a whole are still required before proceeding to *in vivo* AMI modeling. Even so, our data provides important preliminary information needed to establish therapeutic proof-of-concept and advance our collective understanding of the balances between HMOX1 substrate and enzyme.

CHAPTER 6: INTEGRATIVE DISCUSSION

6.1 INTRODUCTION

The overarching objective of this doctoral thesis is to advance our fundamental understanding of heme metabolism and the potential for its pharmacological utility as a therapeutic post-AMI. Elevating levels of heme oxygenase-1 (HMOX1) confers robust cardioprotection prophylactically in pre-clinical models of AMI, yet translational investigations into its use post-AMI have been limited and typically focus on the enzyme alone without consideration for endogenous heme substrate bioavailability or metabolism [292–298]. As a heme surrogate and potent inducer/substrate of HMOX1, hemin could serve as a viable strategy for the treatment of AMI [139,299]. Yet despite being on the market for over 40 years as a clinically-approved drug for the treatment of porphyria, hemin's pharmacokinetic and pharmacodynamic characterization has been limited—leaving fundamental gaps in our collective understanding of hemin pharmacology. Whether hemin was capable of improving cardiac function when initiated post-AMI (and within a clinically-approved human equivalent dose range) had also remained uncertain. Thus, this thesis set out to achieve the following objectives: 1) characterize the effects of hemin and AMI on cardiac heme regulation; 2) perform a direct comparison between hemin treatment initiated pre-injury versus post-injury in cardiomyotubules and pre-clinical AMI; and finally, 3) investigate the effects of timing on hemin intervention. In this final chapter, I present a cumulative summary of my research findings from the preceding thesis chapters, highlight their contributions to the fields of heme metabolism and pharmacology, and identify remaining knowledge gaps, challenges, and opportunities for future research (Fig.6.1). Collectively, this chapter aims to present a synthesis of my doctoral research and contextualize its implications for the development of heme-modulating therapeutics.

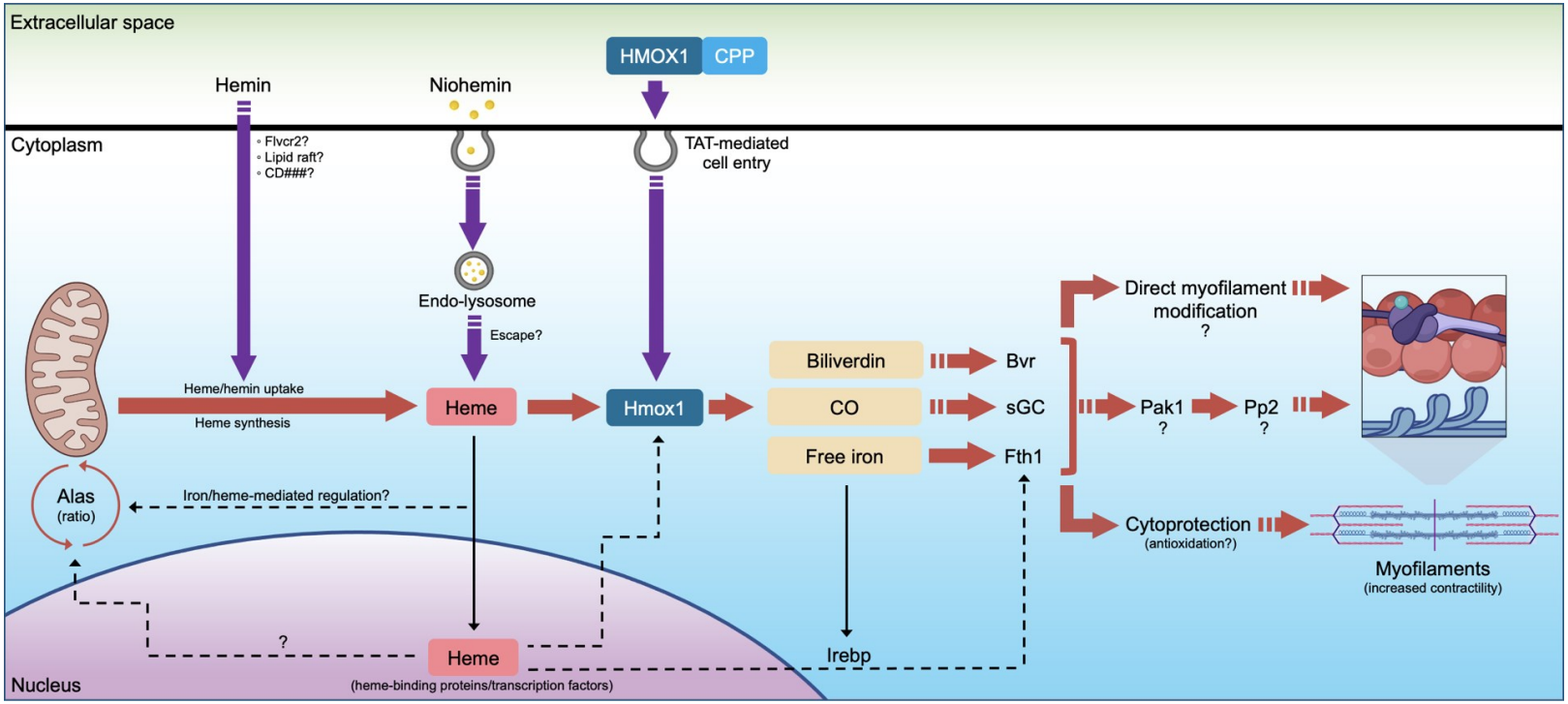

Figure 6. 2 Summary of research findings and future directions. Hemin and Niohemin enter cardiomyotubules via yet-to-be-defined mechanisms, increasing intracellular heme-mediated signaling and catabolism through the induction of Hmox1. HMOX1-CPP enters the cell through TAT-mediated receptors, increasing Hmox1 levels directly and without eliciting heme-signaling. Each pharmacological approach demonstrated cytoprotection. A novel heme-mediated increase in contractility occurs by increasing the ATPase activity of cardiac myofilaments and post-translationally altering myofilament protein phosphorylation and Ca^{2+} sensitivity. Future studies should define uptake and intracellular trafficking mechanisms such as endolysosomal degradation/nanoparticle escape, and seek to resolve the downstream mechanisms by which myofilaments are directly or indirectly (e.g. via Pak1/Pp2 or cytoprotection) modified by hemin or its metabolic byproducts. Alas, delta-aminolevulinic acid synthase; Bvr, biliverdin reductase; CD, cluster of differentiation number; CO, carbon monoxide; CPP, cell-penetrating peptide; Flvcr2, feline leukemia virus subgroup C receptor-related protein-2, Fth1, ferritin heavy chain; Hmox1, heme oxygenase-1; Irebp, iron response element-binding protein; Pak1, p21-activated kinase-1; Pp2, protein phosphatase-2a; sGC, soluble guanylate cyclase; TAT, transactivator of transcription. Created with BioRender.com.

6.2 CUMULATIVE SUMMARY OF RESEARCH FINDINGS

6.2.1 Regulatory context for hemin as a drug

This thesis' novel contributions to the field of hemin pharmacology begin in Chapter 2. In this chapter, I sought to improve the collective understanding of hemin pharmacology and enhance the potential for future pre-clinical and clinical successes in heme-modulating therapeutics. Using information extracted from the primary and regulatory literature, I performed a comprehensive case study of current knowledge related to hemin's biopharmaceutical properties, pre-clinical/clinical pharmacokinetics, and pharmacodynamics. Importantly, this case study is the first to report on information contained within hemin's regulatory submission documents to Health Canada and summarizes the clinical and pre-clinical dosing regimens included in support of hemin's Health Canada approval.

Comprehension of a drug's pharmacologic profile strengthens our ability to treat patients more effectively and to predict and prevent adverse effects. Although information related to hemin pharmacokinetics and pharmacodynamics/mechanisms-of-action was limited, documents submitted to Health Canada revealed valuable insights into hemin dosing strategies that could be applied towards pre-clinical modeling for AMI and inform future clinical studies. Within clinically-recommended doses for porphyria (1-4mg/kg/day), hemin is reported as safe for consecutive daily use in humans for up to at least 13 days (i.v. in patients with porphyria), presenting promising evidence that repeated hemin administration may be safe for prolonged, repetitive use [181,191,202]. Preliminary evidence discovered during the present case study also demonstrates hemin safety when administered within the clinically-recommended range for porphyria in humans early post-AMI, as well as hemin's capacity to induce HMOX1 in the human heart (when administered pre-aortic valve replacement surgery) [195,197]. Thus, preliminary evidence suggests a promising safety and efficacy profile for hemin repurposing—within the clinically-recommended range for porphyria—in the treatment of AMI.

More work is still necessary to characterize hemin pharmacokinetics in patients without porphyria (such as in patients with AMI). Given the range and frequency of hemin dosing outlined in the primary and regulatory literature, a clinical dose-escalation study—with i.v. doses escalating from 4mg•kg^{-1} q.d. (3 days, 7 days , 13 days) to 6mg•kg^{-1} q.d. (3 days, 7 days , 13 days) to 8mg•kg^{-1} q.d. (3 days, 7 days , 13 days)—are suggested to evaluate safety and pharmacokinetics. Primary literature collated in Chapter 2 also suggests a significant difference in hemin uptake between i.v. and i.p. administration in healthy mice, as indicated by an i.v. LD_{50} of 56.3mg hemin•kg^{-1} (single dose over 14 days) and an i.p. LD_{50} of nearly double (112.5mg hemin•kg^{-1}; single dose) [151]. Although delivered intravenously in patients, hemin (32.6mg•kg^{-1} per day) was delivered intraperitoneally in the present body of work to reduce the risk of phlebitis and accidental intramuscular injection associated with repetitive tail vein administrations [175]. Non-pharmacy grade hemin was also administered due to the challenges involved in acquiring pharmacy-grade orphan drugs for research. Thus, further studies comparing the pharmacokinetics of pharmaceutically formulated hemin for injection are still necessary to address how different routes of administration affect hemin uptake, peak concentrations, and metabolism. Ultimately, information related to hemin pharmacology collated within Chapter 2 highlights valuable insights for the advancement of therapeutic hemin repurposing through retrospective analysis of the primary, regulatory, and grey literature.

6.2.2 Rescue of myocardial function by hemin intervention post-infarction

In Chapter 3, I sought to evaluate the translational potential of hemin as a novel treatment for AMI and provide a holistic characterization of the resulting changes in cardiac heme regulation. Here we performed the first temporal characterization of cardiac heme regulation post-AMI, uncovering an apparent dyssynchrony between cardiac heme content and anabolic/catabolic rate-limiting enzyme expression. In the peri-infarct heart, heme content was elevated without proportional changes to HMOX1 or heme-synthesizing enzyme expression (ALAS1, ALAS2). Instead, HMOX1 induction occurred early and acutely post-AMI. This was followed in parallel by progressive switching

between dominant ALAS isoforms (i.e. decreased ALAS1 and increased ALAS2). Previous reports have suggested that ALAS2 induction contributes to human ischemic heart failure through the overproduction of endogenous heme [19], however, our findings show that ALAS2 induction peaks while heme content is abating post-AMI. Using H9C2 cardiomyotubules and healthy mice, we also show that hemin induces ALAS2, demonstrating that ALAS2 does not lead—but instead follows—elevated heme content in the heart. Interestingly, we also show that ALAS2 induction is contrasted by a proportional reduction in ALAS1 in the peri-infarct and hemin-treated hearts. Previous studies have shown that ALAS2 overexpression in proliferating H9C2 cardiomyoblasts significantly decreases ALAS1 protein levels, yet ALAS1 gene expression is alleged to be unchanged in the peri-infarct heart (suggesting that it is translationally regulated) [19]. Thus, we show that the general consensus for classifying ALAS1 as a reference (housekeeping) gene/protein is untenable.

Curiously, increased heme content in the peri-infarct heart was also unmatched by concomitant HMOX1 induction. This was particularly surprising given that heme serves as the canonical inducer of HMOX1 (via Bach1 disinhibition), and highlights the limitations of HMOX1's historical role as a sole surrogate marker for heme content. Originally, we had hypothesized that post-AMI HMOX1 dyssynchrony stemmed from an injury-mediated inability to maintain elevated HMOX1 levels long-term. However, HMOX1 levels were significantly increased with repeated hemin administration post-AMI—without evidence of heme/hemin accumulation in the peri-infarct heart. The exact mechanisms underlying dyssynchronous HMOX1 and heme in the untreated peri-infarct heart remain to be understood, however, a plausible explanation could be the physical separation of heme from its catabolic enzyme (such as through compartmentalization in different subcellular spaces, organelles, or cell types). In the present study, heme content and heme regulatory enzyme expression post-AMI were measured in cardiac tissue without the isolation or sub-cellular fractionation of cardiomyocytes. Thus, it remains unclear whether free heme was present in the same space as HMOX1 (or its repressor, Bach1). It also remains unclear whether cardiomyocytes serve as the primary source of HMOX1's elevated protein signal. Early post-AMI, resident macrophages are activated and monocytes mobilized from the spleen (as well as from blood and bone marrow)

infiltrate the infarcted heart [234]. HMOX1 is also highly expressed in monocytes and macrophages due to their role in heme recycling. Thus, increased HMOX1 levels in the peri-infarct heart could be due to macrophage accumulation post-AMI (independent of heme-dependent induction in cardiomyocytes). Ultimately, further studies investigating the cellular and subcellular source of heme and the effects of AMI and hemin on endogenous heme regulation in non-myocyte cardiac cells (such as macrophages and fibroblasts) are still necessary to elucidate the cause of heme-HMOX1 dyssynchrony.

In Chapter 3, the first direct comparison between hemin treatment initiated pre- versus post-injury was performed, as well as the first temporal characterization of hemin's effects on heme regulation in the healthy heart. Here I show that hemin confers cytoprotection to cardiomyotubules against oxidative injury *in vitro* when administration is initiated prophylactically (but not interventionally), and that interventional administration of hemin (post-AMI) improves left ventricular function but to a lesser extent than hemin pre-AMI. Unlike experimental HMOX1 peptides or gene vectors typically used in HMOX1-targeted therapy, additional steps exist for the hemin-mediated induction of intracellular HMOX1 such as intracellular transport, nuclear uptake/transcription factor transactivation, and HMOX1 translation. Given that the earliest indication of left ventricular HMOX1 induction was observed between 4 and 8h post-hemin in healthy mice, more rapid methods of hemin delivery/HMOX1 elevation might be necessary to improve cardiac outcomes post-AMI.

Several challenges still need to be overcome before hemin can be translated to the clinic. The effects of drugs like hemin on heme regulation as a whole, beyond just HMOX1 induction must be considered and pre-clinical studies must reflect clinical realities such as the need for post-AMI interventions. Collectively, the knowledge collated through Chapter 3 provides important foundational information to further advance our understanding of hemin pharmacodynamics and the therapeutic targeting of heme metabolism in AMI.

6.2.3 Exploring the effects of hemin on late myocardial infarction intervention

In Chapter 4, I sought to investigate the effects of delayed hemin treatment and explore whether hemin has any capacity to attenuate adverse outcomes in pre-clinical models when treatment is initiated late post-AMI. Here I show that hemin significantly improves indices of cardiac contractility and relaxation with delayed administration post-AMI (parameters that were not improved with hemin intervention immediately post-AMI). Interestingly, hemin-mediated inotropy was not associated with a change in infarct size, nor improvements in fibrotic remodeling—eliciting the question of how hemin might confer cardioprotection in late AMI intervention. Using 3D-engineered human cardiac tissues, I establish for the very first time that hemin is capable of increasing cardiac contractile force and rates of relaxation directly—apparently without concurrent changes in Ca^{2+} flux. I also show for the first time that hemin significantly increases the ATPase activity of cardiac myofilaments obtained from healthy mice administered i.p. hemin, and post-translationally alters myofilament protein phosphorylation and Ca^{2+} sensitivity. Thus, hemin may confer inotropic benefits to the heart by increasing ATPase activity and effecting conformational changes to cardiac myofilaments.

Yet, more work is still necessary to understand the mechanisms underlying hemin-mediated cardiac inotropy and their translatability post-AMI. Here I show that *in vivo* hemin administration significantly decreases the phosphorylation of cMyBP-C, desmin, troponin T, and MLC-2 in cardiac myofilaments, however the precise (de)phosphorylation sites affected and their regulation of contractile mechanics remain to be determined. Although beyond the scope of this thesis, introducing point mutations within the phosphorylatable amino acid sites of key myofilament proteins and monitoring their effects on contractility (alone or in combination) could provide valuable insights into the myofilament mechanics underlying hemin-mediated inotropy. More advanced/sensitive tools and techniques may also be required to validate whether hemin-mediated increases in cardiac contractility truly occur independently of increased calcium transients.

In Chapter 4, I also show that hemin increases contractile force in 3D-engineered human cardiac tissues without concomitant changes in Ca^{2+}. However, changes in tissue

transient amplitudes (calcium) were not increased in proportion to changes in twitch amplitudes (contractility) following exposure to isoproterenol controls (a beta-agonist and inducer of intracellular Ca^{2+} uptake), suggesting potential limitations in the sensitivity of calcium detection. Thus, more sensitive tools such as Fura-2 calcium-sensitive dye and/or patch clamping for calcium influx channels could provide greater certainty as to the extent of calcium's contribution in hemin-mediated inotropy. Further work is also necessary to evaluate whether the potential molecular mechanisms underlying hemin-mediated inotropy identified herein in healthy tissues translate to functional changes in whole hearts post-AMI, with age/sex, as well as identify the potential mechanisms behind why hemin fails to increase cardiac contractility early (but not late) post-AMI (e.g. heme dyssynchrony, splenic macrophage recruitment). Even so, Chapter 4 marks a significant contribution to the field of hemin pharmacology through the identification of hemin as a novel cardiac inotrope (in both murine and human tissue models).

6.2.4 Therapeutic development strategies utilizing heme metabolism

In Chapter 5, I investigated the therapeutic potential of two novel strategies designed for more rapid targeted delivery/induction of HMOX1 to the infarcted heart: the encapsulation of hemin into a nanoparticle shell (Niohemin), and the exogenous delivery of functional HMOX1 using a cell-penetrating peptide (HMOX1-CPP). Using spectroscopy, Dynamic Light Scattering, and H9C2 cardiomyotubule culture, we characterized the fundamental physicochemical, pharmacokinetic, and pharmacodynamic properties of HMOX1-CPP and Niohemin, and investigated their therapeutic efficacy relative to hemin; the development of the novel nanoparticle, Niohemin—the first hemin-encapsulating nanoparticle of record using the novel niosome-class nanocarrier—is also documented herein.

Here I show that HMOX1-CPP and Niohemin are readily internalized to the cytoplasm of differentiated H9C2 cardiomyotubules (with Niohemin further co-localizing to lysosomes), and that both strategies are directly capable of conferring cytoprotection to cardiomyotubules against oxidative injury. We further demonstrate that HMOX1-CPP

confers cytoprotection more rapidly than hemin, but that simultaneous combination of the two therapeutics (at individually therapeutic concentrations) decreased overall cell survival. I also show for the first time that Niohemin confers cytoprotection directly to cardiomyotubules *in vitro*, and at a lower concentration than hemin alone—despite equivalent HMOX1 induction at 24h. Finally, I present preliminary evidence suggesting that Niohemin's nanodrug-release kinetics may be affected by an acidified environment *in vitro*, which—if further validated—could provide the fundamental evidence needed to proceed with *in vivo* exploration of pH-directed hemin therapy in an infarcted heart. Importantly, this study is the first to report the encapsulation of hemin within a niosome shell and is the second study to present data on nanoparticle-encapsulated hemin for therapeutic use. This study is also the first to characterize the differential effects between HMOX1-CPP and hemin in cardiomyotubules. Ultimately, Chapter 5 provides valuable insights into the therapeutic benefits/limitations and underlying molecular differences of two translational strategies for HMOX1 elevation: enzyme delivery (HMOX1-CPP) and substrate-mediated induction (hemin).

Further work is still necessary to fully characterize HMOX1-CPP and Niohemin's pharmacokinetics and pharmacodynamic effects. Here I showed that—in contrast to hemin administration at the same timepoints—HMOX1-CPP significantly improved cardiomyotubule viability when administered 4h pre- or simultaneously with H_2O_2 exposure. However, hemin has previously been shown to confer cytoprotection in differentiated H9C2 cardiomyotubules when administered earlier pre-oxidative injury, suggesting that more time may be necessary for its benefits to take optimal therapeutic effect. Unlike HMOX1-CPP (which delivers a functionally active enzyme), hemin requires several steps to increase intracellular HMOX1 levels and elicit antioxidant and anti-inflammatory effects—such as mRNA transcription, translation, protein folding, and the HMOX1-mediated accrual of biliverdin, carbon monoxide, and free iron. Whether differences in cytoprotection are attributable to differences in the rates of increased intracellular HMOX1 or conversion of heme/hemin into cytoprotective metabolites, peptide/hemin clearance, or cumulative HMOX1 activity remains uncertain and requires further temporal study.

Similarly, I show for the first time that niosome-encapsulated hemin directly confers cytoprotection to cardiomyotubules against oxidative injury *in vitro* and at a lower concentration than hemin alone, despite equivalent HMOX1 induction at 24h. These findings suggest that hemin's efficacy may be improved through niosome encapsulation and may not be dependent on peak HMOX1 levels alone, but rather on mechanistic differences in cellular internalization/catabolism between hemin and hemin released from niosomes. Although both HMOX1-CPP and Niohemin are internalized to the cytoplasm of H9C2 cardiomyotubules, it remains unclear how this is mechanistically achieved. Cell-penetrating peptides derived from modified human immunodeficiency virus transactivator of transcription (TAT) protein—such as the HMOX1-CPP described herein—are primarily internalized through clathrin-mediated endocytosis, caveolin-mediated endocytosis, and micropinocytosis [273], however it remains unclear whether these mechanisms are conserved across cardiomyotubules. Similarly, the cellular mechanism(s) underlying hemin internalization—in both its 'free' hemin and niosome-encapsulated states—also remain to be elucidated. Thus, further work characterizing the pharmacokinetic mechanisms of hemin, Niohemin, and HMOX1-CPP internalization is still necessary to optimize therapeutic efficiency in the timing and dosing of drug administration prior to *in vivo* AMI modeling.

In Chapter 5, I also present preliminary evidence suggesting that Niohemin's nanodrug-release kinetics may be affected by an acidified environment *in vitro* (mimicking the acidic shift anticipated in the heart's surrounding environment post-AMI). In differentiated H9C2 cardiomyotubules, acidified media further increased Niohemin-mediated HMOX1 induction compared to more basic media, with no differences observed between pH-modified media controls at baseline. However, further characterization of Niohemin's stability under various pH conditions—through imaging (i.e. transmission electron microscopy) and measurement of the electrical potential between the nanoparticle's surface and surrounding solvent (i.e. zeta potential) under controlled conditions—are needed before proceeding with *in vivo* exploration of pH-directed hemin therapy in an infarcted heart. Long-term stability at clinically-relevant storage temperatures and light exposures—as well as Niohemin's hemostatic stability

(i.e. absence of hemolytic effects) and immunotolerance—must also be measured prior to *in vivo* AMI modeling.

6.3 CONCLUSION

In conclusion, the results presented within this thesis provide valuable contributions to the fields of pharmacology and heme metabolism/regulation. The concept of elevating HMOX1 as a therapeutic strategy against AMI has existed for over 30 years, yet has focused almost exclusively on HMOX1 alone, without consideration of heme bioavailability or post-injury intervention. Here, we present fundamental new information regarding heme regulation in AMI and with pharmacological intervention, and evaluate the therapeutic potential of novel strategies for the treatment of AMI through heme metabolism. Collectively, the findings presented herein provide fundamental information with which to advance the therapeutic targeting of heme metabolism in the heart.

References

1 National Center for Health Statistics. Percentage of angina for adults aged 18 and over, United States, 2019—2022. National Health Interview Survey. Generated interactively: May 11 2023 from. https://wwwn.cdc.gov/NHISDataQueryTool/SHS_adult/index.html

2 Benjamin EJ, Virani SS, Callaway CW, *et al.* Heart Disease and Stroke Statistics-2018 Update: A Report From the American Heart Association. *Circulation*. 2018;137:e67–492.

3 Virani SS, Alonso A, Aparicio HJ, *et al.* Heart Disease and Stroke Statistics-2021 Update: A Report From the American Heart Association. *Circulation*. 2021;143:e254–743.

4 Jenča D, Melenovský V, Stehlik J, *et al.* Heart failure after myocardial infarction: incidence and predictors. *ESC Heart Fail*. 2021;8:222–37.

5 Sulo G, Igland J, Vollset SE, *et al.* Heart Failure Complicating Acute Myocardial Infarction; Burden and Timing of Occurrence: A Nation-wide Analysis Including 86 771 Patients From the Cardiovascular Disease in Norway (CVDNOR) Project. *J Am Heart Assoc*. 2016;5:e002667.

6 Hung J, Teng T-HK, Finn J, *et al.* Trends from 1996 to 2007 in incidence and mortality outcomes of heart failure after acute myocardial infarction: a population-based study of 20,812 patients with first acute myocardial infarction in Western Australia. *J Am Heart Assoc*. 2013;2:e000172.

7 Roger VL. Epidemiology of heart failure. *Circ Res*. 2013;113:646–59.

8 Lin H-H, Chen Y-H, Chang P-F, *et al.* Heme oxygenase-1 promotes neovascularization in ischemic heart by coinduction of VEGF and SDF-1. *J Mol Cell Cardiol*. 2008;45:44–55.

9 Clark JE, Foresti R, Sarathchandra P, *et al.* Heme oxygenase-1-derived bilirubin ameliorates postischemic myocardial dysfunction. *Am J Physiol Heart Circ Physiol*. 2000;278:H643-651.

10 Hangaishi M, Ishizaka N, Aizawa T, *et al.* Induction of heme oxygenase-1 can act protectively against cardiac ischemia/reperfusion in vivo. *Biochem Biophys Res Commun*. 2000;279:582–8.

11 Liu X, Simpson JA, Brunt KR, *et al.* Preemptive heme oxygenase-1 gene delivery reveals reduced mortality and preservation of left ventricular function 1 yr after acute myocardial infarction. *Am J Physiol Heart Circ Physiol*. 2007;293:H48-59.

12 Yet SF, Tian R, Layne MD, *et al.* Cardiac-specific expression of heme oxygenase-1 protects against ischemia and reperfusion injury in transgenic mice. *Circ Res*. 2001;89:168–73.

13 Melo LG, Agrawal R, Zhang L, *et al.* Gene therapy strategy for long-term myocardial protection using adeno-associated virus-mediated delivery of heme oxygenase gene. *Circulation*. 2002;105:602–7.

14 Ryter SW, Choi AMK. Targeting heme oxygenase-1 and carbon monoxide for therapeutic modulation of inflammation. *Transl Res J Lab Clin Med*. 2016;167:7–34.

15 Otterbein LE, Bach FH, Alam J, *et al.* Carbon monoxide has anti-inflammatory effects involving the mitogen-activated protein kinase pathway. *Nat Med*. 2000;6:422–8.

16 Baranano DE, Rao M, Ferris CD, *et al.* Biliverdin reductase: a major physiologic cytoprotectant. *Proc Natl Acad Sci U S A*. 2002;99:16093–8.

17 Lakkisto P, Csonka C, Fodor G, *et al.* The heme oxygenase inducer hemin protects against cardiac dysfunction and ventricular fibrillation in ischaemic/reperfused rat hearts: role of connexin 43. *Scand J Clin Lab Invest*. 2009;69:209–18.

18 Collino M, Pini A, Mugelli N, *et al.* Beneficial effect of prolonged heme oxygenase 1 activation in a rat model of chronic heart failure. *Dis Model Mech*. 2013;6:1012–20.

19 Khechaduri A, Bayeva M, Chang H-C, *et al.* Heme levels are increased in human failing hearts. *J Am Coll Cardiol*. 2013;61:1884–93.

20 Thygesen K, Alpert JS, Jaffe AS, *et al.* Third universal definition of myocardial infarction. *J Am Coll Cardiol*. 2012;60:1581–98.

21 Giordano FJ. Oxygen, oxidative stress, hypoxia, and heart failure. *J Clin Invest*. 2005;115:500–8.

22 Hamanaka RB, Chandel NS. Mitochondrial reactive oxygen species regulate hypoxic signaling. *Curr Opin Cell Biol*. 2009;21:894–9.

23 Inoue T, Ide T, Yamato M, *et al.* Time-dependent changes of myocardial and systemic oxidative stress are dissociated after myocardial infarction. *Free Radic Res*. 2009;43:37–46.

24 Neri M, Fineschi V, Di Paolo M, *et al.* Cardiac oxidative stress and inflammatory cytokines response after myocardial infarction. *Curr Vasc Pharmacol*. 2015;13:26–36.

25 Nian M, Lee P, Khaper N, *et al.* Inflammatory cytokines and postmyocardial infarction remodeling. *Circ Res*. 2004;94:1543–53.

26 Sutton MG, Sharpe N. Left ventricular remodeling after myocardial infarction: pathophysiology and therapy. *Circulation*. 2000;101:2981–8.

27 Swynghedauw B. Molecular mechanisms of myocardial remodeling. *Physiol Rev*. 1999;79:215–62.

28 Kehat I, Molkentin JD. Molecular pathways underlying cardiac remodeling during pathophysiological stimulation. *Circulation*. 2010;122:2727–35.

29 Hill JA, Karimi M, Kutschke W, *et al.* Cardiac hypertrophy is not a required compensatory response to short-term pressure overload. *Circulation*. 2000;101:2863–9.

30 Ito BR. Gradual onset of myocardial ischemia results in reduced myocardial infarction. Association with reduced contractile function and metabolic downregulation. *Circulation*. 1995;91:2058–70.

31 Fukuoka Y, Nakano A, Tama N, *et al.* Impaired myocardial microcirculation in the flow-glucose metabolism mismatch regions in revascularized acute myocardial infarction. *J Nucl Cardiol Off Publ Am Soc Nucl Cardiol*. 2017;24:1641–50.

32 Talman V, Ruskoaho H. Cardiac fibrosis in myocardial infarction-from repair and remodeling to regeneration. *Cell Tissue Res*. 2016;365:563–81.

33 Eadie AL, Simpson JA, Brunt KR. 'Fibroblast' pharmacotherapy - Advancing the next generation of therapeutics for clinical cardiology. *J Mol Cell Cardiol*. 2016;94:176–9.

34 Ottani V, Raspanti M, Ruggeri A. Collagen structure and functional implications. *Micron Oxf Engl 1993*. 2001;32:251–60.

35 Ogilvie LM, Edgett BA, Huber JS, *et al.* Hemodynamic assessment of diastolic function for experimental models. *Am J Physiol Heart Circ Physiol*. 2020;318:H1139–58.

36 Hilfiker-Kleiner D, Landmesser U, Drexler H. Molecular Mechanisms in Heart Failure: Focus on Cardiac Hypertrophy, Inflammation, Angiogenesis, and Apoptosis. *J Am Coll Cardiol*. 2006;48:A56–66.

37 Sutendra G, Dromparis P, Paulin R, *et al.* A metabolic remodeling in right ventricular hypertrophy is associated with decreased angiogenesis and a transition from a compensated to a decompensated state in pulmonary hypertension. *J Mol Med Berl Ger*. 2013;91:1315–27.

38 van den Borne SWM, Diez J, Blankesteijn WM, *et al.* Myocardial remodeling after infarction: the role of myofibroblasts. *Nat Rev Cardiol*. 2010;7:30–7.

39 Brower GL, Gardner JD, Forman MF, *et al.* The relationship between myocardial extracellular matrix remodeling and ventricular function. *Eur J Cardio-Thorac Surg Off J Eur Assoc Cardio-Thorac Surg*. 2006;30:604–10.

40 Hori M, Nishida K. Oxidative stress and left ventricular remodelling after myocardial infarction. *Cardiovasc Res*. 2009;81:457–64.

41 Semenza GL. Hypoxia-inducible factor 1 and cardiovascular disease. *Annu Rev Physiol*. 2014;76:39–56.

42 Dashkevich A, Hagl C, Beyersdorf F, *et al.* VEGF Pathways in the Lymphatics of Healthy and Diseased Heart. *Microcirc N Y N 1994*. 2016;23:5–14.

43 Sanchis-Gomar F, Garcia-Gimenez JL, Pareja-Galeano H, *et al.* Erythropoietin and the heart: physiological effects and the therapeutic perspective. *Int J Cardiol*. 2014;171:116–25.

44 Lee PJ, Jiang BH, Chin BY, *et al.* Hypoxia-inducible factor-1 mediates transcriptional activation of the heme oxygenase-1 gene in response to hypoxia. *J Biol Chem*. 1997;272:5375–81.

45 Mastrogiannaki M, Matak P, Keith B, *et al.* HIF-2alpha, but not HIF-1alpha, promotes iron absorption in mice. *J Clin Invest*. 2009;119:1159–66.

46 Kurian GA, Rajagopal R, Vedantham S, *et al.* The Role of Oxidative Stress in Myocardial Ischemia and Reperfusion Injury and Remodeling: Revisited. *Oxid Med Cell Longev*. 2016;2016:1656450.

47 Tonelli C, Chio IIC, Tuveson DA. Transcriptional Regulation by Nrf2. *Antioxid Redox Signal*. 2018;29:1727–45.

48 Alam J, Stewart D, Touchard C, *et al.* Nrf2, a Cap'n'Collar transcription factor, regulates induction of the heme oxygenase-1 gene. *J Biol Chem*. 1999;274:26071–8.

49 Itoh K, Wakabayashi N, Katoh Y, *et al.* Keap1 represses nuclear activation of antioxidant responsive elements by Nrf2 through binding to the amino-terminal Neh2 domain. *Genes Dev*. 1999;13:76–86.

50 Silvis MJM, Kaffka Genaamd Dengler SE, Odille CA, *et al.* Damage-Associated Molecular Patterns in Myocardial Infarction and Heart Transplantation: The Road to Translational Success. *Front Immunol*. 2020;11:599511.

51 Dutra FF, Bozza MT. Heme on innate immunity and inflammation. *Front Pharmacol*. 2014;5:115.

52 Mendonça R, Silveira AAA, Conran N. Red cell DAMPs and inflammation. *Inflamm Res Off J Eur Histamine Res Soc Al*. 2016;65:665–78.

53 Soares MP, Bozza MT. Red alert: labile heme is an alarmin. *Curr Opin Immunol*. 2016;38:94–100.

54 Wegiel B, Hauser CJ, Otterbein LE. Heme as a danger molecule in pathogen recognition. *Free Radic Biol Med*. 2015;89:651–61.

55 Chen Z, Eadie AL, Hall SR, *et al.* Assessment of hypoxia and TNF-alpha response by a vector with HRE and NF-kappaB response elements. *Front Biosci Sch Ed*. 2017;9:46–54.

56 Luo J-L, Kamata H, Karin M. IKK/NF-kappaB signaling: balancing life and death--a new approach to cancer therapy. *J Clin Invest*. 2005;115:2625–32.

57 Alam J, Cook JL. How many transcription factors does it take to turn on the heme oxygenase-1 gene? *Am J Respir Cell Mol Biol*. 2007;36:166–74.

58 van Uden P, Kenneth NS, Rocha S. Regulation of hypoxia-inducible factor-1alpha by NF-kappaB. *Biochem J*. 2008;412:477–84.

59 Peet C, Ivetic A, Bromage DI, *et al.* Cardiac monocytes and macrophages after myocardial infarction. *Cardiovasc Res*. 2020;116:1101–12.

60 Collet J-P, Thiele H, Barbato E, *et al.* 2020 ESC Guidelines for the management of acute coronary syndromes in patients presenting without persistent ST-segment elevation. *Eur Heart J*. 2021;42:1289–367.

61 O'Gara PT, Kushner FG, Ascheim DD, *et al.* 2013 ACCF/AHA Guideline for the Management of ST-Elevation Myocardial Infarction: A Report of the American College of Cardiology Foundation/American Heart Association Task Force on Practice Guidelines. *J Am Coll Cardiol*. 2013;61:e78–140.

62 Cohen M, Boiangiu C, Abidi M. Therapy for ST-Segment Elevation Myocardial Infarction Patients Who Present Late or Are Ineligible for Reperfusion Therapy. *J Am Coll Cardiol*. 2010;55:1895–906.

63 Antman EM, Anbe DT, Armstrong PW, *et al.* ACC/AHA guidelines for the management of patients with ST-elevation myocardial infarction: a report of the American College of Cardiology/American Heart Association Task Force on Practice Guidelines (Committee to Revise the 1999 Guidelines for the Management of Patients with Acute Myocardial Infarction). *Circulation*. 2004;110:e82-292.

64 Lindsey ML, Brunt KR, Kirk JA, *et al.* Guidelines for in vivo mouse models of myocardial infarction. *Am J Physiol Heart Circ Physiol*. 2021;321:H1056–73.

65 Patten RD, Hall-Porter MR. Small animal models of heart failure: development of novel therapies, past and present. *Circ Heart Fail*. 2009;2:138–44.

66 Lindsey ML, de Castro Brás LE, DeLeon-Pennell KY, *et al.* Reperfused vs. nonreperfused myocardial infarction: when to use which model. *Am J Physiol Heart Circ Physiol*. 2021;321:H208–13.

67 Pei H, Song X, Peng C, *et al.* TNF-α inhibitor protects against myocardial ischemia/reperfusion injury via Notch1-mediated suppression of oxidative/nitrative stress. *Free Radic Biol Med*. 2015;82:114–21.

68 Liu X, Simpson JA, Brunt KR, *et al.* Preemptive heme oxygenase-1 gene delivery reveals reduced mortality and preservation of left ventricular function 1 yr after acute myocardial infarction. *Am J Physiol Heart Circ Physiol*. 2007;293:H48-59.

69 Ayer A, Zarjou A, Agarwal A, *et al.* Heme Oxygenases in Cardiovascular Health and Disease. *Physiol Rev*. 2016;96:1449–508.

70 Kumar S, Bandyopadhyay U. Free heme toxicity and its detoxification systems in human. *Toxicol Lett*. 2005;157:175–88.

71 Aisen P, Enns C, Wessling-Resnick M. Chemistry and biology of eukaryotic iron metabolism. *Int J Biochem Cell Biol*. 2001;33:940–59.

72 Gutteridge JM. Iron promoters of the Fenton reaction and lipid peroxidation can be released from haemoglobin by peroxides. *FEBS Lett*. 1986;201:291–5.

73 McCoubrey WK, Huang TJ, Maines MD. Isolation and characterization of a cDNA from the rat brain that encodes hemoprotein heme oxygenase-3. *Eur J Biochem*. 1997;247:725–32.

74 Scapagnini G, D'Agata V, Calabrese V, *et al.* Gene expression profiles of heme oxygenase isoforms in the rat brain. *Brain Res*. 2002;954:51–9.

75 Hayashi S, Omata Y, Sakamoto H, *et al.* Characterization of rat heme oxygenase-3 gene. Implication of processed pseudogenes derived from heme oxygenase-2 gene. *Gene*. 2004;336:241–50.

76 Maines MD. Heme oxygenase: function, multiplicity, regulatory mechanisms, and clinical applications. *FASEB J Off Publ Fed Am Soc Exp Biol*. 1988;2:2557–68.

77 Maines MD, Trakshel GM, Kutty RK. Characterization of two constitutive forms of rat liver microsomal heme oxygenase. Only one molecular species of the enzyme is inducible. *J Biol Chem*. 1986;261:411–9.

78 Chau L-Y. Heme oxygenase-1: emerging target of cancer therapy. *J Biomed Sci*. 2015;22:22.

79 Lin Q, Weis S, Yang G, *et al.* Heme oxygenase-1 protein localizes to the nucleus and activates transcription factors important in oxidative stress. *J Biol Chem*. 2007;282:20621–33.

80 Dunn LL, Midwinter RG, Ni J, *et al.* New insights into intracellular locations and functions of heme oxygenase-1. *Antioxid Redox Signal*. 2014;20:1723–42.

81 Bindu S, Pal C, Dey S, *et al.* Translocation of heme oxygenase-1 to mitochondria is a novel cytoprotective mechanism against non-steroidal anti-inflammatory drug-induced mitochondrial oxidative stress, apoptosis, and gastric mucosal injury. *J Biol Chem*. 2011;286:39387–402.

82 Hull TD, Boddu R, Guo L, *et al.* Heme oxygenase-1 regulates mitochondrial quality control in the heart. *JCI Insight*. 2016;1:e85817.

83 Sun J, Hoshino H, Takaku K, *et al.* Hemoprotein Bach1 regulates enhancer availability of heme oxygenase-1 gene. *EMBO J*. 2002;21:5216–24.

84 He CH, Gong P, Hu B, *et al.* Identification of activating transcription factor 4 (ATF4) as an Nrf2-interacting protein. Implication for heme oxygenase-1 gene regulation. *J Biol Chem*. 2001;276:20858–65.

85 Yang G, Nguyen X, Ou J, *et al.* Unique effects of zinc protoporphyrin on HO-1 induction and apoptosis. *Blood*. 2001;97:1306–13.

86 Exner M, Minar E, Wagner O, *et al.* The role of heme oxygenase-1 promoter polymorphisms in human disease. *Free Radic Biol Med*. 2004;37:1097–104.

87 Chen Y-H, Lin S-J, Lin M-W, *et al.* Microsatellite polymorphism in promoter of heme oxygenase-1 gene is associated with susceptibility to coronary artery disease in type 2 diabetic patients. *Hum Genet*. 2002;111:1–8.

88 Qiao H, Sai X, Gai L, *et al.* Association between heme oxygenase 1 gene promoter polymorphisms and susceptibility to coronary artery disease: a HuGE review and meta-analysis. *Am J Epidemiol*. 2014;179:1039–48.

89 Doberer D, Haschemi A, Andreas M, *et al.* Haem arginate infusion stimulates haem oxygenase-1 expression in healthy subjects. *Br J Pharmacol*. 2010;161:1751–62.

90 Poss KD, Tonegawa S. Heme oxygenase 1 is required for mammalian iron reutilization. *Proc Natl Acad Sci U S A*. 1997;94:10919–24.

91 Kovtunovych G, Eckhaus MA, Ghosh MC, *et al.* Dysfunction of the heme recycling system in heme oxygenase 1-deficient mice: effects on macrophage viability and tissue iron distribution. *Blood*. 2010;116:6054–62.

92 Yet SF, Perrella MA, Layne MD, *et al.* Hypoxia induces severe right ventricular dilatation and infarction in heme oxygenase-1 null mice. *J Clin Invest*. 1999;103:R23-29.

93 Yachie A, Niida Y, Wada T, *et al.* Oxidative stress causes enhanced endothelial cell injury in human heme oxygenase-1 deficiency. *J Clin Invest*. 1999;103:129–35.

94 Radhakrishnan N, Yadav SP, Sachdeva A, *et al.* Human heme oxygenase-1 deficiency presenting with hemolysis, nephritis, and asplenia. *J Pediatr Hematol Oncol*. 2011;33:74–8.

95 Sharma VS, Magde D. Activation of soluble guanylate cyclase by carbon monoxide and nitric oxide: a mechanistic model. *Methods San Diego Calif*. 1999;19:494–505.

96 Sato K, Balla J, Otterbein L, *et al.* Carbon monoxide generated by heme oxygenase-1 suppresses the rejection of mouse-to-rat cardiac transplants. *J Immunol Baltim Md 1950*. 2001;166:4185–94.

97 Verma A, Hirsch DJ, Glatt CE, *et al.* Carbon monoxide: a putative neural messenger. *Science*. 1993;259:381–4.

98 Ingi T, Cheng J, Ronnett GV. Carbon monoxide: an endogenous modulator of the nitric oxide-cyclic GMP signaling system. *Neuron*. 1996;16:835–42.

99 Anderson GJ, Frazer DM. Current understanding of iron homeostasis. *Am J Clin Nutr*. 2017;106:1559S-1566S.

100 Shah R, Agarwal AK. Anemia associated with chronic heart failure: current concepts. *Clin Interv Aging*. 2013;8:111–22.

101 Huang C-H, Chang C-C, Kuo C-L, *et al.* Serum iron concentration, but not hemoglobin, correlates with TIMI risk score and 6-month left ventricular performance after primary angioplasty for acute myocardial infarction. *PloS One*. 2014;9:e104495.

102 Frise MC, Cheng H-Y, Nickol AH, *et al.* Clinical iron deficiency disturbs normal human responses to hypoxia. *J Clin Invest*. 2016;126:2139–50.

103 Vulapalli SR, Chen Z, Chua BHL, *et al.* Cardioselective overexpression of HO-1 prevents I/R-induced cardiac dysfunction and apoptosis. *Am J Physiol Heart Circ Physiol*. 2002;283:H688-694.

104 Brunt KR, Tsuji MR, Lai JH, *et al.* Heme oxygenase-1 inhibits pro-oxidant induced hypertrophy in HL-1 cardiomyocytes. *Exp Biol Med Maywood NJ*. 2009;234:582–94.

105 Pachori AS, Smith A, McDonald P, *et al.* Heme-oxygenase-1-induced protection against hypoxia/reoxygenation is dependent on biliverdin reductase and its interaction with PI3K/Akt pathway. *J Mol Cell Cardiol*. 2007;43:580–92.

106 Nath KA, Balla G, Vercellotti GM, *et al.* Induction of heme oxygenase is a rapid, protective response in rhabdomyolysis in the rat. *J Clin Invest*. 1992;90:267–70.

107 Allwood MA, Kinobe RT, Ballantyne L, *et al.* Heme oxygenase-1 overexpression exacerbates heart failure with aging and pressure overload but is protective against

isoproterenol-induced cardiomyopathy in mice. *Cardiovasc Pathol Off J Soc Cardiovasc Pathol*. 2014;23:231–7.

108 Chen C, Huo R, Tong Y, *et al.* Systemic heme oxygenase-1 transgenic overexpression aggravates pressure overload-induced cardiac hypertrophy in mice. *Cell Physiol Biochem Int J Exp Cell Physiol Biochem Pharmacol*. 2011;28:25–32.

109 Jais A, Einwallner E, Sharif O, *et al.* Heme oxygenase-1 drives metaflammation and insulin resistance in mouse and man. *Cell*. 2014;158:25–40.

110 Mense SM, Zhang L. Heme: a versatile signaling molecule controlling the activities of diverse regulators ranging from transcription factors to MAP kinases. *Cell Res*. 2006;16:681–92.

111 Gray HB, Winkler JR. Electron transfer in proteins. *Annu Rev Biochem*. 1996;65:537–61.

112 White KA, Marletta MA. Nitric oxide synthase is a cytochrome P-450 type hemoprotein. *Biochemistry*. 1992;31:6627–31.

113 Tuteja N, Chandra M, Tuteja R, *et al.* Nitric Oxide as a Unique Bioactive Signaling Messenger in Physiology and Pathophysiology. *J Biomed Biotechnol*. 2004;2004:227–37.

114 Murad F. Shattuck Lecture. Nitric oxide and cyclic GMP in cell signaling and drug development. *N Engl J Med*. 2006;355:2003–11.

115 Priviero FBM, Webb RC. Heme-dependent and independent soluble guanylate cyclase activators and vasodilation. *J Cardiovasc Pharmacol*. 2010;56:229–33.

116 Chen J-J. Heme-regulated eIF-2α kinase. *Transl Control Gene Expr*. 2000;529–46.

117 Otterbein LE, Foresti R, Motterlini R. Heme Oxygenase-1 and Carbon Monoxide in the Heart: The Balancing Act Between Danger Signaling and Pro-Survival. *Circ Res*. 2016;118:1940–59.

118 Anderson KE, Sassa S, Bishop DF, *et al.* Disorders of Heme Biosynthesis: X-Linked Sideroblastic Anemia and the Porphyrias. In: Valle DL, Antonarakis S, Ballabio A, *et al.*, eds. *The Online Metabolic and Molecular Bases of Inherited Disease*. New York, NY: McGraw-Hill Education 2019. ommbid.mhmedical.com/content.aspx?aid=1181451356 (accessed 6 January 2024)

119 Ajioka RS, Phillips JD, Kushner JP. Biosynthesis of heme in mammals. *Biochim Biophys Acta*. 2006;1763:723–36.

120 Melefors O, Goossen B, Johansson HE, *et al.* Translational control of 5-aminolevulinate synthase mRNA by iron-responsive elements in erythroid cells. *J Biol Chem*. 1993;268:5974–8.

121 Surinya KH, Cox TC, May BK. Transcriptional regulation of the human erythroid 5-aminolevulinate synthase gene. Identification of promoter elements and role of regulatory proteins. *J Biol Chem*. 1997;272:26585–94.

122 Gutiérrez L, Caballero N, Fernández-Calleja L, *et al.* Regulation of GATA1 levels in erythropoiesis. *IUBMB Life*. 2020;72:89–105.

123 Handschin C, Lin J, Rhee J, *et al.* Nutritional regulation of hepatic heme biosynthesis and porphyria through PGC-1alpha. *Cell*. 2005;122:505–15.

124 Sassa S, Granick S, Bickers DR, *et al.* Studies on the inheritance of human erythrocyte delta-aminolevulinate dehydratase and uroporphyrinogen synthetase. *Enzyme*. 1973;16:326–33.

125 Moore MR, Goldberg A, Yeung-Laiwah AA. Lead effects on the heme biosynthetic pathway. Relationship to toxicity. *Ann N Y Acad Sci*. 1987;514:191–203.

126 Sassa S, Kappas A. Succinylacetone inhibits delta-aminolevulinate dehydratase and potentiates the drug and steroid induction of delta-aminolevulinate synthase in liver. *Trans Assoc Am Physicians*. 1982;95:42–52.

127 Andrews NC. When is a heme transporter not a heme transporter? When it's a folate transporter. *Cell Metab*. 2007;5:5–6.

128 Koury MJ, Ponka P. New insights into erythropoiesis: the roles of folate, vitamin B12, and iron. *Annu Rev Nutr*. 2004;24:105–31.

129 Shayeghi M, Latunde-Dada GO, Oakhill JS, *et al.* Identification of an intestinal heme transporter. *Cell*. 2005;122:789–801.

130 Vagany V, Robinson S, Chernova T, *et al.* Complex response to physiological and drug-induced hepatic heme demand in monoallelic ALAS1 mice. *Mol Genet Metab Rep*. 2021;29:100818.

131 Rishi G, Subramaniam VN. The liver in regulation of iron homeostasis. *Am J Physiol Gastrointest Liver Physiol*. 2017;313:G157–65.

132 Donovan A, Lima CA, Pinkus JL, *et al.* The iron exporter ferroportin/Slc40a1 is essential for iron homeostasis. *Cell Metab*. 2005;1:191–200.

133 Gozzelino R, Jeney V, Soares MP. Mechanisms of cell protection by heme oxygenase-1. *Annu Rev Pharmacol Toxicol*. 2010;50:323–54.

134 Chiou B, Connor JR. Emerging and Dynamic Biomedical Uses of Ferritin. *Pharm Basel Switz*. 2018;11:124.

135 Nemeth E, Tuttle MS, Powelson J, *et al.* Hepcidin regulates cellular iron efflux by binding to ferroportin and inducing its internalization. *Science*. 2004;306:2090–3.

136 Ganz T, Nemeth E. Hepcidin and iron homeostasis. *Biochim Biophys Acta*. 2012;1823:1434–43.

137 Eisenstein RS, Garcia-Mayol D, Pettingell W, *et al.* Regulation of ferritin and heme oxygenase synthesis in rat fibroblasts by different forms of iron. *Proc Natl Acad Sci U S A*. 1991;88:688–92.

138 Mancias JD, Wang X, Gygi SP, *et al.* Quantitative proteomics identifies NCOA4 as the cargo receptor mediating ferritinophagy. *Nature*. 2014;509:105–9.

139 Muñoz M, García-Erce JA, Remacha ÁF. Disorders of iron metabolism. Part II: iron deficiency and iron overload. *J Clin Pathol*. 2011;64:287–96.

140 Andrews NC. Iron homeostasis: insights from genetics and animal models. *Nat Rev Genet*. 2000;1:208–17.

141 Wang G, Hamid T, Keith RJ, *et al.* Cardioprotective and antiapoptotic effects of heme oxygenase-1 in the failing heart. *Circulation*. 2010;121:1912–25.

142 Hinkel R, Lange P, Petersen B, *et al.* Heme Oxygenase-1 Gene Therapy Provides Cardioprotection Via Control of Post-Ischemic Inflammation: An Experimental Study in a Pre-Clinical Pig Model. *J Am Coll Cardiol*. 2015;66:154–65.

143 Domenger C, Grimm D. Next-generation AAV vectors-do not judge a virus (only) by its cover. *Hum Mol Genet*. 2019;28:R3–14.

144 Paulk N. Gene Therapy: It's Time to Talk about High-Dose AAV. GEN - Genet. Eng. Biotechnol. News. 2020. https://www.genengnews.com/insights/gene-therapy-its-time-to-talk-about-high-dose-aav/ (accessed 18 July 2023)

145 Vitali SH, Mitsialis SA, Liang OD, *et al.* Divergent cardiopulmonary actions of heme oxygenase enzymatic products in chronic hypoxia. *PloS One*. 2009;4:e5978.

146 Ryter SW, Otterbein LE. Carbon monoxide in biology and medicine. *BioEssays News Rev Mol Cell Dev Biol*. 2004;26:270–80.

147 Hopper CP, Meinel L, Steiger C, *et al.* Where is the Clinical Breakthrough of Heme Oxygenase-1 / Carbon Monoxide Therapeutics? *Curr Pharm Des*. 2018;24:2264–82.

148 Motterlini R, Haas B, Foresti R. Emerging concepts on the anti-inflammatory actions of carbon monoxide-releasing molecules (CO-RMs). *Med Gas Res*. 2012;2:28.

149 Nakao A, Neto JS, Kanno S, *et al.* Protection against ischemia/reperfusion injury in cardiac and renal transplantation with carbon monoxide, biliverdin and both. *Am J Transplant Off J Am Soc Transplant Am Soc Transpl Surg*. 2005;5:282–91.

150 Venkatachalam AB, Livingstone SM, Hu Q, *et al.* Delivery of Soluble Heme Oxygenase 1 Cell-Penetrating Peptide into Liver Cells in in vitro and ex vivo Models of Cold Ischemia. *Eur Surg Res Eur Chir Forsch Rech Chir Eur*. 2017;58:51–68.

151 Tenhunen R, Tokola O, Lindén IB. Haem arginate: a new stable haem compound. *J Pharm Pharmacol*. 1987;39:780–6.

152 Konrad FM, Knausberg U, Höne R, *et al.* Tissue heme oxygenase-1 exerts anti-inflammatory effects on LPS-induced pulmonary inflammation. *Mucosal Immunol*. 2016;9:98–111.

153 Chi X, Guo N, Yao W, *et al.* Induction of heme oxygenase-1 by hemin protects lung against orthotopic autologous liver transplantation-induced acute lung injury in rats. *J Transl Med*. 2016;14:35.

154 Jadhav A, Torlakovic E, Ndisang JF. Hemin therapy attenuates kidney injury in deoxycorticosterone acetate-salt hypertensive rats. *Am J Physiol Renal Physiol*. 2009;296:F521-534.

155 Han Q, Yeung SC, Ip MSM, *et al.* Intermittent hypoxia-induced NF-κB and HO-1 regulation in human endothelial EA.hy926 cells. *Cell Biochem Biophys*. 2013;66:431–41.

156 Worou M-E, Belmokhtar K, Bonnet P, *et al.* Hemin decreases cardiac oxidative stress and fibrosis in a rat model of systemic hypertension via PI3K/Akt signalling. *Cardiovasc Res*. 2011;91:320–9.

157 Datla SR, Dusting GJ, Mori TA, *et al.* Induction of heme oxygenase-1 in vivo suppresses NADPH oxidase derived oxidative stress. *Hypertens Dallas Tex 1979*. 2007;50:636–42.

158 Green D, Reynolds N, Klein J, *et al.* The inactivation of hemostatic factors by hematin. *J Lab Clin Med*. 1983;102:361–9.

159 Ryter SW, Choi AMK. Targeting heme oxygenase-1 and carbon monoxide for therapeutic modulation of inflammation. *Transl Res J Lab Clin Med*. 2016;167:7–34.

160 Otterbein LE, Bach FH, Alam J, *et al.* Carbon monoxide has anti-inflammatory effects involving the mitogen-activated protein kinase pathway. *Nat Med*. 2000;6:422–8.

161 Baranano DE, Rao M, Ferris CD, *et al.* Biliverdin reductase: a major physiologic cytoprotectant. *Proc Natl Acad Sci U S A*. 2002;99:16093–8.

162 Collino M, Pini A, Mugelli N, *et al.* Beneficial effect of prolonged heme oxygenase 1 activation in a rat model of chronic heart failure. *Dis Model Mech*. 2013;6:1012–20.

163 Food and Drug Administration. Panhematin-Orphan Drug Designations and Approvals. https://www.accessdata.fda.gov/scripts/opdlisting/oopd/detailedIndex.cfm?cfgridkey=683 (accessed 28 March 2021)

164 Shan H, Li T, Zhang L, *et al.* Heme oxygenase-1 prevents heart against myocardial infarction by attenuating ischemic injury-induced cardiomyocytes senescence. *EBioMedicine*. 2019;39:59–68.

165 Eadie AL, Brunt KR, Herder M. Exploring the Food and Drug Administration's review and approval of Entresto (sacubitril/valsartan). *Pharmacol Res Perspect*. 2021;9:e00794.

166 Hart B, Lundh A, Bero L. Effect of reporting bias on meta-analyses of drug trials: reanalysis of meta-analyses. *BMJ*. 2012;344:d7202.

167 Heneghan CJ, Onakpoya I, Thompson M, *et al.* Zanamivir for influenza in adults and children: systematic review of clinical study reports and summary of regulatory comments. *BMJ*. 2014;348:g2547.

168 Rising K, Bacchetti P, Bero L. Reporting bias in drug trials submitted to the Food and Drug Administration: review of publication and presentation. *PLoS Med*. 2008;5:e217; discussion e217.

169 Turner EH, Matthews AM, Linardatos E, *et al.* Selective publication of antidepressant trials and its influence on apparent efficacy. *N Engl J Med*. 2008;358:252–60.

170 Vitry AI. Reporting of studies on new medicines in major medical journals: a case study in breast cancer. *Clin Pharmacol Ther*. 2010;87:398–400.

171 Recordati Rare Diseases Inc. (Disclosed by Health Canada). Panhematin® (Hemin for Injection) Module 2.5: Clinical Overview. https://clinical-information.canada.ca/ci-rc-vu.pdf?file=clinical-overview.pdf&id=212276 (accessed 7 August 2023)

172 Di Pierro E, Granata F. Nutrients and Porphyria: An Intriguing Crosstalk. *Int J Mol Sci*. 2020;21:3462.

173 Recordati Rare Diseases Canada Inc. Panhematin® Product Monograph. 2018. https://pdf.hres.ca/dpd_pm/00046317.PDF (accessed 7 August 2023)

174 Bonkowsky HL, Tschudy DP, Collins A, *et al.* Repression of the overproduction of porphyrin precursors in acute intermittent porphyria by intravenous infusions of hematin. *Proc Natl Acad Sci U S A*. 1971;68:2725–9.

175 Food and Drug Administration. Highlights of Prescribing Information-Panhematin label 05/2020. 2020. https://dailymed.nlm.nih.gov/dailymed/fda/fdaDrugXsl.cfm?setid=9984267a-4d57-4444-9bb5-16bca7dea691&type=display (accessed 28 April 2021)

176 Recordati Rare Diseases Inc. (Disclosed by Health Canada). Panhematin® (Hemin for Injection) Module 2.7.1: Summary of Biopharmaceutic Studies and Associated Analytical Methods. https://clinical-information.canada.ca/ci-rc-vu.pdf?file=summary-biopharm.pdf&id=212276 (accessed 7 August 2023)

177 Watson CJ, Pierach CA, Bossenmaier I, *et al.* Use of hematin in the acute attack of the 'inducible' hepatic prophyrias. *Adv Intern Med*. 1978;23:265–86.

178 Pierach CA, Bossenmaier I, Cardinal R, *et al.* Hematin therapy in porphyric attacks. *Klin Wochenschr*. 1980;58:829–32.

179 McColl KE, Moore MR, Thompson GG, *et al.* Treatment with haematin in acute hepatic porphyria. *Q J Med*. 1981;50:161–74.

180 Lamon JM, Frykholm BC, Hess RA, *et al.* Hematin therapy for acute porphyria. *Medicine (Baltimore)*. 1979;58:252–69.

181 Lamon JM, Frykholm BC, Hess RA, Tschudy DP. Hematin therapy in acute porphyria. *ASCI Genet*. 1977;471A:128.

182 Anderson KE, Collins S. Open-label study of hemin for acute porphyria: clinical practice implications. *Am J Med*. 2006;119:801.e19-24.

183 Hemin for Injection (Panhematin): Budget Impact Analysis. Ottawa: CADTH; 2019 Oct. (CADTH Technology Review;no 24.

184 Stein P, Badminton M, Rees D. Update review of the acute porphyrias. *Br J Haematol*. 2017;176. doi: 10.1111/bjh.14459

185 Recordati Rare Diseases Inc. (Disclosed by Health Canada). Panhematin® (Hemin for Injection) Module 2.7.4: Summary of Clinical Safety. https://clinical-information.canada.ca/ci-rc-vu.pdf?file=summary-clin-pharm.pdf&id=212276 (accessed 10 August 2023)

186 Tokola O, Lindén IB, Tenhunen R. The effects of haem arginate and haematin upon the allylisopropylacetamide induced experimental porphyria in rats. *Pharmacol Toxicol*. 1987;61:75–8.

187 Siegert SWK, Holt RJ. Physicochemical properties, pharmacokinetics, and pharmacodynamics of intravenous hematin: a literature review. *Adv Ther*. 2008;25:842–57.

188 Bloomer JR. Liver metabolism of porphyrins and haem. *J Gastroenterol Hepatol*. 1998;13:324–9.

189 Badminton MN, Deybach J-C. Treatment of an acute attack of porphyria during pregnancy. *Eur J Neurol*. 2006;13:668–9.

190 Bonkovsky HL, Maddukuri VC, Yazici C, *et al.* Acute porphyrias in the USA: features of 108 subjects from porphyrias consortium. *Am J Med*. 2014;127:1233–41.

191 Tokola O, Tenhunen R, Volin L, *et al.* Pharmacokinetics of intravenously administered haem arginate. *Br J Clin Pharmacol*. 1986;22:331–5.

192 Sears DA, Huser HJ. Plasma hematin-binding and clearance in the rhesus monkey. *Proc Soc Exp Biol Med Soc Exp Biol Med N Y N*. 1966;121:111–6.

193 Recordati Rare Diseases Inc./Orphan Europe SARL,. Normosang Summary of Product Characteristics, Labelling and Package Leaflet.

194 Recordati Rare Diseases Inc. (Disclosed by Health Canada). Panhematin® (Hemin for Injection) Module 2.7.2: Summary of Clinical Pharmacology Studies. https://clinical-information.canada.ca/ci-rc-vu.pdf?file=summary-clin-pharm.pdf&id=212276 (accessed 10 August 2023)

195 Andreas M, Oeser C, Kainz F-M, *et al.* Intravenous Heme Arginate Induces HO-1 (Heme Oxygenase-1) in the Human Heart. *Arterioscler Thromb Vasc Biol*. 2018;38:2755–62.

196 Does Heme Oxygenase-1 Induction Ameliorate Cardiac Injury After Myocardial Infarction? | ClinicalTrials.gov. https://www.clinicaltrials.gov/study/NCT00483587?term=NCT00483587&rank=1 (accessed 17 September 2023)

197 Ruifrok W-PT. Erythropoietin in Heart Failure: Effects beyond Erythropoiesis (Thesis) Chapter 7. 2011. https://pure.rug.nl/ws/portalfiles/portal/14459371/12complete.pdf (accessed 17 September 2023)

198 Food and Drug Administration. Guidance for Industry: Estimating the Maximum Safe Starting Dose in Initial Clinical Trials for Therapeutics in Adult Healthy Volunteers (2005).

199 Frei P, Minder EI, Corti N, *et al.* Liver Transplantation because of Acute Liver Failure due to Heme Arginate Overdose in a Patient with Acute Intermittent Porphyria. *Case Rep Gastroenterol*. 2012;6:190–6.

200 Dhar GJ, Bossenmaier I, Cardinal R, *et al.* Transitory renal failure following rapid administration of a relatively large amount of hematin in a patient with acute intermittent porphyria in clinical remission. *Acta Med Scand*. 1978;203:437–43.

201 Kostrzewska E, Gregor A, Tarczyńska-Nosal S. Heme arginate (Normosang) in the treatment of attacks of acute hepatic porphyrias. *Mater Medica Pol Pol J Med Pharm*. 1991;23:259–62.

202 Simionatto CS, Cabal R, Jones RL, *et al.* Thrombophlebitis and disturbed hemostasis following administration of intravenous hematin in normal volunteers. *Am J Med*. 1988;85:538–40.

203 Peterson A, Bossenmaier I, Cardinal R, *et al.* Hematin treatment of acute porphyria. Early remission of an almost fatal relapse. *JAMA*. 1976;235:520–2.

204 McColl KE, Thompson GT, Moore MR, *et al.* Haematin therapy and leucocyte delta-aminolevulinic-acid-synthase activity in prolonged attack of acute porphyria. *Lancet Lond Engl*. 1979;1:133–4.

205 Morris DL, Dudley MD, Pearson RD. Coagulopathy associated with hematin treatment for acute intermittent porphyria. *Ann Intern Med*. 1981;95:700–1.

206 Petersen JM, Pierach CA. Hematin-induced hemolysis in acute porphyria. *Ann Intern Med*. 1984;101:877–8.

207 Khanderia U. Circulatory collapse associated with hemin therapy for acute intermittent porphyria. *Clin Pharm*. 1986;5:690–2.

208 Green D, Ts'ao CH. Hematin: effects on hemostasis. *J Lab Clin Med*. 1990;115:144–7.

209 Bonkowsky HL, Tschudy DP, Collins A, *et al.* Repression of the overproduction of porphyrin precursors in acute intermittent porphyria by intravenous infusions of hematin. *Proc Natl Acad Sci U S A*. 1971;68:2725–9.

210 Pierach CA, Bossenmaier I, Cardinal R, *et al.* Hematin therapy in porphyric attacks. *Klin Wochenschr*. 1980;58:829–32.

211 Bissell DM. Treatment of acute hepatic porphyria with hematin. *J Hepatol*. 1988;6:1–7.

212 Dhar GJ, Bossenmaier I, Petryka ZJ, *et al.* Effects of hematin in hepatic porphyria. Further studies. *Ann Intern Med*. 1975;83:20–30.

213 Berberat PO, Katori M, Kaczmarek E, *et al.* Heavy chain ferritin acts as an antiapoptotic gene that protects livers from ischemia reperfusion injury. *FASEB J Off Publ Fed Am Soc Exp Biol*. 2003;17:1724–6.

214 Anderson CP, Shen M, Eisenstein RS, *et al.* Mammalian iron metabolism and its control by iron regulatory proteins. *Biochim Biophys Acta*. 2012;1823:1468–83.

215 Yoshino K, Munakata H, Kuge O, *et al.* Haeme-regulated degradation of delta-aminolevulinate synthase 1 in rat liver mitochondria. *J Biochem (Tokyo)*. 2007;142:453–8.

216 Kubota Y, Nomura K, Katoh Y, *et al.* Novel Mechanisms for Heme-dependent Degradation of ALAS1 Protein as a Component of Negative Feedback Regulation of Heme Biosynthesis. *J Biol Chem*. 2016;291:20516–29.

217 Chapple SJ, Keeley TP, Mastronicola D, *et al.* Bach1 differentially regulates distinct Nrf2-dependent genes in human venous and coronary artery endothelial cells adapted to physiological oxygen levels. *Free Radic Biol Med*. 2016;92:152–62.

218 Bodyak N, Kang PM, Hiromura M, *et al.* Gene expression profiling of the aging mouse cardiac myocytes. *Nucleic Acids Res*. 2002;30:3788–94.

219 Sudan K, Vijayan V, Madyaningrana K, *et al.* TLR4 activation alters labile heme levels to regulate BACH1 and heme oxygenase-1 expression in macrophages. *Free Radic Biol Med*. 2019;137:131–42.

220 Zenke-Kawasaki Y, Dohi Y, Katoh Y, *et al.* Heme induces ubiquitination and degradation of the transcription factor Bach1. *Mol Cell Biol*. 2007;27:6962–71.

221 Lavrovsky Y, Schwartzman ML, Levere RD, *et al.* Identification of binding sites for transcription factors NF-kappa B and AP-2 in the promoter region of the human heme oxygenase 1 gene. *Proc Natl Acad Sci U S A*. 1994;91:5987–91.

222 Jürgensen JS, Rosenberger C, Wiesener MS, *et al.* Persistent induction of HIF-1alpha and -2alpha in cardiomyocytes and stromal cells of ischemic myocardium. *FASEB J Off Publ Fed Am Soc Exp Biol*. 2004;18:1415–7.

223 Xu B, Zhang J, Strom J, *et al.* Myocardial ischemic reperfusion induces de novo Nrf2 protein translation. *Biochim Biophys Acta*. 2014;1842:1638–47.

224 Frangogiannis NG. The mechanistic basis of infarct healing. *Antioxid Redox Signal*. 2006;8:1907–39.

225 Li L, Grenard P, Nhieu JTV, *et al.* Heme oxygenase-1 is an antifibrogenic protein in human hepatic myofibroblasts. *Gastroenterology*. 2003;125:460–9.

226 Sawicki KT, Shang M, Wu R, *et al.* Increased Heme Levels in the Heart Lead to Exacerbated Ischemic Injury. *J Am Heart Assoc*. 2015;4:e002272.

227 Warnatz H-J, Schmidt D, Manke T, *et al.* The BTB and CNC homology 1 (BACH1) target genes are involved in the oxidative stress response and in control of the cell cycle. *J Biol Chem*. 2011;286:23521–32.

228 Figueiredo RT, Fernandez PL, Mourao-Sa DS, *et al.* Characterization of heme as activator of Toll-like receptor 4. *J Biol Chem*. 2007;282:20221–9.

229 Corsonello A, Pedone C, Incalzi RA. Age-related pharmacokinetic and pharmacodynamic changes and related risk of adverse drug reactions. *Curr Med Chem*. 2010;17:571–84.

230 Granick S. The induction in vitro of the synthesis of delta-aminolevulinic acid synthetase in chemical porphyria: a response to certain drugs, sex hormones, and foreign chemicals. *J Biol Chem*. 1966;241:1359–75.

231 Guo W, Bachman E, Vogel J, *et al.* The effects of short-term and long-term testosterone supplementation on blood viscosity and erythrocyte deformability in healthy adult mice. *Endocrinology*. 2015;156:1623–9.

232 Rifkind AB, Gillette PN, Song CS, *et al.* Induction of hepatic delta-amino-levulinic acid synthetase by oral contraceptive steroids. *J Clin Endocrinol Metab*. 1970;30:330–5.

233 Choi S-Y, Koh KH, Jeong H. Isoform-specific regulation of cytochromes P450 expression by estradiol and progesterone. *Drug Metab Dispos Biol Fate Chem*. 2013;41:263–9.

234 Tomczyk M, Kraszewska I, Szade K, *et al.* Splenic Ly6Chi monocytes contribute to adverse late post-ischemic left ventricular remodeling in heme oxygenase-1 deficient mice. *Basic Res Cardiol*. 2017;112:39.

235 Cho KH, Han X, Ahn JH, *et al.* Long-Term Outcomes of Patients With Late Presentation of ST-Segment Elevation Myocardial Infarction. *J Am Coll Cardiol*. 2021;77:1859–70.

236 McNair PW, Bilchick KC, Keeley EC. Very late presentation in ST elevation myocardial infarction: Predictors and long-term mortality. *Int J Cardiol Heart Vasc*. 2019;22:156–9.

237 Bouisset F, Gerbaud E, Bataille V, *et al.* Percutaneous Myocardial Revascularization in Late-Presenting Patients With STEMI. *J Am Coll Cardiol*. 2021;78:1291–305.

238 Al Rimon R, Nelson VL, Brunt KR, *et al.* High-impact opportunities to address ischemia: a focus on heart and circulatory research. *Am J Physiol Heart Circ Physiol*. 2022;323:H1221–30.

239 De Luca L, Veneziano FA, Karaboue M. Late Presenters with ST-Elevation Myocardial Infarction: A Call to Action. *J Clin Med*. 2022;11:5169.

240 Yang FH, Pyle WG. Reduced cardiac CapZ protein protects hearts against acute ischemia-reperfusion injury and enhances preconditioning. *J Mol Cell Cardiol*. 2012;52:761–72.

241 Simpson JA, Brunt KR, Iscoe S. Repeated inspiratory occlusions acutely impair myocardial function in rats. *J Physiol*. 2008;586:2345–55.

242 Carter SG, Karl DW. Inorganic phosphate assay with malachite green: an improvement and evaluation. *J Biochem Biophys Methods*. 1982;7:7–13.

243 Patton C, Thompson S, Epel D. Some precautions in using chelators to buffer metals in biological solutions. *Cell Calcium*. 2004;35:427–31.

244 Zhao Y, Rafatian N, Feric NT, *et al.* A Platform for Generation of Chamber-Specific Cardiac Tissues and Disease Modeling. *Cell*. 2019;176:913-927.e18.

245 Gillis TE, Klaiman JM, Foster A, *et al.* Dissecting the role of the myofilament in diaphragm dysfunction during the development of heart failure in mice. *Am J Physiol Heart Circ Physiol*. 2016;310:H572-586.

246 Kane AE, Bisset ES, Keller KM, *et al.* Age, Sex and Overall Health, Measured As Frailty, Modify Myofilament Proteins in Hearts From Naturally Aging Mice. *Sci Rep*. 2020;10:10052.

247 Foster AJ, Platt MJ, Huber JS, *et al.* Central-acting therapeutics alleviate respiratory weakness caused by heart failure-induced ventilatory overdrive. *Sci Transl Med*. 2017;9:eaag1303.

248 Shaw EE, Wood P, Kulpa J, *et al.* Relaxin alters cardiac myofilament function through a PKC-dependent pathway. *Am J Physiol-Heart Circ Physiol*. 2009;297:H29–36.

249 Alkhalil M, Choudhury RP. Reperfusion Treatment in Late Presentation Acute Myocardial Infarction. *Circ Cardiovasc Interv*. 2018;11:e007287.

250 Wang R, Wang Z, Wu L. Carbon monoxide-induced vasorelaxation and the underlying mechanisms. *Br J Pharmacol*. 1997;121:927–34.

251 Jiang LH, Gawler DJ, Hodson N, *et al.* Regulation of cloned cardiac L-type calcium channels by cGMP-dependent protein kinase. *J Biol Chem*. 2000;275:6135–43.

252 Abramochkin DV, Haertdinov NN, Porokhnya MV, *et al.* Carbon monoxide affects electrical and contractile activity of rat myocardium. *J Biomed Sci*. 2011;18:40.

253 Uemura K, Adachi-Akahane S, Shintani-Ishida K, *et al.* Carbon monoxide protects cardiomyogenic cells against ischemic death through L-type Ca2+ channel inhibition. *Biochem Biophys Res Commun*. 2005;334:661–8.

254 Kuo IY, Ehrlich BE. Signaling in Muscle Contraction. *Cold Spring Harb Perspect Biol*. 2015;7:a006023.

255 Barrick SK, Greenberg MJ. Cardiac myosin contraction and mechanotransduction in health and disease. *J Biol Chem*. 2021;297:101297.

256 Cardiac Myosin Binding Protein C | Circulation Research. https://www.ahajournals.org/doi/full/10.1161/01.RES.84.10.1117 (accessed 15 January 2024)

257 Monasky MM, Taglieri DM, Patel BG, *et al.* p21-activated kinase improves cardiac contractility during ischemia-reperfusion concomitant with changes in troponin-T and myosin light chain 2 phosphorylation. *Am J Physiol Heart Circ Physiol*. 2012;302:H224-230.

258 MacDonald JK, Pyle WG, Reitz CJ, *et al.* Cardiac contraction, calcium transients, and myofilament calcium sensitivity fluctuate with the estrous cycle in young adult female mice. *Am J Physiol Heart Circ Physiol*. 2014;306:H938-953.

259 Kooij V, Holewinski RJ, Murphy AM, *et al.* Characterization of the cardiac myosin binding protein-C phosphoproteome in healthy and failing human hearts. *J Mol Cell Cardiol*. 2013;60:116–20.

260 Sumandea MP, Pyle WG, Kobayashi T, *et al.* Identification of a functionally critical protein kinase C phosphorylation residue of cardiac troponin T. *J Biol Chem*. 2003;278:35135–44.

261 Ke Y, Wang L, Pyle WG, *et al.* Intracellular localization and functional effects of P21-activated kinase-1 (Pak1) in cardiac myocytes. *Circ Res*. 2004;94:194–200.

262 Ohtakara K, Inada H, Goto H, *et al.* p21-activated kinase PAK phosphorylates desmin at sites different from those for Rho-associated kinase. *Biochem Biophys Res Commun*. 2000;272:712–6.

263 Claeyssen C, Bulangalire N, Bastide B, *et al.* Desmin and its molecular chaperone, the αB-crystallin: How post-translational modifications modulate their functions in heart and skeletal muscles? *Biochimie*. 2024;216:137–59.

264 Scruggs SB, Solaro RJ. The significance of regulatory light chain phosphorylation in cardiac physiology. *Arch Biochem Biophys*. 2011;510:129–34.

265 Scruggs SB, Hinken AC, Thawornkaiwong A, *et al.* Ablation of ventricular myosin regulatory light chain phosphorylation in mice causes cardiac dysfunction in situ and affects neighboring myofilament protein phosphorylation. *J Biol Chem*. 2009;284:5097–106.

266 Indicators for Ca2+, Mg2+, Zn2+ and Other Metal Ions. *Invitrogen: Molecular Probes™ Handbook—A Guide to Fluorescent Probes and Labeling Technologies, 11th Edition (2010)*. https://www.thermofisher.com/ca/en/home/references/molecular-probes-the-handbook/indicators-for-ca2-mg2-zn2-and-other-metal-ions/fluorescent-ca2-indicators-excited-with-uv-light.html (accessed 26 November 2023)

267 Walters AM, Porter GA, Brookes PS. Mitochondria as a drug target in ischemic heart disease and cardiomyopathy. *Circ Res*. 2012;111:1222–36.

268 Weber TP, Meissner A, Boknik P, *et al.* Hemin, inducer of heme-oxygenase 1, improves functional recovery from myocardial stunning in conscious dogs. *J Cardiothorac Vasc Anesth*. 2001;15:422–7.

269 Virani SS, Alonso A, Aparicio HJ, *et al.* Heart Disease and Stroke Statistics—2021 Update. *Circulation*. 2021;143. doi: 10.1161/CIR.0000000000000950

270 Li P, Hofmann PA, Li B, *et al.* Myocardial infarction alters myofilament calcium sensitivity and mechanical behavior of myocytes. *Am J Physiol*. 1997;272:H360-370.

271 Geenen DL, Malhotra A, Scheuer J. Regional variation in rat cardiac myosin isoenzymes and ATPase activity after infarction. *Am J Physiol*. 1989;256:H745-750.

272 Fearnley CJ, Roderick HL, Bootman MD. Calcium signaling in cardiac myocytes. *Cold Spring Harb Perspect Biol*. 2011;3:a004242.

273 Ruseska I, Zimmer A. Internalization mechanisms of cell-penetrating peptides. *Beilstein J Nanotechnol*. 2020;11:101–23.

274 Ma J, Lau CK, Obed A, *et al.* A cell penetrating heme oxygenase protein protects heart graft against ischemia/reperfusion injury. *Gene Ther*. 2009;16:320–8.

275 He X-H, Wang Y, Yan X-T, *et al.* Transduction of PEP-1-heme oxygenase-1 fusion protein reduces myocardial ischemia/reperfusion injury in rats. *J Cardiovasc Pharmacol*. 2013;62:436–42.

276 Sun W, Hu Q, Ji W, *et al.* Leveraging Physiology for Precision Drug Delivery. *Physiol Rev*. 2017;97:189–225.

277 Mitchell MJ, Billingsley MM, Haley RM, *et al.* Engineering precision nanoparticles for drug delivery. *Nat Rev Drug Discov*. 2021;20:101–24.

278 Galper MW, Saung MT, Fuster V, *et al.* Effect of computed tomography scanning parameters on gold nanoparticle and iodine contrast. *Invest Radiol*. 2012;47:475–81.

279 Holme MN, Fedotenko IA, Abegg D, *et al.* Shear-stress sensitive lenticular vesicles for targeted drug delivery. *Nat Nanotechnol*. 2012;7:536–43.

280 Kanamala M, Wilson WR, Yang M, *et al.* Mechanisms and biomaterials in pH-responsive tumour targeted drug delivery: A review. *Biomaterials*. 2016;85:152–67.

281 Liu S, Chen X, Bao L, *et al.* Treatment of infarcted heart tissue via the capture and local delivery of circulating exosomes through antibody-conjugated magnetic nanoparticles. *Nat Biomed Eng*. 2020;4:1063–75.

282 Rinaldi F, Del Favero E, Rondelli V, *et al.* pH-sensitive niosomes: Effects on cytotoxicity and on inflammation and pain in murine models. *J Enzyme Inhib Med Chem*. 2017;32:538–46.

283 Kazi KM, Mandal AS, Biswas N, *et al.* Niosome: A future of targeted drug delivery systems. *J Adv Pharm Technol Res*. 2010;1:374–80.

284 Livingstone S. Generation Of Cell-Penetrating Heme Oxygenase Proteins To Improve The Resistance Of Steatotic Livers To Reperfusion Injury Following Transplantation. Published Online First: 18 June 2013.

285 Moghimi SM, Hunter AC, Andresen TL. Factors controlling nanoparticle pharmacokinetics: an integrated analysis and perspective. *Annu Rev Pharmacol Toxicol*. 2012;52:481–503.

286 Hoshyar N, Gray S, Han H, *et al.* The effect of nanoparticle size on in vivo pharmacokinetics and cellular interaction. *Nanomed*. 2016;11:673–92.

287 Nagano M, Toshima JY, Siekhaus DE, *et al.* Rab5-mediated endosome formation is regulated at the trans-Golgi network. *Commun Biol*. 2019;2:419.

288 Gandek TB, van der Koog L, Nagelkerke A. A Comparison of Cellular Uptake Mechanisms, Delivery Efficacy, and Intracellular Fate between Liposomes and Extracellular Vesicles. *Adv Healthc Mater*. 2023;12:e2300319.

289 Jagadeesh ASV, Fang X, Kim SH, *et al.* Non-canonical vs. Canonical Functions of Heme Oxygenase-1 in Cancer. *J Cancer Prev*. 2022;27:7–15.

290 Tian Y, Lu J, Hao X, *et al.* FTH1 Inhibits Ferroptosis Through Ferritinophagy in the 6-OHDA Model of Parkinson's Disease. *Neurother J Am Soc Exp Neurother*. 2020;17:1796–812.

291 Ben-Mordechai T, Kain D, Holbova R, *et al.* Targeting and modulating infarct macrophages with hemin formulated in designed lipid-based particles improves

cardiac remodeling and function. *J Control Release Off J Control Release Soc*. 2017;257:21–31.

292 Lin H-H, Chen Y-H, Chang P-F, *et al.* Heme oxygenase-1 promotes neovascularization in ischemic heart by coinduction of VEGF and SDF-1. *J Mol Cell Cardiol*. 2008;45:44–55.

293 Clark JE, Foresti R, Sarathchandra P, *et al.* Heme oxygenase-1-derived bilirubin ameliorates postischemic myocardial dysfunction. *Am J Physiol-Heart Circ Physiol*. 2000;278:H643–51.

294 Hangaishi M, Ishizaka N, Aizawa T, *et al.* Induction of Heme Oxygenase-1 Can Act Protectively against Cardiac Ischemia/Reperfusion in Vivo. *Biochem Biophys Res Commun*. 2000;279:582–8.

295 Liu X, Simpson JA, Brunt KR, *et al.* Preemptive heme oxygenase-1 gene delivery reveals reduced mortality and preservation of left ventricular function 1 yr after acute myocardial infarction. *Am J Physiol-Heart Circ Physiol*. 2007;293:H48–59.

296 Yet SF, Tian R, Layne MD, *et al.* Cardiac-specific expression of heme oxygenase-1 protects against ischemia and reperfusion injury in transgenic mice. *Circ Res*. 2001;89:168–73.

297 Liu X, Simpson JA, Brunt KR, *et al.* Preemptive heme oxygenase-1 gene delivery reveals reduced mortality and preservation of left ventricular function 1 yr after acute myocardial infarction. *Am J Physiol Heart Circ Physiol*. 2007;293:H48-59.

298 Melo LG, Agrawal R, Zhang L, *et al.* Gene therapy strategy for long-term myocardial protection using adeno-associated virus-mediated delivery of heme oxygenase gene. *Circulation*. 2002;105:602–7.

299 Thomson AM, Rogers JT, Leedman PJ. Iron-regulatory proteins, iron-responsive elements and ferritin mRNA translation. *Int J Biochem Cell Biol*. 1999;31:1139–52.